

Biomechanical modelling of long bones and body mass estimation in modern and fossil species

A thesis submitted to the University of Manchester for the degree of
Doctor of Philosophy in the Faculty of Life Sciences

2014

Charlotte A. Brassey

Contents

1	Introduction	22
1.1	Limb bone safety factors	25
1.2	Stress estimation in limb bones	28
1.3	Mass estimation and biomechanical analyses of moa hind limbs . .	31
1.4	Body density and soft tissue composition	33
1.5	Alternative format	35
1.6	References	38
2	The role of cross-sectional geometry, curvature, and limb posture in maintaining equal safety factors: A computed tomography study	42
2.1	Introduction	42
2.2	Methods and Materials	42
2.2.1	Skeletal sample	42
2.2.2	Computed tomography and image analysis	42
2.2.3	Maximum force calculations	42
2.2.4	Calculation of scaling exponents	42
2.3	Results	42
2.3.1	Scaling of cross-sectional properties	42
2.3.2	Scaling of long bone curvature	42
2.3.3	Consequences of bone curvature and robusticity on maximum force scaling	42
2.3.4	Scaling of limb orientation	42
2.4	Discussion	42
2.5	Conclusions	42
2.6	Acknowledgements	42

2.7	Literature Cited	42
3	Finite element modelling versus classic beam theory: comparing methods for stress estimation in a morphologically diverse sample of vertebrate long bones	43
3.1	Introduction	43
3.2	Materials and Methods	43
3.2.1	Specimen identification	43
3.2.2	Finite element analysis	43
3.2.3	Simple beam theory	43
3.3	Results	43
3.3.1	Compression	43
3.3.2	Bending	43
3.3.3	Torsion	43
3.4	Discussion	43
3.5	Conclusions	43
3.6	Acknowledgements	43
3.7	References	43
3.8	Supplementary Material	44
3.8.1	(S1) MATLAB code for calculating A , t and t_{min}	44
3.8.2	(S2) Convergence analysis of mesh density	49
4	More than one way of being a moa: differences in leg bone robustness map divergent evolutionary trajectories in Dinornithidae and Emeidae (Dinornithiformes)	52
4.1	Introduction	52
4.2	Materials and Methods	52
4.2.1	Convex hull calibration on modern ratites	52
4.2.2	Reconstruction of moa skeletons and mass estimation	52
4.2.3	Computed tomography (CT)	52
4.2.4	Estimating hind limb robustness using finite element analysis	52
4.3	Results	52
4.3.1	Moa body mass estimates	52
4.3.2	Finite element analysis	52
4.4	Discussion	52

4.4.1	Body mass estimates	52
4.4.2	Finite element analysis results	52
4.5	Acknowledgements	52
4.6	Author Contributions	52
4.7	References	52
5	Scaling of convex hull volume to body mass in modern primates, non-primate mammals and birds: applications to the fossil record	53
5.1	Introduction	53
5.2	Methods	53
5.3	Results	53
5.4	Discussion	53
5.4.1	Convex hull mass estimation	53
5.4.2	Scaling of body mass with vol_{CH}	53
5.5	Conclusions	53
5.6	Acknowledgements	53
5.7	Author contributions	53
5.8	References	53
5.9	Supporting Information	54
5.9.1	(S1) Literature values for bird and mammal body density .	54
5.9.2	(S2) Literature values for percentage contribution of feathers to total body mass in birds	54
5.10	Supporting Information References	62
6	Discussion	66
6.1	Assumptions and interpretations of biological models	68
6.2	Body mass in biomechanical modelling	71
6.3	Linear regressions in comparative anatomy	76
6.4	The application of X-ray imaging to vertebrate morphology	80
6.5	Future work	82
6.5.1	How fat was the Dodo?	82
6.5.2	Analysis of moa hind limb muscle moment arms	84
6.5.3	Whole bone strain mapping of murine tibiae: Rapid-scan computed tomography and digital volume correlation	85
6.6	References	87

Word Count: 62,011 (including tables)

List of Figures

Introduction	22
1.1 Variation in form and function within the bones of the human (<i>Homo sapiens</i>) skeleton	24
1.2 Postural modification in a subadult emu (<i>Dromaius novaehollandiae</i>)	27
1.3 Diversity of long bone shapes present in modern bird and mammal hind limbs	30
1.4 Morphology of Dinornithiform tibiotarsi	32
1.5 The process of convex hulling	34
The role of cross-sectional geometry, curvature, and limb posture in maintaining equal safety factors: A computed tomography study	42
2.1 Calculating the cross-sectional properties of long bones	42
2.2 Calculating the curvature angle and radius of curvature of long bones	42
2.3 Sketches of load cases considered	42
2.4 Mammal consensus tree	42
2.5 Bird consensus tree	42
2.6 Radius of curvature scaled against bone length	42
2.7 Regression of maximum resistible force before yield against body mass	42
2.8 Mammal species-specific curves of force against bone angle	42
2.9 Bird species-specific curves of force against bone angle	42
2.10 Bone angle scaled against body mass	42
Finite element modelling versus classic beam theory: comparing	

methods for stress estimation in a morphologically diverse sample of vertebrate long bones	43
3.1 Three-dimensional volumetric models of vertebrate long bones considered in this study	43
3.2 The relationship between loading regime and load vector	43
3.3 Calculating shaft curvature and diaphyseal cross-sectional properties	43
3.4 Load parameters and boundary conditions for FEA models	43
3.5 Comparison of FEA and beam theory values under various loading conditions and correlations with bone geometry	43
3.6 Distribution of Von Mises stress at midshaft of a flamingo (<i>Phoenicopterus</i>) femur under compressional and torsional loading	43
3.7 Distribution of Von Mises stress at midshaft under bending	43
3.8 Individual species plots of stress against load vector	43
3.9 Species curves of combined stress against bone orientation	43
3.10 Whole bone distribution of Von Mises stress under bending	43
3.11 Supplementary Figure 1	49
3.12 Supplementary Figure 1 (cont.)	50
3.13 Supplementary Figure 2	51
 More than one way of being a moa: differences in leg bone robustness map divergent evolutionary trajectories in Dinornithidae and Emeidae (Dinornithiformes)	 52
4.1 The convex hulling process	52
4.2 Loading regimes for finite element analysis of <i>Dinornis</i> femur	52
4.3 Moa convex hulls	52
4.4 The relationship between convex hull volume and literature values for mass in extant ratites	52
4.5 Finite element analysis results	52
4.6 Inset of Figure 5	52
4.7 The distribution of Von Mises stress within the moa finite element models	52
 Scaling of convex hull volume to body mass in modern primates, non-primate mammals and birds: applications to the fossil record	 53

5.1	Simplified example of the convex hulling process	53
5.2	Convex hulling applied to the human skull	53
5.3	Effect of subdividing neck of <i>C. dromedaries</i> on convex hull volume	53
5.4	Consensus trees used in phylogenetic analysis	53
5.5	OLS regression results	53
5.6	Scaling of density against mass in birds	53
	Discussion	66
6.1	Time series of specimen acquisitions in U.K. natural history museums	72
6.2	Proportion of NMS specimens possessing associated body mass . .	73
6.3	Dodo point cloud and convex hull	83
6.4	<i>Dinornis robustus</i> myological reconstruction	84
6.5	In-situ loading rig for 4D CT scanning	86
6.6	4-point bending of mouse tibia during CT scanning	86

List of Tables

Introduction	22
The role of cross-sectional geometry, curvature, and limb posture in maintaining equal safety factors: A computed tomography study	42
2.1 Specimen List	42
2.2 SMA regression of long bone length and cross-sectional properties against body mass	42
2.3 OLS and phylogenetically based regressions of long bone length and cross-sectional properties against body mass	42
2.4 Allometry of radius of curvature against bone length in mammal and bird hind limbs	42
2.5 SMA scaling exponents of maximum force against recorded/literature body mass	42
2.6 Test for common slopes between SMA regression slopes of maximum force against assigned body mass	42
2.7 Average safety factors (SF); ratios of safety factors between loading regimes and test for the effect of phylogeny and skeletal element upon mean safety factors	42
Finite element modelling versus classic beam theory: comparing methods for stress estimation in a morphologically diverse sample of vertebrate long bones	43
3.1 Specimen list, body mass and basic geometric properties of long bones	43
3.2 Supplementary Table 1	51

More than one way of being a moa: differences in leg bone robustness map divergent evolutionary trajectories in Dinornithidae and Emeidae (Dinornithiformes)	52
4.1 Convex hull specimen list and sources of body mass	52
4.2 Finite element analysis specimen list and sources of body mass . .	52
4.3 Moa convex hull volume and body segment volumes	52
4.4 Body mass estimates of moa individuals	52
4.5 Finite element analysis results for torsional loading	52
4.6 Moa body mass estimates (kg) and 95%CI derived from palaeognath-specific regressions of femoral and tibiotarsal metrics	52
Scaling of convex hull volume to body mass in modern primates, non-primate mammals and birds: applications to the fossil record	53
5.1 Convex hull specimen list and sources of body mass	53
5.2 Supporting Information Table S1.	55
5.3 Supporting Information Table S2.	57

Abstract

Thesis Title: Biomechanical modelling of long bones and body mass estimation in modern and fossil species

Name: Charlotte A. Brassey

Institution: University of Manchester

Degree Title: Doctor of Philosophy

Date: March 2014

The thesis presented herein utilizes a variety of methods to address the biomechanical function of vertebrate hind limb bones in both modern and fossil species. In an innovative application of beam theory, the maximum force a long bone is capable of withstanding before yield is calculated under a variety of simplified loading conditions for a phylogenetically diverse sample of modern birds and mammals. In doing so, new insights are gained into the combined role of limb bone geometry and load vector in achieving mass-invariant safety factors under static loading. In particular, the avian femur is found to scale with sufficient allometry such that no postural modification is required to maintain constant safety factors across several orders of magnitude in body mass. In a methodological study, two techniques for estimating stress (simple beam theory and finite element analysis, FEA) are compared across a sample of morphologically diverse long bones. The extent to which stress estimates derived from the two modelling techniques diverge is found to correlate to aspects of the underlying bone morphology such as shaft curvature and cross-sectional asymmetry, and important recommendations are made regarding the appropriate application of both methods to skeletal material. A novel 'convex hull' volumetric mass prediction technique for fossil birds is applied to two species of extinct moa (*Dinornithiformes*) from New Zealand. The resulting mass estimates are incorporated into a FEA study of the femora and tibiotarsi of modern ratites and moa. The 'stout southern' moa (*Pachyornis australis*) is confirmed as possessing extremely robust limbs, whilst the 'terrible robust' moa (*Dinornis robustus*) is found to possess equally, if not less, robust limb bones than those of modern ratites. The results are subsequently interpreted in the context of moa habitat range and shared ancestry. Finally the convex hull mass estimation technique is extended to modern primates, and the scaling of body mass with convex hull volume is compared across birds, primates and non-primate mammals. The allometric scaling of convex hull volume in birds and primates is considered in light of interspecific variation in muscle volume, body fat and integumentary structures, and is particularly relevant to those reconstructing the soft-tissue architecture of fossil species.

Declaration

No portion of the work referred to in this thesis has been submitted in support of an application for another degree or qualification of this or any other university or other institute of learning.

Copyright Statement

- I The author of this thesis (including any appendices and/or schedules to this thesis) owns certain copyright or related rights in it (the "Copyright") and she has given the University of Manchester certain rights to use such Copyright, including for administrative purposes.
- II Copies of this thesis, either in full or in extracts and whether in hard or electronic copy, may be made only in accordance with the Copyright, Designs and Patents Act 1988 (as amended) and regulations issued under it or, where appropriate, in accordance with licensing agreements which the University has from time to time. This page must form part of any such copies made.
- III The ownership of certain Copyright, patents, designs trade marks and other intellectual property (the "Intellectual Property") and any reproductions of copyright works in this thesis, for example graphs and tables ("Reproductions"), which may be described in this thesis, may not be owned by the author and may be owned by third parties. Such Intellectual Property and Reproductions cannot and must not be made available for use without the prior written permission of the owner(s) of the relevant Intellectual Property and/or Reproductions.
- IV Further information on the conditions under which disclosure, publication and commercialisation of this thesis, the Copyright and any Intellectual Property and/or Reproductions described in it may take place is available in the University IP Policy (see <http://documents.manchester.ac.uk/DocuInfo.aspx?DocID=487>), in any relevant Thesis restriction declarations deposited in the University Library, The University Library's regulations (see <http://www.manchester.ac.uk/library/aboutus/regulations>) and in The University's policy on Presentation of Theses.

Acknowledgements

Firstly I would like to thank my supervisor Dr Bill Sellers, whose balance of good humour, hard work and attention to detail has shaped the way I think about science. It's been an honour to be his student, and I hope I can follow in his footsteps in always trying to find the fun in science. I would also like to thank my co-supervisor Dr Phil Manning for his encouragement throughout my undergraduate and postgraduate career. Phil was the reason why I decided to pursue a career in research. The enthusiasm he has for his science and public engagement is contagious amongst the group. The time and effort Bill and Phil have contributed to my PhD has made it both productive and highly enjoyable. Additionally, I would like to thank my advisor Professor Richard Preziosi for his advice throughout my PhD, and for giving me the opportunity to teach on his wonderful fieldwork course.

Secondly, I would like to thank all past and present members of the lab. Thanks go to Dr Jon Codd, Dr Robert Nudds, Dr Peter Tickle, Dr Adam van Casteren, Dr Si Furnell, Dr John Lees, Kayleigh Rose, Ciara Stafford, Thomas Püschel, Mark Morris and Dr Kathrin Peyer. Their support and friendship has been invaluable on both an academic and a personal level. I would also like to thank the members of the Manchester Palaeontology Research Group ("Women in Palaeontology"), including Dr Victoria Egerton, Dr Holly Barden, Jennifer Anné, Thomas O'Mahoney and Emma Randle.

I gratefully acknowledge the funding I received from the Natural Environment Research Council that made my Ph.D. work possible. I would also like to recognise the input of several journal editors and anonymous reviewers who have refined and improved my manuscripts along the road.

My thanks also go to the staff of the Henry Moseley X-Ray Imaging Facility, Materials Science, University of Manchester. I would particularly like to thank Professor Philip Withers for providing access to such fantastic facilities, and to Dr Tristan Lowe for his help and guidance over the last four years. Thanks also to the staff of Research Computing Services, in particular Dr Lee Margetts.

I am most grateful to Professor Richard Holdaway for his guidance and unsurpassed knowledge of all things moa. I would also like to thank the many museum curators and CT technicians who have been so patient and accommodating of my requests. Special thanks go to Dr Andrew Kitchener for the time and effort he has invested in my project.

I also thank my friends for providing much needed support. In particular, I thank Stuart Rae for the friendship and humour he has brought to my university experience. Most importantly, I would not have made it this far without the love and encouragement of my family. My parents have been a constant source of support, strength and generosity throughout my education. Thank you for being patient with me when I buried my head in my books. Thank you also to my extended family, and to my new family-in-law.

Perhaps the most surprising result to have come out of our lab in the past four years has been a marriage. When I first wandered into the Biomechanics lab, my future husband genuinely believed I was lost as “girl’s don’t come into our lab very often”. I am eternally grateful that I did. Throughout my Ph.D., Jamie has been my most vocal cheerleader, my sounding board, my shoulder to cry on and my MATLAB help file, often simultaneously. He has faith in me whenever I lose faith in myself. Thank you also to Rosie and Jess, for never failing to make me smile.

Dedicated to my grandparents,
Dorethy and Ken Barrington.

The Author

Charlotte A. Brassey

Research Interests

Biomechanics, computed tomography, finite element analysis, functional morphology, multi-body dynamic analysis, palaeontology, data visualisation, photogrammetry, fossil reconstruction

Education

Ph.D., Biomechanics and Palaeobiology *Expected:* 2014

Thesis Topic: *Biomechanical modelling of long bones and body mass estimation in modern and fossil species*

University of Manchester, Faculty of Life Sciences, Manchester, UK

Supervisors: William Sellers, Ph.D. and Phil Manning, Ph.D.

B.Sc., Geography and Geology June 2009

University of Manchester, School of Earth, Atmospheric and Environmental Science, Manchester, UK

Research Experience

Post-Doctoral Research Associate February 2014 to present

Dinosaur Scanning and Visualisation

Natural History Museum, London

Supervisor: Dr Paul Barrett

Laboratory Assistant August 2009 to January 2010

School of Biological Sciences

University of Canterbury, Christchurch, New Zealand

Supervisor: Professor Richard Holdaway

Refereed Journal Publications

1. **Brassey, C.**, Sellers, W. (2014) "Scaling of convex hull volume to body mass in modern primates, non-primate mammals and birds.". *PLoS ONE*, 9(3): e91691

2. **Brassey, C.**, Holdaway, R., Packham, A., Anne, J., Manning, P., Sellers, W. (2013) "More than one way of being a moa: differences in leg bone robustness map divergent evolutionary trajectories in Dinornithidae and Emeidae (Dinornithiformes)." *PLoS ONE*, 8(12): e82668.
3. **Brassey, C.**, Kitchener, A., Withers, P., Manning, P., Sellers, W. (2013) "The role of cross-sectional geometry, curvature and limb posture in maintaining equal safety factors: A computed tomography study." *The Anatomical Record*, 296:395-413.
4. **Brassey, C.**, Margetts, L., Kitchener, A., Withers, P., Manning, P., Sellers, W. (2012) "Finite element modelling versus classic beam theory: comparing methods for stress estimation in a morphologically diverse sample of vertebrate long bones." *Royal Society Interface*, 10:20120823.
5. Sellers, W., Hepworth-Bell, J., Falkingham, P., Bates, K., **Brassey, C.**, Egerton, V., Manning, P. (2012) "Minimum convex hull mass estimates of complete mounted skeletons." *Biology Letters*, 8(5):842-845.

Grants

PRACE Distributed European Computing Initiative (Co-investigator) 2013
 > 6 million core hours awarded on HeCTOR supercomputer

Awards

Travel Awards

- NERC Engaging the Public with your Research Sept 2012
- Geological Society of America International Section Travel Grant Oct 2013

Student Awards - University of Manchester

- Postgraduate of the Year - Faculty of Life Sciences 2014
- Shortlisted for Best Paper in the Faculty of Life Sciences 2013
- University of Manchester Glass Award 2009
 - The Glass Award acknowledges outstanding academic achievement, and is awarded to the top 0.5% of undergraduates each year
- Angela Jane Speakman Prize for aptitude in palaeontology 2009
- MacKenzie and Guilford Prize for best performance in Geology 2009

Conference Presentations

Campus Talks

- Imperial College London 3D Imaging Community: "Application of open-source photogrammetry to the field of palaeontology". March 2014
- Faculty of Life Sciences Publishing Forum: "Publishing during your thesis: the perspective of a PhD student". June 2013
- Manchester Organismal Biology Meeting: "Hind limb robustness in the extinct moa of New Zealand: A finite element study". May 2013
- Faculty of Life Sciences PhD student conference: "The role of cross-sectional geometry, curvature and limb posture in maintaining equal safety factors: A computed tomography study". May 2013
- University of Manchester Image-Based Modelling Club: "The Paleo Diet: FEA of leg bones, shrinking dinosaurs and celebrating your curves". April 2013.
- Faculty of Life Sciences PhD student conference: "Stress estimation in long bones: Finite element analysis vs. simple beam theory". May 2012.

International Conferences

- Society of Vertebrate Palaeontology, Los Angeles, CA. Alfred Romer Sherwood Pre-Doctoral Prize Session. November 2013
- Global Young Scientist Summit, Nanyang Technological University, Singapore. Selected as one of 5 doctoral students to represent the University of Manchester. January 2014

Posters

International Meetings

- Geological Society of America: "More than one way of being a moa: difference in leg bone robustness map divergent evolutionary trajectories in Dinornithidae and Emeidae (Dinornithiformes)". October 2013

University of Manchester

- Queen's Anniversary Prize recognition event: "Finite element modelling vs. classic beam theory; comparing methods for stress estimation in a morphologically diverse sample of vertebrate long bones". May 2014.
- Faculty of Life Sciences Research Symposium: "Finite element modelling versus classic beam theory: comparing stress estimates in a morphologically diverse sample of long bones". Sept 2012.

- Manchester Organismal Biology Meeting: "Scaling of cross-sectional geometric properties in vertebrate long bones: a computed tomography study". May 2011.

Teaching Experience

Demonstrator	Summer 2012 and 2013
Biol20682 - Field course in Tropical Biology (Ecuador)	
Instructor: Professor Richard Preziosi	
Demonstrator	Autumn 2011-13
Introduction to Laboratory Science	
Instructor: Professor Amanda Bamford	

Public Engagement

STEM ambassador with CRB certification	2011-Present
Royal Society Summer Exhibition 'X-Appeal' team member	2014
TeenTech Expo - University of Manchester	2013
Science Uncovered - Natural History Museum, London	2013
Issues of Biological Interest - Turton Sixth Form College	2013
Royal Society Summer Exhibition 'Chemical Ghosts' team member	2012
I'm a Scientist, Get Me Out of Here - Wellcome Trust	2012
Lab in a Lorry - Institute of Physics	2012
Manchester Science Festival - Museum of Science and Industry	2012
Biomimicry Leap Day Event - Moor Allerton Preparatory School	2012

Software Programmes

Mathematics:

MATLAB, R, Mathematica, and others

Modelling:

Geomagic, Avizo, 3DsMax, VTK, Abaqus, GaitSym, VisualSFM

Professional Service

Reviewer: Journal of Biomechanics, PLoS ONE

Chair: Faculty of Life Sciences PhD Conference, May 2013

Science Advisor: BBC Series "Secrets of Bones", aired early 2014

Media Coverage

ScienceNOW magazine (AAAS)

"Curves are tough on the bones" (2012)

LiveScience blog

"The Paleo-Diet: Dinosaurs loose weight on new study" (2012)

NBC News

"Extinct giant moa bird wasn't so giant after all" (2013)

References

William I. Sellers (Supervisor)

Reader

Phone: +44 (0)161 275 1719

Computational and Evolutionary Biology

william.sellers@manchester.ac.uk

University of Manchester

Richard Preziosi (Advisor)

Professor

Phone: +44 (0)161 275 5959

Environmental Research Group

richard.preziosi@manchester.ac.uk

University of Manchester

To paraphrase John Currey (2002):

Some biomechanical studies will leave you with the feeling that animals are just a collection of levers held together by mathematical formulae. Others seem to suggest that animals are just "oohs" and "aahs" separated by a great deal of hand-waving.

This thesis will occasionally lurch from one extreme to the other, but I've tried to make it travel down the middle.

Chapter 1

Introduction

Bone is a complex hierarchical structure consisting of the fibrous protein collagen, mineralized with calcium phosphate (Currey, 2002). In the fossil record, mineralization of the appendicular skeleton first appears in the paired fins of jawless fish dating from the Devonian (419-359Mya) (Janvier et al., 2004). Bone becomes increasingly abundant throughout the Devonian, with the diversification of both placoderms (jawed fish) and osteichthyans (bony fish), and by the Late Devonian the first tetrapods were making their way onto land supported by rigid bony limb girdles and ribcages (Coates, 2006).

The appearance of bone therefore significantly predated the terrestrialization of vertebrates, and various evolutionary scenarios have been formulated to explain the origin of bone. Physiology-based hypotheses argue that the skeleton arose as a reservoir for biolimiting minerals (Halstead Tarlo, 1964), whilst others favour a functional hypothesis linked to sensory perception (Thomson, 1977), defence against predation (Romer, 1933) or a feeding function in predatory conodonts (Donoghue and Sansom, 2002). The metabolic mechanism for producing bone can therefore be interpreted as a later ‘exaptation’ for providing support and a surface for muscle attachment, whilst the subsequent mechanism for depositing an increased quantity of phosphates, and the arrangement of bones into an internal skeleton, are adaptations for support (Gould and Vrba, 1982).

The bones comprising the modern vertebrate skeleton serve a range of functions. Tabular (flat) bones may act either for protection (as in the cranial bones, see Figure 1.1A) or as an attachment site for extensive muscles (as in the

scapula, see Figure 1.1B) (Currey, 2002), whilst the ossicles of the mammalian inner ear play a role in hearing. Whilst the ultimate form of any skeletal element reflects a compromise between the many functions it is required to undertake, the appendicular skeleton is primarily adapted for a support role. Within the appendicular skeleton, short bones are roughly the same size in all directions (as in the wrist bones and the centra of vertebrae, see Figure 1.1C) and have evolved to carry typically compressive loads over short distances (Currey, 2002). In contrast, long tubular bones (for example, the femur and tibia, see Figure 1.1D and E) are elongated in one direction and can be subject to large bending loads due to their relatively large moment arms. This thesis comprises a biomechanical functional analysis of such long bones in the vertebrate hind limb, in both extant and extinct species.

The changes in bone shape during life are often explained by Wolff's Law (Wolff, 1986), in which bone is remodelled in response to the distribution of stresses and strains during loading. This conforms to the strict adaptionist view of the form-function relationship in biology, in which traits are explained as structures optimally designed by natural selection for their functions. However the applicability of Wolff's Law, and the adaptionist programme more generally, has come into question (Gould and Lewontin, 1979; Pearson and Lieberman, 2004, and references therein). In reality, the ultimate form of a bone is dependent upon phyletic, developmental and physiological constraints, in addition to the loading regime to which it is subjected. Yet the plasticity of bone in response to its function does allow us, with caution (Bertram and Swartz, 1991), to make inferences regarding the biomechanical environment in which the bone has developed.

This dissertation utilizes a variety of methods to address the biomechanical function of vertebrate hind limb bones. First, a scaling study is conducted to investigate the role of bone geometry and posture in maintaining safety factors in the hind limbs of modern birds and mammals. The finite element method is then utilised to quantify the errors associated with applying simple beam theory to estimate stress levels in a selection of modern bones. Finite element analysis and a new 'minimum skeletal volume' mass estimation technique is then applied to a sample of ratite long bones, to answer questions regarding the hind limb

robustness of the extinct moa bird of New Zealand. This relationship between minimum skeletal volume and body mass in ratites is subsequently incorporated into a larger study including primates and non-primate mammals, in order to investigate the scaling of body density and size-related changes in body composition. A final chapter summarizes the findings of each chapter and integrates these data into the context of recent advances in biomechanical modelling.

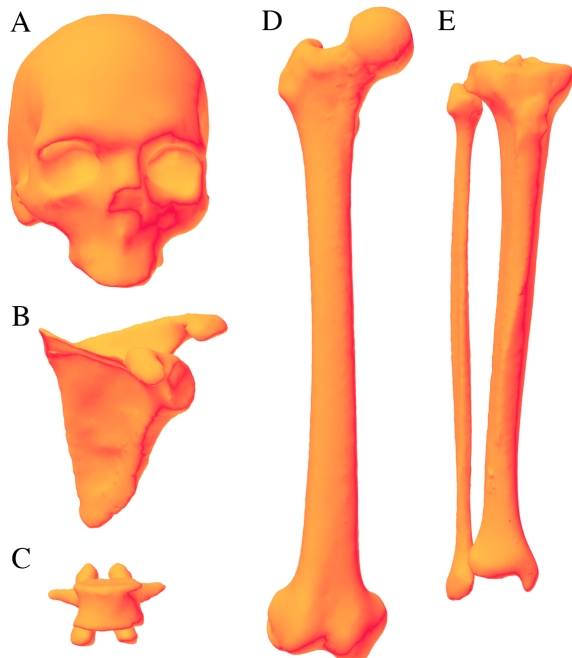


Figure 1.1: Variation in form and function within the bones of the human (*Homo sapiens*) skeleton. A, the cranium of the skull and; B, the scapula are examples of tabular bones serving the protect organs and act as muscle attachment sites; C, a lumbar vertebrae in which the centrum acts as a short bone transmitting compressive stress short distances; D, the femur and; E, the tibia and fibula are examples of long bones within the hind limb, providing a support role and acting as attachment sites for locomotor musculature. Image rendered from Visible Human CT data included in Chapter 5 using 3DsMax software.

1.1 Limb bone safety factors

Larger mammals and birds tend to adopt a more upright columnar stance during locomotion than smaller individuals (Biewener, 1989; Gatesy and Biewener, 1991). This has been linked to challenges associated with the scaling of skeletal support structures: if animals scaled geometrically, skeletal stress is predicted to scale as body mass^{0.33}. By becoming more upright, ground reaction forces incurred during locomotion pass closer to the centre of the joints and bending moments about the bone are reduced (Figure 1.2). Cortical bone is considerably stronger in compression than tension (yield stresses of 180MPa and 128MPa respectively, Cezayirlioglu et al. 1985) and such postural modifications have been suggested as a means by which safety factors (the ratio of a bone's failure strength to the maximum stress it is likely to encounter) are held relatively constant across mammals spanning several orders of magnitude in body mass (Rubin and Lanyon, 1982; Biewener, 1983).

It has become clear that the scaling behaviour of the vertebrate skeleton frequently deviates from geometric similarity however (Garcia and da Silva, 2006, and references therein), and increased limb robustness may function alongside postural modification in achieving mass-invariant safety factors. Furthermore the shift from a crouched to erect posture reflects not only the need to reduce external bending moments on the appendicular skeleton, but also acts to increase the mechanical advantage of antigravity muscles. Additionally, a crouched posture may be maintained in small individuals despite the structural advantages conferred by becoming upright, in order to increase duty factor and meet the requirements for greater power during the push-off phase of locomotion (Usherwood, 2013).

Chapter 2 of this thesis provides a unique insight into the contributions of limb bone cross-sectional geometry, curvature and posture towards maintaining equal safety factors across several orders of magnitude in body mass. Specifically, this chapter tests the null hypothesis that scaling of bone geometry alone is sufficient to maintain equal safety factors under static compressive, bending and torsional loading regimes across a broad sample of modern birds and mammals. Rather than scaling estimated stress values against body mass, a novel approach

is taken in which the maximum force a bone is capable of withstanding before yield is calculated using simple beam equations. The scaling behavior of maximum force against literature-assigned body mass is then investigated in a large and phylogenetically diverse sample, and inferences made regarding the postural modifications required to achieve mass-invariant safety factors.

Particular attention is paid to the contrasting scaling behaviour of the mammalian and avian femur. Modern birds employ a knee-based hind limb retraction system (as opposed to a mammalian hip-based system) in which the femur remains subhorizontal through the stride cycle at low to moderate speeds (Gatesy, 1995). This postural constraint and its associated loading regime has been suggested as a limiting factor on the maximum body size in modern birds (Gatesy, 1991). Chapter 2 of this dissertation contributes to this discussion by presenting new data regarding the scaling of maximum resistible force in the avian femur.

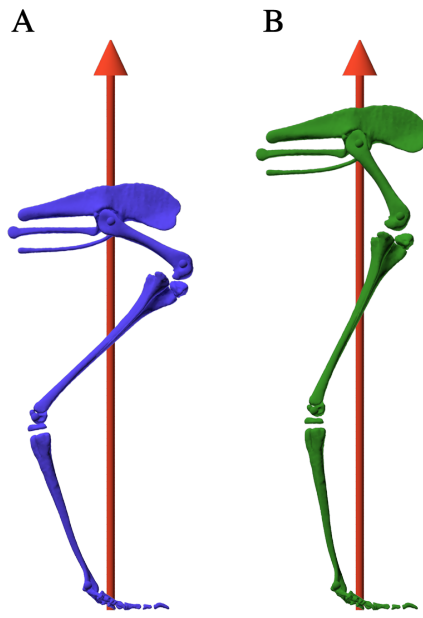


Figure 1.2: Rendering of a 3D model illustrating postural modification in a subadult emu (*Dromaius novaehollandiae*). A, Individual in a crouched posture with femur, tibiotarsus and tarsometatarsus held at a steep angle relative to the vector of the ground reaction force (GRF, red arrow). The knee and ankle joint centres are a considerable distance from the GRF vector; B, Same individual in a more erect posture with the joint centres and bone long axes more closely aligned with the GRF vector.

1.2 Stress estimation in limb bones

In Chapter 2, computed tomography (CT) is applied to vertebrate long bones in order to calculate values for cross-sectional properties such as cross-sectional area (CA), second moment of area (I) and polar moment of area (J). The *relative* values of such properties are commonly used in comparative anatomy studies when attempting to infer *in vivo* function. In physical anthropology, for example, differences in the cross-sectional properties of limb bones have been used to infer differing habitual behaviours between pre-industrial and industrialised human populations (Ruff and Hayes, 1983), between populations with contrasting foraging styles (Stock and Pfeiffer, 2001) and between men and women in subsistence economies (Marchi et al., 2006). Similarly in palaeontology, the ‘athletic ability’ of large quadrupedal dinosaur species has been compared to modern quadrupedal mammals using a metric incorporating both length and cross-sectional properties of the hind limb bones (Alexander, 1985).

However, in some cases, an estimate of *actual* skeletal stress (or maximum resistible force as in Chapter 2) is required. Reliable estimates of skeletal stress are necessary when calculating safety factors, estimating maximum body size (Hokkanen, 1986) and in reconstructing locomotion via forward dynamic analysis (Sellers et al., 2009). In such instances, bone cross-sectional properties are incorporated into classical ‘beam equations’ used by engineers to predict the stress behavior of regular slender objects. Application of beam theory to the problem of stress estimation rests upon implicit assumptions regarding the geometry of the object in question. For example, the standard beam equations commonly applied in comparative anatomy assume a high aspect ratio (length/diameter; l/d) of 16 or greater (Turner and Burr, 1993), a constant wall thickness and a straight shaft (i.e. do not account for bone curvature).

The preceding work in Chapter 2 casts doubt upon the ability of an interspecific sample of long bones to meet these assumptions. Values for shaft curvature are often high and are found to scale with body mass in some groups, aspect ratio values are typically low and cortical wall thickness is highly irregular. In reality, the morphology of vertebrate long bones can range from extremely beam-like

avian tibiotarsii to irregular mammalian femora displaying large crests, trochanters and other eminences (Figure 1.3). However, the extent to which stress estimates are affected when long bones invalidate the assumptions of beam theory has not previously been tested.

Chapter 3 of this thesis comprises a methodological study of two commonly used techniques for estimating stress in vertebrate long bones. This study compares the stress estimates derived from simple beam theory to those of finite element analysis (FEA) for a morphologically diverse sample of long bones. FEA is a numerical technique in which stresses and displacements can be calculated for a computer model representing the 3D geometry of a ‘real world’ object under given loads. FEA therefore incorporates irregularities in bone shape into skeletal stress estimates that would otherwise be ignored by simple beam theory. This chapter tests the hypothesis that stress estimates derived for long bones under both beam theory and FEA will differ, and the extent to which the two methods differ will be correlated to aspects of the underlying bone morphology (in particular, the extent to which a long bone deviates from an idealized slender beam).

Chapter 3 represents a cautionary tale for palaeontologists and anthropologists applying beam theory to data sets characterised by high morphological diversity. This study suggests improvements to commonly used beam theory equations, and makes important recommendations about when full FEA analysis is essential for reasonable biomechanical predictions.

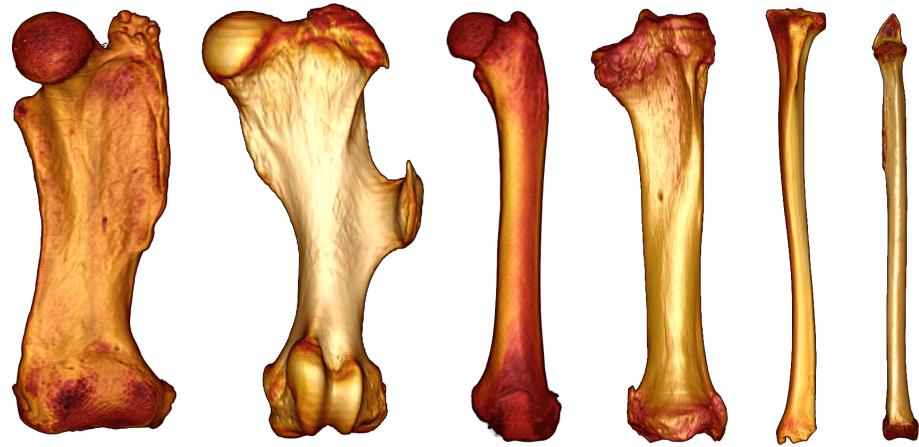


Figure 1.3: The diversity of long bone shapes present in modern bird and mammal hind limbs. From left to right: Echidna femur (*Tachyglossus aculeatus*), white rhino femur (*Ceratotherium simum*), Daurian pika femur (*Ochotona dauurica*), giraffe tibia (*Giraffa camelopardalis*), Blanford's fox tibia (*Vulpes cana*), common guillemot tibiotarsus (*Uria aalge*). Scaled to match length. Images rendered in OsiriX using CT data included in Chapter 2.

1.3 Mass estimation and biomechanical analyses of moa hind limbs

The mass of an organism is a critical constraint on its development, ecology, physiology, reproduction and biomechanics (Sellers et al., 2012). In Chapters 2 and 3, body mass is incorporated into biomechanical models in the form of loads applied to the skeleton. In studies such as these, accurate values for body mass are essential if the results of biomechanical analyses are to be interpreted reliably. The preceding chapters focus solely upon extant species for which body mass data exists, either directly from carcasses or from the published literature. When conducting functional analyses of extinct taxa, however, body mass must be inferred from the skeleton itself.

Chapter 4 of this thesis furthers the work of Alexander (1983a,b) on the hind limb biomechanics of the extinct groups of New Zealand ratites, the moa (Aves: Dinornithiformes). Prior to human settlement, New Zealand's terrestrial ecosystems were dominated by avian herbivores to an unparalleled extent (Worthy and Holdaway, 2002). One such avian herbivore, the flightless moa, diversified into 9 species of widely varying habitat and body size (Worthy and Scofield, 2012). Building upon the work of Chapter 3, this chapter applies FEA to estimate the stress levels in the hind limb long bones of two families of moa.

Given the reputation of moa as being ‘robust’ (*Dinornis robustus*, the robust terrible bird; and *Pachyornis australis*, the southern stout bird), this chapter tests the hypothesis that the limb bones of Dinornithiformes will experience lower levels of stress than those of related modern ratites under equivalent loading conditions. Previous biomechanical analyses of Dinornithiformes had been restricted to simple beam models (Alexander, 1983a,b). However there is considerable divergence in hind limb morphology between families (Figure 1.4) and, as highlighted in Chapter 3, the magnitude of errors associated with applying beam theory to estimate stress will vary as a function of the underlying morphology. For the purpose of this study, it was therefore considered more appropriate to follow the FEA methodology outlined in Chapter 3.

Values for body mass incorporated into the FEA models were estimated using a novel 3D volumetric technique known as ‘convex hulling’. Previous estimates of moa body mass have been derived using predictive equations based upon hind limb dimensions such as tibiotarsal length or femoral circumference (Dickison, 2007). This approach is problematic in two ways however. Prior studies have found some species of moa to possess extremely robust limb bones (relative to overall body size) compared to modern ratites (Alexander, 1983b). Applying predictive equations derived from modern ratite bone dimensions may therefore result in considerable overestimation of body mass. Secondly, incorporating mass estimates derived from femoral geometry for example, into FEA of the same femur is highly circular.

This study therefore presents a new volume-based mass estimation equation applicable to fossil theropods, and provides a comparison of hind limb robustness across extant and extinct ratites. These results are interpreted in the context of moa habitat range and shared ancestry, and cast new light on island gigantism in flightless birds.

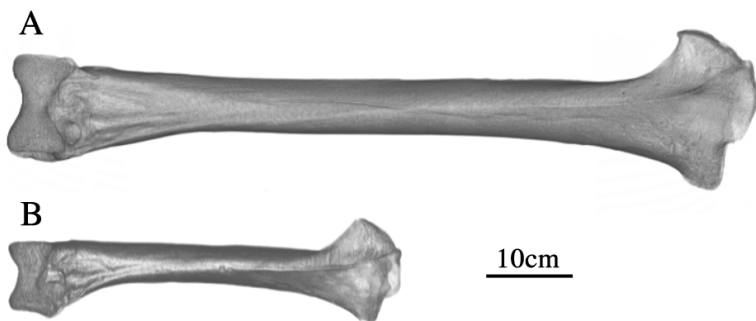


Figure 1.4: Morphology of Dinornithiform tibiotarsi. A, *Dinornis robustus*; B, *Pachyornis australis*. The tibiotarsus of *P. australis* possesses a much lower aspect (length/diameter) ratio and is more asymmetrical in cross-section at the midshaft. Image rendered in OsiriX software from CT data included in Chapter 5.

1.4 Body density and soft tissue composition

In the convex hulling process introduced in Chapter 4, minimum ‘shrink-wrap’ convex polygons are fitted around skeletal elements, providing a minimum estimate of body volume for the specimen (Figure 1.5). Convex hulling was first applied to natural history specimens as a mass prediction technique (Sellers et al., 2012) in which a calibration curve is derived by regressing minimum volume against body mass. This has subsequently been applied to fossil skeletons, by estimating the mass of giant sauropod dinosaurs such as *Giraffatitan brachai* (Sellers et al., 2012) and *Argentinosaurus huinculensis* (Sellers et al., 2013). It is in this capacity that convex hulling is applied to fossil birds in Chapter 4.

Chapter 5 builds upon the work of the previous chapter by including an additional primate-specific convex hull mass prediction equation, to complement those already existing for quadrupedal mammals (Sellers et al., 2012) and ratite birds (Brassey et al., 2013a). Primate-specific mass prediction equations are particularly of interest to those in the field of physical anthropology. In the past, mass estimation techniques applied to hominid remains have been limited to predictive equations based upon single skeletal elements or multivariate regressions of several skeletal metrics (Auerbach and Ruff, 2005). This study presents the first whole-body volumetric mass estimation technique applicable to primates, including both phylogenetically-corrected and -uncorrected equations.

Additionally, Chapter 5 goes further by investigating the scaling behaviour of convex hull volume to body mass across primates, non-primate mammals and flightless birds. Specifically, this study tests the null hypothesis that convex hull volume will scale isometrically with respect to body mass across these groups. Any significant deviation from isometry is understood as representing a mass-dependent change in carcass apparent density (body mass/convex hull volume). This is subsequently interpreted in terms of the ‘missing mass’ of soft tissues excluded by the convex hulling process (Figure 1.5) including muscle mass, integument and body fat, all of which vary considerably between species. This discussion is particularly relevant to those working in the field of fossil

reconstruction for whom modelling of soft tissue architecture is an on-going challenge.

Finally, Chapter 5 includes a critique of convex hulling as a mass prediction technique. Whilst volumetric techniques have been heralded as "the best approach currently available" (Sellers et al., 2012, pg. 4), they are not without their difficulties. This study highlights important caveats to the application of volumetric mass estimation to fossils, and emphasises the need for accurate skeletal mounts when working with museum specimens. In this case, sensitivity analyses involving the manipulation of 3D skeletal models and subsequent convex hulling is suggested as a means to quantify the errors in mass and inertial properties associated with mounting bias.



Figure 1.5: Convex hulling. A, the skin outline of a squirrel monkey (*Saimiri Sciureus*) hind limb derived from CT data; B, the femur and tibia segmented from the CT scan; C, the convex hulls fitted to the femur and tibia outlined in blue. Note the extent of 'missing' soft tissue not included within the bounds of the convex hulls, particularly around the femur.

1.5 Alternative format

The thesis is being presented in the alternative format in accordance with the rules and regulations of the University of Manchester. All four results chapters presented herein have been published as articles in peer-reviewed journals during the course of my PhD. These chapters have been inserted in their final typeset as specified by the individual journals. As such, each chapter differs in layout and referencing style. Listed below are the details of each article, its final journal destination and the contribution of each author to the work presented.

Chapter 2: The role of cross-sectional geometry, curvature, and limb posture in maintaining equal safety factors: A computed tomography study.

Authors: Charlotte A. Brassey, Andrew C. Kitchener, Philip J. Withers, Phillip L. Manning and William I. Sellers

Destination: Anatomical Record, 296(3): 395-413. doi: 10.1002/ar.22658

Contribution of authors: All museum work was carried out myself, with the assistance of Dr A. Kitchener (National Museums Scotland). My supervisors Dr. W. Sellers and Dr. P. Manning provided advice and guidance on data collection and analysis. CT facilities at the Henry Moseley X-Ray Facility were provided by Prof. P. Withers. All CT data was collected myself, under the supervision of facility technicians. I conducted all image processing and statistical analyses. As the first author on this paper, I was fully responsible for writing the text of the manuscript. All co-authors reviewed and provided comments. These comments, along with corrections advised by two anonymous reviewers during the peer-review process, were incorporated into the final published version presented here.

Chapter 3: Finite element modelling versus classic beam theory: comparing methods for stress estimation in a morphologically diverse sample of vertebrate long bones.

Authors: Charlotte A. Brassey, Lee Margetts, Andrew C. Kitchener, Philip J.

Withers, Phillip L. Manning and William I. Sellers

Destination: Royal Society Interface, 10. doi: 10.1098/rsif.2012.0823

Contribution of authors: All CT data used in this study was previously collected by myself as part of the first manuscript. My supervisors Dr. W. Sellers and Dr. P. Manning provided advice and guidance on data collection and analysis. CT facilities at the Henry Moseley X-Ray Facility were provided by Prof. P. Withers. Advise and assistance regarding FEA was provided by Dr. L. Margetts. I created all models, ran the FEA and conducted the statistical analysis. As the first author on this paper, I was fully responsible for writing the text of the manuscript. All co-authors reviewed and provided comments. These comments, along with corrections advised by three anomymous reviewers during the peer-review process, were incorporated into the final published version presented here.

Chapter 4: More than one way of being a moa: differences in leg bone robustness map divergent evolutionary trajectories in Dinornithidae and Emeidae (Dinornithiformes).

Authors: Charlotte A. Brassey, Richard N. Holdaway, Abigail G. Packham, Jennifer Anné, Phillip L. Manning and William I. Sellers

Destination: PLoS ONE, 8(12): e82668. doi: 10.1371/journal.pone.0082668

Contribution of authors: The CT data used in this study consisted of data previously collected as part of the first manuscript, and scans undertaken by myself and Prof. R. Holdaway in New Zealand. My supervisors Dr. W. Sellers and Dr. P. Manning provided advice and guidance on data collection and analysis. This chapter represents a continuation of work begun by A. Packham as part of her Masters thesis, however none of her data have been presented in the manuscript. LiDAR data was collected in the University Museum of Zoology, Cambridge by Dr. W. Sellers, Dr. P. Manning, J. Anne and myself. I created all models, ran the FEA and conducted the statistical analysis. As the first author on this paper, I was fully responsible for writing the text of the

manuscript. All co-authors reviewed and provided comments. These comments, along with corrections advised by three anonymous reviewers during the peer-review process, were incorporated into the final published version presented here.

Chapter 5: Scaling of convex hull volume to body mass in modern primates, non-primate mammals and birds.

Authors: Charlotte A. Brassey and William I. Sellers

Destination: PLoS ONE, 9(3): e91691. doi: 10.3171/journal.pone.0091691

Contribution of authors: The LiDAR data used in this study was collected as part of two previous studies. The non-primate mammal data was originally published in 2012 in a study by W. Sellers, on which I was a co-author (Sellers et al., 2012). The ratites included in the ‘bird’ dataset of this study were originally scanned by myself as part of the moa FEA study forming the third data chapter of this thesis. The primate CT data was made freely available by Kyoto University’s Primate Research Institute and was downloaded from their website. I created all primate and bird models. Models already existed for the non-primate mammals and are the same as those published by Sellers et al. I ran the convex hulling operations and conducted the statistical analysis. As the first author on this paper, I was fully responsible for writing the text of the manuscript. My co-author reviewed and provided comments. These comments, along with corrections advised by three reviewers during the peer-review process, were incorporated into the final published version presented here.

1.6 References

- Alexander, R. (1983a). Allometry of the leg bones of moas (Dinornithes) and other birds. *Journal of Zoology*, 200(2):215–231.
- Alexander, R. (1983b). On the massive legs of a moa (*Pachyornis elephantopus*, Dinornithes). *Journal of Zoology*, 201(3):363–376.
- Alexander, R. (1985). Mechanics of posture and gait of some large dinosaurs. *Zoological Journal of the Linnean Society*, 83(1):1–25.
- Auerbach, B. M. and Ruff, C. B. (2005). Human body mass estimation: a comparison of "morphometric" and "mechanical" methods. *American Journal of Physical Anthropology*, 126(4):331–342.
- Bertram, J. E. A. and Swartz, S. M. (1991). The ‘law of bone transformation’: A case of crying Wolff? *Biological Reviews*, 66(3):245–273.
- Biewener, A. A. (1983). Allometry of quadrupedal locomotion: the scaling of duty factor, bone curvature and limb orientation to body size. *Journal of Experimental Biology*, 105(1):147.
- Biewener, A. A. (1989). Scaling body support in mammals: limb posture and muscle mechanics. *Science*, 245(4913):45–48.
- Brassey, C. A., Holdaway, R. N., Packham, A. G., Anne, J., Manning, P. L., and Sellers, W. I. (2013a). More Than One Way of Being a Moa: Differences in Leg Bone Robustness Map Divergent Evolutionary Trajectories in Dinornithidae and Emeidae (Dinornithiformes). *PLoS ONE*, 8(12):e82668.
- Brassey, C. A., Kitchener, A. C., Withers, P. J., Manning, P. L., and Sellers, W. I. (2013b). The Role of Cross-Sectional Geometry, Curvature, and Limb Posture in Maintaining Equal Safety Factors: A Computed Tomography Study. *The Anatomical Record: Advances in Integrative Anatomy and Evolutionary Biology*, 296(3):395–413.
- Brassey, C. A., Margetts, L., Kitchener, A. C., Withers, P. J., Manning, P. L., and Sellers, W. I. (2012). Finite element modelling versus classic beam theory: comparing methods for stress estimation in a morphologically diverse

- sample of vertebrate long bones. *Journal of The Royal Society Interface*, 10(79):20120823.
- Brassey, C. A. and Sellers, W. I. (2014). Scaling of convex hull volume to body mass in modern primates, non-primate mammals and birds. *PLoS ONE*, 9:e91691.
- Cezayirlioglu, H., Bahniuk, E., Davy, D. T., and Heiple, K. G. (1985). Anisotropic yield behavior of bone under combined axial force and torque. *Journal of Biomechanics*, 18(1):61–69.
- Coates, M. I. (2006). The Devonian tetrapod *Acanthostega gunnari* Jarvik: postcranial anatomy, basal tetrapod interrelationships and patterns of skeletal evolution. *Transactions of the Royal Society of Edinburgh: Earth Sciences*, 87(03):363–421.
- Currey, J. D. (2002). *Bones: Structure and Mechanics*. Princeton University Press, Oxford.
- Dickison, M. R. (2007). *The allometry of giant flightless birds*. PhD thesis, Duke University, Durham, NC, USA.
- Donoghue, P. C. J. and Sansom, I. J. (2002). Origin and early evolution of vertebrate skeletonization. *Microscopy research and technique*, 59(5):352–72.
- Garcia, G. J. M. and da Silva, J. K. L. (2006). Interspecific allometry of bone dimensions: A review of the theoretical models. *Physics of Life Reviews*, 3(3):188–209.
- Gatesy, S. M. (1991). Hind limb scaling in birds and other theropods: implications for terrestrial locomotion. *Journal of Morphology*, 209(1):83–96.
- Gatesy, S. M. (1995). Functional evolution of the hindlimb and tail from basal theropods to birds. In Thomason, J. J., editor, *Functional Morphology in Vertebrate Palaeontology*, pages 219–234. Cambridge University Press, Cambridge.
- Gatesy, S. M. and Biewener, A. A. (1991). Bipedal locomotion: effects of speed, size and limb posture in birds and humans. *Journal of Zoology*, 224(1):127–147.

- Gould, S. J. and Lewontin, R. C. (1979). The Spandrels of San Marco and the Panglossian Paradigm: A Critique of the Adaptationist Programme. *Proceedings of the Royal Society of London. Series B. Biological Sciences*, 205(1161):581–598.
- Gould, S. J. and Vrba, E. S. (1982). Exaptation-a missing term in the science of form. *Paleobiology*, 8(1):4–15.
- Halstead Tarlo, L. B. (1964). The origin of bone. In Blackwood, H. J., editor, *Bone and Tooth*, pages 3–17. Pergamon Press, New York.
- Hokkanen, J. E. I. (1986). The size of the largest land animal. *Journal of Theoretical Biology*, 118:491–499.
- Janvier, P., Arsenault, M., and Desbiens, S. (2004). Calcified cartilage in the paired fins of the osteostracan *Escuminaspis laticeps* (Traquair 1880), from the Late Devonian of Miguasha (Quebec, Canada), with a consideration of the early evolution of the pectoral fin endoskeleton in vertebrates. *Journal of Vertebrate Paleontology*, 24(4):773–779.
- Marchi, D., Sparacello, V. S., Holt, B. M., and Formicola, V. (2006). Biomechanical approach to the reconstruction of activity patterns in Neolithic Western Liguria, Italy. *American Journal of Physical Anthropology*, 131(4):447–455.
- Pearson, O. M. and Lieberman, D. E. (2004). The aging of Wolff's "law": ontogeny and responses to mechanical loading in cortical bone. *Yearbook of Physical Anthropology*, 47:63–99.
- Romer, A. S. (1933). Eurypterid influence on vertebrate history. *Science*, 78(2015):114–117.
- Rubin, C. T. and Lanyon, L. E. (1982). Limb mechanics as a function of speed and gait: a study of functional strains in the radius and tibia of horse and dog. *Journal of Experimental Biology*, 101(1):187.
- Ruff, C. B. and Hayes, W. C. (1983). Cross-sectional geometry of Pecos Pueblo femora and tibiae-a biomechanical investigation: I. Method and general patterns of variation. *American Journal Of Physical Anthropology*, 60(3):359–381.

- Sellers, W. I., Hepworth-Bell, J., Falkingham, P. L., Bates, K. T., Brassey, C. A., Egerton, V. M., and Manning, P. L. (2012). Minimum convex hull mass estimations of complete mounted skeletons. *Biology Letters*, 8(5):842–845.
- Sellers, W. I., Manning, P. L., Lyson, T., Stevens, K., and Margetts, L. (2009). Virtual palaeontology: Gait reconstruction of extinct vertebrates using high performance computing. *Palaeontologia Electronica*, 12(3):11A.
- Sellers, W. I., Margetts, L., Coria, R. A., and Manning, P. L. (2013). March of the Titans: The Locomotor Capabilities of Sauropod Dinosaurs. *PLoS ONE*, 8(10):e78733.
- Stock, J. and Pfeiffer, S. (2001). Linking structural variability in long bone diaphyses to habitual behaviours: Foragers from the Southern African Later Stone Age and the Andaman Islands. *American Journal of Physical Anthropology*, 115(4):337–348.
- Thomson, K. S. (1977). On the individual history of cosmine and a possible electroreceptive function of the pore-canal system in fossil fishes. In Andrews, S. M., Miles, R. S., and Walker, A. D., editors, *Problems in vertebrate evolution*, pages 247–271. Academic Press. London, London.
- Turner, C. and Burr, D. (1993). Basic biomechanical measurements of bone: a tutorial. *Bone*, 14:595–608.
- Usherwood, J. R. (2013). Constraints on muscle performance provide a novel explanation for the scaling of posture in terrestrial animals. *Biology Letters*, 9(4):20130414.
- Wolff, J. (1986). *The law of bone remodelling* [translated from the 1892 original, Das Gesetz der Transformation der Knochen, by P. Maquet and R. Furlong]. Springer-Verlag, Berlin.
- Worthy, T. H. and Holdaway, R. N. (2002). *The Lost World of the Moa*. Indiana University Press, Bloomington.
- Worthy, T. H. and Scofield, R. P. (2012). Twenty-first century advances in knowledge of the biology of moa (Aves: Dinornithiformes): A new morphological analysis and moa diagnoses revised. *New Zealand Journal of Zoology*, 39(2):87–153.

Chapter 2

The role of cross-sectional geometry, curvature, and limb posture in maintaining equal safety factors: A computed tomography study

Anatomical Record (2013). 296(3): 395-413.

The Role of Cross-Sectional Geometry, Curvature, and Limb Posture in Maintaining Equal Safety Factors: A Computed Tomography Study

CHARLOTTE A. BRASSEY,¹ ANDREW C. KITCHENER,^{2,3} PHILIP J. WITHERS,⁴
PHILLIP L. MANNING,⁵ AND WILLIAM I. SELLERS^{1*}

¹Faculty of Life Sciences, University of Manchester, Manchester, United Kingdom

²Department of Natural Sciences, National Museum of Scotland, Edinburgh, United Kingdom

³Institute of Geography, School of Geosciences, University of Edinburgh, Drummond Street, Edinburgh, United Kingdom

⁴Henry Moseley X-Ray Imaging Facility, School of Materials, University of Manchester, Manchester, United Kingdom

⁵School of Earth, Atmospheric and Environmental Sciences, University of Manchester, Manchester, United Kingdom

ABSTRACT

The limb bones of an elephant are considered to experience similar peak locomotory stresses as a shrew. "Safety factors" are maintained across the entire range of body masses through a combination of robusticity of long bones, postural variation, and modification of gait. The relative contributions of these variables remain uncertain. To test the role of shape change, we undertook X-ray tomographic scans of the leg bones of 60 species of mammals and birds, and extracted geometric properties. The maximum resistible forces the bones could withstand before yield under compressive, bending, and torsional loads were calculated using standard engineering equations incorporating curvature. Positive allometric scaling of cross-sectional properties with body mass was insufficient to prevent negative allometry of bending (F_b) and torsional maximum force (F_t) (and hence decreasing safety factors) in mammalian (femur $F_b \propto M_b^{0.76}$, $F_t \propto M_b^{0.80}$; tibia $F_b \propto M_b^{0.80}$, $F_t \propto M_b^{0.76}$) and avian hindlimbs (tibiotarsus $F_b \propto M_b^{0.88}$, $F_t \propto M_b^{0.89}$) with the exception of avian femoral F_b and F_t . The minimum angle from horizontal a bone must be held while maintaining a given safety factor under combined compressive and bending loads increases with M_b , with the exception of the avian femur. Postural erectness is shown as an effective means of achieving stress similarity in mammals. The scaling behavior of the avian femur is discussed in light of unusual posture and kinematics. Anat Rec, 00:000–000, 2013. © 2013 Wiley Periodicals, Inc.

Key words: safety factors; effective mechanical advantage (EMA); posture; force; cross-sectional geometry

Grant sponsor: Henry Moseley X-Ray Imaging Facility; Grant numbers: EP/F007906 and EP/I02249X. Grant sponsor: Natural Environment Research Council Doctoral Training Grant; Grant numbers: NE/1528134/1.

*Correspondence to: Charlotte A. Brassey, Faculty of Life Sciences, University of Manchester, Manchester M13 9PL, United Kingdom. E-mail: charlotte.brassey-2@postgrad.manchester.ac.uk

Received 25 May 2012; Accepted 16 December 2012.

DOI 10.1002/ar.22658

Published online in Wiley Online Library
(wileyonlinelibrary.com).

In engineering terms, the “factor of safety” of a structure is the ratio of its failure strength to the maximum stress it is likely to encounter (Alexander, 1989). This term is also applied in animal biomechanics, reflecting the margin of safety present in vertebrate long bones (Alexander, 1981). Long-bone safety factors experimentally recorded during a range of routine activities such as running and jumping of mammals and birds spanning several orders of magnitude in body mass are remarkably similar, with the ratio of the bone yield stress to the peak stress varying from 1.4 to 4.1 (Rubin and Lanyon, 1982; Biewener, 1983). This relatively narrow range of values can be explained by a number of factors. First, the deposition of skeletal material is subject to strong selective pressures, and safety factors reflect a compromise between optimal stiffness and minimal weight. Not only must bone be grown and maintained, but also accelerated and decelerated through each stride during locomotion, and it is therefore adaptive to minimize the mass of bone wherever possible (Currey, 2003). Second, other physiological constraints also contribute to the ultimate geometry of long bones, such as their functioning as calcium reservoirs and stores of hematopoietic tissues. Third, the basic tetrapod body plan is highly conserved and bone material properties are relatively consistent throughout the evolution of vertebrates (Erickson et al., 2002). These factors would all tend to restrict the range of values of observed safety factors.

Limb safety factors are probably maintained across species via a combination of osteological, behavioral and postural modifications. If animals scaled their support structures isometrically, stress would increase in proportion to body mass^{1/3}. However, scaling exponents calculated for cross-sectional bone parameters are consistently above those predicted by isometry for various groups of birds and mammals (Cubo and Casinos, 1998; Garcia and da Silva, 2006). Therefore, several alternative scaling models have been formulated, in which structural support elements are posited to scale allometrically to reduce the rate at which stress increases (and safety factors decrease) with body mass (McMahon, 1973; McMahon, 1975; Garcia and da Silva, 2004).

Positive allometric scaling of duty factor would reduce strain rate in the long bones of heavier species, and has been identified in a sample of varanid lizards (Clemente et al., 2011). However, duty factor at a given Froude number appears mass-invariant across a broad sample of mammals and birds (Biewener, 1983; Gatesy and Biewener, 1991). Alexander and Jayes (1983) found different sized mammals used equal duty factors at low Froude numbers, while at high Froude numbers noncursorial mammals used larger duty factors than cursorial mammals.

Similarly, unusual asymmetrical gaits lacking a whole-body aerial phase have been reported in some large mammals (Hutchinson et al., 2003; Schmitt et al., 2006), and may assist in reducing vertical oscillations in the center of mass while ambling (Gambaryan, 1976). Yet other large mammals, such as the white rhinoceros, *Ceratotherium simum*, employ a galloping gait while maintaining safety factors in excess of those of other larger quadrupeds (Alexander and Pond, 1992).

The theory of postural modification (Biewener, 1989), in which larger species maintain stress levels by aligning limb segments closer to the line of action of the

ground reaction force (GRF) is a means by which mammals can achieve mass-invariant safety factors. By vertically aligning joints more closely to the point of limb attachment, an increasing proportion of total load is born in compression rather than bending. Bone is much stronger in compression than tension (Currey, 2002), and a decrease in tensile stress would cause a reduction in total strain and a subsequent increase in safety factor. Similarly, by increasing the effective mechanical advantage (EMA; the ratio of muscle moment arm to GRF moment arm) of the antigravity muscles, less muscular force is required to oppose GRF, which should again reduce bone loading. Positive allometric scaling of EMA in limbs has been found to characterize a wide range of mammals, spanning from a mouse to a horse (0.1–300 kg in body mass; (Biewener, 1989), and across several species of cercopithecine primates (Polk, 2002). However, changes of posture with body mass may be more complex than originally thought, and in animals larger than 300–500 kg, all options for postural modification may be exhausted (data for EMA scaling in this size range is sparse; but see Ren et al., 2010). Stronger positive allometric scaling of long-bone dimensions may therefore be required to achieve stress similarity in the largest individuals (Christiansen, 1999b; Economos, 1983).

Evidence for “differential scaling” of hind limb dimensions between small and large mammal groups remains equivocal however. Campione and Evans (2012) failed to find any significant differences in femoral length or circumference scaling exponents to body mass between size classes, regardless of whether the boundary was drawn at 20, 50, or 100 kg. Interestingly, postural data from Biewener (1989, 2005) cited above have been reinterpreted as demonstrating two postural groups (crouched, 0.01–1 kg; erect, 1–300 kg) which would suggest two distinct scaling patterns in EMA (Reilly et al., 2007). In this interpretation, large erect mammals experienced a significant increase in EMA with body size, enabling a size-dependent decrease in the relative mass of limb musculature required to maintain their posture. In contrast, small crouched mammals failed to scale EMA significantly with body mass. Limb posture was found to remain relatively constant across the “crouched” size range, with low stresses instead being maintained by relatively increasing limb muscle mass.

Unlike mammals, the sprawling limbs of iguanas and alligators are characterized by decreasing EMA with an increasingly erect posture (Blob and Biewener, 2001), although this is interpreted as being related to torsional loading due to their unusual hindlimb retraction system (Reilly et al., 2005). There are no existing data regarding the scaling of avian EMA across their entire size range (Biewener, 2005), although smaller birds have been found to possess a more crouched posture (calculated as hip height normalized against total segment length) relative to large flightless birds (Gatesy and Biewener, 1991).

A problem common among previous studies of bone scaling is that, in general, they concentrate on a particular measure (such as diameter or second moment of area) as a proxy for bone stress. However, to evaluate biomechanical arguments relating to bone loading and safety factors effectively, we need to consider more than these single measures: bone stress is a function of bone length, curvature, cross-sectional geometry, and angle,

and these can be combined mathematically to evaluate the actual relative stiffness of a particular bone. Previous studies that have addressed the scaling of stress (or proxies for relative strength) to body mass have focused on specific phylogenetic groups (Demes and Jungers, 1993; Rocha-Barbosa and Casinos, 2011). In this study, we calculate the maximum force a bone is capable of withstanding before yield under several static loading regimes, to investigate the scaling of safety factors with body size in a wide range of birds and mammals. We consider the impact of bone robusticity, curvature, and angle on safety factors, and discuss the results in the context of locomotion and peak dynamic forces.

METHODS AND MATERIALS

Skeletal Sample

Data were recorded from the femora and tibiae of 31 species of terrestrial mammals and 29 species of birds, ranging in body mass from 12.5 g (*Sorex araneus*, Common shrew) to 4.03 tons (*Elephas maximus*, Indian elephant). Specimens were selected to include as broad a range of body masses and as many clades as possible (a full list of specimens is included in Table 1). Only skeletally mature individuals were included in the final analyses to avoid any ontogenetic growth allometry. In mammals, skeletal maturity was indicated by fusion of the epiphyses, whereas in birds, it was determined by the loss of surface porosity (Tumarkin-Deratzian et al., 2006) and plumage records when available. Most specimens were sourced from museum collections (National Museums Scotland, Edinburgh; The Manchester Museum and The World Museum, Liverpool), with additional primate CT scans sourced from the Digital Morphology Museum, Kyoto University Primate Research Institute (KUPRI; www.pri.kyoto-u.ac.jp). When an associated body mass for the individual was not available from museum records, values were assigned from the literature (Table 1). External length measurements were taken with digital calipers, with the exception of the largest mammal bones, which were measured with an anthropometer.

Computed Tomography and Image Analysis

CT was carried out on whole bones specimens. Small bird and mammal bones (up to 300 mm in length, 51/60 in this study) were mounted in floral foam (OASIS, Smithers-Oasis UK, Washington, UK) in an array of up to 13 bones, and scanned in the Henry Moseley X-ray Imaging Facility, University of Manchester (X-Tek HMX 225 Custom Bay, Nikon Metrology, Tring, UK). Voxel size ranged between 53 and 119 μm , depending upon maximum bone length. Beam voltage (50–160 kV) and beam current (185–331 μA) were selected to maximize contrast between cortical bone and air. CT data were imported into CT Pro (Nikon Metrology, Tring, UK), the center of rotation determined, noise levels reduced, and the level of beam hardening selected. CT scans comprised between 652 and 2,499 tomographic slices. Data were exported in unsigned 16-bit DICOM format (VG Studio Max v. 2.0, Volume Graphics, Heidelberg, Germany).

Large bird and mammal specimens ($N=6$) were scanned in a helical CT scanner at the University of Liverpool Small Animal Teaching Hospital (Siemens SOMATOM Volume, Erlangen, Germany). Nominal pixel spacing

ranged between 191 and 790 $\mu\text{m voxel}^{-1}$, beam voltage between 120 and 140 kV and beam current between 100 and 227 μA . CT data were imported into Syngo (Siemens, Erlangen, Germany) for reconstruction with a dedicated kernel (B70s very sharp kernel, Siemens Medical Solutions). A tomographic slice ranged from 1–3 mm in thickness, with scans comprising 173–380 slices in total.

CT data for a small number of primates ($N=3$) were sourced from the Digital Morphology Museum, KUPRI. Scans were taken of whole carcasses, resulting in pixel spacings of 468–684 $\mu\text{m voxel}^{-1}$. Femora and tibiae were isolated from primate skeletons (OsiriX 32-bit, v. 3.8), and exported as unsigned 16-bit DICOMs.

As different pixel spacings were used for different-sized specimens, we compared measurements calculated from CT images against those taken manually with calipers to ensure no bias was introduced by imaging small and large bones at varying pixel spacings (with the exception of KUPRI specimens, to which access was not possible). For anteroposterior diameter (d_{AP}), for example, percentage deviation between CT and caliper-derived values was <5%, and no relationship was found between deviation and body mass M_b (kg) of the specimen (deviation $N=93.7 \log M_b^{0.62}$, $r^2=0.02$, $P>0.05$). Image calibration therefore did not unduly influence our results, and comparisons made between images derived from different machines under different conditions are valid.

Individual bones were cropped from original CT scans consisting of multiple specimens (MATLAB, v. 7.10, Mathworks, Natick, Massachusetts), exported as TIFF files and read into OsiriX. Splint-like fibulae were frequently damaged, unattached, or entirely missing from museum-sourced tibiae and to facilitate comparison these were removed from any specimens where they were present.

Tomographic slices were imported into ImageJ (version 1.46, www.rsbweb.nih.gov/ij) as virtual stacks. The “slice geometry” function of the BoneJ plug-in (version 1.2.4, Doube et al., 2010) for ImageJ was used to calculate internal bone geometric properties from a CT image taken at 50% midshaft length. Orthogonal anteroposterior and mediolateral axes were assigned to each specimen using the “orientation” function of the BoneJ plug-in. Minimum threshold pixel values for bone were defined as 40% of the difference between maximum cortical bone values and minimum values of air within the medullary cavity for each individual specimen. All pixels above the designated minimum threshold were considered as “bone” for the purposes of image analysis. Only *Elephas* was found to possess significant trabecular fill of the medullary cavity but since this still represented a very small fraction of solid bone it was digitally removed and not included in subsequent analysis.

Maximum Force Calculations

Cortical area (CA, mm^2) was calculated as the area of compact bone (defined by threshold values) within a given cross section. Both maximum and minimum values for second moment of area (I_{max} and I_{min}) and values in the anteroposterior and mediolateral direction (I_{AP} and I_{ML}) were calculated directly from the CT images, reflecting bending resistance about said axes (see Fig. 1). Polar moments of area (J , mm^4) were calculated as the sum of

TABLE 1. Specimen list

Binomial name	Common name	Sex	Museum	Accession number	Body mass (kg)
Birds					
<i>Buteo buteo</i>	Common buzzard	U	MM	BB.9009.8	0.875 ^[1]
<i>Haliaeetus albicilla</i>	White-tailed eagle	U	NMS	Z.2000.23	4.795 ^[1]
<i>Accipiter nisus</i>	Eurasian sparrowhawk	U	MM	BB.9009.3.1	0.238 ^[1]
<i>Anas crecca</i>	Common teal	U	WML	1982.1081	0.341 ^[1]
<i>Branta leucopsis</i>	Barnacle goose	U	MM	BB.9009.1	1.687 ^[1]
<i>Apteryx haastii</i>	Great spotted kiwi	M	NMS	Z.1913.48	1.900 ^[2]
<i>Uria aalge</i>	Common guillemot	U	MM	BB.9009.5.1	0.993 ^[1]
<i>Fratercula arctica</i>	Atlantic puffin	U	WML	23.7.84.3	0.381 ^[1]
<i>Haematopus ostralegus</i>	Eurasian oystercatcher	U	MM	BB.9009.4.1	0.526 ^[1]
<i>Larus marinus</i>	Great black-backed gull	F	NMS	BL1	0.860*
<i>Columba mayeri</i>	Pink pigeon	U	NMS	PS103.04	0.303 ^[1]
<i>Pezophaps solitaria</i>	Rodrigues solitaire	U	WML	T9598	11.30 ^[3]
<i>Raphus cucullatus</i>	Dodo	U	WML	1981.144	10.20 ^[4]
<i>Gallus sonneratii</i>	Sonnerat's junglefowl	M	NMS	035.47.03	0.963 ^[1]
<i>Lagopus scoticus</i>	Red grouse	F	NMS	035.04.01	0.516 ^[1]
<i>Numida meleagris</i>	Helmeted guinea fowl	U	MM	BB.9009.2.1	1.299 ^[1]
<i>Gavia immer</i>	Great northern diver	F	NMS	Z.1994.36.2	4.100*
<i>Gallinula chloropus</i>	Common moorhen	M	NMS	Z.2004.20.1	0.340 ^[1]
<i>Rallus aquaticus</i>	Water rail	M	NMS	PS 24.2000	0.125*
<i>Ardea cinerea</i>	Grey heron	U	MM	BB.8989.9.1	1.443 ^[1]
<i>Phalacrocorax carbo</i>	Great cormorant	F	NMS	Z.2004.185	1.356*
<i>Phoenicopterus ruber</i>	Rosy flamingo	F	NMS	Z.2000.193.1	2.600*
<i>Diomedea exulans</i>	Wandering albatross	U	NMS	Z.1921.143.163	7.650 ^[1]
<i>Strigops habroptilus</i>	Kakapo	U	NMS	Z.1938.56.1	1.670 ^[1]
<i>Strix aluco</i>	Tawny owl	U	MM	BB.7283.766	0.475 ^[1]
<i>Pygoscelis papua ellsworthi</i>	Gento penguin	M	NMS	Z.2007.66	4.04*
<i>Struthio camelus</i>	Ostrich	U	NMS	Z.1930.15.1	83.50 ^[1]
<i>Casuarius unappendiculatus</i>	Northern cassowary	F	NMS	Z.1995.119.1	58.00 ^[5]
<i>Tinamus solitarius</i>	Solitary tinamou	F	NMS	PS 276/04	1.550 ^[1]
Mammals					
<i>Giraffa camelopardalis</i>	Giraffe	M	NMS	Z.2001.148.3	1192 ^[6]
<i>Acinonyx jubatus</i>	Cheetah	M	NMS	GH353.09	50.17 ^[7]
<i>Nasua nasua</i>	Ring-tailed coati	U	MM	A.2305.9	3.60 ^[7]
<i>Mustela putorius</i>	European polecat	M	NMS	Z.2000.307.4	1.11 ^[7]
<i>Vulpes cana</i>	Blanford's fox	M	NMS	Z.2004.46.13	1.630*
<i>Pteropus rodricensis</i>	Rodrigues fruit bat	M	NMS	Z.2003.144.4	0.305*
<i>Petaurus breviceps</i>	Sugar glider	M	NMS	Z.2000.175.2	0.096*
<i>Erinaceus europaeus</i>	European hedgehog	U	WML	1988.226	0.682 ^[7]
<i>Procavia capensis</i>	Rock hyrax	M	NMS	Z.2009.076	3.14 ^[7]
<i>Lepus europaeus</i>	European hare	U	WML	1982.706	2.85 ^[7]
<i>Ochotona daurica</i>	Daurian pika	U	NMS	Pika 3.	0.128 ^[7]
<i>Oryctolagus cuniculus</i>	European rabbit	U	WML	1988.22w	1.74 ^[7]
<i>Ornithorhynchus anatinus</i>	Platypus	U	WML	28.12.65.1	1.501 ^[7]
<i>Tachyglossus aculeatus</i>	Short-beaked echidna	M	NMS	Z.2009.81	6.80*
<i>Callicebus cupreus</i>	Red titi	M	NMS	Z.2004.171	1.210*
<i>Callimico goeldii</i>	Goeldi's monkey	M	NMS	Z.2001.61.4	0.468*
<i>Cheirogaleus medius</i>	Fat-tailed dwarf lemur	U	NMS	R150/97	0.231*
<i>Chlorocebus aethiops</i>	Grevet monkey	M	KUPRI	PRI-CA14	5.50 ^[8]
<i>Galago senegalensis</i>	Senegal bushbaby	F	NMS	Z.2002.94.2	0.220*
<i>Gorilla beringei</i>	Eastern lowland gorilla	M	NMS	Z.2001.156	139.5 ^[8]
<i>Hylobates lar</i>	Lar gibbon	F	KUPRI	PRI-9265	5.60 ^[8]
<i>Pan paniscus</i>	Bonobo	M	W.Sellers	-	39.00 ^[8]
<i>Pan troglodytes</i>	Common chimpanzee	F	NMS	Z.2009.120	39.50 ^[8]
<i>Pithecia pithecia</i>	White-faced saki	F	NMS	Z.2003.42.1	3.800*
<i>Pongo pygmaeus</i>	Bornean orangutan	F	W.Sellers	-	37.00 ^[8]
<i>Saimiri sciureus</i>	Squirrel monkey	F	KUPRI	PRI-Ss116	0.774 ^[8]
<i>Elephas maximus</i>	Indian elephant	F	NMS	Z.2001.147	4025*
<i>Cavia aperea</i>	Brazilian guinea pig	F	NMS	Z.2004.149.3	0.334*
<i>Fukomys anselli</i>	Ansell's mole rat	F	NMS	Z.2009.124.2	0.0225*
<i>Sciurus vulgaris</i>	Red squirrel	M	NMS	Z.2003.107.5	0.371*
<i>Sorex araneus</i>	Common shrew	F	NMS	Z.2003.11	0.0124*

MM, Manchester Museum; NMS, National Museum of Scotland, Edinburgh; WML, World Museum, Liverpool; KUPRI, Kyoto Primate Research Institute, Kyoto. Associated body mass (kg) denoted with asterisk. Assigned body masses taken from following sources: [1] (Dunning, 1993), [2] (Davies, 2003), [3] (Livezey, 1993), [4] (Angst et al., 2011), [5] (Davies, 2002), [6] (Smithers, 1983), [7] (Silva and Downing, 1995), [8] (Wisconsin National Primate Research Centre, 2011).

two orthogonal measures of second moment of area for each cross section ($I_{\max} + I_{\min}$) (Boriesi and Schmidt, 2002), and reflect resistance to torsion.

When calculating the stress acting within a bone, a value for body mass (recorded or estimated) must be included in the form of force (F , the multiple of mass and gravitational acceleration). For example, the compressive stress (σ_c) acting on a bone loaded in pure axial compression is typically calculated as:

$$\sigma_c = \frac{F}{CA} \quad (1)$$

where CA is the cross sectional area (m^2). However, if predicted stress values were subsequently scaled against body mass, the mass variable would be present on both sides of the equation and the correlation would be invalid. We therefore rearrange commonly used equations for stress to solve for force, substituting in geometric parameters and values for yield stress. As such, we calculate the maximum force a bone is capable of withstanding before yield for the given loading condition. Maximum compressive force is therefore:

$$F_c = \sigma_c CA \quad (2)$$

This equation ignores the potential effects of induced bending as a result of compressive forces acting longitudinally around curvature of the shaft. Considerable curvature of hind limb bones has been identified in both mammals (Bertram and Biewener, 1988) and birds (Cubo et al., 1999), and any potential scaling effects must be incorporated into final estimates of maximum force. The moment arm of the axial load exerting a bending moment about the midshaft was calculated as the orthogonal distance taken from a chord joining proximal and distal epiphyses, to the centroid at midshaft (Biewener, 1983) in a custom MATLAB script. The angle of curvature (ξ) was then calculated at the proximal epiphysis, as the intersection between the proximal-distal chord and the centroid-proximal chord (see Fig. 2). The combined effect of compressive and induced bending forces were calculated as:

$$F_c = \frac{\sigma_c I_{AP} CA}{I_{AP} \cos \xi + CA (0.5l) r_{AP} \sin \xi} \quad (3)$$

where l is the total element length (m), and r_{AP} is the distance (m) from the section centroid to the periosteal contour along the anteroposterior axis, and I_{AP} is the second moment of area in the anteroposterior direction (m^4) (rearranged from Alexander, 1974).

Maximum bending force (F_b) in the AP direction is estimated as:

$$F_b = \frac{\sigma_b I_{AP}}{(0.5l) r_{AP}} \quad (4)$$

assuming the bone is held horizontally and clamped at midshaft to act as a cantilever (rearranged from Alexander, 1974). Again, this ignores any potential effects of curvature on total force values. Instead, maximum resistible force when bending a curved bone in the plane of initial curvature was estimated by incorporating the value k into eq. 4 as:

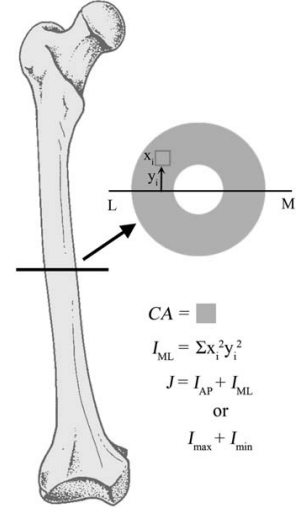


Fig. 1. Calculation of cortical area (CA), second moments of area (I), and polar moment of area (J). I is calculated for a cross section as the sum of the area of every "pixel" multiplied by the squared distance of said pixel from the axis of interest.

$$F_b = \frac{\sigma_b I_{AP}}{(0.5l) r_{AP} k} \quad (5)$$

where

$$k = 1 + 0.5 \frac{I_{AP}}{d_{ML} r_{AP}^2} \left[\frac{1}{R - r_{AP}} + \frac{1}{R} \right] \quad (6)$$

when d_{ML} is the diameter (m) in the mediolateral direction, and R is the radius of curvature (m) calculated according to the intersecting chords theorem (Roark, 1965) (see Fig. 2).

The maximum torsional force (F_t) a bone is capable of resisting before yield was calculated as:

$$F_t = \frac{\sigma_t J}{(l_{alt}) r_{max}} \quad (7)$$

where the torsional moment arm l_{alt} (m) is considered to be proportional to the length of the alternative bone element (femur length in the case of a twisting tibia, and vice versa) upon which the force due to the body mass acts as a lever (Clemente et al., 2011). Diagrams of the three load cases considered above are shown in Fig. 3. Maximum section radius r_{max} (m) was used in the calculation of torsional moment, and resulting torsional forces therefore reflect maximum possible values. The calculation of F_t in this manner is likely to be very approximate, as the application of polar moments of area rests upon an assumption of thin-walled hollow tubes with axial symmetry (i.e., a uniform cylindrical cross-sectional shape) (Roark, 1965), a situation frequently invalidated in vertebrate long bones (Brassey et al., 2013). Furthermore, the possibility of a hindlimb element being loaded in pure torsion *in vivo* is extremely unlikely, and

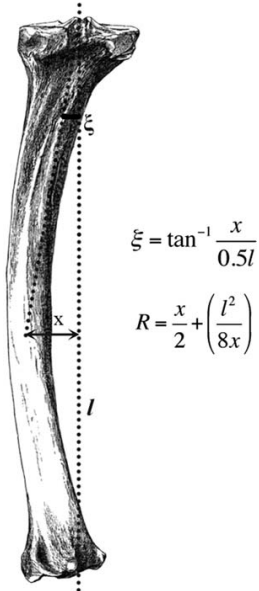


Fig. 2. Calculation of curvature angle (ξ) and radius of curvature (R). l , total chord length; x , orthogonal distance between centroid at mid-shaft and chord connecting proximal and distal epiphyses.

therefore calculated torsional loads may be unreasonably high. With these caveats in mind, torsional force is included in the present study to facilitate comparison with better-understood compressive and bending force.

The evolutionary history of vertebrates has been broadly characterized by conservation of material properties (Erickson et al., 2002), and locomotory challenges have been overcome predominantly by changes in bone size and shape. The potential for high intraspecific ontogenetic variation in Young's modulus (E) must be recognized (*Ursus maritimus* femur under torsion at 3 months, $E=6.7$ GPa; at 6 months, $E=11.2$ GPa; (Currey, 2002)). However, osteologically mature long-bone material properties are relatively restricted across broad phylogenetic groups, particularly when viewed in context of the immense diversity in morphology and body size characterizing the same groups. Young's modulus ranges between 10 and 20 GPa in intact avian long bones (Cubo and Casinos, 2000), and 15–25 GPa in mammal long bones (Zioupos et al., 2000; Erickson et al., 2002).

Cortical bone is weaker in tension than compression, and values of $\sigma_c=180$ MPa and $\sigma_b=128$ MPa for yield stress were used in the above equations (Cezayirlioglu et al., 1985). Under torsion, cortical bone is weaker still, and a value of 53 MPa for σ_t was used to calculate maximum torsional force (Cezayirlioglu et al., 1985).

The maximum body mass (M_b^{max}) a leg bone is capable of supporting under a given loading condition was calculated as:

$$M_b^{max} = \frac{F}{ga} \quad (8)$$

where g is gravitational acceleration (9.81 m s^{-2}), and a is a fraction reflecting the proportion of body mass sup-

ported by the hindlimbs (Alexander and Pond, 1992). In the case of birds, $a=1$. The broad phylogenetic diversity of the mammalian sample in question does not permit species-specific values of a to be assigned, and a value of 0.4 was used for mammals throughout. Safety factors were then calculated as the ratio of maximum body mass to given body mass:

$$SF = \frac{M_b^{max}}{M_b} \quad (9)$$

The relationship between maximum combined compressive and bending force (F_{cb}), and limb orientation was described as:

$$F_{cb} = \frac{\sigma_b I_{AP} CA}{(\sin \theta I_{AP} \cos \xi) + CA(0.5l)r_{AP}(\sin \theta \sin \xi + \cos \theta)} \quad (10)$$

where θ is the angle from the horizontal (Alexander, 1974). Values of combined force (F_{cb}) were calculated for θ between 0 and 90 degree, and curves describing the relationship between the resulting safety factors and bone angle plotted. The maximum angle from vertical (θ_{max}) at which each bone may be held for a given SF was given as the intersection of each species-specific curve with horizontal lines representing various factors of safety (12–20). These values are considerably larger than the typical safety factors calculated from peak dynamic stress (Biewener, 1982; Rubin and Lanyon, 1982), and reflect the static nature of this model. Values for θ_{max} were plotted against body mass to investigate scaling of hindlimb posture with body size.

Calculation of Scaling Exponents

Slopes were fitted by means of standardized major axis (SMA), a type II regression, in the "smatr" package (Warton et al., 2006) of statistical software "R" (www.cran.r-project.org). SMA is an appropriate regression model to use when error is introduced in both X and Y variables (particularly when the error rate of the X variable is over one-third of that on the Y ; (McArdle, 1988) and when the values being compared are of fundamentally different types (e.g., mass and distance). In this instance, error was introduced on the X axes through the inclusion of literature values for some body masses. However, when correlation coefficients do not approach 1, the potential for strong slope inflation relative to ordinary least squares (OLS) slopes must be taken into account (Warton et al., 2006). When exploring the relationship between bone length to radius of curvature, and θ_{max} to body mass (Table 4, Fig. 10), characterized by low r^2 values, Type-I OLS regressions were therefore preferred.

In addition to conventional statistical methods, we applied a phylogenetically based model to account for evolutionary relationships and statistical nonindependence of residuals. We constructed a composite phylogeny using Mesquite ver. 2.75 (<http://mesquiteproject.org>), with tree topology and branch lengths based on existing published phylogenies (see Figs. 4 and 5). Both dependent and independent variables were log transformed. A phylogenetic variance-covariance matrix was exported from Mesquite (export PDDIST function), and the MATLAB program "Regressionv2.m" (Lavin et al., 2008) used

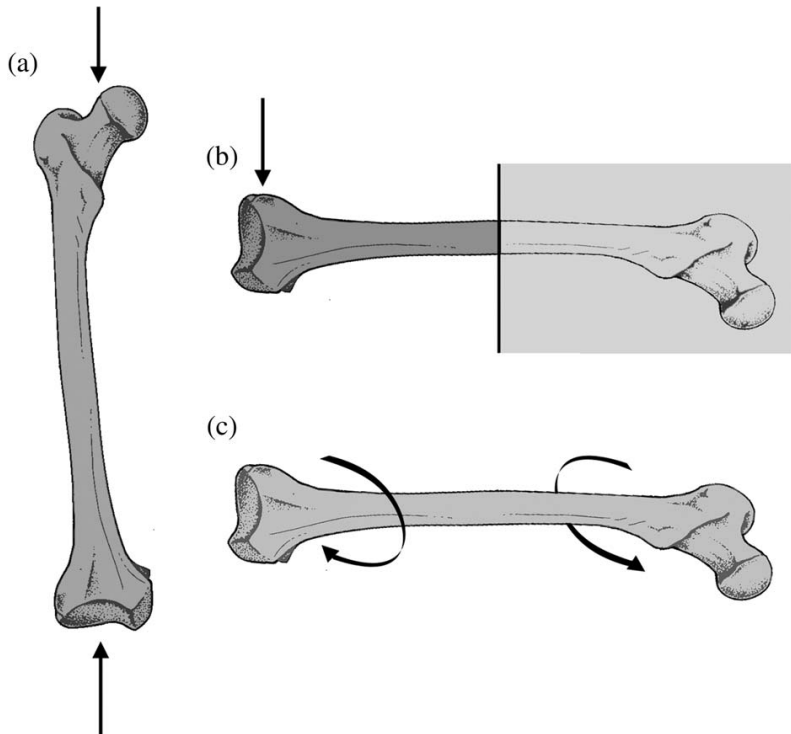


Fig. 3. Sketched of load cases considered. (a) axial compression; (b) clamped at midshaft and loaded under bending; (c) torsion.

to implement nonphylogenetic and phylogenetic regressions. Unlike ordinary least squared (OLS), phylogenetic generalized least squares (PGLS) assumes residuals are correlated, and are given by a Brownian motion model of evolution inferring a relatively strong phylogenetic signal. To estimate the strength of the phylogenetic signal in residual variation, correlation between residuals was also modeled as an Ornstein-Uhlenbeck evolutionary process (RegOU) which is often used to model the wandering motion of a population back and forth around an optimum peak (Felsenstein, 1988; Lavin et al., 2008). To compare the goodness of fit of the three models (nonphylogenetic, PGLS and RegOU), the Akaike Information Criterion (AIC) is included in Table 3 (smaller value implies better fit of model to data). As a general rule of thumb, models with an AIC of <2 units greater than the minimum AIC value are also said to have considerable support, while a difference of 4–7 units suggests considerably less support (Gartner et al., 2010). The optimal Ornstein–Uhlenbeck transformation parameter (d) was also estimated using the Regressionv2.m program. When $d=1$, the PGLS model is said to best fit the data, while a d value of 0 suggests the OLS model is the best fit (Lavin et al., 2008).

A one-sample test of slope was used to determine if SMA slope values differed from a specified scaling exponent, by testing for correlation between the residual and fitted axis scores (Warton et al., 2006). Differences

between SMA slopes were tested for using a Bartlett-corrected likelihood ratio (lr) test in smatr, which is analogous to an ANCOVA on OLS slopes. Mean radius of curvature and safety factor values were compared between phylogenetic groups ("mammal" vs. "bird") and between hindlimb elements ("femur" vs. "tibia") using a two-way ANOVA with post hoc Tukey HSD test implemented in R.

RESULTS

Scaling of Cross-sectional Properties

Scaling exponents for external dimensions and cross-sectional properties against body mass are provided in Tables 2 and 3, including both untransformed and phylogenetically corrected values. With the exception of avian tibiotarsal length and d_{AP} , nonphylogenetic OLS models provided better fits to the data (i.e., had a more negative AIC value) as compared to the phylogenetic PGLS and RegOU models (Table 3). However, RegOU models typically had AIC values ≤ 2 units greater than the comparable OLS model, suggesting this phylogenetic model also had considerable support. Values for the optimal Ornstein–Uhlenbeck transformation parameter (d) were typically much closer to zero than one, suggesting that the OLS model provided a better fit to the data than the PGLS (Lavin et al., 2008). For this reason, the chosen sample was not considered to be biasing the regressions,

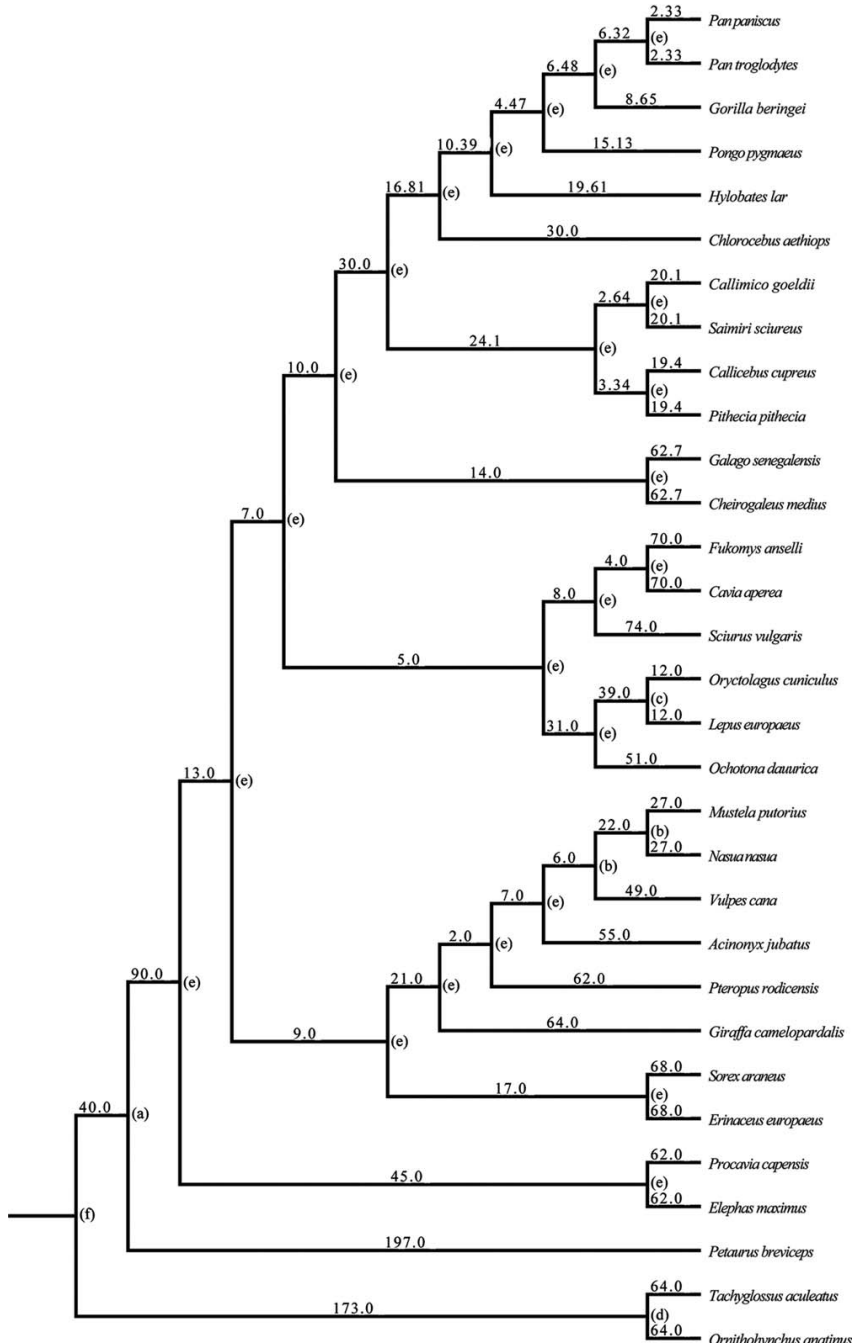


Fig. 4. Mammal consensus tree. Branch lengths given in millions of years (Mya). Tree topology based upon class-level genomic sequence study (Prasad and Allard, 2008), and several order-level molecular studies: Carnivora (Agnarsson et al., 2010); Rodentia (Blanga-Kanfi et al., 2009); Artiodactyla (Decker et al., 2009); Afrotheria (Seiffert,

2007); Primates (Arnold et al., 2010). Branch lengths taken from the following sources: [a] (Beck, 2008); [b] (Eizirik et al., 2010); [c] (Matthee et al., 2004); [d] (Rowe et al., 2008); [e] (Springer et al., 2003); [f] (Woodburne et al., 2003).

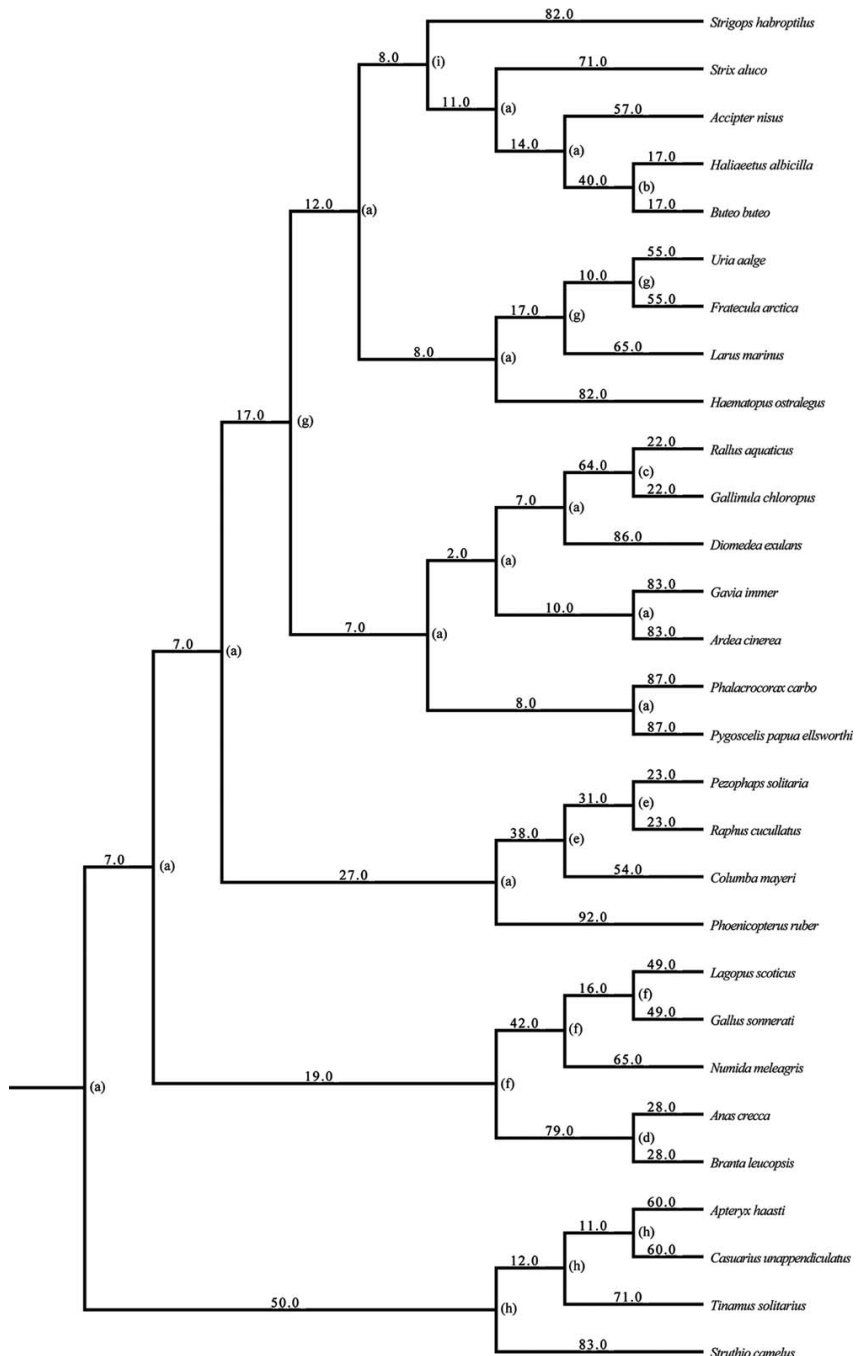


Fig. 5. Bird consensus tree. Branch lengths given in millions of years (Mya). Tree topology based upon class-level molecular study (Hackett et al. 2008) and an additional ratite genome study (Phillips et al., 2010). Branch lengths taken from following sources: [a] (Brown et al., 2008); [b] (do Amaral et al., 2009); [c] (Fain et al., 2007); [d] (Gonzalez et al., 2009); [e] (Pereira et al., 2007); [f] (Pereira and Baker, 2006); [g] (Pereira and Baker, 2008); [h] (Phillips et al., 2010); [i] (Wright et al., 2008).

TABLE 2. SMA regression of long-bone length and cross-sectional properties against body mass

	<i>n</i>	<i>a</i>	<i>b</i>	95% CI	<i>r</i> ²	<i>P</i> (isometry)
Mammal femur						
<i>l</i>	31	-1.18	0.35	0.31–0.40	0.89	0.26
<i>d</i> _{AP}	31	0.74	0.37	0.35–0.40	0.96	0.002**
CA	31	-4.77	0.74	0.68–0.80	0.96	0.01*
<i>I</i> _{AP}	31	-10.32	1.46	1.36–1.56	0.97	0.01*
<i>J</i>	31	-10.05	1.46	1.37–1.57	0.97	0.007**
Mammal tibia						
<i>l</i>	31	-1.16	0.31	0.28–0.35	0.90	0.33
<i>d</i> _{AP}	31	0.69	0.39	0.34–0.43	0.91	0.01*
CA	31	-4.89	0.73	0.67–0.80	0.94	0.03*
<i>I</i> _{AP}	31	-10.72	1.44	1.33–1.56	0.95	0.06
<i>J</i>	31	-10.37	1.47	1.34–1.61	0.94	0.03*
Bird femur						
<i>l</i>	29	-1.21	0.34	0.29–0.4	0.83	0.80
<i>d</i> _{AP}	29	0.79	0.42	0.38–0.47	0.92	<0.001***
CA	29	-4.8	0.82	0.72–0.93	0.90	0.001**
<i>I</i> _{AP}	29	-10.3	1.67	1.48–1.91	0.90	<0.001***
<i>J</i>	29	-9.85	1.68	1.49–1.88	0.91	<0.001***
Bird tibia						
<i>l</i>	29	-0.98	0.38	0.32–0.44	0.85	0.10
<i>d</i> _{AP}	29	0.72	0.39	0.36–0.43	0.95	<0.001***
CA	29	-4.86	0.82	0.75–0.89	0.95	<0.001***
<i>I</i> _{AP}	29	-10.38	1.64	1.50–1.79	0.95	<0.001***
<i>J</i>	29	-10.12	1.64	1.50–1.79	0.95	<0.001***

Regression statistics in the form $\log Y = a \log M_b^b$, where Y is an osteological parameter and M_b is body mass in kilograms. Slopes were fitted to the data by means of Model II SMA regression. Scaling exponents are given in bold. Asterisks denote level of significance (likelihood ratio test) between calculated slope and those predicted by isometry: * $P<0.05$; ** $P<0.01$; *** $P<0.001$. 95% confidence intervals (CI) and r^2 values are provided.

and only uncorrected Type I and II models are discussed in further detail.

To ensure the inclusion of fliers/gliders (*Pteropus rodricensis*, *Petaurus breviceps*), saltators (*Lepus europaeus*, *Oryctolagus cuniculus*), and aquatic species (*Ornithorhynchus anatinus*) was not heavily biasing mammalian regressions, models were re-run while excluding these specialist species. For regressions of cross-sectional properties against body mass (Table 2), original slope values and re-run slope values were not significantly different from one another ($lr=0.23$, $P=0.64$). Likewise, for regressions of estimated maximum force against body mass (Table 5), no difference was found in slope values upon excluding specialist species ($lr=0.36$, $P=0.55$). All slopes that were originally found to be significant remained so, correlation coefficients improved slightly, and interpretation of results was not affected.

We also investigated the effects of removing primates from the mammalian sample. No difference was found between slopes including and excluding primates, when regressing cross-sectional properties against body mass ($lr=0.77$, $P=0.38$), or regressing estimated maximum force against body mass ($lr=0.44$, $P=0.51$). Primate quadrupedalism is characterized as hindlimb dominated (Demers et al., 1994). We therefore investigated the effects of assigning primates a hindlimb loading ratio of $a=0.6$, while holding the remainder of the mammals at 0.4. For regressions of maximum angle (θ_{max}) against body mass (Fig. 10), no difference was found between

original slopes and those with primate-specific hindlimb loading ratios ($lr=0.32$, $P=0.57$). Despite containing several different locomotor groups, no attempt was made to subdivide the avian sample, as results elsewhere have suggested scaling exponents are not significantly different among functional groups (Dobie et al., 2012).

Length did not scale differently from isometry across several orders of magnitude in body size of mammals ($r=0.21$, $P=0.26$) and birds ($r=0.31$, $P=0.10$), with all confidence intervals including the value of 0.33 predicted by geometric similarity (Table 2). With the exception of *I*_{AP} of the mammalian tibia, all other dimensions scale more strongly than isometry ($r=0.39$, $P<0.03$ in mammals; $r=0.57$, $P\leq 0.001$ in birds). Cross-sectional properties scale with greater positive allometry in avian hindlimbs than those of mammals (Table 2), although this difference is significant only for scaling exponents of femoral and tibial *I*_{AP} ($lr=4.05$, $P<0.05$) and femoral *J* ($lr=3.93$, $P<0.05$).

Scaling of Long-Bone Curvature

The scaling exponents of radius of curvature (R) against bone length are given in Table 4. As radius of curvature is a linear measurement, geometric similarity would predict $R \propto l^1$. In both the mammalian tibia and avian femur, there is a significant relationship between R and length ($r^2>0.46$, $P<0.001$), with both exponents' confidence intervals including 1. The relationship between curvature and bone length in the mammal femur is weak but significant ($r^2=0.15$, $P=0.02$), and the confidence intervals of the slope (0.04–0.88) exclude isometry. For a given body mass, the avian femur is the most curved (smallest R), yet scales R the fastest with length ($R \propto l^{0.94}$) (Fig. 6). In contrast, the avian tibiotarsus is the least curved element investigated, and fails to scale R significantly with body mass ($r^2=0.07$, $P=0.09$).

Applying a two-way ANOVA, the “phylogeny” variable (mammals vs. birds) has a significant effect on mean R ($df=116$, $F=5.91$, $P<0.02$). A post hoc Tukey HSD test indicates mean R is significantly higher in the avian tibiotarsus than the mammal tibia ($df=116$, $P<0.001$), while there is no significant difference between bird and mammal femora. The “element” variable (femur vs. tibia) in a two-way ANOVA is significant ($df=116$, $F=10.7$, $P<0.001$), with a pairwise comparison of means indicating a significant difference between R values in the avian stylopodium and zeugopodium ($df=116$, $P<0.001$), yet no such difference is present in the mammal hindlimb.

Consequences of Bone Curvature and Robusticity on Maximum Force Scaling

The scaling exponents of maximum force a bone is able to withstand before yielding against body mass under various loading regimes are given in Table 5. All slopes are highly significant ($r^2>0.83$, $P<0.001$). If force were found to scale with body mass as $F \propto M_b^{-1}$, constant safety factors would be achieved. Negative allometry implies safety factors are decreasing with size, while positive allometry implies increasing safety factors with body mass. For all loading regimes considered, the mammalian femur and tibia and avian tibiotarsus scale force with negative allometry, with 95% confidence intervals

TABLE 3. OLS and phylogenetically based regressions of long-bone length and cross-sectional properties against body mass

	OLS				PGLS				RegOU							
	b	±95%	r ²	AIC	ln ML	b	±95%	r ²	AIC	ln ML	±95%	b	r ²	AIC	ln ML	d
Mammal femur																
<i>l</i>	0.33	0.045	0.89	-27.3	16.7	0.32	0.030	0.92	-0.23	15.0	0.32	0.035	0.91	-26.5	15.8	0.49
<i>d_{AP}</i>	0.37	0.025	0.96	-57.5	31.8	0.36	0.025	0.97	-47.0	26.5	0.36	0.025	0.96	-56.6	32.3	0.12
CA	0.72	0.055	0.96	-9.58	7.79	0.71	0.050	0.96	3.27	1.37	0.72	0.055	0.96	-8.87	8.43	0.08
<i>I_{AP}</i>	1.43	0.095	0.97	24.1	-9.07	1.42	0.105	0.96	47.4	-20.7	1.43	0.090	0.97	25.4	-8.68	0.06
<i>J</i>	1.44	0.090	0.97	22.7	-8.35	1.42	0.090	0.97	41.5	-17.7	1.44	0.090	0.97	23.7	-7.87	0.06
Mammal tibia																
<i>l</i>	0.30	0.035	0.91	-40.5	23.3	0.30	0.035	0.90	-19.2	12.6	0.30	0.035	0.91	-38.5	23.3	0.02
<i>d_{AP}</i>	0.37	0.040	0.92	-29.5	17.8	0.36	0.035	0.93	-19.6	12.8	0.37	0.035	0.92	-28.1	18.1	0.19
CA	0.71	0.055	0.95	-6.17	6.09	0.72	0.055	0.96	7.00	0.50	0.71	0.055	0.95	-4.75	6.38	0.17
<i>I_{AP}</i>	1.41	0.110	0.96	30.8	-12.4	1.46	0.100	0.96	48.4	-21.2	1.41	0.100	0.96	32.5	-12.3	0.14
<i>J</i>	1.43	0.115	0.95	37.0	-15.5	1.46	0.110	0.96	51.8	-22.9	1.43	0.110	0.95	38.6	-15.3	0.16
Bird femur																
<i>l</i>	0.31	0.055	0.83	-49.8	27.9	0.30	0.055	0.82	-46.1	26.0	0.31	0.050	0.83	-49.1	28.6	0.26
<i>d_{AP}</i>	0.41	0.045	0.92	-57.9	31.9	0.42	0.060	0.88	-41.9	23.9	0.41	0.040	0.92	-55.9	31.9	0.10
CA	0.78	0.090	0.90	-14.9	10.5	0.80	0.115	0.87	-0.93	3.46	0.78	0.095	0.90	-12.9	10.4	0.10
<i>I_{AP}</i>	1.60	0.195	0.90	28.3	-11.1	1.65	0.245	0.86	43.1	-18.5	1.60	0.190	0.90	30.3	-11.1	0.11
<i>J</i>	1.60	0.185	0.91	23.3	-8.63	1.65	0.235	0.88	38.6	-16.3	1.60	0.180	0.91	25.3	-8.64	0.10
Bird tibia																
<i>l</i>	0.35	0.050	0.85	-47.7	26.8	0.33	0.050	0.86	-49.5	27.8	0.33	0.045	0.86	-47.9	27.9	1.05
<i>d_{AP}</i>	0.38	0.030	0.95	-78.3	42.1	0.38	0.040	0.93	-62.7	34.3	0.38	0.030	0.95	-79.3	42.2	0.10
CA	0.80	0.065	0.95	-33.0	19.5	0.79	0.085	0.93	-23.0	14.5	0.80	0.070	0.95	-31.0	19.5	0.10
<i>I_{AP}</i>	1.60	0.135	0.95	5.45	0.27	1.61	0.205	0.92	25.2	-9.61	1.60	0.135	0.95	7.45	0.27	0.11
<i>J</i>	1.58	0.125	0.95	2.19	1.90	1.58	0.185	0.92	21.2	-7.6	1.58	0.130	0.95	4.19	1.90	0.08

OLS, ordinary least squares; PGLS, phylogenetically generalized least squares; RegOU, phylogenetic regression with Ornstein-Uhlenbeck process; AIC, Akaike Information Criterion; ln ML, natural log maximum likelihood; *d*, restricted maximum likelihood estimate of the Ornstein-Uhlenbeck transformation parameter; ±95%, 95% confidence intervals of the slope value. Scaling exponents are given in bold.

TABLE 4. Allometry of radius of curvature against bone length in mammal and bird hindlimbs

	OLS regression results				
	A	b	95% CI	r ²	P
Mammal femur	1.74	0.46	0.04–0.88	0.15	0.02*
Mammal tibia	0.88	0.88	0.52–1.23	0.46	0.001**
Bird femur	0.43	0.94	0.63–1.25	0.59	0.001**
Bird tibia	2.14	0.53	-0.25 to 1.31	0.07	0.09
Two-way ANOVA	<i>F</i>	<i>p</i>			
"Phylogeny"	5.91	0.017*			
"Element"	10.69	0.001**			
Interaction	14.06	<0.001***			
Post hoc Tukey HSD test	<i>P</i>				
MF:MT	0.99				
BF:BT	<0.001***				
MF:BF	0.79				
MT:BT	<0.001***				
MF:BT	<0.001***				
MT:BF	0.90				

The effect of "phylogeny" (mammal vs. bird) and skeletal "element" (femur vs. tibia) on mean radius of curvature was tested in a two-way ANOVA. A post hoc Tukey HSD test of multiple means indicates pairwise comparisons that are significantly different (*P*<0.05). MF, mammal femur; MT, mammal tibia; BF, bird femur; BT, bird tibiotarsus. A type-I OLS regression was favored due to low correlation coefficients. Scaling exponents are given in bold.

excluding 1 (Table 5, Fig. 7). In the avian femur, force scales with negative allometry under most loading conditions, yet isometry cannot be rejected (confidence intervals include 1) and constant safety factors may be

achieved. For each loading regime, a likelihood ratio test for common slopes was applied (Table 6). Scaling exponents were significantly different between groups under each loading condition (*lr*>8.70, *P*<0.03).

In the case of estimating F_c , incorporating curvature into the equation has the effect of decreasing intercept and slope values in both the mammal femur and tibia, and the avian tibiotarsus (Table 5). In contrast, the scaling exponent of $F_c \propto M_b$ in the avian femur is increased when applying eq. 3. Incorporating curvature into estimates of F_b has very little effect on intercept and slope values. In the avian femur (the most curved element investigated), the ratio of radius of curvature to mid-shaft radius (R/r) was >50 . Such high R/r values result in k values very little above 1 (mean k in avian femur = 1.01), and thus contributes very little to the calculation of F_b .

Average safety factors calculated under each loading regime are reported in Table 7. Applying a two-way ANOVA, the phylogeny variable has a highly significant effect on mean SF across loading conditions ($df=116$, $F>10.5$, $P<0.002$). A post hoc Tukey HSD test indicates mean safety factors are significantly higher in the mammalian femur than in the avian equivalent, while no such relationship exists between the mammal tibia-avian tibiotarsus. The element variable in a two-way ANOVA is also significant for compression and bending loading regimes ($df=116$, $F > 3.92$, $P<0.05$), with a pairwise comparison of means indicating safety factors are significantly lower in the mammalian zeugopodium than stylopodium ($P=0.05$).

It must be reiterated that the above safety factor values are calculated using static loading models and assume 40% of total body mass is borne through the hindlimbs in the case of mammals, as reported elsewhere (Alexander, 1989; Christiansen, 1998). When testing for the effect of phylogeny on mean safety factors, this hind-limb loading coefficient is incorporated to ensure that we are comparing like for like between bipedal birds and quadrupedal mammals.

Scaling of Limb Orientation

Species-specific safety factor curves (Figs. 8 and 9) indicate a relationship between SF and posture, in which safety factors increase as bones are held close to vertical. When a horizontal line is drawn on these graphs, intersections with SF curves represent the angle respective bones must be held at to achieve a common safety factor. As safety factors are generally lower in birds, it is possible to find a suitable value of SF that may be used to compare almost all species. However, in mammals the minimum safety factor of some species is greater than the maximum safety factor of others. Therefore, a safety factor of 15 was chosen to encompass most of the bird and mammal species. The species excluded by this safety factor (such as the common shrew, mole rat, and pika) all operate at very low bone stresses and postural angle is therefore irrelevant. Plotting θ_{max} against body mass for a safety factor of 15 (Fig. 10) gives a significant positive relationship in the case of mammal hindlimb bones, and avian tibiotarsii ($P<0.01$). For all values of safety factors considered here, there is no relationship between θ_{max} and body mass in the avian femur ($P>0.05$).

DISCUSSION

With the exception of measures of length and curvature, bird and mammal hindlimb bones do not conform

to isometry. In addition, despite strong positive allometry of cross-sectional geometric properties, maximum force continues to scale with negative isometry against body mass (Table 5, Fig. 7), demonstrating the allometric scaling of geometry is insufficient on its own to maintain uniform safety factors. The avian femur is shown to behave differently, scaling force to body mass close to isometry and potentially maintaining constant safety factors across a large size range.

Mean safety factors for static compressive loading are universally high (Figs. 8 and 9, Table 7), reaffirming the notion that limb bones do not fail under static compression alone. Incorporating curvature into equations for compression results in large decreases in estimated maximum F_c , yet still does not put bones in danger of actually failing under compressive loading. If curved bones under compression are assumed to fail in tension (due to induced bending), then incorporating the lower value of σ_b into eq. 3 would result in a further decrease in compressive safety factors.

The low correlation coefficient between curvature and length found in the mammal femur ($r^2=0.15$) is similar to those identified in previous studies (Biewener, 1983; Bertram and Biewener, 1992), in which the mammal femur was found not to scale curvature with body mass. In contrast to the above studies however, we found mammal femur R to scale below isometry (i.e., larger individuals have more curved bones), with a P value indicating this result is unlikely to have occurred by chance ($P<0.02$). However, the low correlation coefficient suggests the majority of variation in femoral curvature is due to a factor other than length. As suggested elsewhere, this may reflect a more complex muscle attachment system in the proximal limb (Bertram and Biewener, 1992), or the need to achieve a higher level of strain to promote tissue remodeling and repair (Lanyon, 1980). In the case of birds, avian femora R was also found to scale with slight negative allometry, although scatter was extremely high compared with previous studies (Cubo et al., 1999) and 95% confidence intervals included 1. Our results would suggest that scaling of curvature contributes little toward achieving mass-invariant safety factors.

Safety factors under bending typically fall between 3 and 20 (Table 7). Some individual bones, such as the heron (*Ardea cinerea*) femur and platypus (*Ornithorhynchus anatinus*) tibia, have safety factors of less than 1 under bending however, indicating that their hindlimbs could not support their body weight when statically loaded in horizontal bending. When compared with curved elements typically considered in engineering, vertebrate bones are relatively straight (as determined by R/r value), and application of eq. 5 to the estimation of F_b does not produce results significantly different to those of eq. 4. Safety factors under torsion are particularly low (Table 7), with several species possessing SF values of less than 1. However, the modeled load conditions are extreme and represent the condition where the bone is immobilized and a significant fraction of body weight acts with the lever arm of the alternative bone element. In practice, torsion is likely to be a minor contributor to total loading in mammal bones (although exceptions may exist in the limbs of small crouched mammals (Keller and Spengler, 1989; Butcher et al., 2011), and these results are unlikely to reflect the

TABLE 5. SMA Scaling exponents of maximum force against recorded/literature body mass

	<i>a</i>	<i>b</i>	95% CI	<i>r</i> ²	<i>P</i>
Compression					
MF	3.48	0.74	0.68–0.80	0.96	<0.001***
MT	3.37	0.74	0.67–0.80	0.94	<0.001***
BF	3.45	0.82	0.72–0.93	0.90	<0.001***
BT	3.40	0.82	0.75–0.89	0.95	<0.001***
Compression (incorporating curvature)					
MF	3.03	0.67	0.59–0.76	0.89	<0.001***
MT	2.74	0.74	0.64–0.85	0.86	<0.001***
BF	2.88	0.92	0.79–1.07	0.85	<0.001***
BT	2.83	0.77	0.66–0.90	0.85	<0.001***
Bending					
MF	1.78	0.76	0.70–0.82	0.95	<0.001***
MT	1.47	0.80	0.73–0.87	0.94	<0.001***
BF	1.83	0.95	0.82–1.11	0.86	<0.001***
BT	1.51	0.88	0.80–0.96	0.94	<0.001***
Bending (incorporating curvature)					
MF	1.78	0.76	0.70–0.82	0.96	<0.001***
MT	1.46	0.80	0.73–0.87	0.94	<0.001***
BF	1.83	0.95	0.82–1.10	0.86	<0.001***
BT	1.51	0.88	0.80–0.96	0.94	<0.001***
Torsion					
MF	1.32	0.80	0.73–0.87	0.95	<0.001***
MT	1.09	0.76	0.69–0.84	0.93	<0.001***
BF	1.20	0.93	0.79–1.09	0.83	<0.001***
BT	1.30	0.89	0.82–0.99	0.96	<0.001***

Regression statistics in the form $\log Y = a \log M_b^b$, where Y is calculated force (N) and M_b is body mass in kilograms. Slopes were fitted by means of model-II SMA regression. MF, mammal femur; MT, mammal tibia; BF, bird femur; BT, bird tibiotarsus. Scaling exponents are given in bold.

absolute values of torsion that occur during normal use. Furthermore, it is feasible that the particularly low safety factors calculated for the avian femur under torsion (Table 7) are a function of considering torsional lever arm to be proportional to the length of the particularly elongated avian tibiotarsus.

With the exception of the avian hindlimb under torsion, safety factors are lower in the zeugopodium than the stylopodium (Table 7). This may be explained by the well-documented phenomenon whereby the mass of bone contributes to the moment of inertia about the hip joint in proportion to the square of distance from the joint. Therefore, distal segments of the limb tend to be as light as possible to reduce the inertial forces needed to accelerate the leg during the stride, particularly in fast-moving cursors (Currey, 2003). This is reflected in an increased risk of fracture in the proximal-distal direction in the lower limbs (Van Staa et al., 2001).

Overall, these results provide further support for the hypothesis of postural modification as an effective means by which safety factors are maintained in terrestrial mammals (Biewener, 1989). Large mammals are functionally adapted to position their hindlimbs closer to vertical to achieve safety factors equal to those of small crouched mammals (Fig. 10). The heaviest mammals in this sample (*Elephas maximus* and *Giraffa camelopardalis*) are required to maintain values of θ close to 90 degree to achieve a static safety factor of 15 (*E. maximus* tibia fails to intersect safety factor line entirely; Fig. 8). Under unpredictable dynamic loading conditions, instantaneous peak stress values (and minimum θ) are likely to be significantly greater. The possibility of differential

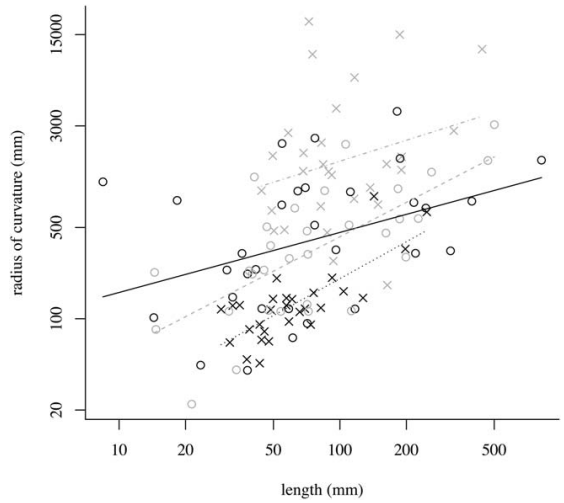


Fig. 6. Radius of curvature (mm) against bone length (mm). Black open circle, solid line, mammal femur; gray open circle, dashed line, mammal tibia; black cross, dotted line, bird femur; gray cross, dot-dash line, bird tibiotarsus. No significant relationship exists between bone length and radius of curvature in the bird tibiotarsus. Model-I OLS regression equations are mammal femur, $y=1.74x^{0.46}$; mammal tibia, $y=0.88x^{0.88}$; bird femur, $y=0.43x^{0.94}$.

scaling of limb bone dimensions was not investigated here using separate regressions of bone dimensions against body mass in small and large individuals. Yet, it is clear that the potential to increase θ further is limited in large individuals, and stronger positive allometry of bone geometry may be necessary to maintain safety factors in very large extant and extinct vertebrates (Bertram and Biewener, 1990; Christiansen, 1999a,b; Chinnery, 2004). In the future, incorporating kinematic scaling (GRF and limb postural measurements during stance) with bone morphological scaling across a broad size range may illuminate this further. In particular, postural data from the >300-kg size range of mammals is needed to compliment existing morphological data before any “break point” in behavioral and skeletal scaling can be distinguished.

While for a given value of θ , a general trend of lower safety factors in larger mammals is apparent (Fig. 8), interesting exceptions exist. The femur of the cheetah (*Acinonyx jubatus*) is predicted to experience lower SF than that of an elephant (Fig. 8). This is probably due to the long, gracile nature of the element (Day and Jayne, 2007), and may function to increase stride length and maintain high duty factors (hence lower peak limb force) in this cursor while minimizing limb mass (Hudson et al., 2011). It is also possible that the safety factors in this species are lower than in other animals. In the mammal tibia, the lowest safety factor occurs in the platypus (*O. anatinus*). These semiaquatic monotremes possess specializations for swimming that negatively affect their terrestrial locomotion, and are restricted to a walking gait on land (Fish et al., 2001). Furthermore when walking at slow speeds, the ventral side of their body remains in contact with the ground, reducing the

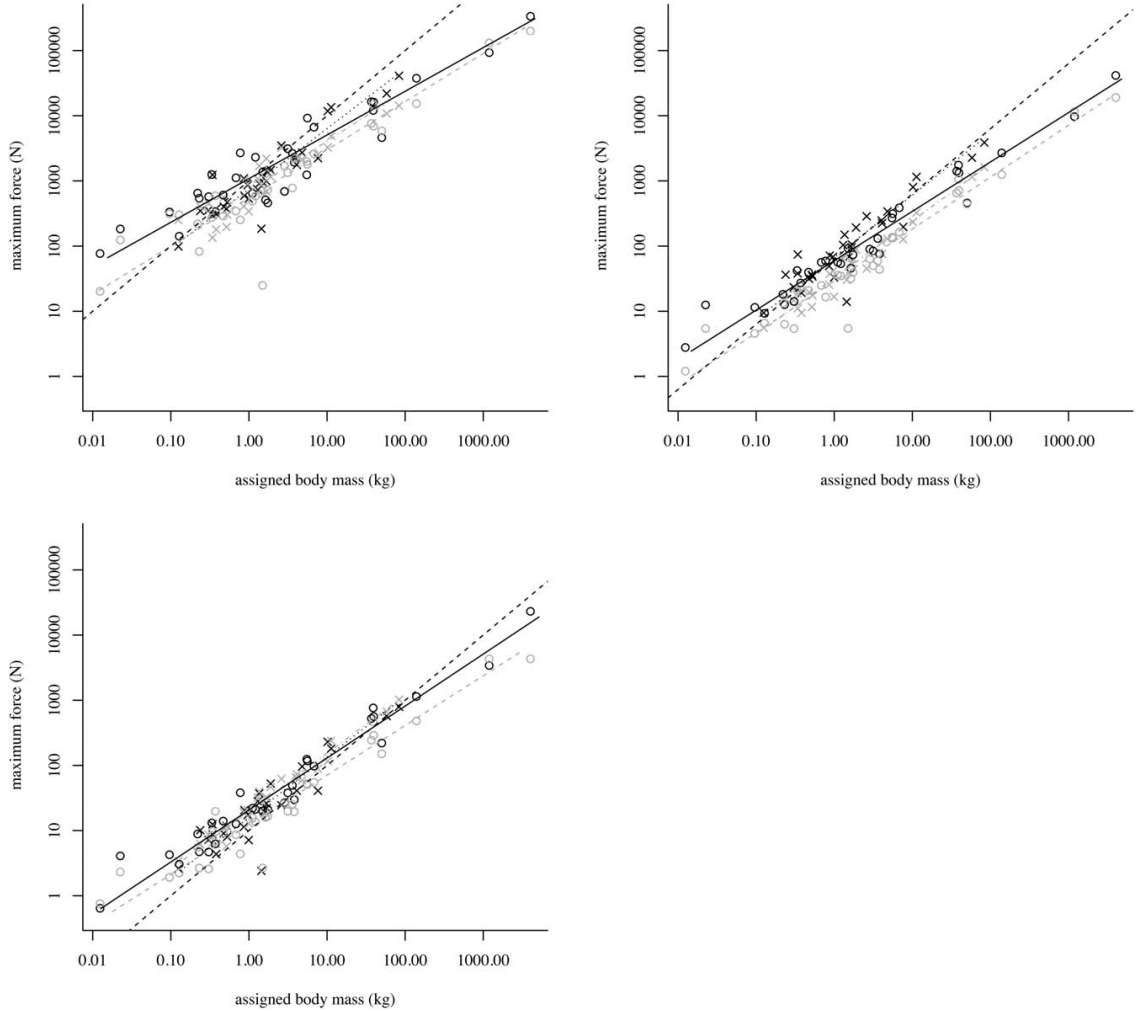


Fig. 7. SMA regressions of maximum resistible force before yield (N) against body mass (kg). Refer to Fig. 6 for symbols. (a) compressional loading regime (incorporating curvature); (b) bending loading regime (incorporating curvature); (c) torsional loading regime. Black dashed line reflects a slope value of 1. See Table 5 for slope values.

requirement for body mass to be supported by the limbs alone (Pridmore, 1985).

The safety factor curves of several small mammals fail to intersect lines representing safety factors of 12–20 (Fig. 8) for values of θ between 0 and 90 degree. These animals are able to operate at high safety factors, allowing them to adopt a crouched posture and abduction of the limbs (particularly the stylopodia) which would contribute significantly to bending loads (Blob and Biewener, 1999), as previously reported in several small mammals, including rodents, opossums, and mustelids (Jenkins, 1971; Gasc, 1993; Fischer, 1994). These results corroborate the interpretations of Reilly et al. (2007) for small crouched mammals, in which there was no significant change in EMA across the size range of 0.01–1 kg,

with posture instead being maintained by relatively increasing the cross-sectional area of antigravity muscles.

Attempts at reconstructing the ancestral mode of locomotion used by early mammals have combined palaeontological and modern biomechanical data (Gasc, 2001). The high safety factors and significant degree of torsional loading present in the femur of the crouching marsupial, Virginia opossum (*Didelphis virginiana*), have been interpreted as characteristic of basal mammalian species (Butcher et al., 2011). Considerable bending of the limb bones in the mediolateral direction was also identified, and linked to anteroposteriorly flattened cross sections in basal therapsids (Blob, 2001). Here, predicted values of F_b and F_t (calculated in both AP and ML

TABLE 6. Test for common slopes between SMA regression slopes of maximum force against assigned body mass

	Compression	Bending	Torsion
	Test for common slope		
lr	10.01	10.09	8.70
P	0.02*	0.02*	0.03*

Compression and bending slopes incorporate effects of bone curvature. Likelihood ratios (lr) calculated for slopes. The null hypothesis (H_0) of a common slope/intercept is rejected when $P < 0.05$.

directions) for the marsupial sugar glider (*Petaurus bevíceps*), and the monotremes *O. anatinus* and the short-beaked echidna (*Tachyglossus aculeatus*) are not significant outliers in regressions of maximum force against body mass. The non-eutherian mammals included in this study do not possess robust hindlimbs (relative to eutherians) that would be indicative of significantly higher bending and torsional loads. In the absence of additional kinematic and morphometric data from quadrupedal, terrestrial/arbooreal marsupials, and monotremes, the estimated levels of torsion and mediolateral bending in ancestral mammal limb loading remain unclear.

In line with previously published results (Cubo and Casinos, 1998; Doube et al., 2012), cross-sectional properties of avian hindlimbs scale more strongly than in corresponding mammalian limbs. Tibiotarsus length scales as $l \propto M_b^{0.38}$, higher than reported elsewhere (Prange et al., 1979; Olmos et al., 1996), but similar to that of Doube et al. (2012). In the absence of postural modifications, safety factors are still predicted to scale with body mass in the avian tibiotarsus despite positive allometric scaling of cross-sectional geometry. For a given safety factor, the value of θ_{\max} in the bird tibiotarsus is absolutely higher, and scales to body mass more slowly than in mammal hindlimb bones (Fig. 10). To achieve constant tibiotarsal safety factors across their size range, this sample of birds are required to modify θ_{\max} far less than mammal limb bones. From these results, we may hypothesize that in birds EMA does not scale around the knee as rapidly as recorded in mammals ($EMA \propto M_b^{0.24}$) (Biewener, 1989), although this remains to be tested with kinematic data.

In contrast to the wide arc of tibiotarsal retraction at the knee (50–80 degree), the avian femur typically rotates through less than 10 degree at the hip during the support phase at low/moderate speeds (Gatesy and Biewener, 1991). A knee-based retractor system and subhorizontal femur act to keep the center of mass positioned over the feet, which has shifted anteriorly following the reduction of tail length in the non-avian theropod lineage, matched by the shift from hip to knee-based limb flexure in avian theropods (Gatesy, 1995). That modern flightless birds have failed to attain maximum body masses comparable to those of non-avian theropods has previously been attributed to this subhorizontal femoral posture (Gatesy, 1991). The stylopodia of non-avian theropods have been found to scale differently to those of modern birds, suggesting they were subject to an alternative loading regime in which femora were oriented more parallel to the GRF. Axial loading of colum-

TABLE 7. Average safety factors (SF), ratios of safety factors between loading regimes, and test for the effect of phylogeny and skeletal element upon mean safety factors

	Compression	Bending	Torsion
SF			
BF	88.4	7.68	1.83
BT	76.2	3.37	2.01
MF	396.8	18.66	6.38
MT	209.3	9.17	4.13
Ratio			
BF	52.8	4.46	1
BT	35.8	1.68	1
MF	57.0	2.88	1
MT	52.6	2.50	1
Two-way ANOVA			
Phylogeny			
F	18.06	10.46	13.48
P	<0.001***	0.002**	<0.001***
Element			
F	3.92	7.26	1.40
P	0.05*	0.008**	0.24
Interaction			
F	2.85	0.99	1.81
P	0.09	0.32	0.18
Post hoc Tukey test (P)			
MF:MT	0.05*	0.05*	0.29
BF:BT	0.99	0.66	0.99
MF:BF	<0.001***	0.02*	0.003**
MT:BT	0.27	0.39	0.36
MF:BT	<0.001***	<0.001***	0.005**
MT:BF	0.36	0.97	0.28

The effect of phylogenetic grouping and skeletal element on mean safety factors is tested in a two-way ANOVA. A post hoc Tukey test of multiple means indicates pairwise comparisons that are significantly different. Asterisks denote level of significance: * $P < 0.05$; ** $P < 0.01$; *** $P < 0.001$. MF, mammal femur; MT, mammal tibia; BF, bird femur; BT, bird tibiotarsus.

nar limbs may therefore have facilitated the evolution of gigantism in the theropod lineage (Gatesy, 1991). In contrast, it has been suggested that the shift to a more horizontal femur has led to femoral scaling becoming a constraint on modern avian body size (Gatesy, 1991).

However, here, we find bird femora scale with extreme robusticity, with $d_{AP} \propto l^{1.24}$ and $I_{AP} \propto l^{4.91}$ (Table 2). As a result, force scales close to isometry with body mass across all loading regimes, and constant safety factors in the subhorizontal femur may be achieved via scaling of bone geometry alone. Postural constraints do not appear to be the limiting factor in modern bird size, and may instead be attributed to the problems associated with contact incubation (Birchard and Deeming, 2009). The avian eggshell reflects a compromise between strength against the forces of parental body mass acting during incubation, and fragility necessary for the developed chick to successfully hatch. Safety factors for eggshell breakage have been shown to scale negatively against body mass (Ar and Rahn, 1979) assuming contact incubation. However, further work incorporating both morphometric and kinematic datasets is needed before the hypothesis of mass-invariant safety factors in the avian femur can be confidently accepted.

When plotting species-specific curves of maximum SF against θ in avian hindlimbs (Fig. 9), the lowest safety factors are not always associated with the heaviest

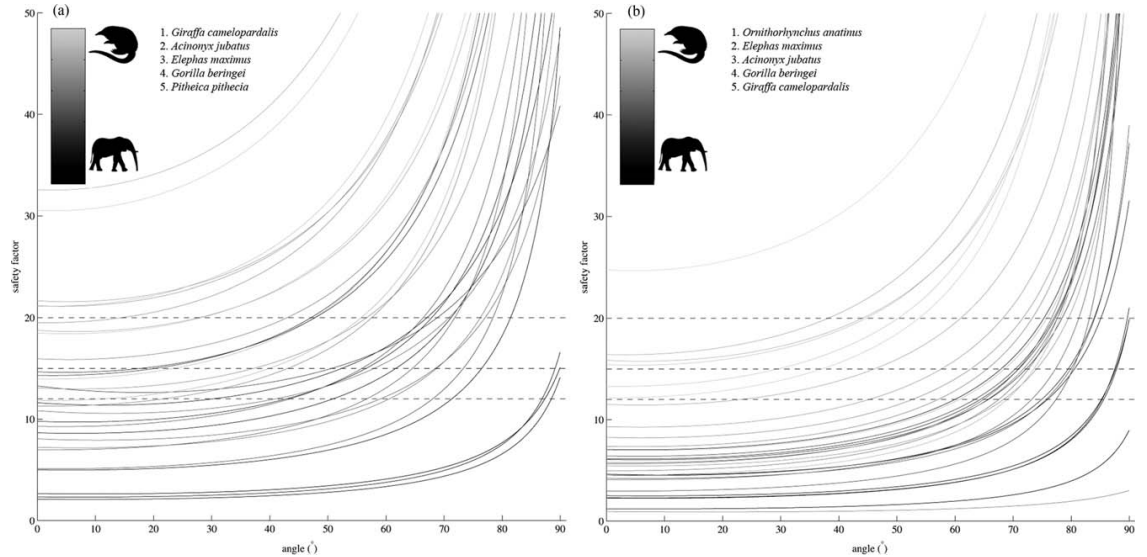


Fig. 8. Mammal species-specific curves of combined force (F_{cb}) against angle from the horizontal (θ) in degrees. (a) mammal femur; (b) mammal tibia. Dashed horizontal lines represent safety factors of 12, 15, and 20, respectively. Shade of individual curve follows gradient from black (heaviest individual) to light gray (lightest individual). Top five species possessing lowest safety factors under bending are listed.

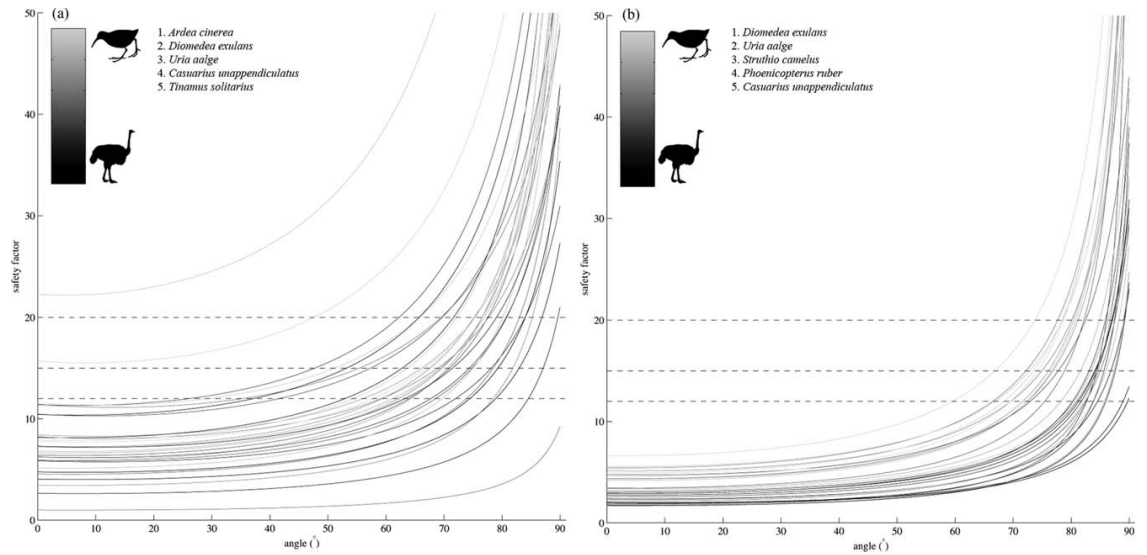


Fig. 9. Bird species-specific curves of combined force (F_{cb}) against angle from horizontal (θ) in degrees. (a) bird femur; (b) bird tibiotarsus. Annotations follow those of Fig. 8.

flightless birds in the sample (*Struthio camelus*, *Casuarius unappendiculatus*, *Raphus cucullatus*, and *Pezophaps solitaria*). Instead, low values of SF are associated with wading birds (*Ardea cinerea*, *Phoenicopterus ruber*), diving birds (*Uria aalge*), and long-distance dynamic soarers (*Diomedea exulans*). The shift away from cursor-

iality toward specialized locomotor groups appears to be characterized by a decrease in safety factors in avian hindlimbs. Unlike mammals, in which the largest species tend to experience the lowest safety factors (based on bone geometry alone; Fig. 8), a strong behavioral signal may also be present in birds.

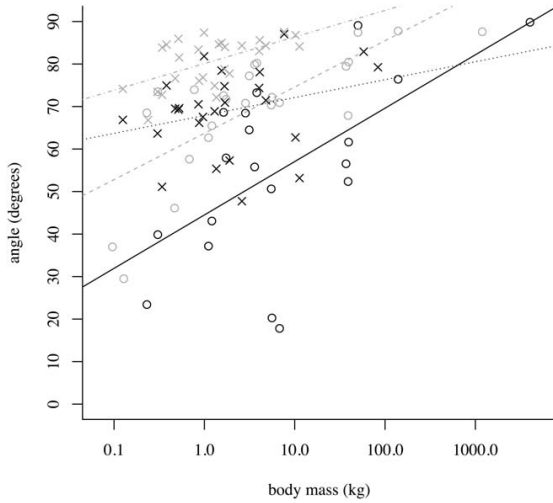


Fig. 10. Bone angle (θ) scales with body mass. Refer to Fig. 6 for symbols. The minimum angle from horizontal at which a bone may be held statically when subject to combined compressive and bending force, while maintaining a safety factor of 15, scales significantly with M_b (with the exception of the avian femur). Model-I OLS regression equations are: mammal femur, $y=44.5x^{12.6}$; mammal tibia, $y=63.7x^{10.9}$; bird femur, $y=67.9x^{4.21}$ (not significantly different from zero; $P>0.07$); bird tibia, $y=80.1x^{6.26}$. When individual species curves do not intersect the safety factor line (see Figs. 10 and 9), they are not included in the analysis.

There are a number of important considerations of the analysis presented above. In common with most analyses of bone loading, we calculate values for maximum resistible force before yield and θ_{\max} using static loading models. Even analyses such as EMA, in which the magnitude and direction of the instantaneous GRF at midstance are measured, are considered static analyses as they ignore any loading associated with the relative accelerations of each limb segment. During locomotion, peak stresses experienced within bones are due to muscle contractions, rather than the effects of gravity (Rubin and Lanyon, 1984; Biewener, 1991). It therefore follows that muscle forces should primarily determine bone dimensions, rather than static loads (Kokshenev et al., 2003). Here, we find the maximum static force a bone is capable of withstanding scales to body mass with negative allometry ($F_b \propto M_b^{-0.87-0.89}$, with the exception of the avian femur), and interpret this as a decrease in safety factor with size. However, experimental results suggest peak muscle force scales to body mass approximately as $M_b^{0.8}$ (Alexander et al., 1981). Therefore, if bone allometry is coupled with muscle force allometry, it appears constant safety factors to peak muscle force may be frequently achieved via scaling of bone geometry alone.

In addition, predicted values of F_b were calculated using Euler-Bernoulli simple beam theory, in which potential deformation caused by shear is ignored (Gere and Goodno, 2012). Standard engineering practice suggests that that beam theory equations are reasonably accurate only for objects with an aspect ratio ($l:d$) of 16 or greater (Turner and Burr, 1993), which is only some-

times the case for long bones. Roughly half the present sample have a $l:d$ of less than 16, and a greater proportion of total σ under bending will consist of shear stress. F_b may be better approximated by the less frequently used Timoshenko beam theory, in which shear deformations are included (Gere and Goodno, 2012). Further work is needed to understand the magnitude of errors associated with ignoring shear deformations, and FEA may be a useful computational tool for such analyses (Brassey et al., 2013).

CONCLUSIONS

Scaling of cross-sectional geometry alone does not achieve mass-invariant safety factors in mammalian hindlimbs. The angle from vertical at which mammals must hold their limb bones to achieve stress similarity scales significantly with body mass. In contrast, more extreme positive allometry in the avian femur may be capable of preventing safety factors from decreasing with body size. If constant safety factors are maintained in the subhorizontal avian theropod femur, this postural constraint does not appear to act as a limiting factor on maximum body size. The theory of postural adjustment to maintain safety factors is broadly supported on an order-level in mammals. However, idiosyncratic behavioral and locomotor signals are found to overlay frequently the relationship between force, bone angle, and body mass, particularly in birds. The applicability of EMA scaling to birds, and outside the sprawling rodent-erect ungulate dichotomy in mammals, remains to be tested.

ACKNOWLEDGEMENTS

The authors are grateful to the staff of the Henry Mosley X-ray Imaging Facility, University of Manchester; Professor Paul Mumford, Dr Tristan Lowe; The University of Liverpool Small Animal Hospital: Martin Baker; Manchester Museum: Henry McGhie, Judith White; Liverpool World Museum: Tony Parker. The comments of two anonymous reviewers were very useful in refining the manuscript.

LITERATURE CITED

- Agnarsson I, Kuntner M, May-Collado LJ. 2010. Dogs, cats, and kin: a molecular species-level phylogeny of Carnivora. *Mol Phylogenet Evol* 54:726–745.
- Alexander RMN. 1974. The mechanics of jumping by a dog (*Canis familiaris*). *J Zool* 173:549–573.
- Alexander, RMN. 1981. Factors of safety in the structure of Animals. *Sci Prog* 67:109–130.
- Alexander RMN. 1989. Dynamics of Dinosaurs and Other Extinct Giants. New York: Columbia University Press.
- Alexander RMN, Jayes AS. 1983. A dynamic similarity hypothesis for the gaits of quadrupedal mammals. *J Zool* 201:135–152.
- Alexander RMN, Pond C. 1992. Locomotion and bone strength of the white rhinoceros, *Ceratotherium simum*. *J Zool* 227:63–69.
- Alexander RMN, Jayes AS, Maloiy GMO, Wathuta EM. 1981. Allometry of the leg muscles of mammals. *J Zool* 194:539–552.
- Angst D, Buffetaut E, Abourachid A. 2011. The end of the fat dodo? A new mass estimate for *Raphus cucullatus*. *Naturwissenschaften* 98:233–236.
- Ar A, Rahn H. 1979. The avian egg: mass and strength. *The Condor* 81:331–337.
- Arnold C, Matthews LJ, Nunn CL. 2010. The 10kTrees website: a new online resource for primate phylogeny. *Evol Anthropol* 19:114–118.

- Beck R. 2008. A dated phylogeny of marsupials using a molecular supermatrix and multiple fossil constraints. *J Mammal* 89:175–189.
- Bertram J, Biewener A. 1988. Bone curvature: sacrificing strength for load predictability? *J Theor Biol* 131:75–92.
- Bertram J, Biewener A. 1990. Differential scaling of the long bones in the terrestrial Carnivora and other mammals. *J Morphol* 204:157–169.
- Bertram J, Biewener A. 1992. Allometry and curvature in the long bones of quadrupedal mammals. *J Zool* 226:455–467.
- Biewener A. 1982. Bone strength in small mammals and bipedal birds: do safety factors change with body size? *J Exp Biol* 98:289–301.
- Biewener A. 1983. Allometry of quadrupedal locomotion: the scaling of duty factor, bone curvature and limb orientation to body size. *J Exp Biol* 105:147–171.
- Biewener A. 1989. Scaling body support in mammals: limb posture and muscle mechanics. *Science* 245:45–48.
- Biewener A. 1991. Musculoskeletal design in relation to body size. *J Biomech* 24:19–29.
- Biewener A. 2005. Biomechanical consequences of scaling. *J Exp Biol* 208:1665–1676.
- Birchard G, Deeming D. 2009. Avian eggshell thickness: scaling and maximum body mass in birds. *J Zool* 279:95–101.
- Blanga-Kanfi S, Miranda H, Penn O, Pupko T, DeBry RW, Huchon D. 2009. Rodent phylogeny revised: analysis of six nuclear genes from all major rodent clades. *BMC Evol Biol* 9:71.
- Blob R. 2001. Evolution of hindlimb posture in nonmammalian therapsids: biomechanical tests of paleontological hypotheses. *Paleobiology* 27:14–38.
- Blob R, Biewener A. 1999. In vivo locomotor strain in the hindlimb bones of *Alligator mississippiensis* and *Iguana iguana*: implications for the evolution of limb bone safety factor and non-sprawling limb posture. *J Exp Biol* 202:1023–1046.
- Blob R, Biewener A. 2001. Mechanics of limb bone loading during terrestrial locomotion in the green iguana (*Iguana iguana*) and American alligator (*Alligator mississippiensis*). *J Exp Biol* 204:1099–1122.
- Boresi AP, Schmidt RJ. 2002. Advanced Mechanics of Materials. 6th ed. New Jersey: John Wiley & Sons.
- Brassay CB, Margretts L, Kitchener AC, Withers PJ, Manning PL, Sellers WI. 2013. Finite element modelling versus simple beam theory: comparing methods for estimating stress in a diverse sample of vertebrate long bones. *J R Soc Interface* 10: 20120823.
- Brown JR, Rest JS, Garcia-Moreno J, Sorenson MD, Mindell DP. 2008. Strong mitochondrial DNA support for a Cretaceous origin of modern avian lineages. *BMC Biol* 6:6.
- Butcher M, White B, Hudzik N. 2011. In vivo strains in the femur of the Virginia opossum (*Didelphis virginiana*) during terrestrial locomotion: testing hypotheses of evolutionary shifts in mammalian bone loading and design. *J Exp Biol* 214:2631–2640.
- Campione NE, Evans DC. 2012. A universal scaling relationship between body mass and proximal limb bone dimensions in quadrupedal terrestrial tetrapods. *BMC Biol* 10:60.
- Cezayirlioglu H, Bahnuik E, Davy DT, Heiple KG. 1985. Anisotropic yield behavior of bone under combined axial force and torque. *J Biomech* 18:61–69.
- Chinnery B. 2004. Morphometric analysis of evolutionary trends in the ceratopsian postcranial skeleton. *J Vert Paleo* 24:591–609.
- Christiansen P. 1998. Strength indicator values of theropod long bones, with comments on limb proportions and cursorial potential. *Gaia* 15:241–255.
- Christiansen P. 1999a. Long bone scaling and limb posture in non-avian theropods: evidence for differential allometry. *J Vert Paleo* 19:666–680.
- Christiansen P. 1999b. Scaling of the limb long bones to body mass in terrestrial mammals. *J Morphol* 239:167–190.
- Clemente CJ, Withers PC, Thompson G, Lloyd D. 2011. Evolution of limb bone loading and body size in varanid lizards. *J Exp Biol* 214:3013–3020.
- Cubo J, Casinos A. 2000. Mechanical properties and chemical composition of avian long bones. *Eur J Morphol* 38:112–121.
- Cubo J, Casinos A. 1998. The variation of the cross-sectional shape in the long bones of birds and mammals. *Ann Sci Nat Zool* 19:51–62.
- Cubo J, Menten L, Casinos A. 1999. Sagittal long bone curvature in birds. *Ann Sci Nat Zool* 20:153–159.
- Currey JD. 2002. Bones: Structure and Mechanics. Oxford: Princeton University Press.
- Currey JD. 2003. How well are bones designed to resist fracture? *J Bone Miner Res* 18:591–598.
- Davies SJF. 2002. Ratites and Tinamous. Oxford: Oxford University Press.
- Davies SJF. 2003. Ratites. In: Hutchins M, editor. Grzimek's Animal Life Encyclopedia, Volume 8: Tinamous and Ratites. Farmington Hills, MI: Gale Group. p 89–90.
- Day L, Jayne B. 2007. Interspecific scaling of the morphology and posture of the limbs during the locomotion of cats (Felidae). *J Exp Biol* 210:642–654.
- Decker J, Pires JC, Conant GC, McKay SD, Heaton MP, Chen K, Cooper A, Vilki J, Seabury CM, Caetano AR et al. 2009. Resolving the evolution of extant and extinct ruminants with high-throughput phylogenomics. *PNAS* 106:18644–18649.
- Demes B, Jungers WL. 1993. Long-bone cross-sectional dimensions, locomotor adaptations and body-size in prosimian primates. *J Hum Evol* 25:57–74.
- Demes B, Larson SG, Stern JT, Jr., Jungers WL, Biknevicius AR, Schmitt, D. 1994. The kinetics of primate quadrupedalism. *J Hum Evol* 26:353–374.
- do Amaral FR, Sheldon FH, Gamauf A, Haring E, Riesing M, Silveira LF, Wajntal, A. 2009. Patterns and processes of diversification in a widespread and ecologically diverse avian group, the buteonine hawks (Aves, Accipitridae). *Mol Phylogenet Evol* 53:703–715.
- Doube M, Kłosowski M, Arganda-Carreras I. 2010. BoneJ: free and extensible bone image analysis in ImageJ. *Bone* 47:1076–1079.
- Doube M, Yen SCW, Kłosowski MM, Farke AA, Hutchinson JR, Shefelbine, SJ. 2012. Whole-bone scaling of the avian pelvic limb. *J Anatomy* 221:21–29.
- Dunning JB. 1993. CRC Handbook of Avian Body Mass. Boca Raton: CRC Press.
- Economos A. 1983. Elastic and/or geometric similarity in mammalian design? *J Theor Biol* 103:167–172.
- Eizirik E, Murphy WJ, Koepfli KP, Johnson WE, Drago JW, Wayne RK, O'Brian SJ. 2010. Pattern and timing of diversification of the mammalian order Carnivora inferred from multiple nuclear gene sequences. *Mol Phylogenet Evol* 56:49–63.
- Erickson G, Cataneo J III, Keaveny T. 2002. Evolution of the biomechanical material properties of the femur. *Anat Rec* 268:115–124.
- Fain M, Krajewski C, Houde P. 2007. Phylogeny of “core Gruiformes” (Aves: Grues) and resolution of the Limpkin-Sunbird problem. *Mol Phylogenet Evol*, 43:515–529.
- Felsenstein J. 1988. Phylogenies and quantitative characters. *Annu Rev Ecol Syst* 19:445–471.
- Fischer M. 1994. Crouched posture and high fulcrum, a principle in the locomotion of small mammals: the example of the rock hyrax (*Procavia capensis*)(Mammalia: Hyracoidea). *J Hum Evol* 26:501–524.
- Fish F, Frappell PB, Baudinette RV, MacFarlane PM. 2001. Energistics of terrestrial locomotion of the platypus *Ornithorhynchus anatinus*. *J Exp Biol* 204:797–803.
- Gambaryan PP. 1976. How Mammals Run. New York: John Wiley & Sons Inc.
- Garcia G, da Silva J. 2004. On the scaling of mammalian long bones. *J Exp Biol* 207:1577–1584.
- Garcia G, da Silva J. 2006. Interspecific allometry of bone dimensions: a review of the theoretical models. *Phys Life Rev* 3:188–209.
- Gartner GEA, Hicks JW, Manzani PR, Andrade DV, Abe AS, Wang T, Secor SM, Gardland T, Jr. 2010. Phylogeny, ecology, and heart position in snakes. *Physiol Biochem Zool* 83:43–54.
- Gasc JP. 1993. Asymmetrical gait of the Saharan rodent *Meriones shawi shawi* (Duvernoy, 1842) (Rodentia, Mammalia): a high-speed cineradiographic analysis. *Can J Zool* 71:790–798.
- Gasc JP. 2001. Comparative aspects of gait, scaling and mechanics in mammals. *Comp Biochem Phys A* 131:121–133.

- Gatesy S. 1991. Hind limb scaling in birds and other theropods: implications for terrestrial locomotion. *J Morph* 209:83–96.
- Gatesy S. 1995. Functional evolution of the hindlimb and tail from basal theropods to birds. In: Thomason JJ, editor. *Functional Morphology in Vertebrate Palaeontology*. Cambridge: Cambridge University Press. p 219–234.
- Gatesy S, Biewener A. 1991. Bipedal locomotion: effects of speed, size and limb posture in birds and humans. *J Zool* 224:127–147.
- Gere JM, Goodno BJ. 2012. *Mechanics of Materials*. Stamford: Cengage Learning.
- Gonzalez J, Düttrmann H, Wink M. 2009. Phylogenetic relationships based on two mitochondrial genes and hybridization patterns in Anatidae. *J Zool* 279:310–318.
- Hackett S, Kimball RT, Reddy S, Bowie RCK, Braun EL, Braun MJ, Chojnowski JL, Cox WA, Han KL, Harshman J et al. 2008. A phylogenomic study of birds reveals their evolutionary history. *Science* 320:1763–1767.
- Hudson PE, Corr SA, Payne-Davis RC, Clancy SN, Lane E, Wilson AM. 2011. Functional anatomy of the cheetah (*Acinonyx jubatus*) hindlimb. *J Anat* 218:363–374.
- Hutchinson JR, Famini D, Lair R, Kram R. 2003. Are fast-moving elephants really running? *Nature* 422:493–494.
- Jenkins F. 1971. Limb posture and locomotion in the Virginia opossum (*Didelphis marsupialis*) and in other non-cursorial mammals. *J Zool* 165:303–315.
- Keller TS, Spengler DM. 1989. Regulation of bone stress and strain in the immature and mature rat femur. *J Biomech* 22:1115–1127.
- Kokshenev V, Silva J, Garcia G. 2003. Long-bone allometry of terrestrial mammals and the geometric-shape and elastic-force constraints of bone evolution. *J Theor Biol* 224:551–556.
- Lanyon LE. 1980. The influence of function on the development of bone curvature. An experimental study on the rat tibia. *J Zool* 192:457–466.
- Lavin SR, Karasov WH, Ives AR, Middleton KM, Garland T, Jr. 2008. Morphometrics of the avian small intestine compared with that of nonflying mammals: A Phylogenetic Approach. *Physiol Biochem Zool* 81:526–550.
- Livezey B. 1993. An ecomorphological review of the dodo (*Raphus cucullatus*) and solitaire (*Pezophaps solitaria*), flightless Columbiformes of the Mascarene Islands. *J Zool* 230:247–292.
- Matthee CA, van Vuuren BJ, Bell D, Robinson TJ. 2004. A molecular supermatrix of the rabbits and hares (Leporidae) allows for the identification of five intercontinental exchanges during the Miocene. *Syst Biol* 53:433–447.
- McArdle BH. 1988. The structural relationship—regression in biology. *Can J Zool* 66:2329–2339.
- McMahon T. 1973. Size and shape in biology: elastic criteria impose limits on biological proportions, and consequently on metabolic rates. *Science* 179:1201–1204.
- McMahon T. 1975. Allometry and biomechanics: limb bones in adult ungulates. *Am Nat* 109:547–563.
- Olmos M, Casinos A, Cubo J. 1996. Limb allometry in birds. *Ann Sci Nat Zool* 17:39–49.
- Pereira S, Baker A. 2006. A molecular timescale for galliform birds accounting for uncertainty in time estimates and heterogeneity of rates of DNA substitutions across lineages and sites. *Mol Phylogenet Evol* 38:499–509.
- Pereira S, Baker A. 2008. DNA evidence for a Paleocene origin of the Alcidae (Aves: Charadriiformes) in the Pacific and multiple dispersals across northern oceans. *Mol Phylogenet Evol* 46:430–445.
- Pereira S, Johnson KP, Clayton DH, Baker AJ. 2007. Mitochondrial and nuclear DNA sequences support a Cretaceous origin of Columbiformes and a dispersal-driven radiation in the Paleogene. *Syst Biol* 56:656–672.
- Phillips MJ, Gibb GC, Crimp EA, Penny D. 2010. Tinamous and moa flock together: mitochondrial genome sequence analysis reveals independent losses of flight among ratites. *Syst Biol* 59:90–107.
- Polk J. 2002. Adaptive and phylogenetic influences on musculoskeletal design in cercopithecine primates. *J Exp Biol* 205:3399–3412.
- Prange H, Anderson J, Rahn H. 1979. Scaling of skeletal mass to body mass in birds and mammals. *Am Nat* 113:103–122.
- Prasad A, Allard M. 2008. Confirming the phylogeny of mammals by use of large comparative sequence data sets. *Mol Bio Evol* 25:1795–1808.
- Pridmore PA. 1985. Terrestrial locomotion in monotremes (Mammalia, Monotremata). *J Zool* 205:53–73.
- Reilly SM, Willey JS, Biknevicius AR, Blob RW. 2005. Hindlimb function in the alligator: integrating movements, motor patterns, ground reaction forces and bone strain of terrestrial locomotion. *J Exp Biol* 208:993–1009.
- Reilly SM, McElroy EJ, Biknevicius AR. 2007. Posture, gait and the ecological relevance of locomotor costs and energy-saving mechanisms in tetrapods. *Zoology* 110:271–289.
- Ren L, Miller CE, Lair R, Hutchinson JR. 2010. Integration of biomechanical compliance, leverage, and power in elephant limbs. *PNAS* 107:7078–7082.
- Roark RJ. 1965. *Formulas for Stress and Strain*. 4th ed. London: McGraw-Hill.
- Rocha-Barbosa O, Casinos A. 2011. Geometry and evolutionary parallelism in the long bones of cavioid rodents and small artiodactyls. *J Biosci* 36:887–895.
- Rowe T, Rich TH, Vickers-Rich T, Springer M, Woodburne MO. 2008. The oldest platypus and its bearing on divergence timing of the platypus and echidna clades. *PNAS* 105:1238–1242.
- Rubin C, Lanyon L. 1982. Limb mechanics as a function of speed and gait: a study of functional strains in the radius and tibia of horse and dog. *J Exp Biol* 101:187–211.
- Rubin C, Lanyon L. 1984. Dynamic strain similarity in vertebrates: an alternative to allometric limb bone scaling. *J Theor Biol* 107:321–327.
- Schmitt D, Cartmill M, Griffin TM, Hanna JB, Lemelin P. 2006. Adaptive value of ambling gaits in primates and other mammals. *J Exp Biol* 209:2042–2049.
- Seiffert E. 2007. A new estimate of afrotherian phylogeny based on simultaneous analysis of genomic, morphological, and fossil evidence. *BMC Evol Biol* 7:224.
- Silva M, Downing JA. 1995. *CRC Handbook of Mammalian Body Masses*. Boca Raton: CRC Press.
- Smithers RNH. 1983. *The Mammals of the Southern African Subregion*. Pretoria: University of Pretoria.
- Springer MS, Murphy WJ, Eizirik E, O'Brien SJ. 2003. Placental mammal diversification and the Cretaceous-Tertiary boundary. *PNAS* 100:1056–1061.
- Tumarkin-Deratzian AR, Vann DR, Dodson P. 2006. Bone surface texture as an ontogenetic indicator in long bones of the Canada goose *Branta canadensis* (Anseriformes : Anatidae). *Zool J Linn Soc* 148:133–168.
- Turner C, Burr D. 1993. Basic biomechanical measurements of bone: a tutorial. *Bone* 14:595–608.
- Van Staa TP, Dennison EM, Leufkens HGM, Cooper C. 2001. Epidemiology of fractures in England and Wales. *Bone* 29:517–522.
- Warton DI, Wright IJ, Falster DS, Westoby M. 2006. Bivariate line-fitting methods for allometry. *Biol Rev* 81:259–291.
- Wisconsin National Primate Research Centre. 2011. Primate Info Net: Primate Factsheets. Available at: <http://pin.primate.wisc.edu/factsheets/> [Accessed 2011].
- Woodburne M, Rich T, Springer M. 2003. The evolution of tribospheny and the antiquity of mammalian clades. *Mol Phylogenet Evol* 28:360–385.
- Wright T, Schirtzinger EE, Matsumoto T, Eberhard JR, Graves GR, Sanchez JJ, Capelli S, Muller H, Scharpegge J, Chambers GK and Fleischer RC. 2008. A multilocus molecular phylogeny of the parrots (Psittaciformes): support for a Gondwanan origin during the Cretaceous. *Mol Biol Evol* 25:2141–2156.
- Zioupos P, Currey JD, Casinos A. 2000. Exploring the effects of hypermineralisation in bone tissue by using an extreme biological example. *Connect Tissue Res* 41:229–248.

Chapter 3

Finite element modelling versus
classic beam theory: comparing
methods for stress estimation in a
morphologically diverse sample of
vertebrate long bones

Finite element modelling versus classic beam theory: comparing methods for stress estimation in a morphologically diverse sample of vertebrate long bones

Charlotte A. Brassey, Lee Margetts, Andrew C. Kitchener, Philip J. Withers, Phillip L. Manning and William I. Sellers

J. R. Soc. Interface 2013 **10**,
doi: 10.1098/rsif.2012.0823

Supplementary data

"Data Supplement"

<http://rsif.royalsocietypublishing.org/content/suppl/2012/11/20/rsif.2012.0823.DC1.htm>

References

This article cites 39 articles, 8 of which can be accessed free

<http://rsif.royalsocietypublishing.org/content/10/79/20120823.full.html#ref-list-1>

Subject collections

Articles on similar topics can be found in the following collections

[computational biology](#) (165 articles)

Email alerting service

Receive free email alerts when new articles cite this article - sign up in the box at the top right-hand corner of the article or click [here](#)

Research



click for updates

Cite this article: Brassey CA, Margetts L, Kitchener AC, Withers PJ, Manning PL, Sellers WI. 2012 Finite element modelling versus classic beam theory: comparing methods for stress estimation in a morphologically diverse sample of vertebrate long bones. *J R Soc Interface* 10: 20120823.
<http://dx.doi.org/10.1098/rsif.2012.0823>

Received: 8 October 2012

Accepted: 31 October 2012

Subject Areas:

biomechanics, computational biology

Keywords:

finite element analysis, beam theory, biomechanics, curvature, cross-sectional asymmetry

Author for correspondence:

Charlotte A. Brassey
e-mail: charlotte.brassey-2@postgrad.manchester.ac.uk

Electronic supplementary material is available at <http://dx.doi.org/10.1098/rsif.2012.0823> or via <http://rsif.royalsocietypublishing.org>.

Finite element modelling versus classic beam theory: comparing methods for stress estimation in a morphologically diverse sample of vertebrate long bones

Charlotte A. Brassey¹, Lee Margetts^{2,3}, Andrew C. Kitchener^{5,6}, Philip J. Withers⁴, Phillip L. Manning² and William I. Sellers¹

¹Faculty of Life Sciences, ²School of Earth, Atmospheric and Environmental Sciences, ³Research Computing, and

⁴School of Materials, University of Manchester, Manchester M13 9PL, UK

⁵Department of Natural Sciences, National Museums Scotland, Edinburgh EH1 1JF, UK

⁶Institute of Geography, School of Geosciences, University of Edinburgh, Drummond Street, Edinburgh EH8 9XP, UK

Classic beam theory is frequently used in biomechanics to model the stress behaviour of vertebrate long bones, particularly when creating intraspecific scaling models. Although methodologically straightforward, classic beam theory requires complex irregular bones to be approximated as slender beams, and the errors associated with simplifying complex organic structures to such an extent are unknown. Alternative approaches, such as finite element analysis (FEA), while much more time-consuming to perform, require no such assumptions. This study compares the results obtained using classic beam theory with those from FEA to quantify the beam theory errors and to provide recommendations about when a full FEA is essential for reasonable biomechanical predictions. High-resolution computed tomographic scans of eight vertebrate long bones were used to calculate diaphyseal stress owing to various loading regimes. Under compression, FEA values of minimum principal stress (σ_{\min}) were on average 142 per cent ($\pm 28\%$ s.e.) larger than those predicted by beam theory, with deviation between the two models correlated to shaft curvature (two-tailed $p = 0.03$, $r^2 = 0.56$). Under bending, FEA values of maximum principal stress (σ_{\max}) and beam theory values differed on average by 12 per cent ($\pm 4\%$ s.e.), with deviation between the models significantly correlated to cross-sectional asymmetry at midshaft (two-tailed $p = 0.02$, $r^2 = 0.62$). In torsion, assuming maximum stress values occurred at the location of minimum cortical thickness brought beam theory and FEA values closest in line, and in this case FEA values of τ_{torsion} were on average 14 per cent ($\pm 5\%$ s.e.) higher than beam theory. Therefore, FEA is the preferred modelling solution when estimates of absolute diaphyseal stress are required, although values calculated by beam theory for bending may be acceptable in some situations.

1. Introduction

In comparative biology and palaeontology, the relationship between diaphyseal cross-sectional properties of long bones and body mass (M_b) is frequently used as an indicator of skeletal strength and rigidity. In many instances, relative values of such properties as cortical cross-sectional area (A_{corr}), second moment of area (I) and polar moment of area (J) are used in comparative studies, from which skeletal posture and *in vivo* function may be inferred [1–4]. However, in other instances, diaphyseal cross-sectional properties are incorporated into equations to predict *actual* skeletal stress. Reliable estimates of diaphyseal stress are essential in determining maximum upper limits to terrestrial vertebrate body mass [5], estimating safety factors (the ratio of yield

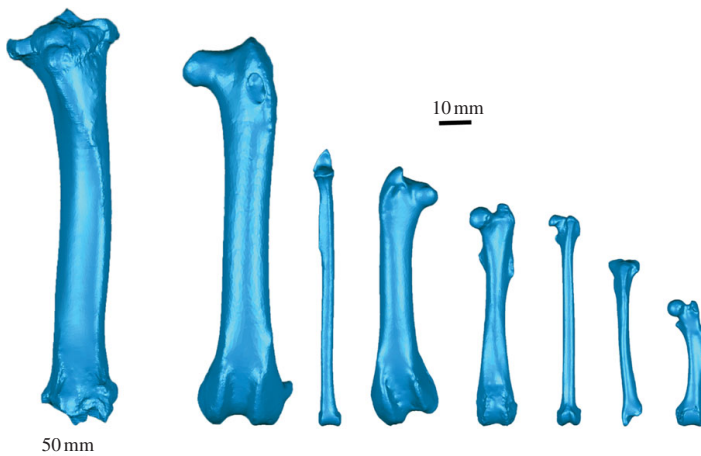


Figure 1. Three-dimensional volumetric models of vertebrate long bones considered in this study. Far left, *Giraffa camelopardalis* tibia. Scale bar: 50 mm. All other models are to same scale (scale bar: 10 mm). From left, *Haliaeetus albicilla* femur, *Uria aalge* tibia, *Phoenicopterus ruber* femur, *Procapia capensis* femur, *Galago senegalensis* femur, *Mustela putorius* tibia and *Erinaceus europaeus* femur.

stress to maximum functional stress), and in reconstructing gaits via locomotion modelling [6]. While the preferred method for obtaining absolute values of stress must always be the *in vivo* application of strain gauges, this is often impractical, owing to ethical constraints associated with the study species, the sample size required or the fossilized nature of the sample.

When a particular biomechanical model is used to estimate stress in a range of specimens, we assume that the mechanical consequences of differing skeletal morphology will be illuminated [7]. Yet, the error magnitude involved in the calculation of stress and strain is also a function of the underlying geometry of the skeletal element (both external morphology and internal architecture). A model's suitability for estimating stress is dependent upon the extent to which each biological specimen in turn meets the conditions of the model. In a sample containing high morphological variability, application of classic beam theory to estimate stress may result in inconsistency in both the direction and the magnitude of errors, and may mask the functional morphological signal of interest.

Euler–Bernoulli beam theory [8] (hereafter referred to as 'classic beam theory') provides a means of calculating deflection of a beam and has been extensively applied to the estimation of stresses in vertebrate long bones, owing in large part to its simplicity [9–12]. Compressive loads acting through the centroid of the cross section generate normal stresses defined as

$$\sigma_{\text{comp}} = \frac{F}{A_{\text{cort}}}, \quad (1.1)$$

where σ_{comp} is compressive stress, F is the applied force and A_{cort} the cross-sectional cortical area [13]. However, in instances when the beam possesses a degree of curvature, axial components of the applied force act longitudinally around the curvature and induce bending moments. In the case of long bones, the extent of induced bending is a function of the radius of curvature of the element, and resultant bending stresses may come to dwarf those of axial compression during dynamic loading [14]. Previous authors have sought to explain the scaling behaviour of long bone

dimensions in terms of maintaining resistance to Euler buckling (failure of a thin-walled straight column under axial compression owing to elastic instability) [15,16], despite concern elsewhere that elastic deformation is unlikely to be an important factor in failure of mammal bones [17]. In addition, such scaling models have so far ignored the potential role of curvature in their calculations. Figure 1 illustrates the varying morphology characteristic of vertebrate hindlimbs included in this study, and highlights the divergence of long bones from the idealized straight beams considered in engineering.

A limited number of biomechanical studies have incorporated curvature into estimates of bending stress [18–20] or have investigated scaling of curvature to body mass [18,21,22]. This is particularly the case in the modelling of stress in primate mandibular symphyses [23,24], as they exhibit a particularly high degree of curvature relative to other skeletal elements. However, there has been no systematic application of curvature-corrected equations to long bones across the comparative anatomy and palaeontological literature, and the effect of ignoring this geometry on beam theory estimates has not been adequately explored.

The bending stress ($\sigma_{\text{bending}}(y)$) varies with position across a symmetric beam and is estimated as

$$\sigma_{\text{bending}}(y) = \frac{M_x y}{I_x}, \quad (1.2)$$

where M_x is the bending moment about the x -axis, y is the perpendicular distance to the neutral section and I_x is the second moment of area about the x -axis [13]. Application of this equation assumes that the cross section is symmetrical about the axis on which loading is occurring, that cross-sectional shape is maintained downshaft, and that plane sections remain undistorted and normal to the long axis following loading, i.e. ignoring shear deformation [13]. In beams possessing a low aspect ratio (length/diameter; l/d), warping owing to transverse shear contributes to the total stress experienced in a cross section. Standard engineering practice suggests that beam theory equations are reasonably accurate for objects only with an l/d ratio of 16 or greater [25], and many vertebrate long bones fall below

this aspect ratio at which shear deformation could justifiably be ignored (table 1). Therefore, values of bending stress calculated using Euler–Bernoulli theory are likely to be underestimates in stout, long bones.

In the biological literature, the relationship between axial compression, bending and load vector has been described by combining equations (1.1) and (1.2)

$$\sigma_{\text{combined}}(y) = \frac{M_x y \sin \theta}{I_x} + \frac{F \cos \theta}{A_{\text{cort}}}, \quad (1.3)$$

where $\sigma_{\text{combined}}(y)$ is the sum of compressive and bending stresses, and θ is the angle between the loading direction and the longest principal axis [29]. Therefore, when $\theta = 0^\circ$, σ_{combined} is equal to σ_{comp} , while when $\theta = 90^\circ$, σ_{combined} is equal to σ_{bending} (figure 2). By combining equations (1.1) and (1.2), total stress can be calculated for long bones loaded neither in pure compression nor pure bending, but at some intermediate angle. However, this equation potentially suffers from the compounded problems of equations (1.1) and (1.2) when applied to irregular geometries.

The maximum shear stress owing to torsion (τ_{torsion}) in a hollow elliptical beam is calculated as

$$\tau_{\text{torsion}} = \frac{2T}{\pi r_{\text{ap}} r_{\text{ml}}^2 (1 - q^4)}, \quad (1.4)$$

where T is the applied torque, r_{ap} and r_{ml} are the radii in the anteroposterior and mediolateral directions, respectively, and q is the ratio of inner radius to outer radius [30]. Equation (1.4) makes the assumption that the endosteal and periosteal contours are similar concentric ellipses. Alternatively, when the cross section is characterized by possessing thin walls, the average τ_{torsion} in a hollow elliptical section can be approximated using an alternative ‘thin-walled ellipse’ model

$$\tau_{\text{torsion}} = \frac{T}{2\pi t(r_{\text{ap}} - 0.5t)(r_{\text{ml}} - 0.5t)}, \quad (1.5)$$

where t is the thickness of the cortical wall (assuming a uniform thickness across the section) [30]. If the highest torsional stresses are considered to occur where the wall thickness is at a minimum (t_{\min}), a modified Bredt’s formula may also be used to approximate τ_{torsion} in sections of varying cortical thickness [31]

$$\tau_{\text{torsion}} = \frac{T}{2t_{\min} A}, \quad (1.6)$$

where A is the area enclosed by the median boundary (figure 3). This ‘minimum wall thickness’ model has been shown to be more suitable in estimating torsional stresses in asymmetric human tibial bones than the hollow ellipse model of equation (1.4) [32].

It is clear that all the beam formulae above are idealized approximations to the loading conditions actually experienced by long bones during dynamic loading, but the degree of error that they introduce is unclear. Classic beam theory remains the most practical and highly favoured modelling solution for very large comparative datasets, and for instances in which information regarding myology and material properties is lacking. However, finite element analysis (FEA) is increasingly becoming the preferred solution for estimating mechanical behaviour when a sample has an irregular and highly variable geometry [32]. Until recently, it was difficult to obtain an accurate model geometry for FEA of complex morphologies, hampering its

species	common name	accession no.	element	M_b (kg)	F (N)	I/d	I_{\max}/I_{\min}	ζ	tipa
<i>Uria aalge</i>	common guillemot	MM.BB.9095.1	tibia	0.99 [26]	0.097	7.13	1.69	0.5	[22]
<i>Gallago senegallus</i>	Senegal quail	NMS.Z.2000.30.70	femur	NMS.Z.2000.30.70	NMS.Z.2000.30.70	3.14 [27]	3.38	0.70	tipa
<i>Erinaceus europaeus</i>	European hedgehog	NMS.Z.2002.942	femur	NMS.Z.2002.942	NMS.Z.2002.942	1.11 [27]	1.26	1.17	femur
<i>Phoenicopterus ruber</i>	Greater flamingo	MM.1982.22.96	femur	MM.1982.22.96	MM.1982.22.96	4.19 [27]	2.60*	1.56	tipa
<i>Haliaeetus albilla</i>	White-tailed eagle	NMS.Z.2000.23	femur	NMS.Z.2000.23	NMS.Z.2000.23	0.68 [27]	0.40	1.13	femur
<i>Mustela putorius</i>	Mustelid weasel	0.022*	0.022*	0.022*	0.022*	0.91	1.23	1.23	tipa
<i>Procaria capensis</i>	Griffon vulture	NMS.Z.2001.1483	tibia	NMS.Z.2001.1483	NMS.Z.2001.1483	0.55	2.08	0.22	tipa

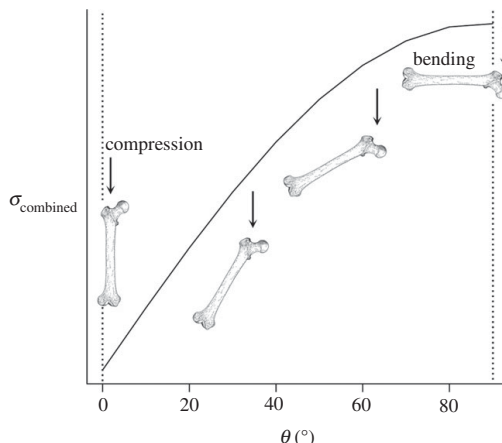


Figure 2. The relationship between loading regimes and load vector (θ). Combined stress is plotted against the angle between the load direction and the longest principal axis of the bone. Stress is at its maximum when the bone is loaded perpendicular to its long axis (i.e. under bending) and decreases as the load vector is brought increasingly in line with the long axis (i.e. under compression).

widespread application to large biological datasets. However, access to computed tomography (CT) facilities capable of providing detailed and structurally faithful three-dimensional models is becoming cheaper and easier. As a result, the scope is broadening for generating a sample size, previously achievable only via simpler modelling techniques. Given the additional complexity of such an approach, it is reasonable to ask whether stress values predicted by CT-based FEA differ significantly from those of classic beam theory when applied to vertebrate long bones. Here, we set out to answer this question by comparing stress predictions of theoretical simple beam equations against those of FEA in a diverse sample of long bones.

We seek to test (i) *geometrical effects* of diaphyseal cross-sectional shape failing to meet the assumptions of beam theory formulae; (ii) *loading effects* of shaft curvature preventing solely compressional and torsional loading; and (iii) *shear stress effects* of incorporating shear stress components into stress estimates. While the incorporation of heterogeneous material properties into FEA is commendable and results in closer agreement between FEA models and *ex vivo* results [33], here we have sought solely to explore the consequences of incorporating the inherent complexity of long bone geometry into such models for the purpose of comparative anatomical studies.

In reality, a synergistic combination of FEA modelling and *ex vivo* experimental validation may provide the best means of reliably testing the mechanics of vertebrate long bones [34]. However, in this study, we provide recommendations for the application of FEA and improvements to existing beam theory equations for the majority of instances when destructive mechanical testing is not feasible.

2. Material and methods

2.1. Specimen identification

Specimens were taken from a pre-existing large dataset of CT scans and were selected in order to avoid any bias towards a

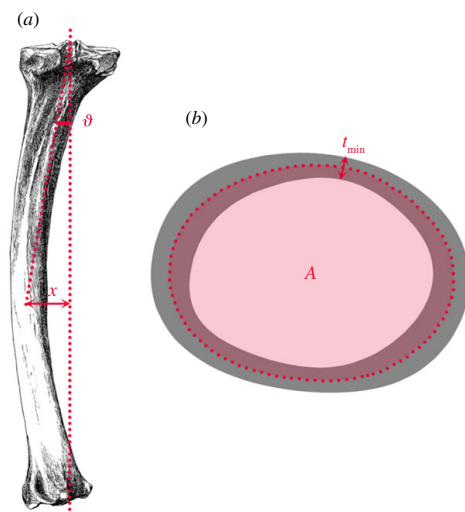


Figure 3. Calculating shaft curvature and diaphyseal cross-sectional properties. (a) Normalized curvature lever arm is calculated as the perpendicular distance from the proximal–distal chord to the centroid at midshaft (x), divided by the radius. The angle of curvature (δ) is the angle between the proximal–distal chord, and the chord joining the proximal-most point with the centroid. (b) t_{\min} is the minimum cortical wall thickness at midshaft, and A is the shaded area enclosed by the median boundary running halfway between the periosteal and endosteal contours.

particular group, skeletal element or body size, making the results of general application. Hindlimb bones from eight species of bird and mammal were acquired from various museum collections (National Museums Scotland, Edinburgh; Manchester Museum; and the World Museum, Liverpool). All specimens were skeletally mature (as determined by fusion of the epiphyses) and free of pathologies. When individual samples did not possess an associated M_b , typical values were assigned from the literature (table 1). External length measurements were taken using digital callipers (accurate to 0.1 mm), with the exception of the giraffe (*Giraffa camelopardalis*), which was measured with an anthropometer (accurate to 1 mm).

2.2. Finite element analysis

All but the largest specimen (*Giraffa*) were scanned in the Henry Moseley X-ray Imaging Facility, University of Manchester (X-Tek HMX 225 Custom Bay, Nikon Metrology Ltd, Tring, UK). Voxel size ranged between 64 and 119 μm , depending upon maximum bone length. Data were exported in unsigned 16-bit DICOM format (VG STUDIO MAX v. 2.0, Volume Graphics, Heidelberg, Germany). *Giraffa* was scanned in a helical CT scanner at the University of Liverpool Small Animal Teaching Hospital (Siemens SOMATOM Volume, Erlangen, Germany) at a resolution of 391 μm and slice thickness of 3 mm, and reconstructed with Syngo (Siemens).

DICOM files were imported into OsiriX v. 3.8 [35], individually thresholded according to their greyscale values to accurately define the periosteal and endosteal surfaces, and surfaces exported as OBJ files, using the three-dimensional surface rendering function. Files were then imported into Geomagic STUDIO v. 12 (Geomagic, USA), the periosteal and endosteal contours isolated from one another, and exported as closed manifold OBJ files (available for download from the Dryad data repository: doi:10.5061/dryad.9ct2f). OBJ files were converted into SAT files, using FORM-Z v. 6.1 (AutoDesSys, USA), and imported

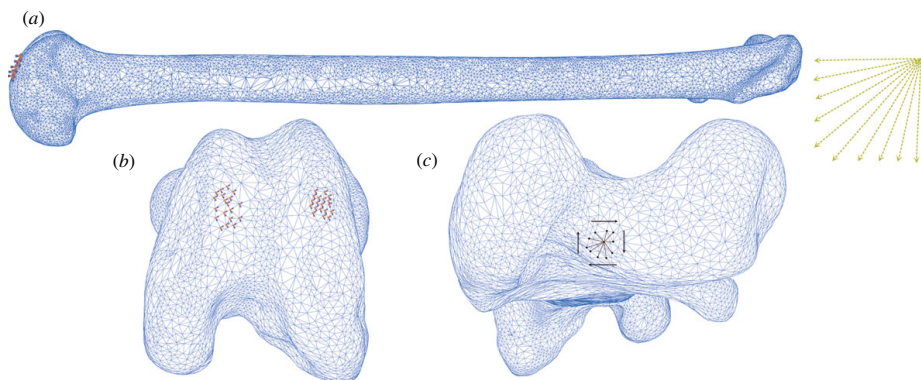


Figure 4. Load parameters and boundary conditions for FEA of the Senegal bushbaby (*Galago senegalensis*) femur. (a) Femur in lateral view. Yellow arrows indicate changing load vector incrementally from parallel to the bone's longest principal axis (compressive loading regime) to perpendicular (bending loading regime), according to the combined compressive–bending model. (b) Markers indicate encastre boundary conditions constraining distal condyles in three directions. (c) Kinematic coupling constraint between a central reference point and 10 nodes forming the load surface, to which a torsional moment is applied.

as solid parts into ABAQUS v. 6.10 (Simula, USA). In order to create a hollow bone part, the endosteal part was subtracted from the periosteal part, using a Boolean operation within ABAQUS. A homologous value for Young's modulus (stress/elastic strain) of 19 GPa and Poisson's ratio of 0.3 were assigned to all finite element models [36].

Hollow bone parts were meshed using a built-in Delaunay meshing algorithm, and for each bone, a one-way sensitivity analysis on the effect of changing element size was conducted. Total element number was progressively increased from approximately 200 000 elements to greater than 1 million elements and stress values were recorded at three locations at midshaft under a simple compressive loading regime. An optimal mesh size was considered to have been reached once stress values converged (i.e. formed a straight line on a plot of stress versus total element number) at all three locations. This occurred when element number exceeded roughly 800 000. However, convergence was reached at different mesh densities for each specimen, and the mesh sizes used for further analyses are detailed in the electronic supplementary material, S2.

A validation analysis carried out by Panagiotopoulou *et al.* [33] previously found four-node and eight-node tetrahedral, and mixed four-node tetrahedral and eight-node hexahedral FEA meshes to perform well, compared with *ex vivo* experimental data. By contrast, eight-node and 20-node hexahedral interpolations deviated significantly from recorded strain magnitudes. We, therefore, chose to carry out a comparison of C3D4 four-node linear tetrahedral and C3D10 10-node quadratic tetrahedral meshes. In mesh sizes beyond 200 000 elements, the difference in stress magnitudes between finite element models with 4 and 10-node tetrahedra was minimal (less than 5%; electronic supplementary material; figure S2). Meshes consisting of 10-node tetrahedra are computationally more expensive than those of 4-node tetrahedra, and C3D4 tetrahedra were, therefore, used throughout.

Each hollow bone model was loaded under combined compression and bending (0–90°), and axial torsion. For each loading regime, total applied load was calculated as 1 per cent of body mass (M_b ; kg) multiplied by gravitational acceleration (G ; 9.81 m s⁻²; table 1). A force equivalent to 1 per cent of M_b was chosen in order to ensure that absolute strain magnitudes were small and deformation remained within the linear elastic region. The actual magnitude of the force is, therefore, largely unimportant in this study because there is a direct linear relationship between force and strain (stress).

For the combined compression–bending models, the condyles of the distal epiphyses were constrained in all three directions at 20

nodes on the distal surface using the ABAQUS 'encastre' boundary condition (figure 4). The applied force was spread across 10 adjacent nodes on the upper surface of the proximal epiphyses (figure 4). In order to minimize the extent of induced bending associated with off-axis application of compressive force, the orientation of the bones' principal axes was calculated using the 'moments of inertia' function of the BONEJ [37] plugin for IMAGEJ (US National Institutes for Health, MD, USA). To simulate compressive loading, the force was applied parallel to the longest principal axis, at nodes corresponding to the location at which the axis emerged onto the proximal epiphyseal surface. To simulate combined compressive and bending loading [29], FEA models for compressive loading were rerun while incrementally modifying the load vector from 10° to 90° from the principal axis.

To load the hollow bones under torsion, the condyles of the distal epiphyses were constrained in all three directions. A constraint control point (CP) was created on the proximal epiphyses, corresponding to the location at which the principal axis emerged onto the surface. The CP was constrained in all three directions, and a kinematic couple created between the load surface (defined as 10 nodes surrounding the CP) and the CP itself (figure 4). A torsional moment about the long axis was applied to the CP and transmitted to the load surfaces via the kinematic coupling. A linear elastic analysis was conducted on all models, and equations were solved using Gaussian elimination. Stress values used in this study were taken at a considerable distance from the constrained nodes. Stresses near constraints are known to be inaccurate in finite element modelling.

For bending and torsional loading regimes, the greatest value of principal stress (i.e. maximum principal stress, σ_{\max}) was extracted from midshaft and used for comparison with beam theory. For models under compression, the most negative value of principal stress (minimum principal stress, σ_{\min}) was recorded. For all loading conditions, the distribution of Von Mises stress (σ_{vm}) at midshaft was also noted. Von Mises stress combines the three principal stresses into one equivalent stress. σ_{vm} is signless and visually intuitive, and is, therefore, used in this study for illustrative purposes.

2.3. Simple beam theory

Basic morphometric properties were collected from the models to use in classic beam analysis. Cross-sectional geometrical properties of the hollow bone models were calculated at midshaft, using BONEJ. The coordinate system of both ABAQUS and IMAGEJ was in agreement, ensuring calculated values of radii and second moments of area corresponded to the load axis of the finite

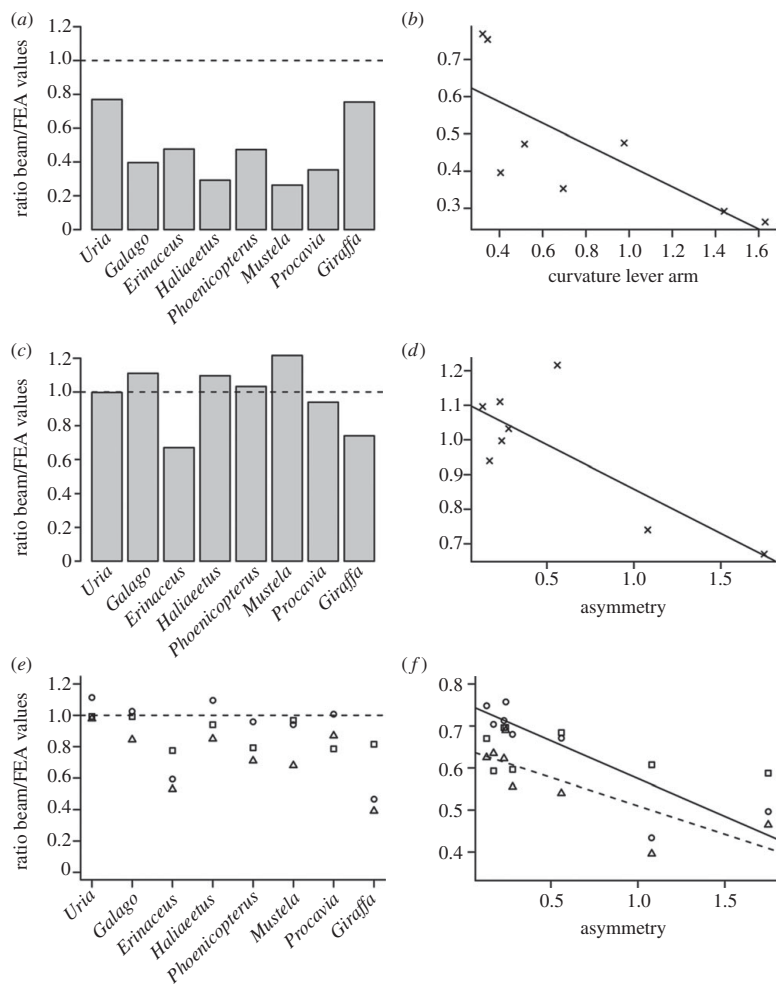


Figure 5. Comparison of FEA and beam theory values under various loading regimes, and correlations with bone geometry. (a) Plot of compressive stress as a ratio of beam theory values/FEA values (σ_{\min}) for each individual. (b) Ordinary least-squares regression of compressive stress ratio against normalized curvature lever arm (slope = -0.28 , intercept = 0.70 , $r^2 = 0.56$). (c) Plot of bending stress as a ratio of beam theory values/FEA values (σ_{\max}) for each individual. (d) Ordinary least-squares regression of bending stress ratio against cross-sectional asymmetry (slope = -0.26 , intercept = 1.37 , $r^2 = 0.62$). (e) Plot of torsional stress as a ratio of beam theory values/FEA values (σ_{tors}) for each individual; triangles, hollow ellipse model; circles, thin-walled ellipse model; squares, minimum wall thickness model. (f) Ordinary least-squares regression of torsional stress ratio against cross-sectional asymmetry. Symbols as in (e). Dashed line fitted to hollow ellipse model (slope = -0.27 , intercept = 1.16 , $r^2 = 0.65$); solid line fitted to thin-walled ellipse model (slope = -0.36 , intercept = 1.47 , $r^2 = 0.77$).

element models. Cross-sectional properties were entered into equation (1.3) to estimate maximum compressive and bending stresses at midshaft, under the same applied load as FEA models. Values of t (taken as mean cortical thickness), t_{\min} and A required for equations (1.5) and (1.6) were calculated using a custom-written script in MATLAB v. 7.10 (The MathWorks Inc., Natick, MA, USA; see the electronic supplementary material, S1) before torsional stresses were estimated in the same manner.

Cross-sectional asymmetry was estimated as the ratio of two orthogonal measures of second moment of area (I_{\max}/I_{\min}). Normalized curvature lever arm (ζ) was calculated as the distance between the chord drawn between the proximal- and distal-most points of the epiphyses, and the location of the centroid at midshaft, divided by the radius (figure 3). Curvature was calculated in order to investigate the effect of irregular morphology on deviation between stress values predicted by FEA and beam theory. At this point, no attempt was made to correct

the simple beam equations for curvature (but see §4 for further details). To test for relationships between bone morphology and deviation of FEA values from beam theory, type I ordinary least-squares regressions were carried out using the SMATR package [38] of statistical software R (www.cran.r-project.org).

3. Results

3.1. Compression

When loaded in axial compression, all FEA models experienced significant levels of induced bending at midshaft. In figure 5a, a beam theory/FEA ratio of 1 suggests complete agreement between the models, whereas values greater than 1 indicate beam theory predictions fall consistently below those of FEA. At mid-cortex, beam theory and FEA

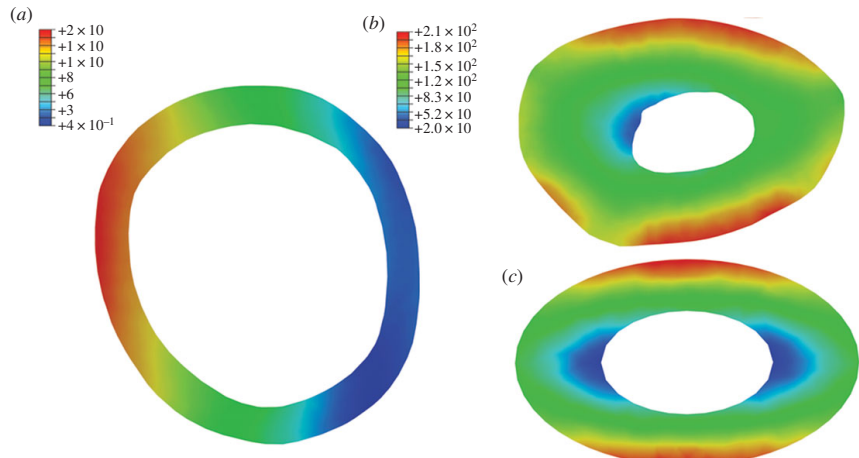


Figure 6. (a) Distribution of Von Mises stress at midshaft of a flamingo (*Phoenicopterus*) femur under compressional loading. Induced bending is indicated by one cortex being placed in compression (low values of σ_{vm}), while the opposite cortex is in tension (high values of σ_{vm}). Value predicted by classic beam theory (approx. 7 kPa) lies between these cortices. Values in legend reported in kilopascals. (b) Distribution of σ_{vm} at midshaft of giraffe (*Giraffa*) tibia under torsion. Note the highest stress values occur where cortical wall thickness is at a minimum. (c) For comparative purposes, the distribution of σ_{vm} in a simple elliptical toroid under torsion. Loads applied in (a) and (b) are species-specific and correspond to 1% of body mass (table 1).

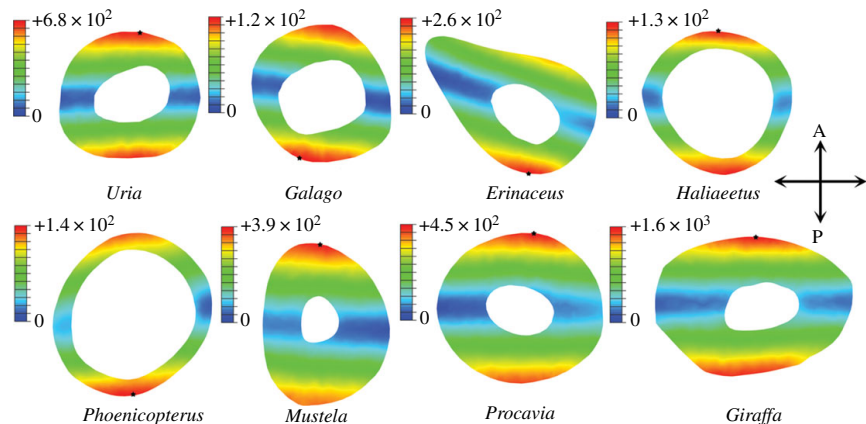


Figure 7. Distribution of Von Mises stress at midshaft of diaphyses under bending. Values in legend reported in kilopascals (kPa). Star indicates location of maximum value of σ_{vm} . Lowest values of σ_{vm} (blue) indicate approximate position of neutral axis of bending. Loads applied are species-specific and correspond to 1% of body mass (table 1).

are in agreement (figure 6a), whereas minimum principal stresses (σ_{min}) furthest from the neutral axis are on average 142 per cent ($\pm 28\%$ s.e.) above predicted beam values. The model with the greatest normalized curvature lever arm (*Mustela putorius*, $\zeta = 1.63$) also displays the greatest deviation of σ_{min} from predicted values (280%). Similarly, the model with the smallest degree of curvature (*Uria aalge*, $\zeta = 0.32$) experienced the least deviation from predicted values (30%). There is a significant relationship between shaft curvature and variation between beam theory and FEA values (two-tailed $p = 0.03$, $r^2 = 0.56$; figure 5b).

3.2. Bending

The location of maximum σ_{vm} (signless) varies between models, alternating between regions of the periosteal surface

under maximum tension or compression (figure 7). Values of σ_{max} predicted by equation (1.3) are on average 12 per cent ($\pm 4\%$ s.e.) different from those calculated in finite element models (figure 5c). For half the species modelled here, equation (1.3) underestimates σ_{max} compared with FEA models, whereas σ_{max} is overestimated in the remaining four species (figure 5c). No significant relationship is found between aspect ratio of the bone and deviation of FEA values from those predicted by beam theory. However, a significant relationship does exist between the asymmetry of the cross section and the ratio of FEA to beam theory values (two-tailed $p = 0.02$, $r^2 = 0.62$; figure 5d).

Under Alexander's [29] model of combined compressive and bending loading, stress increases rapidly as the load vector shifts from parallel to perpendicular to the shaft long axis (figure 8). With the exception of *Giraffa*, the maximum

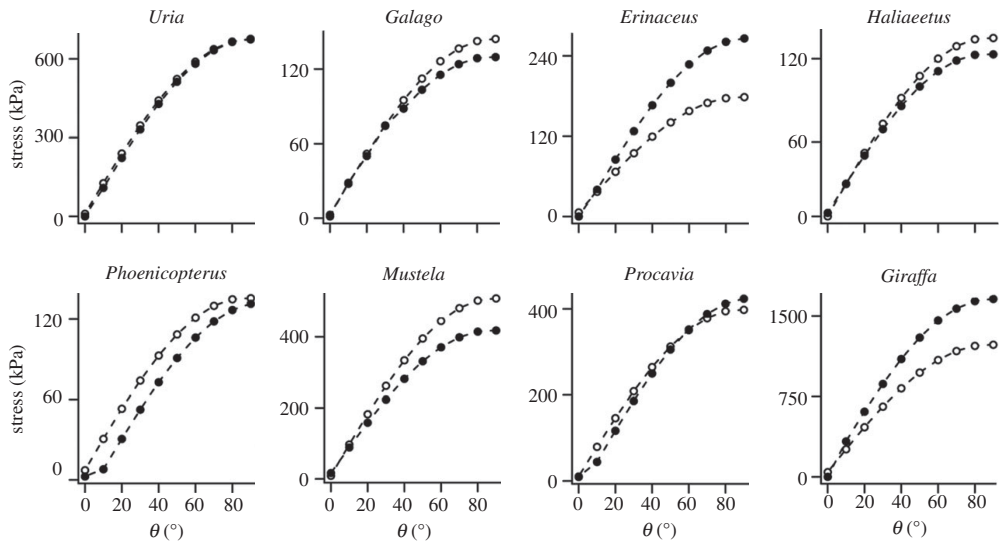


Figure 8. Individual species plots of stress (kPa) against load vector (θ). Solid black circles represent maximum values of σ_{\max} extracted from midshaft of FEA models. Open circles represent values predicted by beam theory, calculated according to equation (1.3). Loads applied are species-specific and correspond to 1% of body mass (table 1).

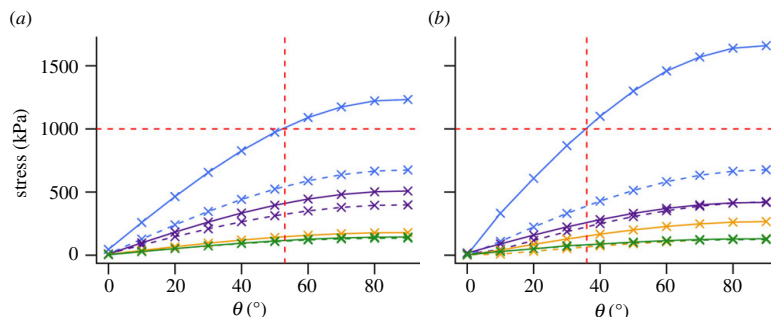


Figure 9. Species curves of σ_{combined} against bone orientation. (a) Stress values calculated according to classic beam theory. (b) Stress values extracted from midshaft of finite element models. Blue solid line, *Giraffa*; blue dashed line, *Uria*; purple solid line, *Mustela*; purple dashed line, *Procavia*; gold solid line, *Erinaceus*; gold dashed line, *Phoenicopterus*; green solid line, *Galago*; green dashed line, *Haliaeetus*. Horizontal red dashed line represents arbitrary value of 1000 kPa discussed in text. Vertical red dashed line represents intercept of horizontal line with stress curve of *Giraffa*, indicating maximum angle from vertical at which tibia may be held whilst not exceeding stress value of 1000 kPa. Loads applied are species-specific and correspond to 1% of body mass (table 1).

deviation between FEA values and simple beam predictions occurs at $\theta = 90^\circ$, i.e. under compression (figure 8). As load vectors shift perpendicular to the bone long axis and bending dominates the loading regime, percentage deviation between FEA and beam theory is at minimum between 50° and 80° , and increases again towards 0° from vertical. A plot of σ_{combined} against bone orientation for FEA and simple beam models for all species is provided in figure 9.

3.3. Torsion

Comparing the values of τ_{torsion} predicted by equations (1.4)–(1.6) with those calculated using FEA, the hollow ellipse model (equation (1.4)) underestimates τ_{torsion} most (FEA values on average are 48% ($\pm 18\%$ s.e.) above those of classic beam theory; figure 5e). The thin-walled ellipse model (equation (1.5)) and minimum wall thickness model (equation (1.6)) both provide reasonable estimates of τ_{torsion} (FEA values on

average 21% ($\pm 16\%$ s.e.) and 14% ($\pm 5\%$ s.e.) above beam theory, respectively). It must be emphasized that the thin-walled ellipse model provides an estimate of *average* τ_{torsion} in a cross section (using mean t in equation (1.5)), while we are comparing these values with *maximum* stress values extracted from FEA models. Applying either the hollow ellipse model or the thin-walled ellipse model, there is a significant relationship between cross-sectional asymmetry and variation between beam theory and FEA values (hollow ellipse model, two-tailed $p = 0.016$, $r^2 = 0.65$; thin-walled ellipse model, two-tailed $p = 0.004$, $r^2 = 0.77$; figure 5f). However, when applying the minimum wall thickness model, no such relationship exists.

4. Discussion

When finite element models were loaded under axial compression, a significant bending stress resulted with values of

σ_{\min} averaging over twice as high as those predicted by beam theory. Previous *in vivo* studies have found that σ_{bending} contributes to total stress to a much greater degree than σ_{comp} during locomotion [39], in part owing to eccentric (off-axis) dynamic loading. The earlier-mentioned results highlight the additional importance of bending moments induced by on-axis forces acting about the longitudinal curvature of a static bone. Hence, pure compression as calculated by equation (1.1) is clearly an unrealistic loading modality for any long bone owing to shaft curvature. Here we show that a long bone, subjected to compressive axial loads, will probably fail, owing to the curvature-induced bending stress long before Euler buckling could be of concern. Therefore, it has been shown again here that in scaling studies there is no basis for the simplification of complex curved geometries down to idealized straight columns necessary to infer buckling as a viable failure mode. The extent to which finite element models deviate from simple beam predictions of compression is not constant, but is instead correlated with normalized curvature lever arm (ζ). This precludes the application of a single correction factor to account for shaft curvature and implies a measure of curvature must be incorporated into simple beam equations and calculations of ‘relative strength’ values, where previous studies have not done so [1,5,16,40].

This may be achieved simply by reusing equation (1.3) and assuming that a bone loaded in compression with a shaft curvature of 5° is equivalent to loading a straight bone at an angle of 5° from its longest principal axis (θ). Compressive loads are split into axial and transverse components as in equation (1.3)

$$\sigma_{\text{comp}} = \frac{F \cos \vartheta}{A_{\text{cort}}} + \frac{M_x y \sin \vartheta}{I_x}, \quad (4.1)$$

where ϑ is the angle between the chord drawn between the proximal- and distal-most points of the epiphyses, and the chord joining the proximal-most point with the centroid at midshaft (figure 3). Having subsequently corrected for curvature in our sample by applying equation (4.1), beam theory results overestimate σ_{comp} relative to FEA values in all but one instance, compared with the consistent underestimation of σ_{comp} when applying equation (1.1). In terms of percentage deviation between models, application of equation (4.1) brought the majority of beam theory predictions closer inline with FEA results than when applying equation (1.1). As such, equation (4.1) provides a worst-case scenario estimate of σ_{comp} , that is of particular interest when calculating safety factors of curved bones under compression.

The Euler–Bernoulli beam equation for estimating bending stress in cylinders (equations (1.2) and (1.3)) ignores potential transverse shear stresses, which may lead to an underestimation of the maximum stress in uniform circular cross sections of up to 12 per cent [41]. Indeed, the bending stress may even exceed normal stresses in some locations within long bones [42]. Here, we also find that FEA values and simple beam values differ on average by 12 per cent, with a maximum deviation of up to 35 per cent (*Giraffa*). Yet in half the models, beam formulae overestimated σ_{bending} relative to FEA values.

Interestingly, no relationship is found between aspect ratio of the bone and percentage deviation between the two estimates of σ_{bending} . Instead, this deviation appears to relate to the cross-sectional shape and the change in shape down-shaft. Those species with the greatest cross-sectional asymmetry (*Giraffa*, *Mustela*, *Erinaceus europaeus*) are found

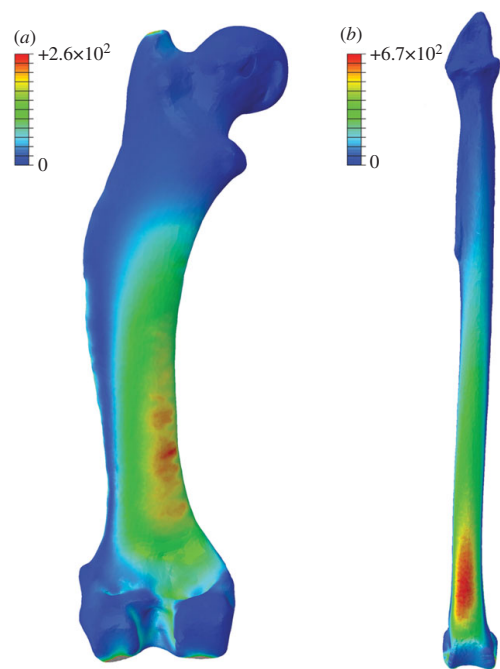


Figure 10. Whole-bone distribution of Von Mises stress under bending loading regime. (a) *Erinaceus* femur. (b) *Uria* tibia. Values in legend reported in kilopascals (kPa). Note the regular increase in σ_{vm} towards the fixed end in the beam-like tibia of the guillemot. In contrast, note the uneven distribution of stresses in the hedgehog femur, probably owing to irregular geometry down-shaft and the occurrence of degree of torsion under bending. Loads applied are species-specific and correspond to 1% of body mass (table 1).

to have the greatest deviation between the two stress estimates (figure 5c and table 1). Therefore, in interspecific samples characterized by high morphological diversity, a measure of asymmetry should be incorporated into estimates of σ_{bending} . In engineering, it is standard practice to account for a lack of mirror symmetry by including an additional measure of product moments of area (I_{xy})

$$\sigma_{\text{bending}} = - \left(\frac{M_y I_x + M_x I_{xy}}{I_x I_y - I_{xy}^2} \right) x + \left(\frac{M_x I_y + M_y I_{xy}}{I_x I_y - I_{xy}^2} \right) y, \quad (4.2)$$

where M_y is the bending moment about the y -axis, x is the perpendicular distance to the centroidal y -axis and I_y is the second moment of area about the y -axis [43]. Inspecting the distribution of σ_{bending} values at midshaft across models (figure 7), it is clear that some bones experience a degree of twisting when loaded under bending. In *Erinaceus* and *Phoenicopterus ruber*, it is particularly noticeable that the neutral section (plane of zero stress where the bone is neither in tension nor in compression) has rotated away from the mediolateral axis. Such torquing of the bone under bending is not accounted for in equations (1.2), (1.3) or (4.2), and most likely results from irregularities in cross-sectional geometry away from the midshaft (i.e. trochanters, flanges, crests; figure 10). Unfortunately, there is no simple way of quantifying or accounting for down-shaft variation in geometry in classic beam theory, and FEA remains the preferred solution for bones of a complex shape.

The combined compression–bending model of equation (1.3) [29] is broadly supported by the results of our FEA models. The predicted increase in total stress as a result of shifting load vectors is present (figure 8). However, the combined model suffers from the compounded problems associated with equations (1.1) and (1.2). The decrease in effective stress as bones are orientated parallel to their load axes has been incorporated into the ‘effective mechanical advantage’ theory, by which safety factors in large mammals are maintained via adoption of increasingly erect postures during the stance phase [44]. The above results highlight the importance of incorporating curvature into such models in the future. As an example, assuming that an arbitrary value of 1000 kPa must be maintained in order to achieve a given safety factor in the tibia of *Giraffa*, equation (1.3) would predict the bone may be held at a maximum of 53° from vertical (figure 9a). By contrast, the stress curve produced under FEA predicts the tibia must not exceed 36° from vertical in order to maintain the same safety factor (figure 9b).

In agreement with results found elsewhere [32], the minimum wall thickness model is found to be most suitable in estimating $\tau_{torsion}$. Equation (1.6) recognizes that minimum torsional strength occurs in regions where cortical thickness is least [30] and is supported by the distribution of cortical stresses noted in finite element models (figure 6b,c). While estimates of $\tau_{torsion}$ based on the hollow ellipse or thin-walled ellipse are still affected by the degree of asymmetry present in the cross section, no such relationship exists when applying the minimum wall thickness model, and equation (1.6) provides a reasonable estimate of $\tau_{torsion}$ as calculated by FEA models.

Figure 6b,c clearly illustrates the divergence of complex bone cross sections from the idealized toroidal cross sections familiar to engineers. Classic beam theory is a technique that rests upon certain geometrical assumptions that are clearly invalidated in the case of irregular long bone morphology, and the consequences are evident in the discrepancy between FEA and beam theory presented here. Both classic beam theory and FEA allow the biomechanical behaviour of long bones to be modelled. As such, the results outlined earlier afford a methodological comparison of two models of reality; however, they are unlikely to reflect *in vivo* loaded behaviour, particularly as both FEA and simple beam models assume uniform elasticity and material density. The results of a previous study, in which an FEA model of an elephant femur was validated by means of laser speckle interferometry [33], found strain magnitudes predicted by FEA models consisting of homogeneous isotropic material properties to differ 60 per cent from *ex vivo* experimental values. By contrast, FEA models incorporating heterogeneous material properties deviated only 5 per cent from experimental values. Incorporating the anisotropic behaviour of bone into FEA models has also been found to improve their accuracy in predicting regions of fracture [45], although further work is needed to clarify the errors associated with assumptions of bone isotropy [46].

Furthermore, the loading conditions considered in the present study are highly idealized, in that forces are applied only at articular surfaces. In reality, peak locomotory forces are generated by contraction of muscles attached at various locations along the length of the shaft, and may be a considerable distance from the centre of joint rotation. Although beyond the scope of this study, future work may focus upon comparing numerical models to *in vivo* strain gauge

derived values of stress under average and extreme locomotor activity. Such a study would be advantageous in incorporating realistic muscle forces, and could illuminate the relative importance of compression, bending and torsion across taxa and locomotor type.

5. Conclusions

For interspecific samples of diverse morphology, reliance upon Euler–Bernoulli classic beam theory to address questions of comparative functional morphology in vertebrate bones will result in estimation errors of varying magnitude and direction. The utility of commonly used beam formulae is a function of the extent to which skeletal elements conform to the assumptions of classic beam theory. While beam-theory-derived values still probably correlate with actual stress values, care must be taken when interpreting mechanical function based on these values. In the small sample of vertebrate bones considered here, application of FEA leads to a change in the rank order of absolute stress values across species compared with beam theory predictions, most noticeably so in the case of compression. It is therefore of concern that real biomechanical signals within the sample may be lost, owing to the use of inappropriate beam formulae. Suggestions are made for alternative methods by which beam theory may be more reliably applied, such as the incorporation of curvature in estimates of σ_{comp} including product moments of area into estimates of $\sigma_{bending}$ and calculating $\tau_{torsion}$ at the location of minimum cortical wall thickness.

In spite of these extensions of beam theory, when absolute values of diaphyseal stress are required for biomechanical analyses, FEA remains the preferred solution. With improvements in computational power, user accessibility and the availability of CT facilities, it is now feasible to generate large datasets of finite element models for the purpose of comparative functional morphology. FEA benefits from the incorporation of whole-bone geometry into models and overcomes problems associated with curvature, asymmetry and shear deformations. With interest in longitudinal variations in bone strength indices increasing [47,48], FEA represents a technique by which muscle attachment sites and trochanters may be studied, when their irregular geometry might otherwise preclude the application of classic beam theory.

Future studies applying FEA to long bone stress estimation should proceed with caution, however, particularly when variables such as applied forces and material properties remain uncertain. This is necessarily the case in palaeontological studies, and, therefore, sensitivity analyses should be carried out in order to quantify the effect of the error introduced by these unknowns. It must be emphasized that applying an overly simplified FEA model to a complex biomechanical problem may result in incorporating just as many assumptions into the analysis as the application of classic beam theory.

The authors are grateful to the staff of the Henry Moseley X-ray Imaging Facility (supported by EPSRC under nos. EP/F007906 and EP/I02249X), University of Manchester; Prof. Paul Mummery, Dr Tristan Lowe; the staff in Research Computing Services, University of Manchester; the University of Liverpool Small Animal Hospital: Martin Baker; Manchester Museum: Henry McGhie, Judith White; Liverpool World Museum: Tony Parker. The comments of four anonymous reviewers were extremely useful in refining the manuscript. This research was supported by the UK Natural Environment Research Council Doctoral Training Grant no. NE/1528134/1.

References

- Habib M, Ruff C. 2008 The effects of locomotion on the structural characteristics of avian limb bones. *Biol. J. Linn. Soc.* **153**, 601–624. (doi:10.1111/j.1096-3642.2008.00402.x)
- Witton M, Habib M. 2010 On the size and flight diversity of giant pterosaurs, the use of birds as pterosaur analogues and comments on pterosaur flightlessness. *PLoS ONE* **5**, e13982. (doi:10.1371/journal.pone.0013982)
- Farke A, Alicea J. 2009 Femoral strength and posture in terrestrial birds and non-avian theropods. *Anat. Rec.* **292**, 1406–1411. (doi:10.1002/ar.20963)
- Christiansen P. 1998 Strength indicator values of theropod long bones, with comments on limb proportions and cursorial potential. *Gaia* **15**, 241–255.
- Hokkanen J. 1986 The size of the largest land animal. *J. Theor. Biol.* **118**, 491–499. (doi:10.1016/S0022-5193(86)80167-9)
- Sellers W, Manning P, Lyson T, Stevens K, Margetts L. 2009 Virtual palaeontology: gait reconstruction of extinct vertebrates using high performance computing. *Palaeontol. Electron.* **12**, 11A.
- Daegling D, Hylander W. 1998 Biomechanics of torsion in the human mandible. *Am. J. Phys. Anthropol.* **105**, 73–87. (doi:10.1002/(SICI)1096-8644(199801)105:1<73::AID-AJPA7>3.0.CO;2-E)
- Euler L. 1744 *De curvis elasticis*. Geneva, Switzerland: Bousquet.
- Young J, Fernández D. 2010 Ontogeny of long bone geometry in capuchin monkeys (*Cebus albifrons* and *Cebus apella*): implications for locomotor development and life history. *Biol. Lett.* **6**, 197–200. (doi:10.1098/rsbl.2009.0773)
- Wilson M, Espinoza N, Shah S, Blob R. 2009 Mechanical properties of the hindlimb bones of bullfrogs and cane toads in bending and torsion. *Anat. Rec.* **292**, 935–944. (doi:10.1002/ar.20929)
- Sparacello V, Pearson O. 2010 The importance of accounting for the area of the medullary cavity in cross-sectional geometry: a test based on the femoral midshaft. *Am. J. Phys. Anthropol.* **143**, 612–624. (doi:10.1002/ajpa.21361)
- Stock J, Shaw C. 2007 Which measures of diaphyseal robusticity are robust? A comparison of external methods of quantifying the strength of long bone diaphyses to cross-sectional geometric properties. *Am. J. Phys. Anthropol.* **134**, 412–423. (doi:10.1002/ajpa.20686)
- Gere J, Goodno B. 2012 *Mechanics of materials*. Stamford, CT: Cengage Learning.
- Main R, Lynch M. 2010 *In vivo* tibial stiffness is maintained by whole bone morphology and cross-sectional geometry in growing female mice. *J. Biomed.* **43**, 2689–2694. (doi:10.1016/j.jbiomech.2010.06.019)
- McMahon T. 1973 Size and shape in biology: elastic criteria impose limits on biological proportions, and consequently on metabolic rates. *Science* **179**, 1201–1204. (doi:10.1126/science.179.4079.1201)
- Garcia G, da Silva J. 2004 On the scaling of mammalian long bones. *J. Exp. Biol.* **207**, 1577–1584. (doi:10.1242/jeb.00890)
- Alexander R. 2003 *Principles of animal locomotion*. Princeton, NJ: Princeton University Press.
- Biewener A. 1983 Allometry of quadrupedal locomotion: the scaling of duty factor, bone curvature and limb orientation to body size. *J. Exp. Biol.* **105**, 147–171.
- Butcher M, Blob R. 2008 Mechanics of limb bone loading during terrestrial locomotion in river cooter turtles (*Pseudemys concinna*). *J. Exp. Biol.* **211**, 1187–1202. (doi:10.1242/jeb.012989)
- Kokshenev V. 2007 New insights into long-bone biomechanics: are limb safety factors invariable across mammalian species? *J. Biomech.* **40**, 2911–2918. (doi:10.1016/j.jbiomech.2007.03.007)
- Bertram J, Biewener A. 1992 Allometry and curvature in the long bones of quadrupedal mammals. *J. Zool.* **226**, 455–467. (doi:10.1111/j.1469-7998.1992.tb07492.x)
- Cubo J, Menten L, Casinos A. 1999 Sagittal long bone curvature in birds. *Ann. Sci. Nat. Zool.* **20**, 153–159. (doi:10.1016/S0003-4339(00)88883-8)
- Hylander W. 1985 Mandibular function and biomechanical stress and scaling. *Am. Zool.* **25**, 315–330.
- Vinyard C, Ravossi M. 1999 Ontogeny, function, and scaling of the mandibular symphysis in papionin primates. *J. Morphol.* **235**, 157–175. (doi:10.1002/(SICI)1097-4687(199802)235:2<157::AID-JMOR5>3.0.CO;2-6)
- Turner C, Burr D. 1993 Basic biomechanical measurements of bone: a tutorial. *Bone* **14**, 595–608. (doi:10.1016/8756-3282(93)90081-K)
- Dunning J. 1993 *CRC handbook of avian body mass*. Boca Raton, FL: CRC Press.
- Silva M, Downing J. 1995 *CRC handbook of mammalian body masses*. Boca Raton, FL: CRC Press.
- Smithers R. 1983 *The mammals of the Southern African subregion*. Pretoria, South Africa: University of Pretoria.
- Alexander R. 1974 The mechanics of jumping by a dog (*Canis familiaris*). *J. Zool.* **173**, 549–573. (doi:10.1111/j.1469-7998.1974.tb04134.x)
- Roark R. 1965 *Formulas for stress and strain*, 4th edn. London, UK: McGraw-Hill.
- Lovejoy C, Burstein A, Heiple K. 1976 The biomechanical analysis of bone strength: a method and its application to platycnemia. *Am. J. Phys. Anthropol.* **44**, 489–505. (doi:10.1002/ajpa.130440312)
- Daegling D. 2002 Estimation of torsional rigidity in primate long bones. *J. Hum. Evol.* **43**, 229–239. (doi:10.1006/jhev.2002.0574)
- Panagiotopoulou O, Wilshin S, Rayfield E, Shefelbine S, Hutchinson J. 2011 What makes an accurate and reliable subject-specific finite element model? A case study of an elephant femur. *J. R. Soc. Interface* **9**, 351–361. (doi:10.1098/rsif.2011.0323)
- Cristofolini L, Schileo E, Juszczyk M, Taddei F, Martelli S, Viceconti M. 2010 Mechanical testing of bones: the positive synergy of finite-element models and *in vitro* experiments. *Phil. Trans. R. Soc. A* **368**, 2725–2763. (doi:10.1098/rsta.2010.0046)
- Rosset A, Spadola L, Ratib O. 2004 OsiriX: an open-source software for navigating in multidimensional DICOM images. *J. Digit. Imaging* **17**, 205–216. (doi:10.1007/s10278-004-1014-6)
- Rubin C, Lanyon L. 1984 Dynamic strain similarity in vertebrates; an alternative to allometric limb bone scaling. *J. Theor. Biol.* **107**, 321–327. (doi:10.1016/S0022-5193(84)80031-4)
- Doube M, Kłosowski M, Arganda-Carreras I. 2010 BoneJ: free and extensible bone image analysis in IMAGEJ. *Bone* **47**, 1076–1079. (doi:10.1016/j.bone.2010.08.023)
- Warton D, Duursma R, Falster D, Taskinen S. 2011 smatr 3: an R package for estimation and inference about allometric lines. *Methods Ecol. Evol.* **3**, 257–259. (doi:10.1111/j.2041-210X.2011.00153.x)
- Biewener A. 1991 Musculoskeletal design in relation to body size. *J. Biomech.* **24**, 19–29. (doi:10.1016/0021-9290(91)90374-V)
- Demes B. 2007 *In vivo* bone strain and bone functional adaptation. *Am. J. Phys. Anthropol.* **133**, 717–722. (doi:10.1002/ajpa.20584)
- Barber J. 2002 *Elasticity*. Dordrecht, The Netherlands: Springer.
- Kourtis L, Carter D, Kesari H, Beaupré G. 2008 A new software tool (VA-BATTS) to calculate bending, axial, torsional and transverse shear stresses within bone cross sections having inhomogeneous material properties. *Comput. Methods Biomed. Eng.* **11**, 463–476. (doi:10.1080/10255840801930728)
- Pilkey W. 2002 *Analysis and design of elastic beams*. New York, NY: John Wiley & Sons.
- Biewener A. 1989 Scaling body support in mammals: limb posture and muscle mechanics. *Science* **245**, 45–48. (doi:10.1126/science.2740914)
- Gómez-Benito M, García-Aznar J, Doblaré M. 2005 Finite element prediction of proximal femoral fracture patterns under different loads. *J. Biomed. Eng.* **127**, 9–14. (doi:10.1115/1.1835347)
- Schileo E, Taddei F, Malandrino A, Cristofolini L, Viceconti M. 2007 Subject-specific finite element models can accurately predict strain levels in long bones. *J. Biomed.* **40**, 2982–2989. (doi:10.1016/j.jbiomech.2007.02.010)
- Doube M. 2009 Three-dimensional geometric analysis of felid limb bone allometry. *PLoS ONE* **4**, e4742. (doi:10.1371/journal.pone.0004742)
- Doube M, Yen S, Kłosowski M, Farke A, Hutchinson J, Shefelbine S. 2012 Whole-bone scaling of the avian pelvic limb. *J. Anat.* **221**, 21–29. (doi:10.1111/j.1469-7580.2012.01514.x)

3.8 Supplementary Material

3.8.1 (S1) MATLAB code for calculating A , t and t_{min}

```
%% Code for calculating torsional x-sectional properties

clear all
close all

%% Load in image

data = imread('hedgehog.tif');

resolution = input('What is the pixel size (mm)?')

%Find centroid of bone shape

[i,j] = find(data(:,:,1)==0);

x0 = mean(j);
y0 = mean(i);

%% find edges radially from centroid

counter = 0;

for theta = 0:0.1:2*pi(); % do following procedures the whole way
    through 360 degrees

    counter = counter + 1;

    pixel = 255;

    rho = 0;
```

```

while(pixel == 255) % identify inner edge by working outwards from
    centroid in polar co-ordinates until pixel value changes from 255

    rho = rho +1;

    [x,y] = pol2cart(theta,rho);

    x1 = x0 + x;

    y1 = y0 + y;

    pixel = data(floor(y1),floor(x1));

end

rho2 = rho;

while(pixel == 0) % carry on above procedure until pixel value is
    back to 255.

    rho2 = rho2 +1;

    [x,y] = pol2cart(theta,rho2);

    x2 = x0 + x;

    y2 = y0 + y;

    pixel = data(floor(y2),floor(x2));

end

new_data(counter,:) = [theta x1 y1 x2 y2 (x1+x2)/2 (y1+y2)/2 rho
    rho2]; % record locations of inner, outer and median edges. Last
    columns are inner and outer radius

end

%% calculate length of circumference and area inside each edge

inner_circ = 0;

```

```

inner_area = 0;

for iii = 1:length(new_data(:,1))-1

dist_i = sqrt((new_data(iii+1,2)-new_data(iii,2)).^2 + (new_data
(ii+1,3)-new_data(iii,3)).^2);

inner_circ = inner_circ + dist_i; % circumference

dist_j = sqrt((new_data(iii+1,2)-x0).^2 + (new_data(iii+1,3)-y0)
.^2);

dist_k = sqrt((new_data(iii,2)-x0).^2 + (new_data(iii,3)-y0).^2)
;

s = (dist_i+dist_j+dist_k)/2; % s is the semiperimeter of very
thin triangle from centroid to edge

area_triangle = sqrt(s*(s-dist_i)*(s-dist_j)*(s-dist_k));% Heron
's formula for area of a triangle

inner_area = inner_area + area_triangle; % area enclosed by
inner circumference

end

outer_circ = 0;

outer_area = 0;

for iii = 1:length(new_data(:,1))-1

dist_i = sqrt((new_data(iii+1,4)-new_data(iii,4)).^2 + (new_data
(ii+1,5)-new_data(iii,5)).^2);

outer_circ = outer_circ + dist_i; % circumference

dist_j = sqrt((new_data(iii+1,4)-x0).^2 + (new_data(iii+1,5)-y0)
.^2);

```

```

dist_k = sqrt((new_data(iii,4)-x0).^2 + (new_data(iii,5)-y0).^2)
;

s = (dist_i+dist_j+dist_k)/2; % s is the semiperimeter of very
thin triangle from centroid to edge

area_triangle = sqrt(s*(s-dist_i)*(s-dist_j)*(s-dist_k)); %
Heron's formula for area of a triangle

outer_area = outer_area + area_triangle; % area enclosed by
outer circumference

end

mid_circ = 0;

mid_area = 0;

for iii = 1:length(new_data(:,1))-1

dist_i = sqrt((new_data(iii+1,6)-new_data(iii,6)).^2 + (new_data
(ii+1,7)-new_data(iii,7)).^2);

mid_circ = mid_circ + dist_i; % circumference

dist_j = sqrt((new_data(iii+1,6)-x0).^2 + (new_data(iii+1,7)-y0)
.^2);

dist_k = sqrt((new_data(iii,6)-x0).^2 + (new_data(iii,7)-y0).^2)
;

s = (dist_i+dist_j+dist_k)/2; % s is the semiperimeter of very
thin triangle from centroid to edge

area_triangle = sqrt(s*(s-dist_i)*(s-dist_j)*(s-dist_k)); %
Heron's formula for area of a triangle

mid_area = mid_area + area_triangle; % area enclosed by mid
circumference

```

```
end

innerradius = new_data(1:end, 8);

outerradius = new_data(1:end, 9);

thickness = outerradius-innerradius;

U = (mid_circ*resolution)/1000;

meanthickness = (mean(thickness)*resolution)/1000

minthickness = (min(thickness)*resolution)/1000

CSA = (outer_area-inner_area)*(resolution^2)/1000000

medianA = (mid_area*(resolution^2))/1000000
```

3.8.2 (S2) Convergence analysis of mesh density

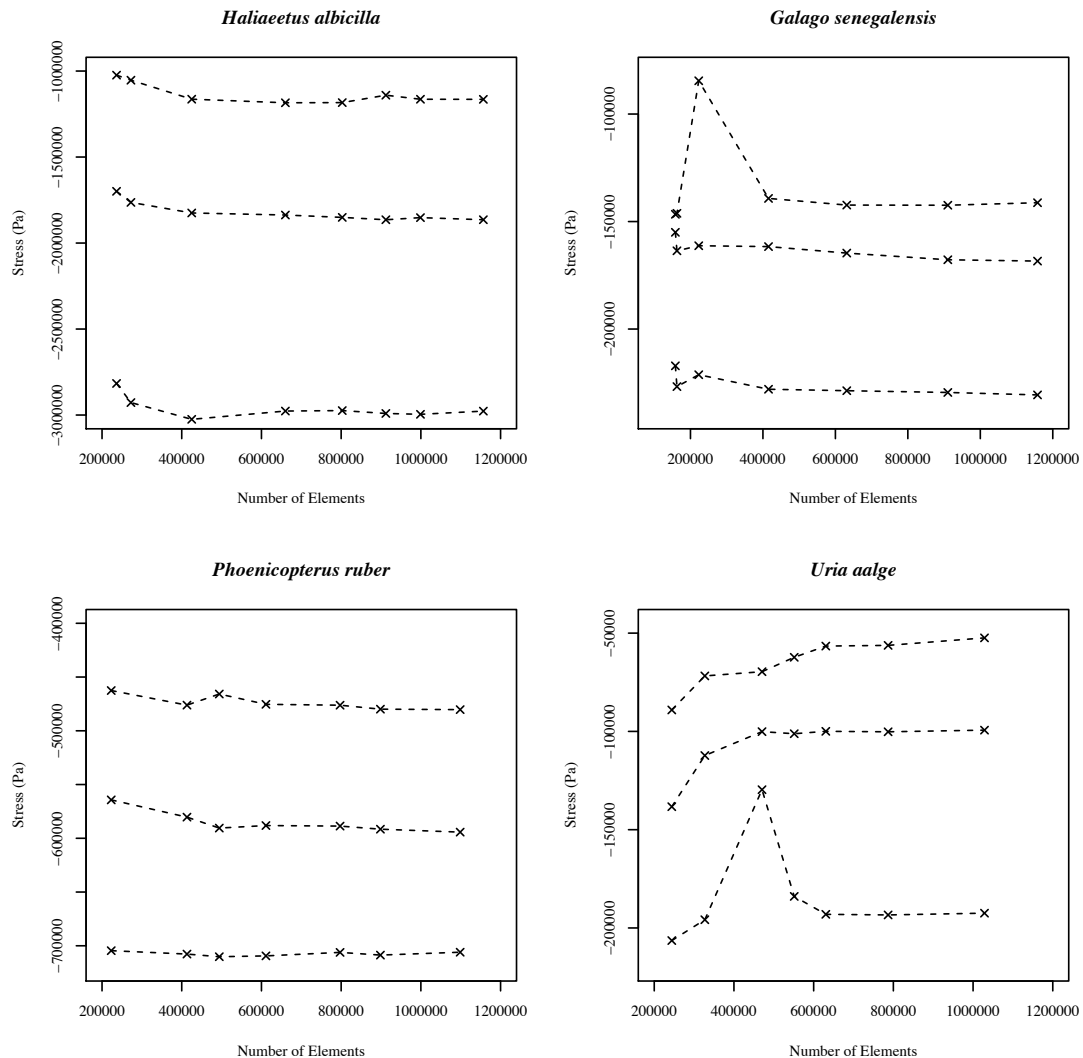


Figure 3.11: Supplementary Figure 1 - Sensitivity analysis of mesh density upon stress values: maximum principal stress plotted against total number of elements. Three lines on each graph represent three midshaft locations at which convergence was tested in each specimen

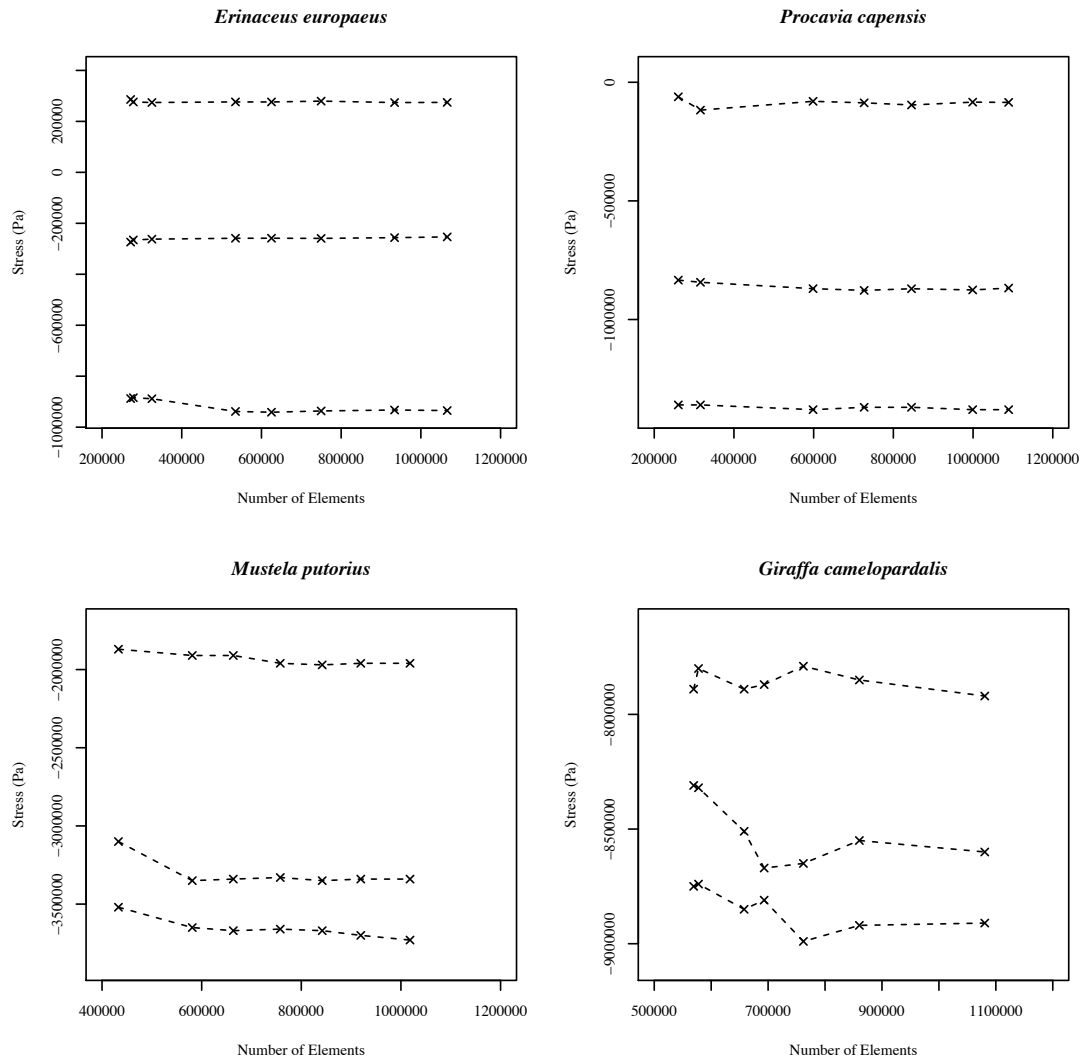


Figure 3.12: Supplementary Figure 1 (cont.)

Species	Total element no.	Element Size	Average aspect ratio	Aspect ratio > 10
<i>Mustela putorius</i>	847,940	0.21mm	1.72	0%
<i>Procavia capensis</i>	999,074	0.23mm	1.71	0%
<i>Haliaeetus albicilla</i>	912,190	0.47mm	1.69	0.002%
<i>Galago senegalensis</i>	910,316	0.13mm	1.94	0.011%
<i>Phoenicopterus ruber</i>	898,530	0.33mm	1.71	0.005%
<i>Giraffa camelopardalis</i>	860,307	2.25mm	1.73	0.004%
<i>Erinaceus europaeus</i>	934,058	0.14mm	1.69	0.001%
<i>Uria aalge</i>	786,812	0.22mm	1.84	0.062%

Table 3.2: Supplementary Table 1 - Model-specific optimal mesh densities and mesh diagnostics: Mesh densities and element sizes used in further analyses. Aspect ratio refers to the ratio of element height:width, and should ideally be kept close to unity

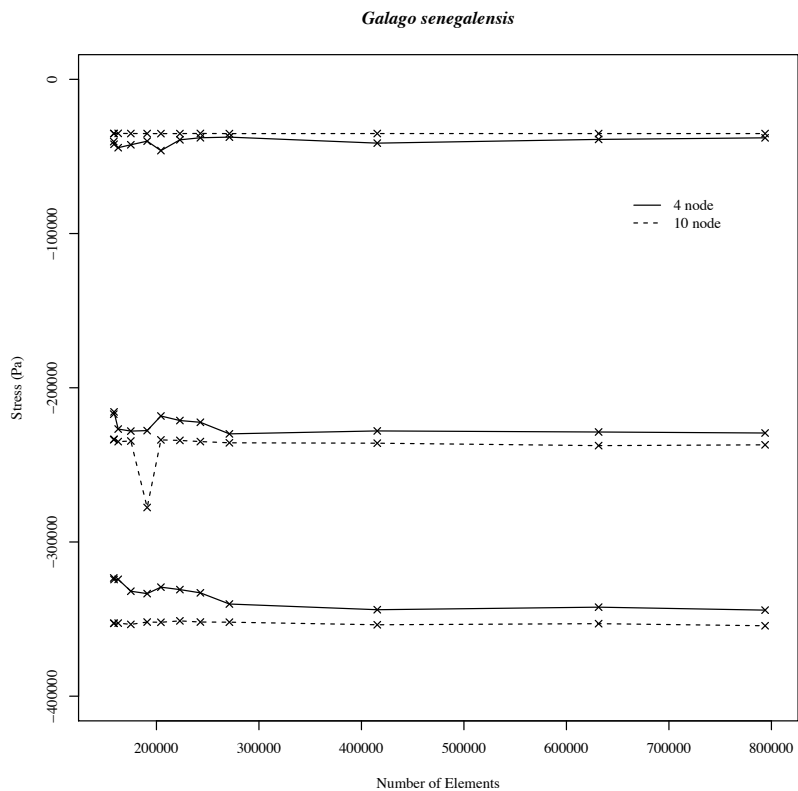


Figure 3.13: Supplementary Figure 2 - Sensitivity analysis of element shape upon stress values in Senegal bushbaby (*G. senegalensis*): Maximum principal stress measured at three midshaft locations against mesh density for linear 4-node and quadratic 10-node tetrahedra.

Chapter 4

More than one way of being a moa:
differences in leg bone robustness
map divergent evolutionary
trajectories in Dinornithidae and
Emeidae (Dinornithiformes)

PLoS ONE (2013). 8(12): e82668

More than One Way of Being a Moa: Differences in Leg Bone Robustness Map Divergent Evolutionary Trajectories in Dinornithidae and Emeidae (Dinornithiformes)

Charlotte A. Brassey^{1*}, Richard N. Holdaway², Abigail G. Packham¹, Jennifer Anné³, Philip L. Manning³, William I. Sellers¹

1 Faculty of Life Sciences, University of Manchester, Manchester, United Kingdom, **2** School of Biological Sciences, University of Canterbury, Christchurch, New Zealand, **3** School of Earth, Atmospheric and Environmental Science, University of Manchester, Manchester, United Kingdom

Abstract

The extinct moa of New Zealand included three families (Megalapterygidae; Dinornithidae; Emeidae) of flightless palaeognath bird, ranging in mass from <15 kg to >200 kg. They are perceived to have evolved extremely robust leg bones, yet current estimates of body mass have very wide confidence intervals. Without reliable estimators of mass, the extent to which dinornithid and emeid hindlimbs were more robust than modern species remains unclear. Using the convex hull volumetric-based method on CT-scanned skeletons, we estimate the mass of a female *Dinornis robustus* (Dinornithidae) at 196 kg (range 155–245 kg) and of a female *Pachyornis australis* (Emeidae) as 50 kg (range 33–68 kg). Finite element analysis of CT-scanned femora and tibiotarsi of two moa and six species of modern palaeognath showed that *P. australis* experienced the lowest values for stress under all loading conditions, confirming it to be highly robust. In contrast, stress values in the femur of *D. robustus* were similar to those of modern flightless birds, whereas the tibiotarsus experienced the highest level of stress of any palaeognath. We consider that these two families of Dinornithiformes diverged in their biomechanical responses to selection for robustness and mobility, and exaggerated hindlimb strength was not the only successful evolutionary pathway.

Citation: Brassey CA, Holdaway RN, Packham AG, Anné J, Manning PL, et al. (2013) More than One Way of Being a Moa: Differences in Leg Bone Robustness Map Divergent Evolutionary Trajectories in Dinornithidae and Emeidae (Dinornithiformes). PLoS ONE 8(12): e82668. doi:10.1371/journal.pone.0082668

Editor: Cornelius Kupczik, Friedrich-Schiller-University Jena, Germany

Received August 13, 2013; **Accepted** October 26, 2013; **Published** December 18, 2013

Copyright: © 2013 Brassey et al. This is an open-access article distributed under the terms of the Creative Commons Attribution License, which permits unrestricted use, distribution, and reproduction in any medium, provided the original author and source are credited.

Funding: This work was funded by a Natural Environment Research Council Doctoral Training Grant (NE/1528134/1). The Henry Moseley X-Ray Imaging Facility (University of Manchester) is supported by the Engineering and Physical Sciences Research Council under nos. EP/F007906 and EP/I02249X. The funders had no role in study design, data collection and analysis, decision to publish, or preparation of the manuscript.

Competing Interests: The authors have declared that no competing interests exist.

* E-mail: charlotte.brassey-2@postgrad.manchester.ac.uk

Introduction

Before their rapid extinction coinciding with the arrival of Polynesian colonists [1], New Zealand's moa (Dinornithiformes) included some of the largest palaeognath birds, ranging in size from <15 kg to >200 kg. Recent genetic [2], radiocarbon [3], and stable isotope studies [4] have illuminated moa evolution, palaeogeography, and palaeoecology. Yet the most striking feature of dinornithiform biology, the immense range in body size and limb morphology between families (Megalapterygidae; Dinornithidae; Emeidae) and species and their resulting biomechanics, remain poorly understood. Stress levels within the extremely robust legs of the emeid *Pachyornis elephantopus* are predicted to have remained low during locomotion [5], with unusually high safety factors (the ratio of failure strength to the maximum stress it is likely to encounter) and poor running ability inferred in this species [6,7]. Yet the more gracile giant moa (two species of *Dinornis*, which comprise the Dinornithidae) is reconstructed as being proficiently cursorial [8].

Estimation of safety factors and running speeds requires reliable values for body mass. Previous attempts at predicting moa body

mass have favoured linear regression techniques [9,10]. Yet the very nature of their unusually proportioned limbs makes mass estimation based on single linear dimensions problematic. This paper applies a volume-based mass estimation technique to two representative moa species, from the two families with most divergent morphologies, *Dinornis robustus*, the larger South Island dinornithid, and *Pachyornis australis*, the smaller of the two South Island emeids. *D. robustus* occupied the widest range of habitats of any moa, including lowland dry forests and shrublands, rainforests, subalpine shrublands and fellfields, whereas during the Holocene *P. australis* was confined to subalpine shrublands and fellfields where it was sympatric with *D. robustus* and *Megalapteryx didinus*.

To perform a comparative biomechanical analysis of skeletal elements, it is first necessary to derive a value for applied load for each model. Typical loads can be estimated as a multiple of the force acting on the skeleton due to gravity, and to calculate this we need to know the living body mass of the animal. As noted above, the extreme morphologies of moa long bones make body mass estimates for moa based on linear measurements unreliable. Here, we estimate moa body mass using a whole body volume technique. Subsequently we undertake a sensitivity analysis to quantify the

Table 1. Convex hull specimen list and sources of body mass.

species	accession no.	volume (m^3)	M_b (kg)	M_b source	Scaling equation	x	n
<i>Struthio camelus</i>	UMZC374	0.0717	60.7	[48]	$y = 0.374\log x - \log 1.259$	femur length	15
<i>Casuarius casuarius</i>	UMZC371.D	0.0172	27.0	[49,50]	$y = 4.69x + 189.6$	tibiotarsal length	3
<i>Dromaius novaehollandiae</i>	UMZC363	0.0214	20.06	*	$y = 6.35x + 92.6$	femur length	3
<i>Rhea americana</i>	UMZC378.99	0.0177	16.3	[51,52]**	$y = 10.21x + 140.2$	tibiotarsal length	3
<i>Rhea pennata</i>	UMZC378ki	0.0159	14.9	[51,52]**	$y = 10.21x + 140.2$	tibiotarsal length	3
<i>Apteryx australis</i>	UMZC378.A	0.00106	2.96	[53]	$y = 3.6x + 20.33$	femur circumference	30
<i>Apteryx australis lawryi</i>	UMZC378.55	0.00137	2.41	[53]	$y = 3.6x + 20.33$	femur circumference	30

Body mass (M_b) was estimated for the convex hull individuals by first generating species-specific least squares regressions of known body mass against a linear metric from the hind limb as reported in the literature.

*Regression equation of *Dromaius novaehollandiae* femoral length against body mass derived from carcasses of known body mass from the University of Manchester.

**Regression equation of *Rhea* spp. tibiotarsal length against body mass generated from previously published raw data and one carcass from the University of Manchester.

doi:10.1371/journal.pone.0082668.t001

effect of model reconstruction upon moa body mass estimates. We hypothesised that our volumetric technique would yield lower body mass estimates than those based on the diameter or circumference of the femur or tibiotarsus, given the unusual breadth of dinornithiform limb bones. This would therefore yield different estimates of the loads the bones had to carry, and the limitations on those loads.

We then compared the biomechanics of modern ratite and moa hind limbs bones using finite element analysis. Finite element analysis is a computerised technique in which a digital model is divided into a series of elements forming a continuous mesh. Material properties, boundary constraints and load conditions are applied to the model, and the resulting stresses and strains during loading are calculated. Previous biomechanical analyses of moa hind limbs have relied upon simplified beam theory models [5,11], in which complex organic structures are simplified into slender beams. However, in a broad sample of morphologically diverse mammal and bird long bones, the errors introduced into stress calculations resulting from this simplification have been shown to be neither consistent in magnitude nor direction [12]. Factors such as shaft curvature, low values of aspect ratio (length/diameter) and variations in cortical wall thickness are characteristic of organic structures such as long bones, yet these are typically unaccounted for in simple beam equations [12]. However, finite element analysis allows the complex 3D geometry of bones to be incorporated into stress equations, and with access to computed tomography (CT) facilities becoming cheaper and easier, it is now feasible to generate a larger comparative dataset of 3D models on which to perform biomechanical analyses.

Here we use our new body mass estimates and finite element models for moa to compare limb bone robustness of these Dinornithiformes to those of modern palaeognaths and discuss the results in the context of habitat preferences and locomotor modes. Given the reputation of moa as being 'robust' (*Dinornis robustus*, the etymon of robust terrible bird; and *Pachyornis australis*, the southern thick/stout bird), we might hypothesise that their limb bones ought to experience lower levels of stress than modern palaeognaths when loaded under equivalent conditions. The present study is the first attempt to quantify such biomechanical variation in the different lineages of this order of large birds.

Materials and Methods

Convex hull calibration on modern ratites

All skeletal material included in this study was accessed with the permission of the relevant museum (University Museum of Zoology, Cambridge; National Museums Scotland, Edinburgh; Museum of New Zealand, Te Papa Tongarewa) and reside within their permanent collections. The mounted skeletons of modern species of ratites were scanned using a Z+F Imager 5010 LiDAR (light radar) scanner at the University Museum of Zoology, Cambridge (UMZC) (see Table 1). Reconstructions were carried out in Z+F LaserControl and Geomagic Studio v.12 (Geomagic, USA), and point clouds representing individual skeletons were isolated (see Figure 1a). Each individual was then subdivided into functional units: feet (phalanges), hand (metacarpals and phalanges), metatarsus, shank (tibiotarsus), thigh (femur), distal wing (radius and ulna), proximal wing (humerus), trunk (pelvis, ribs, sternum, sternal ribs), neck and skull. The neck was subdivided into 5 parts to ensure a tight-fitting convex hull around its curvature. Each functional unit was saved as a point cloud, and the minimum convex hull calculated using the qhull command of MATLAB (MathWorks, USA) (see Figure 1b) from which enclosed volumes were calculated. A convex hull is defined as the smallest convex object that can be fitted around selection of points, and in practical terms can be visualised as stretching a rubber sheet around the given set of points.

Unfortunately, associated body masses were not available for the mounted museum skeletons. We measured linear dimensions (femur and tibiotarsal length, and midshaft circumference) directly from the skeletons. Body masses were then estimated using species-specific regression equations, derived either from the literature or generated by the authors based on published raw values (see Table 1). Literature-derived values for body mass were then regressed against convex hull volume in R [13]. Unlike previous studies [14], convex hull volume was not converted to a minimum mass by multiplying by density. Values for avian body density are sparse in the literature (see later Discussion), and frequently refer to plucked carcasses. Furthermore, post-mortem collapse and infilling of air sacs with fluid most likely causes a significant increase in body density relative to live birds. However it is likely that the body density of ratites does not vary much between species. Convex hull volume (vol) was therefore immediately regressed against literature mass to avoid introducing further

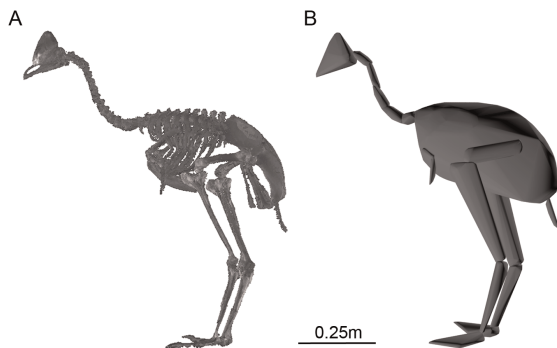


Figure 1. The convex hulling process (a) Point cloud data for *C. casuarinus* derived from LiDAR (light radar) scanning; (b) convex hulls of each body segment.

doi:10.1371/journal.pone.0082668.g001

uncertainty into the analysis. A summary of the existing empirical data for avian body density is included later in the discussion.

Regression analyses were carried out in the R package ‘smatr’ [15] using both Type-I (least squares linear regression, LR; linear regression through the origin, LRO) and Type-II (major axis regression, MA; standard major axis regression, SMA) line-fitting techniques on untransformed data which met the requirements of normality and homoscedasticity. Linear regression, MA and SMA are all least-squares line-fitting methods, but differ in the direction in which distances between the line and data points are measured. For more details regarding their application, see Warton et al. [16].

Reconstruction of moa skeletons and mass estimation

The two moa individuals were selected from the collection of the Museum of New Zealand Te Papa Tongarewa on the basis of possessing pelvis and complete hindlimb skeletons. The specimen of *P. australis* (S.27896) lacked several ribs. The South Island giant moa (*Dinornis robustus*) specimen (S.34088) lacked several vertebrae and the skull; the skull of a second large *D. robustus* individual (S.34089) was therefore included. Skeletal elements were digitally remounted in accordance with recent reconstructions, in which the vertebral column is bent forward and downward into a loop and the head is held only slightly higher than the top of the pelvis [9]. As the *D. robustus* specimen lacked many vertebrae, two additional vertebrae were added to the reconstructed vertebral column of *P. australis* (due to differences in vertebral formulae between Emeidae and Dinornithidae [9]) which was subsequently scaled up geometrically to fit the larger *D. robustus*.

The process of digitally remounting skeletons from disarticulated elements introduces a degree of uncertainty into our mass predictions. In particular, the positioning of the sternum and ribs defined the volume of the convex hulled trunk, which itself contributed most to the total volume of the bird. In both moa specimens, several thoracic and sternal ribs lacked their ventral extremities or were absent. The convex hulling process was therefore repeated with the sternum in higher ($cvol_{min}$) or lower ($cvol_{max}$) positions dorsoventrally, to allow for uncertainty in the positioning of the sternum in the living bird. The final confidence intervals for our moa mass estimates were therefore calculated by inserting the values for $cvol_{max}$ and $cvol_{min}$ into the convex hull equation, using the upper and lower values of the prediction interval respectively.

Computed tomography (CT)

The 3D models forming the basis of our finite element analysis were derived from CT scans of femora and tibiotarsi. In most instances, femora and tibiotarsi were acquired from the bird collection of the National Museum of Scotland, Edinburgh (Table 2). All museum-sourced specimens were deemed skeletally mature (on the basis of plumage records and surface rugosity of the femoral and tibiotarsal shaft [17]), and were free of pathologies. However, for the emu (*Dromaius novaehollandiae*) and rhea (*Rhea americana*) hindlimb “bones” were extracted from whole carcass CT scans of the individuals. The emu was euthanised at an age of 10 weeks, and should therefore be considered to be subadult ([18] and see later Discussion). In each specimen, the stylopodium and zeugopodium were sourced from the same individual, and whenever possible, from the same limb. For the emu and rhea, body mass (M_b , kg) was recorded post-mortem. For museum specimens, associated body masses were not available and values were therefore assigned using literature species-specific scaling equations (see Table 2).

Small modern palaeognaths (*Tinamus solitarius*, *Apteryx haastii*) were scanned at the Henry Moseley X-ray Imaging Facility, University of Manchester (X-Tek HMX 225 Custom Bay, Nikon Metrology Ltd, UK) at a voxel spacing of 85–119 µm. *Rhea americana*, *Dromaius novaehollandiae*, *Casuarius unappendiculatus*, and *Struthio camelus* were scanned in a helical CT scanner at the University of Liverpool Small Animal Teaching Hospital (Siemens SOMATOM Volume, Germany) at pixel spacings of 270–867 µm and slice thicknesses between 1–1.5 mm. The two dinornithiform skeletons were scanned by Pacific Radiology (Southern Cross Hospital, Wellington, New Zealand) in a helical CT scanner (BrightSpeed, GE Healthcare, USA) at a pixel spacing of 320–977 µm and a slice thickness of 0.625 mm.

Estimating hind limb robustness using finite element analysis

Hindlimb bone scans were segmented in Avizo v.7.1 (VSG Inc., USA), and periosteal and endosteal surfaces were isolated and repaired in Geomagic v.12 (Geomagic, USA). OBJ files were converted into SAT file format using Form•Z (AutoDesSys®) and imported into Abaqus (Simula®, USA) in which finite element analysis was undertaken. The finite element analysis carried out in this study follows the methodology of Brassey et al [12]. An instance was created in Abaqus containing both parts, and a Boolean operation used to subtract the endosteal part from the periosteal part to create a hollow bone model. A homologous value for Young’s modulus of 19 GPa and Poisson’s ratio of 0.3 were assigned to all models [19]. Hollow bone parts were meshed using a built-in Delaunay meshing algorithm within Abaqus.

The total number of elements in each model was set at c. 1 million (range, 960,059–1,030,551). A previous sensitivity analysis found stress values predicted by finite element analysis converged above 800,000 elements in a broad sample of vertebrate long bones [12], and a value of 1 million was chosen to ensure convergence. The same study compared stress values between 4-node linear tetrahedral meshes and 10-node quadratic tetrahedral meshes, and found stress values to converge in models exceeding 200,000 elements. C3D10 tetrahedra are computationally more expensive [20], and C3D4 tetrahedral meshes were therefore used throughout this study.

Models were loaded under combined compression and bending (0–90° of vector orientation in the parasagittal plane) and torsion. Total load applied was equivalent to 10% of body mass. A small multiple of body mass was chosen to ensure that total strain values were small, and deformation remained within the linear elastic

Table 2. Finite element analysis specimen list and sources of body mass.

species	accession no.	M_b (kg)	M_b source	Scaling equation	x	n	F (N)
<i>Struthio camelus</i>	NMS 1930.15.1	100	[48]	$y = 0.374\log x - 1.259$	femur length	15	980.6
<i>Casuarius unappendiculatus</i>	NMS 1995.119.1	49.8	[49,50]	$y = 4.69x + 189.6$	tibiotarsal length	3	488.1
<i>Dromaius novaehollandiae</i>	-	16.05	-	carcass weight	-	-	157.4
<i>Rhea americana</i>	-	7.85	-	carcass weight	-	-	77.01
<i>Apteryx haasti</i>	NMS 1913.48	2.80	[53]	$y = 3.6x + 20.33$	femur circumference	30	27.47
<i>Tinamus solitarius</i>	NMS PS276/04	1.46	[53]	$y = 8.17x + 9.673$	femur circumference	28	14.32

Body mass estimated for the finite element analysis specimens using the same species-specific regressions of known body mass against a linear metric from the hind limb, as in Table 1. For *Dromaius novaehollandiae* and *Rhea americana*, body mass was recorded directly from the carcass. F, total force applied to the finite element model in Newtons.

doi:10.1371/journal.pone.0082668.t002

region (as in [12,21]). For femora, the applied force was spread across 10 adjacent nodes on the medial surface of the femoral head (Figure 2a). For tibiotarsi the load was applied on 10 nodes across the intercondylar eminence. To simulate combined compressive-bending loading, force was initially applied parallel to the principal

axis of the bone, and then the load vector incrementally modified from 10–90° from the principal axis.

All models were also loaded under axial torsion. The condyles of the distal epiphyses were constrained in all three directions, and a constraint control point (CP) created on the proximal epiphyses. For femoral torsion, the moment was not applied on the femoral head: rather, the CP was located on the proximal surface between the head and the major trochanter, corresponding to the location at which the bone's longest principal axis emerged at the surface (Figure 2b) [12]. This orientation ensured that torsion was about the long axis of the femur. The CP was constrained in three directions, and a kinematic coupling created between 10 nodes surrounding the CP, and the CP itself (Figure 2c). A torsional moment about the bone's principal axis was applied at the CP (proportional to 10% of body mass), and transmitted via kinematic coupling to the load surface. For all loading regimes, 20 nodes on the surface of the distal epiphyses were constrained using the 'encastre' boundary condition (Figure 2c).

A linear elastic analysis was carried out on all models, and equations solved using Gaussian elimination. Zones of stress concentration are likely to occur at fixed boundaries as a result of reaction forces at constrained nodes. Stress values were recorded therefore from the midshaft of the bone models, a considerable distance from the fixed boundary nodes. For all loading regimes, the greatest value of Von Mises stress located on the periosteal surface at midshaft (σ_{vm}) was extracted. The effect of sternal position on stress estimates in the dinornithiform individuals was investigated by substituting minimum and maximum values for moa body mass in the analysis. Point cloud and CT data are available from animalsimulation.org.

Results

Moa Body Mass Estimates

Individual body segment volumes and total convex hull volumes are given in Table 3. Figure 3 shows the convex hull reconstructions calculated for the moa specimens. The relationship between convex hull volume and body mass in extant ratites is given in Figure 4. All regression techniques produce very similar answers, were all highly statistically significant ($p < 0.005$) and had high correlation coefficients ($r^2 > 0.95$). Following the logic of Sellers et al. [14], we also applied the LRO (linear regression through the origin) equation ($y = 893.4x$, 95% CI = 740–1048, $p = 0.003$, $r^2 = 0.97$) to estimate the live mass of our dinornithiform individuals. LRO arguably makes better biological sense as an individual with zero volume must have zero mass, and Type-I regressions are recommended where the regression model will be

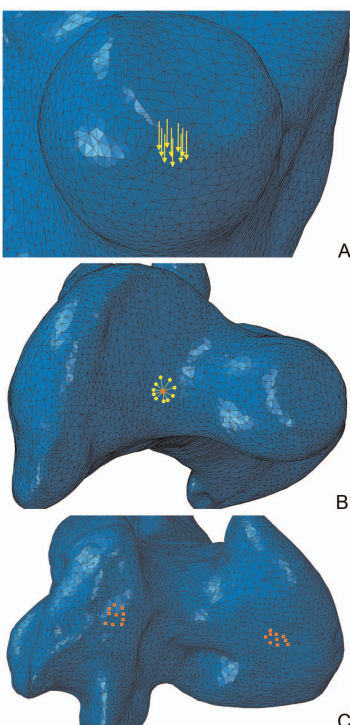


Figure 2. Loading regimes for finite element analysis of *Dinornis* femur (a) Medial view of femoral head, yellow arrows originate from the nodes to which force is applied. The direction of force is aligned parallel to the long axis of the bone, i.e. loading in compression. (b) Dorsal view of the proximal femoral epiphysis. Orange dot represents constrained control point, and is surrounded by 10 yellow dots representing the nodes to which torsion is applied via the kinematic coupling. (c) Ventral view of the distal femoral condyles. Orange squares represent nodes subject to encastre boundary conditions.

doi:10.1371/journal.pone.0082668.g002

Table 3. Moa convex hull volumes and body segment volumes.

	cvol (m ³)	
	<i>D. robustus</i>	<i>P. australis</i>
Trunk	0.1595 (0.152–0.172)	0.0360 (0.033–0.039)
Femora	0.0111	0.0040
Tibiotarsi	0.0212	0.0084
Tarsometatarsii	0.0118	0.0045
Toes	0.0066	0.0020
Neck	0.0030	0.0006
Skull	0.0055	0.0007
Total	0.2187	0.0562

Trunk values include minimum and maximum volumes defined by shifting the sternum dorsoventrally. Segment values consist of the sum total of left and right elements.

doi:10.1371/journal.pone.0082668.t003

used in a predictive capacity [22]. The data point for *C. casuarinus* appeared to be an outlier (Figure 4). This probably resulted from the uncertainty in the body mass estimate for *C. casuarinus*, as there are few published accounts of individual cassowary limb proportions and their corresponding body mass. However, removing the data point had no significant effect on the value of the slope (with *C. casuarinus* $b = 893.4$, without *C. casuarinus* $b = 861.4$, $p = 0.52$). Predicted masses, including the results of the sensitivity analyses, are shown in Table 4: the average mass for *D. robustus* was 196 kg (95% confidence interval 155–245 kg), and that for *P. australis* 50 kg (95% confidence interval 33–68 kg).

Finite Element Analysis

Maximum Von Mises stresses (σ_{vm}) when femora and tibiotarsi were loaded from compression (0°) to cantilever bending (90°) and torsion are shown in Figures 5 and 6. The location of peak stresses within finite element models typically correspond to those predicted by simple beam models. However both femora experienced induced bending when loaded in compression (Figure 7a). This can partially be explained by curvature-induced bending [12], but for femora it is particularly so because of the off-axis application of force on the femoral head. The avian tibiotarsus

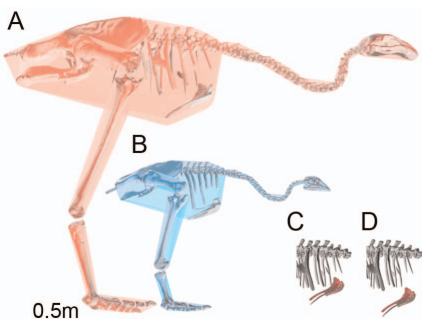


Figure 3. Moa convex hulls (a) *Dinornis robustus* (S.34088/89) reconstruction of convex hulls; (b) *Pachyornis australis* (S.27896) (a and b are to the same scale); (c) and (d) show different positions of the sternum in *D. robustus*.
doi:10.1371/journal.pone.0082668.g003

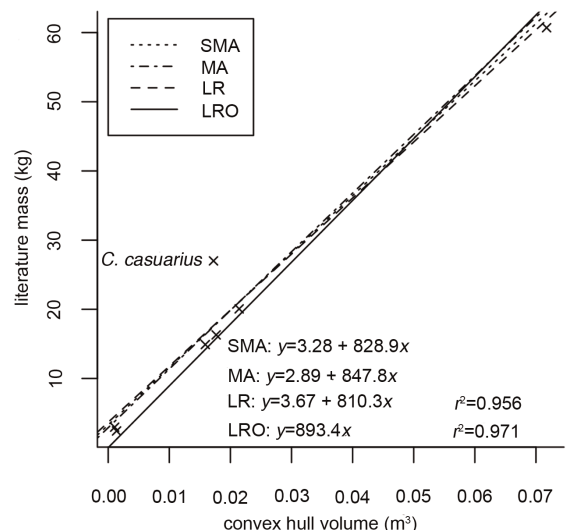


Figure 4. The relationship between convex hull volume and literature values for mass in extant ratites. LR, linear regression; SMA, standardized major axis regression; MA, major axis regression; LRO, linear regression forced through the origin.
doi:10.1371/journal.pone.0082668.g004

is typically less curved than the femur [23], and the load was applied across the intercondylar eminence. For these reasons, the dinornithiform tibiotarsi experienced lower bending stresses when loaded parallel to their long axes (Figure 7b).

Under bending, the distribution of stresses in finite element models closely matched the predictions of a fixed cantilever beam model. Von Mises stress increased incrementally towards the fixed end (Figure 7c), with a band of low stress values (neutral plane) located between the compressional and tensional cortices (Figure 7d). When loaded in torsion, Von Mises stress increased radially from the endosteal to periosteal surface, with the highest values of σ_{vm} located in areas of minimum cortical wall thickness (Figure 7e).

The lowest values of σ_{vm} were found in the femur and tibiotarsus of *P. australis* (Figure 5a,b), with confidence intervals not overlapping those of any other palaeognath under high levels of bending. The stress values measured in *D. robustus* femur were intermediate, overlapping those of *A. haastii* and *T. solitarius*. The *D. robustus* tibiotarsus exhibited the highest values for σ_{vm} under bending, but with values overlapping those of *S. camelus* and *Dr. novaehollandiae*. When the tibiotarsus of *D. robustus* was loaded predominantly in compression, however, σ_{vm} values were lower than those for *S. camelus* and *Dr. novaehollandiae* (Figure 6). Under torsion (Table 5), both dinornithiforms exhibited low values of σ_{vm} , with their confidence intervals failing to overlap those of modern species. The *P. australis* tibiotarsus was significantly less stressed than that of *D. robustus* under torsion.

Discussion

Body mass estimates

Our estimate of 195 kg for the body mass of *D. robustus* was just over 80% of the estimate of 238 kg [10] based on the averaged femoral circumference of seven *D. robustus* individuals calculated from a ratite-specific regression. However, our maximum range

Table 4. Body mass estimates of moa individuals.

	mass (kg)	95% prediction interval (kg)
<i>D. robustus</i>		
<i>cvol</i>	195.7	159.8–231.5
<i>cvol_{min}</i>	189.4	154.5–224.3
<i>cvol_{max}</i>	207.3	169.5– 245.0
<i>P. australis</i>		
<i>cvol</i>	50.3	35.2–65.4
<i>cvol_{min}</i>	47.9	32.8–62.5
<i>cvol_{max}</i>	52.9	37.5– 68.2

cvol, mean convex hull; *cvol_{max}*, maximum convex hull volume with sternum positioned ventrally; *cvol_{min}*, minimum convex hull volume with sternum positioned dorsally. Bold values indicate minimum and maximum body mass values inserted into FE sensitivity analysis.

doi:10.1371/journal.pone.0082668.t004

calculated through sensitivity analyses (155–245 kg) was considerably narrower than confidence intervals calculated from the linear regression (164–346 kg). Applying palaeognath-specific scaling equations of femoral and tibiotarsal length and diameter against body mass [24], mass estimates for this specimen of *D. robustus* range between 226–517 kg depending upon the metric used (Table 6). Our volume-based mass predictions are therefore lower than those produced by linear regression techniques.

Our estimate of 50 kg (range 33–68 kg) for the Pleistocene-aged *P. australis* is also lower than the species mean of 116 kg (95% CI 86–158 kg) predicted on the basis of ratite femoral circumference of all Pleistocene-aged individuals [10]. Yet, our estimate falls within the range (44–90 kg) of values for *P. australis* calculated from femoral length for birds of that period [9]. Applying the ratite scaling equations derived by Cubo and Casinos [24] mass estimates range between 94–144 kg, again being considerably higher than our volume-based mass prediction (Table 6).

A major advantage of volume-based reconstructions is the inclusion of information from the whole skeleton [14]. When dealing with skeletal extremes, such as the hyper-robust femora of *Pachyornis*, mass predictions based on a single linear dimension can result in significant under- or over-estimations. Furthermore, when a range of scaling equations are derived from single linear dimensions, it leads to uncertainty in which dimension is most appropriate to use as a mass predictor. As can be seen in Table 6, applying a mass prediction equation based on femoral length results in significantly higher estimates than those based on femoral diameter. In particular, the choice of ecologically or locomotorily specialized limbs is problematic when applying mass prediction equations to single elements. In contrast, volumetric approaches incorporate the maximum amount of information from a skeleton in one measure, avoid the single bone problem [14] when animals have unusual sized limbs and require no a priori assumption of which skeletal element ought to be used in the predictive equation.

Because the convex hull volume is the minimum possible volume, by taking the mean predicted mass of the moa models and their convex volumes, we estimated a maximum possible body density of 895 kg/m³ for the individuals. This compares to values ranging from 730 kg/m³ for a sample of flying birds [25], 894–968 kg/m³ for junglefowl and broiler chickens [26], 888 kg/m³ for an ostrich [27], 900 kg/m³ for a duck [28] and 937 kg/m³ for a goose [29]. These literature values were estimated using a variety

of methodologies, and no single study has adequately dealt with the question of avian body density. Furthermore, the present analysis does not account for the presence or absence of gizzard stones in extant or extinct specimens. The total mass of gizzard stones may reach 1 kg in modern ostrich [30], whilst 5 kg of gastroliths have been found in association with a *Dinornis robustus* [31]. However given the mass estimates presented here, dinornithiform gastroliths likely contribute only 2–3% of total body mass.

Finite element analysis results

Having generated predictions for the body mass of *D. robustus* and *P. australis* that were lower than published values, we incorporated these new estimates for M_b into the finite element analysis of the hind limb bones as a value for applied force. For every loading condition considered, values of σ_{vm} extracted from the finite element analysis were lowest in the leg bones of *P. australis* (Figure 5a,b), and this species is confirmed as having been extremely robust. Hyper-robustness of limbs could conceivably be an adaptation towards unpredictable loading conditions. Indeed, the ‘rough and tumble’ lifestyle of many birds has been put forward as an explanation as to why the hollow long bones of birds do not confirm to mechanical predictions for minimal mass [32]. *P. australis*’ habitat range during the Holocene was restricted to subalpine regions of the northwest South Island, and robust limbs would have proved advantageous in upland environments with uneven terrain.

This does not explain the hyper-robustness of *P. australis* limbs however. Warm Holocene-like climatic conditions have been exceptional during the past 1 million years, with glacial conditions being the climatic norm [33]. As a species, *P. australis* occupied different altitude ranges as climate changed during glacials, interglacials and transitions, and spent most of its evolutionary history in lowland low-relief environments. Limb robustness in *P. australis* is therefore unlikely to be a specific adaptation to upland environments. Indeed, the larger sister-species *P. elephantopus* occupied lowland regions throughout the Quaternary despite appearing to possess even more robust limbs.

In contrast to *P. australis*, values of σ_{vm} in the legs of *D. robustus* were comparable to, or exceeded those of modern ratites under compression and bending (Figure 5a,b). Despite deriving a lower estimate of body mass, *D. robustus* is therefore reconstructed as a gracile ratite. *D. robustus* remains have been identified from a range of habitats spanning lowland forest, shrubland and subalpine locations, where it co-existed with *P. australis*. Alongside *M. didinus*, their bones are common in the same subalpine caves in northwest Nelson where Holocene *P. australis* remains are found, yet neither taxon exhibited the same degree of robustness seen in *P. australis*. Hindlimb robustness does not therefore appear to be correlated with habitat preference in diornithiforms, with the hyper-robust *P. australis* and relatively gracile *D. robustus* living sympatrically throughout the Holocene. Despite this spatiotemporal overlap, our sample of diornithiforms exhibits greater variance in tibiotarsal robustness than that of modern ratite species spanning several continents and diverse habitats. An alternative hypothesis is therefore required to explain the disparity in moa hindlimb biomechanics.

The robustness of *P. australis*’ hindlimbs may be associated with the evolution of different leg bone length proportions that characterise emeids compared to other moa and large palaeognaths. A distinguishing synapomorphy of the Emeidae is the relatively short tarsometatarsus, and the associated mediolateral expansion of this element and the distal tibiotarsus. Reducing the length of the ‘effective hindlimb’ (tibiotarsus plus tarsometatarsus)

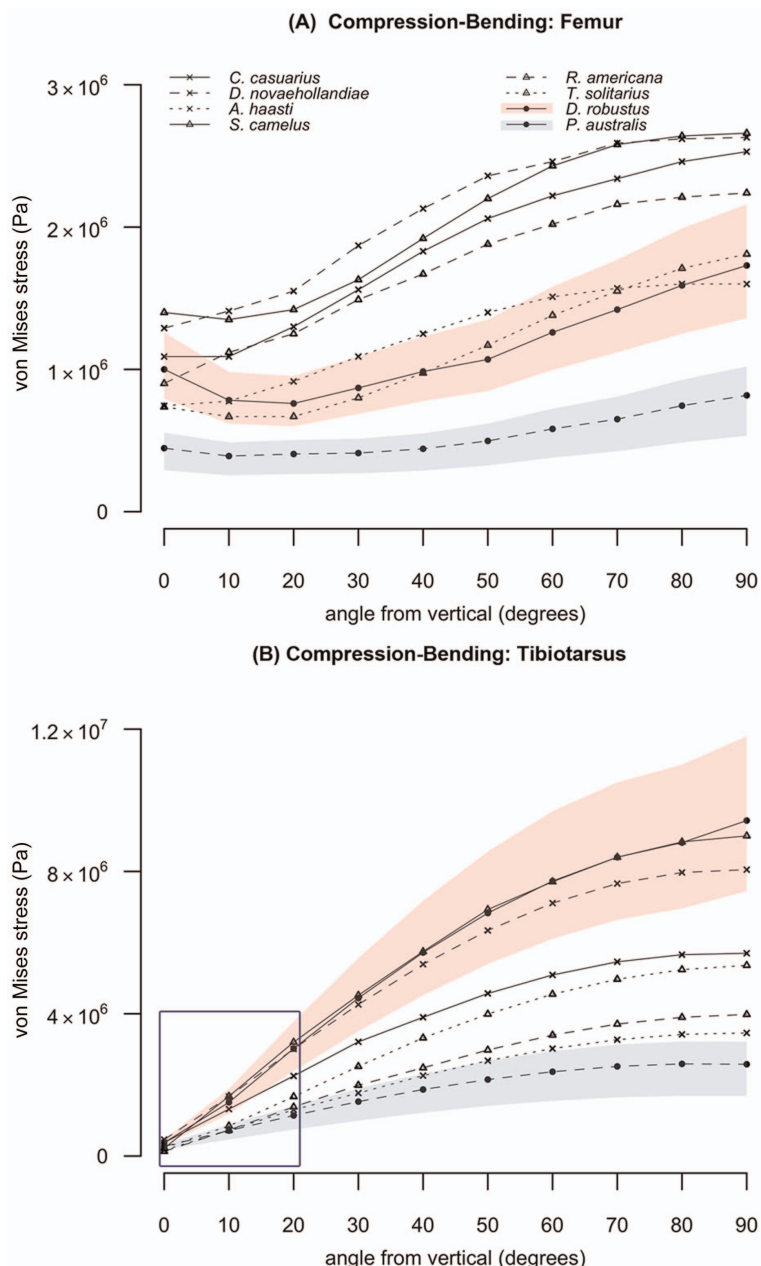


Figure 5. Finite element analysis results. Combined compression-bending results for the femur (a) and tibiotarsus (b). Values represent maximum von Mises stress (Pa) recorded at the midshaft of the bone. Pink and blue shaded areas represent the range of stress values estimated by finite element analysis when incorporating maximum and minimum values for body mass in *D. robustus* and *P. australis* respectively. Area enclosed by dark blue box is expanded in Figure 6.
doi:10.1371/journal.pone.0082668.g005

and increasing mediolateral width would result in increased resistance to lateral loading whilst limiting maximum stride length. The suite of modifications that resulted in the distinctive tarsometatarsal of emeids implies a divergence in locomotor capabilities or other habitual behaviours between *P. australis* and

D. robustus whilst occupying the same habitat. To test the hypothesis that *P. australis* and *D. robustus* occupied distinct ecological niches whilst occupying the same habitat, future biomechanical analyses of Dinornithiformes would benefit from incorporating additional data regarding gastrolith, coprolith and

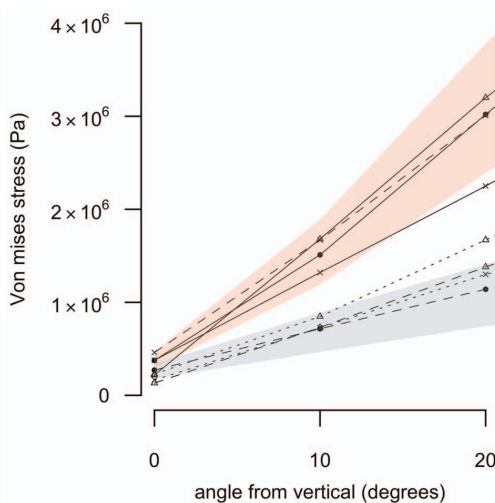


Figure 6. (inset of Figure 5) Combined compression-bending of the tibiotarsus between 0–20° from vertical. Values represent maximum von Mises stress (Pa) recorded at the midshaft of the bone. Legend as in figure 5.
doi:10.1371/journal.pone.0082668.g006

bone stable isotopic composition as indicators of diet preference and territory range [34].

The distinction between *P. australis* and *D. robustus* is less pronounced during compressive-bending loading of the femur

Table 5. Finite element analysis results for torsional loading.

	von Mises stress (Pa)	
	femur	tibiotarsus
<i>C. casuarius</i>	2.21×10^7	3.07×10^7
<i>D. novaehollandiae</i>	3.33×10^7	4.17×10^7
<i>A. haasti</i>	3.06×10^7	4.67×10^7
<i>S. camelus</i>	1.96×10^7	2.98×10^7
<i>R. americana</i>	2.92×10^7	3.20×10^7
<i>T. solitarius</i>	5.51×10^7	1.14×10^8
<i>D. robustus</i>	9.45×10^6	2.07×10^7
(mass-dependent range)	7.46×10^6 – 1.18×10^7	1.63×10^7 – 2.59×10^7
<i>P. australis</i>	6.30×10^6	1.09×10^7
(mass-dependent range)	4.12×10^6 – 7.84×10^6	7.14×10^6 – 1.36×10^7

Values represent maximum von Mises stress (Pa) recorded at the midshaft of the bone. For the two moa species, the range of von Mises stresses based on minimum and maximum body mass estimates (Table 4) is also presented.

doi:10.1371/journal.pone.0082668.t005

compared to the tibiotarsus. Under torsional loading of the femur, the stress values estimated from the sensitivity analysis of the moa individuals overlap considerably (Table 5). The avian femur is constrained to a subhorizontal posture at low to moderate speeds [35], and locomotor/behavioural specialisations within moa are played out via modifications to the tibiotarsus and tarsometatarsus. In a broad sample of modern birds, species with the highest

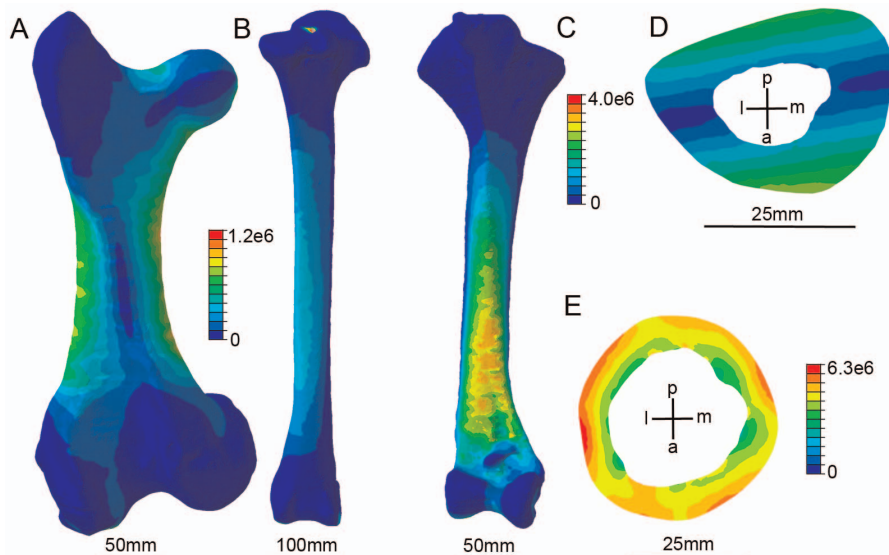


Figure 7. The distribution of Von Mises stress within moa finite element models. (a) *Dinornis* femur loaded in compression (0° from the longest principal axis) experienced a significant degree of bending due to off-axis application of force on the femoral head. (b) *Dinornis* tibiotarsus experienced lower values of σ_{vm} under compression, and underwent less bending due to application of forces on the intercondylar eminence. (c) *Pachyornis* tibiotarsus loaded in bending (90° from the longest principal axis). σ_{vm} increases towards the fixed end of the beam, with localised areas of stress related to variations in cortical wall thickness. (d) Slice through midshaft of c. Values of σ_{vm} are highest at the extreme compressional and tensional cortices with a neutral axis of lowest stress values running between. (e) Slice through midshaft of *Pachyornis* femur loaded in torsion. Stress values increase radially from the endosteal to periosteal surface, with the highest stresses located in regions where cortical wall thickness is at a minimum. For (d) and (e), bone orientation is indicated by coordinate system (a-p, anteroposterior; m-l, mediolateral).
doi:10.1371/journal.pone.0082668.g007

Table 6. Moa body mass estimates (kg) and 95%CI based derived from palaeognath-specific regressions of femoral and tibiotarsal metrics published by Cubo and Casinos [24].

	<i>Dinornis robustus</i> (kg)	<i>Pachyornis australis</i> (kg)
Femur length	488 (357–709)	144 (115–187)
Femur diameter (AP)	237 (200–287)	115 (100–133)
Femur diameter (ML)	289 (231–384)	111 (95–137)
Tibiotarsus length	517 (382–738)	115 (74–107)
Tibiotarsus diameter (AP)	226 (178–296)	94 (79–114)
Tibiotarsus diameter (ML)	311 (254–406)	124 (107–152)

doi:10.1371/journal.pone.0082668.t006

predicted tibiotarsal safety factors under static bending included aerial hunters, hindlimb-propelled divers, and waders [23] rather than ground-dwelling galliformes and ratites. High safety factors in the tibiotarsus of modern birds do not reflect cursoriality, but are instead correlated with habitual behaviours such as prey capture or a preference for compliant substrates (both of which imply load unpredictability).

The emu individual included within our finite element analysis dataset was subadult at the time of euthanasia. As such, the stress values estimated using finite element analysis might not reflect those of a skeletally mature individual. The femur and tibiotarsus of the subadult emu experienced some of the highest values of σ_{vm} for modern ratites under combined compression-bending (Figure 5). A kinematic study of emu locomotion found significant ontogenetic increases in principal strain in the hind limb, despite negative allometric scaling of shaft curvature and constant relative limb loading throughout growth [36]. Higher values of σ_{vm} than those found in our emu individual might therefore be expected in fully adult individuals.

A homogeneous value for Young's modulus was applied to all ratite finite element models. The intra-element variation of material properties in vertebrate long bones have been discussed extensively elsewhere [37], and reported values for Young's modulus in avian bone vary significantly between species and between limb bones [38]. Furthermore, both the moa and kiwi have been found to possess bone histology atypical of most ornithurines, consisting of annual growth rings in their limb bones [39,40]. By assigning a single value for Young's modulus across species, potential material effects that may contribute to total stiffness of the ratite hind limb are ignored. Furthermore we include a subadult emu in our sample, despite evidence to suggest ontogenetic variation in material properties across vertebrates [41]. In addition, the safety factor at which a limb bone operates is both a function of the experienced strain and the yield strain of the material. Here we assume that yield strain does not change and we directly compare stress values derived from our finite element models between species. Yet a weak, but highly significant, negative correlation does exist between yield strain and Young's modulus [42]. However the variation in Young's modulus and yield strain between bird species, skeletal elements and age groups has yet to be adequately described using a consistent material testing technique. As such, attempting to incorporate species-specific values into a comparative finite element analysis would currently act to increase uncertainty in estimated stress values and resulting safety factors. Therefore, the analysis presented here deals with the geometric differences between moa skeletons only, and the variability in elastic bone material properties and their

subsequent effect on finite element analysis results will require further work (but see [21]).

Moa exhibited considerable divergence in their hindlimb morphology, and consequently biomechanical functionality, between families. Moa possessed a variety of adaptations to flightlessness, but only one of the three lineages – Emeidae – evolved more robust limb bones. Here we include only one representative from each of the Dinornithidae and Emeidae, and in effect carry out a two-species comparison. We therefore cannot conclude that the differences in limb robustness between moa families solely reflect alternative locomotor capabilities, but may also be associated with divergent life history strategies, physiologies, or separate evolutionary histories. In island giant species, an overreliance upon selection-based explanations (assuming biomechanics to be critical in all species) should be avoided. In a two-species comparative study, some degree of genetic differentiation is to be expected as a result of the speciation process and subsequent genetic drift alone, and therefore a more appropriate null hypothesis might have been that our two species ought to have been different as a result of their separate evolutionary histories, rather than no difference existing [43]. The New Zealand avifaunal fossil record is one of the best of the world for the Holocene and late Pleistocene [9], and the few moa fossils found to date earlier than the Pleistocene [44,45] support the contention based on extensive genetic evidence, that the dinornithids and emeids split between 4–6 million years ago [46]. The two families therefore spent a considerable amount of time on separate evolutionary trajectories. However, in the absence of a detailed pre-Pleistocene fossil record, the pattern of morphological change within each genetic lineage throughout the Cenozoic remains unknown.

The past decade has seen remarkable improvements in our knowledge of this extinct order of birds. Within the context of this new generation of dinornithiform research, the present study marks the first attempt at understanding moa biomechanics. However, the present analysis deals with static loadings. Safety factors during locomotion are mediated not only through bone robusticity, but also by posture and behaviour. The use of multi-body dynamics analysis, grounded in neontological studies, is needed to illuminate the origins of the profound differences between leg structure in families of moa, and the trade-off between cursoriality and safety factors in flightless giant birds in general. Moreover, the now-routine specific identification and sexing of moa bones [47], combined with a multi-proxy approach to dietary analysis and biomechanical modelling, has the potential to further our understanding of species dispersal, foraging strategies and predator-prey interactions within the Dinornithiformes. Alongside *Aepyornis maximus*, *D. robustus* was one of the largest palaeognath birds to have ever existed. As such, understanding the biomechanical constraints associated with such extremes in body mass in Aves may provide further insights into terrestrial locomotion and limits to body size during the transition from non-avian theropods to modern birds.

Acknowledgments

We thank Mathew Lowe at Cambridge Museum of Zoology, Alan Tennyson at Te Papa Tongarewa, Trevor Worthy at Flinders University, Darren Tod and Jane Rourke at Pacific Radiology, Martin Baker at the University of Liverpool, Tristan Lowe and Philip Withers at the Henry Moseley X-Ray Imaging Facility, University of Manchester and several anonymous reviewers.

Author Contributions

Conceived and designed the experiments: CAB RNH AGP WIS. Performed the experiments: CAB RNH JA PLM WIS. Analyzed the data:

CAB. Contributed reagents/materials/analysis tools: PLM WIS. Wrote the paper: CAB RNH WIS.

References

- Holdaway RN, Jacomb C (2000) Rapid extinction of the moas (Aves: Dinornithiformes): model, test, and implications. *Science* 287: 2250.
- Allentoft ME, Rawlence NJ (2012) Moa's Ark or volant ghosts of Gondwana? Insights from nineteen years of ancient DNA research on the extinct moa (Aves: Dinornithiformes) of New Zealand. *Ann Anat* 194: 36–5.
- Allentoft ME, Collins M, Harker D, Haile J, Oskam CL, et al. (2012) The half-life of DNA in bone: measuring decay kinetics in 158 dated fossils. *Proc R Soc B* doi:10.1098/rspb.2012.1745.
- Rawlence NJ, Metcalf JL, Wood JR, Worthy TH, Austin JJ, et al. (2012) The effect of climate and environmental change on the megafaunal moa of New Zealand in the absence of humans. *Quat Sci Rev* 50: 141–153.
- Alexander RMN (1985) The legs of ostriches (*Struthio*) and moas (*Pachyornis*). *Acta Biotheat* 34: 165–174.
- Cracraft J (1976) Covariation patterns in the postcranial skeleton of moas (Aves, Dinornithidae): A factor analytic study. *Paleobiol* 2: 166–173.
- Alexander RMN (1989) Dynamics of Dinosaurs and Other Extinct Giants. New York: Columbia University Press. 167 p.
- Hutchinson JR (2004) Biomechanical modeling and sensitivity analysis of bipedal running ability. II. Extinct taxa. *J Morph* 262: 441–461.
- Worthy TH, Holdaway RN (2002) The Lost World of the Moa: Prehistoric Life of New Zealand. Bloomington: Indiana University Press. 718 p.
- Dickison M (2009) The Allometry of Giant Flightless Birds. Duke University: PhD Thesis.
- Alexander RMN (1983) On the massive legs of a moa (*Pachyornis elephantopus*, Dinornithidae). *J Zool* 201: 363–376.
- Brassey CA, Margets L, Kitchener AC, Withers PJ, Manning PL, et al. (2012) Finite element modelling versus classic beam theory: comparing methods for stress estimation in a morphologically diverse sample of vertebrate long bones. *J R Soc Interface* 10: 20120823–20120823.
- R Core Team (2013) R: A Language and Environment for Statistical Computing. R Foundation for Statistical Computing. Vienna, Austria. Available: <http://www.R-project.org>.
- Sellers WI, Hepworth-Bell J, Falkingham PL, Bates KT, Brassey CA, et al. (2012) Minimum convex hull mass estimations of complete mounted skeletons. *Biol Lett* 8: 842–845.
- Warton DI, Duursma RA, Falster DS, Taskinen S (2011) Smatr 3—an R package for estimation and inference about allometric lines. *Method Ecol Evol* 3: 257–259.
- Warton DI, Wright IJ, Falster DS, Westoby M (2006) Bivariate line-fitting methods for allometry. *Biol Rev* 81: 259–291.
- Tumarkin-Deratzian AR, Vann DR, Dodson P (2006) Bone surface texture as an ontogenetic indicator in long bones of the Canada goose *Branta canadensis* (Anseriformes: Anatidae). *Zoo J Linn Soc* 148: 133–168.
- Goonewardene LA, Wang Z, Okine E, Zuidhof MJ, Dunk E, et al. (2003) Comparative Growth Characteristics of Emus (*Dromaius novaehollandiae*). *J App Poultry Res* 12: 27–31.
- Rubin CT, Lanyon LE (1984) Dynamic strain similarity in vertebrates; an alternative to allometric limb bone scaling. *J Theor Biol* 107: 321–327.
- Ramos A, Simões JA (2006) Tetrahedral versus hexahedral finite elements in numerical modelling of the proximal femur. *Med Eng Phys* 28: 916–924.
- Panagiotopoulou O, Wilshin SD, Rayfield EJ, Shefelbine SJ, Hutchinson JR (2012) What makes an accurate and reliable subject-specific finite element model? A case study of an elephant femur. *J R Soc Interface* 9: 351–361.
- Smith RJ (2009) Use and misuse of the reduced major axis for line fitting. *Am J Phys Anthr* 140: 476–486.
- Brassey CA, Kitchener AC, Withers PJ, Manning PL, Sellers WI (2013) The Role of Cross-Sectional Geometry, Curvature, and Limb Posture in Maintaining Equal Safety Factors: A Computed Tomography Study. *Anat Rec* doi:10.1002/ar.22658.
- Cubo J, Casinos A (1997) Flightlessness and long bone allometry in Palaeognathiformes and Sphenisciformes. *Neth J Zool* 47: 209–226.
- Hazlehurst GA, Rayner JM (1992) Flight characteristics of Triassic and Jurassic Pterosauria: an appraisal based on wing shape. *Paleobiol* 18: 447–463.
- Allen V, Paxton H, Hutchinson JR (2009) Variation in Center of Mass Estimates for Extant Sauropods and its Importance for Reconstructing Inertial Properties of Extinct Archosaurs. *Anat Rec* 292: 1442–1461.
- Hutchinson JR, Ng-Thow-Hing V, Anderson FC (2007) A 3D interactive method for estimating body segmental parameters in animals: Application to the turning and running performance of *Tyrannosaurus rex*. *J Theor Biol* 246: 660–680.
- Welty JC, Baptista M (1988) The Life of Birds. California: Brooks/Cole. 720 p.
- Alexander RMN (1983) Allometry of the leg bones of moas (Dinornithidae) and other birds. *J Zool* 200: 215–231.
- Noble JC (1991) On ratites and their interaction with plants. *Chil J Nat Hist* 64: 85–118.
- Burrows CJ, McCulloch B, Trotter MM (1981) The diet of moas based on gizzard contents samples from Pyramid Valley, North Canterbury and Scaifes Lagoon, Lake Wanaka, Otago. *Rec Cant Mus* 9: 309–336.
- Currey JD, Alexander RMN (1985) The thickness of the walls of tubular bones. *J Zool* 206: 453–468.
- Petit JR, Raynaud D, Barkov NI, Barnola JM, Basile I, et al. (1999) Climate and atmospheric history of the past 420,000 years from the Vostok ice core, Antarctica. *Nature* 399: 429–436.
- Wood JR, Wilmshurst JM, Richardson SJ, Rawlence NJ, Wagstaff SJ, et al. (2013) Resolving lost herbivore community structure using coprolites of four sympatric moa species (Aves: Dinornithiformes). *PNAS*. doi:10.1073/pnas.1307700110.
- Gatesy SM (1995) Functional evolution of the hindlimb and tail from basal theropods to birds. In: Thomason JJ, editor. *Functional Morphology in Vertebrate Palaeontology*. Cambridge: Cambridge University Press. pp. 219–234.
- Main RP, Biewener AA (2007) Skeletal strain patterns and growth in the emu hindlimb during ontogeny. *J Exp Biol* 210: 2676–2690.
- Currey JD (2007) Variability of the mechanical properties of bone, and its evolutionary consequences. *J R Soc Interface* 4: 127–135.
- Cubo J, Casinos A (2000) Mechanical properties and chemical composition of avian long bone. *Euro J Morph* 38:112–121.
- Turvey ST, Green OR, Holdaway RN (2005) Cortical growth marks reveal extended juvenile development in New Zealand moa. *Nature* 435: 940–943.
- Bourdon E, Castanet J, De Ricqlès A, Scofield RP, Tennyson A, et al. (2009) Bone growth marks reveal protracted growth in New Zealand kiwi (Aves, Apterygidae). *Biol Lett* 5: 639–642.
- Currey JD (2006) *Bones: Structure and Mechanics*. Princeton: Princeton University Press. 456 p.
- Currey JD (1999) What determines the bending strength of compact bone? *J Exp Biol* 202: 2495–2503.
- Garland TR Jr, Adolph SC (1994) Why not to do two-species comparative studies: Limitations on inferring adaptation. *Physiol Zool* 67: 797–828.
- Worthy TH, Edwards AR, Millener PR (1991) The fossil record of moas (Aves: Dinornithiformes) older than the Otira (last) Glaciation. *J R Soc New Zeal* 21: 101–118.
- Tennyson AD, Worthy TH, Jones CM, Scofield RP, Hand SJ (2010) Moa's Ark: Miocene fossils reveal the great antiquity of moa (Aves: Dinornithiformes) in Zealandia. *Rec Aust Mus* 62: 105–114.
- Bunce M, Worthy TH, Phillips MJ, Holdaway RN, Willemsen E, et al. (2009) The evolutionary history of the extinct ratite moa and New Zealand Neogene paleogeography. *PNAS*. doi:10.1073/pnas.0906660106
- Worthy TH, Scofield RP (2012) Twenty-first century advances in knowledge of the biology of the moa (Aves: Dinornithiformes): a new morphological analysis and moa diagnoses revised. *New Zeal J Zool* 39: 87–152.
- Smith NC, Jespers KJ, Wilson AM (2010) Ontogenetic scaling of locomotor kinetics and kinematics of the ostrich (*Struthio camelus*). *J Exp Biol* 213: 1347–1355.
- Prange HD, Anderson JF, Rahn H (1979) Scaling of skeletal mass to body mass in birds and mammals. *Am Nat* 113: 103–122.
- Reid B (1987) Food intake and growth rate of Cassowary chicks (*Casuarius spp.*) reared at Mendi, Southern Highland Papua New Guinea. *Int Zoo Yearbook* 26: 189–198.
- Picasso MB (2011) Postnatal ontogeny of the locomotor skeleton of a cursorial bird: greater rhea. *J Zool* 286: 303–311.
- Gatesy SM, Biewener AA (1991) Bipedal locomotion: effects of speed, size and limb posture in birds and humans. *J Zool* 224: 127–147.
- Worthy TH, Worthy JP, Tennyson AD, Salisbury SW, Hand SJ, et al. (2013) Miocene fossils show that kiwi (*Apteryx*, Apterygidae) are not phyletic dwarves. *Proc. 8th Meeting. Soc. Avian Paleo. Evol. Vienna. Serie A.*

Chapter 5

Scaling of convex hull volume to body mass in modern primates, non-primate mammals and birds: applications to the fossil record

PLoS ONE (2014). 9(3): e91691.

Scaling of Convex Hull Volume to Body Mass in Modern Primates, Non-Primate Mammals and Birds

Charlotte A. Brassey*, William I. Sellers

Faculty of Life Sciences, University of Manchester, Manchester, United Kingdom

Abstract

The volumetric method of 'convex hulling' has recently been put forward as a mass prediction technique for fossil vertebrates. Convex hulling involves the calculation of minimum convex hull volumes (vol_{CH}) from the complete mounted skeletons of modern museum specimens, which are subsequently regressed against body mass (M_b) to derive predictive equations for extinct species. The convex hulling technique has recently been applied to estimate body mass in giant sauropods and fossil ratites, however the biomechanical signal contained within vol_{CH} has remained unclear. Specifically, when vol_{CH} scaling departs from isometry in a group of vertebrates, how might this be interpreted? Here we derive predictive equations for primates, non-primate mammals and birds and compare the scaling behaviour of M_b to vol_{CH} between groups. We find predictive equations to be characterised by extremely high correlation coefficients ($r^2=0.97-0.99$) and low mean percentage prediction error (11–20%). Results suggest non-primate mammals scale body mass to vol_{CH} isometrically ($b=0.92$, 95%CI = 0.85–1.00, $p=0.08$). Birds scale body mass to vol_{CH} with negative allometry ($b=0.81$, 95%CI = 0.70–0.91, $p=0.011$) and apparent density (vol_{CH}/M_b) therefore decreases with mass ($r^2=0.36$, $p<0.05$). In contrast, primates scale body mass to vol_{CH} with positive allometry ($b=1.07$, 95%CI = 1.01–1.12, $p=0.05$) and apparent density therefore increases with size ($r^2=0.46$, $p=0.025$). We interpret such departures from isometry in the context of the 'missing mass' of soft tissues that are excluded from the convex hulling process. We conclude that the convex hulling technique can be justifiably applied to the fossil record when a large proportion of the skeleton is preserved. However we emphasise the need for future studies to quantify interspecific variation in the distribution of soft tissues such as muscle, integument and body fat.

Citation: Brassey CA, Sellers WI (2014) Scaling of Convex Hull Volume to Body Mass in Modern Primates, Non-Primate Mammals and Birds. PLoS ONE 9(3): e91691. doi:10.1371/journal.pone.0091691

Editor: Alistair Robert Evans, Monash University, Australia

Received December 16, 2013; **Accepted** February 14, 2014; **Published** March 11, 2014

Copyright: © 2014 Brassey, Sellers. This is an open-access article distributed under the terms of the Creative Commons Attribution License, which permits unrestricted use, distribution, and reproduction in any medium, provided the original author and source are credited.

Funding: This work was funded by the Natural Environment Research Council's Doctoral Training Grant (NE/1528134/1). The funders had no role in study design, data collection and analysis, decision to publish, or preparation of the manuscript.

Competing Interests: The authors have declared that no competing interests exist.

* E-mail: charlotte.brassey-2@postgrad.manchester.ac.uk

Introduction

An animal's form and function is bound by physical laws. They determine the strength of structures, the rate of heat transfer and the dynamics of locomotion [1], and their consequences are dependent upon the mass of the body on which they act. As such, an organism's mass is a critical constraint on its growth, physiology, ecology and biomechanics. Quantitative predictions of the mass properties of extinct taxa are therefore crucial to understanding their palaeobiology, and considerable effort has gone into deriving such mass estimates.

Common practice when estimating fossil body mass has been to take a skeletal dimension from modern species, such as femur circumference [2] or glenoid diameter [3], and use this value as the independent variable in a regression against body mass [4]. This method has been subject to considerable discussion in the literature and concerns have been raised regarding logarithmic transformation of the dataset [5], the choice of regression model [6] and the extrapolation of the model beyond the range of extant data [7]. Bivariate regressions also suffer from the 'single bone problem', in which reliance upon a single metric derived from a highly specialised skeletal element to predict body mass may result in considerable over- or underestimation [8]. When only

fragmentary material is preserved, however, this remains the only available method for predicting body mass of extinct species.

In contrast, volumetric techniques require a reconstruction of the entire skeleton and do not rely upon single skeletal elements for mass estimation. Early attempts at volumetric reconstructions involved the construction of physical scale models and estimates of fluid displacement [9–11]. More recently, digital models have been created with the purpose of estimating mass and inertial properties of individual body segments [12–17]. In these instances, 3D mathematical slices may be fitted to given frontal and sagittal profiles [12,13], B-spline objects can be fitted to control points on the skeleton [14,15] or a single continuous surface may be lofted between several B-spline curves [16,17]. The digital models can then be 'fleshed out' to reflect body contours *in vivo*. In these studies, the authors reflect upon the issues associated with 'artistic' modelling of fossil body shape, and carry out sensitivity analyses in order to quantify the effect of soft tissue reconstructions on mass estimates. Furthermore, in order to estimate mass, a value for body density (ρ_b) must be assigned to the volumetric model. Values for body density are sparsely reported in the literature (see discussion and Table S1 for more detail) and in the case of fossil species, a value of 1000–1024 kg/m^{−3} (the density of water) is often assigned [11–17]. Additional inferences must then be made regarding the size and location of air-filled cavities such as lungs and air sacs.

Convex hulling is an alternative approach to body mass estimation that has recently been put forward, which combines aspects of both volumetric modelling and linear regression [8,18]. Much the same as other volumetric techniques, convex hulling benefits from including the maximum amount of information from the skeleton into the mass estimate and circumvents the ‘single bone problem’ compared with regressions based on isolated limb bone dimensions. Convex hulling also sidesteps the requirements for soft tissue reconstructions that are necessary in other volumetric mass estimates, and has been applied to estimate fossil body mass in two species of giant bird [8] and sauropod dinosaurs [18,19]. The convex hull (*CH*) is one of the oldest and most important structures within the field of computational geometry. The convex hull $CH(S)$ of set of points S is the smallest convex polytope that contains S [20] (Figure 1), which, intuitively in 2D, can be thought of as stretching a rubber band around a given set of points. The practical application of calculating convex hulls has ranged from determining trait space in biotic community assemblages [21] to collision detection in computer games design [22] and solving shortest-path problems in transport logistics [23].

When applied to the problem of fossil mass estimation, the convex hulling process is used to calculate a minimum body volume from vertebrate skeletons. Digital models of the skeleton can be acquired using imaging techniques such as light radar (LiDAR), computed tomography (CT) or photogrammetry [24]. Whole skeletons are then segmented into functional units (i.e. trunk, thigh, skull etc.) and converted to point clouds (Figure 2A.). Each point cloud consists of a large dataset of points or vertices (typically ranging from 10^3 – 10^6 depending upon the functional unit in question) representing the surface of the skeletal element that are saved as x , y , and z coordinates. The convex hulling operation then works to fit the smallest convex polytope around that set of points, resulting in a tight-fitting hull around the skeleton and a minimum value for the convex wrapping volume (vol_{CH}) (Figures 2B–C).

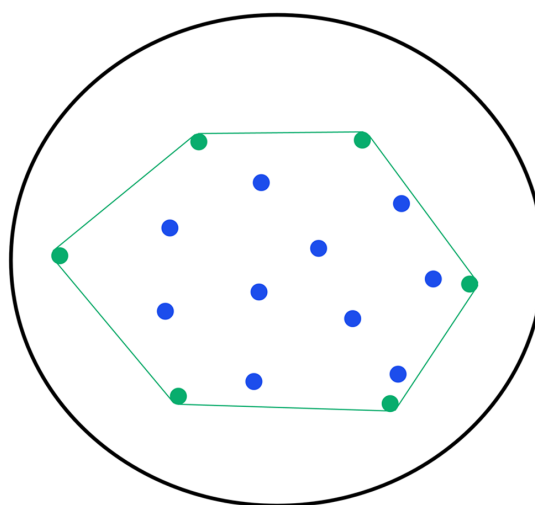


Figure 1. Simplified example of the convex hulling process. Black ellipse represents the initial extent of a rubber band stretched to encompass all coloured points. Green polygon represents the convex hull defined by the rubber band ‘snapping to’ the green boundary points. The internal (blue) points lie within the convex hull and do not contribute to defining its maximum extent.
doi:10.1371/journal.pone.0091691.g001

Rather than apply this technique directly to fossil skeletons, previous authors have used the convex hull method to derive calibration curves from modern species for mass prediction. Sellers et al. [18] calculated vol_{CH} in a range of quadrupedal mammals and multiply this value by an average density of 893 kg/m^{-3} to generate a minimum convex hull mass. This mass was then regressed against literature estimates for live body mass to produce a predictive equation. In contrast, Brassey et al. [8] directly regressed vol_{CH} against literature mass estimates when deriving a ratite-specific calibration curve in order to avoid uncertainty associated with assigning a particular density. There is however an implicit assumption that the predictive model is being applied to a fossil species closely related to (and hence likely to possess similar body density to) the modern calibration dataset. In this instance, a ratite-specific curve was applied to fossil moa.

Mass estimation techniques previously applied to hominid remains have been classified into two groups; ‘mechanical’ methods which rely upon a functional relationship between weight-bearing postcranial elements and mass, and ‘morphometric’ methods which directly reconstruct mass from preserved features such as bi-iliac breadth [25]. To the authors’ knowledge, whole-body volumetric mass estimation techniques have not previously been applied to hominids, or primates more generally, perhaps because of the often-fragmentary nature of the primate fossil record. However the hominin skeletons of AL 288-1 (*Australopithecus afarensis*) [26] and KNM-WT 15000 (*Homo erectus*) [27] are exceptional for early hominids in possessing a considerable proportion of limb bone and ribcage material, and a volumetric reconstruction may be feasible in these cases. Similarly, Miocene apes such as the African genus *Proconsul* [28] and new Spanish specimens including *Pierolapithecus* [29] are also known from reasonably complete skeletons, and there are also strepsirrhine examples such as *Darwinius* [30] and the giant lemurs of Madagascar [31].

In the case of linear predictive equations derived from limb bones (i.e. the ‘mechanical’ methods above), there are good biomechanical reasons why weight-bearing postcranial elements should be highly correlated with mass [32]. We know that convex hull calibration curves derived for modern species of birds and quadrupedal mammals are characterised by extremely high correlation coefficients (r^2 of 0.97 and 0.98 respectively). However before we apply this technique any further, it is prudent to likewise consider the biomechanical reasons why minimum body volume is informative with regards to body mass. Specifically, when vol_{CH} scaling departs from isometry in a group of vertebrates, how might this be interpreted?

The aims of this study are therefore:

- To derive a primate-specific convex hull calibration curve to complement those already existing for non-primate mammals and birds
- To compare vol_{CH} allometry between modern vertebrate groups
- To interpret the scaling behaviour of vol_{CH} in the context of interspecific variations in body density, composition and body plan.

Methods

All skeletal material included in this study was accessed with the permission of the relevant museum or institution (University Museum of Zoology Cambridge, UMZC; Oxford University Museum of Natural History, OUMNH; Kyoto University Primate

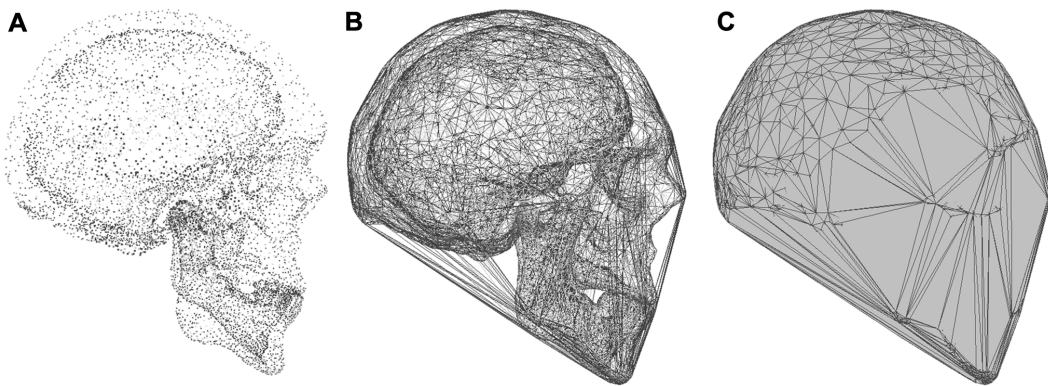


Figure 2. Convex hulling applied to a human skull. A, point cloud representing both the inner and outer surface contours of the skull; B, illustrates fit of the convex hull around the maximum extent of the skull; C, convex manifold (water-tight) polytope fitted by the hulling operation.
doi:10.1371/journal.pone.0091691.g002

Research Institute, KUPRI; The National Library of Medicine, NLM) and reside within their permanent collections. A list of specimens is included in Table 1 and the convex hulling method has been described in detail elsewhere [8,18]. Briefly, mounted skeletons of ratites (UMZC) and non-primate mammals (OUMNH) were scanned using a Z+F Imager 5010 and 5006i LiDAR respectively. The museum galleries containing the specimens were scanned several times from various angles to ensure adequate coverage of the skeletons. Registration and aligning of the LiDAR scans was carried out in Z+F LaserControl and individual skeletons were isolated and exported to Geomagic Studio v.12 (Geomagic, USA) as point clouds. CT scans of primate carcasses sourced from KUPRI, the human male sourced from the Visible Human Project (<http://www.nlm.nih.gov/research/visible>), plus additional CTs of two primates and two neognath birds from the University of Manchester were imported as DICOM files into OsiriX [34]. CT slice thickness ranged between 1–2.7 mm, with pixel spacings of 0.38–0.98 mm/pixel. The surface of each skeleton was rendered in 3D and exported to Geomagic Studio.

Individual skeletons were subdivided into functional units. In the mammals, the body was divided into the trunk (including the pelvis, ribs, sternum and scapula), thigh (femur), shank (tibia), forearm (radius and ulna), upper arm (humerus), neck and skull. In the case of ungulates, the metatarsals and metacarpals were considered as separate segments from the phalanges. For all other mammals, the tarsals and phalanges were combined into one functional unit for hulling. The long necks of the giraffe (*Giraffa camelopardalis*) and camel (*Camelus dromedarius*) were segmented into two parts to ensure a tight-fitting hull around their length (Figure 3). The long tails of the gibbon (*Chlorocebus aethiops*), squirrel monkey (*Saimiri sciureus*) and Japanese macaque (*Macaca fuscata*) were divided into multiple segments for the same reason. The antlers of the cervids were not included. The skeleton of the birds was subdivided into the trunk (pelvis, ribs, scapula and sternum plus keel and clavicle in the neognaths), thigh (femur), shank (tibiotarsus), tarsometatarsus, proximal wing (humerus), distal wing (radius and ulna), hand (metacarpals and phalanges), feet (phalanges), neck and skull. As in the long-necked mammals, bird necks were subdivided to ensure a tight fit.

The gorilla (*Gorilla gorilla*) was CT scanned as disarticulated body parts and some digital rearticulation of the skeleton was necessary prior to convex hulling. The lateral margins of both iliac

crests had not been included in the CT and required restoration. The scapulae had been disassociated from the ribcage and were repositioned before convex hulling of the trunk. Furthermore the skull associated with the male gorilla carcass (KUPRI298-317) was not available, and the skull of a different male gorilla was scaled up geometrically based on limb length in its place. Both the lesser and greater apes in the sample were CT scanned lying in the supine position. In contrast the non-hominoid primates were scanned lying on their side. As a result, the latter group displayed considerable curvature of the spine dorsoventrally. This was corrected by straightening the spine in 3DsMax (Autodesk, USA) in order to ensure all primate trunks were of a comparable shape before hulling. CT data are available from <http://www.pri.kyoto-u.ac.jp/> and <http://www.nlm.nih.gov/research/visible/>, and convex hulls are available for download from <http://www.animalsimulation.org>.

Once subdivided, body segments were saved as .obj files. The convex hulling process was carried out in MATLAB (MathWorks, USA) using the ‘convhulln’ function. Convhulln implements the Quickhull (‘qhull’) algorithm for computing the convex hull [35]. Total vol_{CH} of a skeleton was calculated as the sum total of segment volumes. Body mass (M_b , kg) was regressed against vol_{CH} (m^3) for three groups (non-primate mammals, primates and birds) in MATLAB (see Table 1 for M_b sources). Slopes were fitted by means of ordinary least squares (OLS) regressions, as Type-I models are recommended when regressions will be used in a predictive capacity [6]. Slopes were compared in a one-way analysis of covariance (ANCOVA) using the ‘multcomp’ function in MATLAB, with subsequent pair-wise post hoc Tukey HSD test. Apparent density of the convex hulled skeleton (ρ_{CH} , kg/m^{-3}) was also calculated as vol_{CH}/M_b .

In order to account for evolutionary relationships, phylogenetically based regression models were also applied. This methodology is described in detail elsewhere [36]. Composite phylogenies were constructed in Mesquite ver. 2.75 (<http://mesquiteproject.org>) using tree topologies and branch lengths derived from previous publications (Figure 4A–C). The MATLAB program ‘Regressionv2.m’ [49] was used to implement multiple phylogenetic regressions. Phylogenetic generalised least squares (PGLS) assumes residuals are correlated due to shared ancestry and can be described by a Brownian motion model of evolution. Alternatively the Ornstein-Uhlenbeck (OU) evolutionary process models stabilising selection around an optimum [49]. The goodness-of-fit of

Table 1. Convex hull specimen list and sources of body mass.

species	accession no.	sex	volume (m^3)	M_b (kg)	M_b source
<i>Struthio camelus</i>	UMZC374	–	7.17×10^{-2}	60.7	[8]
<i>Casuarius casuarius</i>	UMZC371.D	–	1.72×10^{-2}	27.0	[8]
<i>Dromaius novaehollandiae</i>	UMZC363	–	2.14×10^{-2}	20.06	[8]
<i>Rhea americana</i>	UMZC378.gg	–	1.77×10^{-2}	16.3	[8]
<i>Rhea pennata</i>	UMZC378ki	–	1.59×10^{-2}	14.9	[8]
<i>Apteryx australis</i>	UMZC378.A	–	1.10×10^{-3}	2.96	[8]
<i>Apteryx australis lawryi</i>	UMZC378.SS	F	1.40×10^{-3}	2.41	[8]
<i>Branta leucopsis</i>	–	–	1.10×10^{-3}	1.69	[*]
<i>Numida meleagris</i>	–	F	1.00×10^{-3}	1.40	[*]
<i>Bison bison</i>	OUMNH17430	M	4.73×10^{-1}	558.5	[16]
<i>Bos taurus</i>	OUMNH17432	–	2.19×10^{-1}	323.7	[16]
<i>Camelus dromedaries</i>	OUMNH17427	–	3.21×10^{-1}	427.0	[16]
<i>Cervus elaphus</i>	OUMNH17431	M	8.40×10^{-2}	89.5	[16]
<i>Dicerorhinus sumatrensis</i>	OUMNH1439	–	3.61×10^{-1}	470.3	[16]
<i>Elephas maximus</i>	OUMNH10686	M	2.09×10^0	2352.0	[16]
<i>Equus caballus</i>	OUMNH17428	–	3.70×10^{-1}	517.5	[16]
<i>Giraffa camelopardalis</i>	OUMNH19507	–	4.35×10^{-1}	638.2	[16]
<i>Loxodonta africana</i>	OUMNH4004	–	2.75×10^0	2734.9	[16]
<i>Megaloceros giganteus</i>	OUMNH17433	–	3.01×10^{-1}	435.6	[16]
<i>Rangifer tarandus</i>	OUMNH17529	–	7.57×10^{-2}	95.8	[16]
<i>Sus scrofa</i>	OUMNH17426	–	7.79×10^{-2}	107.4	[16]
<i>Tapirus indicus</i>	OUMNH17425	–	1.70×10^{-1}	295.3	[16]
<i>Ursus maritimus</i>	OUMNH17459	–	1.11×10^{-1}	206.1	[16]
<i>Chlorocebus aethiops</i>	KUPRI28	M	3.70×10^{-3}	3.78	[*]
<i>Macaca fuscata</i>	KUPRI375	F	5.10×10^{-3}	6.60	[*]
<i>Saimiri sciureus</i>	KUPRI290	F	6.00×10^{-4}	0.759	[*]
<i>Hylobates agilis</i>	KUPRI277	M	5.40×10^{-3}	6.75	[*]
<i>Hylobates lar</i>	KUPRI182	F	6.60×10^{-3}	6.65	[33]
<i>Gorilla gorilla</i>	KUPRI298-317	M	9.57×10^{-2}	176.0	[*]
<i>Pan troglodytes</i>	–	M	4.18×10^{-2}	50.9	[33]
<i>Pongo pygmaeus</i>	–	F	3.25×10^{-2}	45.0	[*]
<i>Homo sapiens</i>	NLM	M	4.91×10^{-2}	68.9	[*]

UMZC, University Museum of Zoology, Cambridge; OUMNH, Oxford Museum of Natural History; KUPRI, Kyoto University Primate Research Institute; NLM, National Library of Medicine. Sources of body mass (M_b); [*] carcass weight; [33] estimated using predictive equation for Hominoid body mass based upon radial head surface area (mm^2) derived from CT images.

doi:10.1371/journal.pone.0091691.t001

the regression models is compared using uncorrected Akaike Information Criterion (AIC), in which smaller values imply a better fit. Models with an AIC value of <2 units greater than the minimum value are also said to have considerable support [50]. The optimal Ornstein-Uhlenbeck transformation parameter (d) was also estimated, where $d=1$ suggests the PGLS models fits the data better and $d=0$ suggests a better fit for the OLS model.

Results

Total vol_{CH} estimated for the skeletons are given in Table 1. The results of the OLS and phylogenetically corrected regressions of M_b against vol_{CH} are given in Table 2, and for OLS are plotted in Figure 5. Prior to \log_{10} transformation the datasets did not meet the requirements for normality (Shapiro-Wilks test) and homoscedasticity (Breusch-Pagan test). Model results are therefore only

reported for \log_{10} transformed data. For all the groups considered here, the phylogenetically uncorrected OLS regression model provides a better fit to the data as indicated by lower AIC values for OLS models compared to PGLS and OU models (Table 2). This is further supported by d values of ≤ 0.011 , again suggesting a better fit to the data in the OLS models than PGLS. The need for phylogenetic correction in this instance therefore remains equivocal, and for the sake of comparisons between our sample groups we only discuss \log_{10} transformed OLS models further. However the potential for phylogenetic biasing, particularly of the primate slope, is considered further in the discussion.

Geometric similarity would predict M_b to scale to vol_{CH} with a slope of 1. Non-primate mammals do not scale M_b to vol_{CH} significantly differently from isometry ($b = 0.92$, 95%CI = 0.85–1.00, $p = 0.08$). In contrast, primates scale M_b to vol_{CH} significantly faster than isometry ($b = 1.07$, 95%CI = 1.01–1.12, $p = 0.05$) whilst

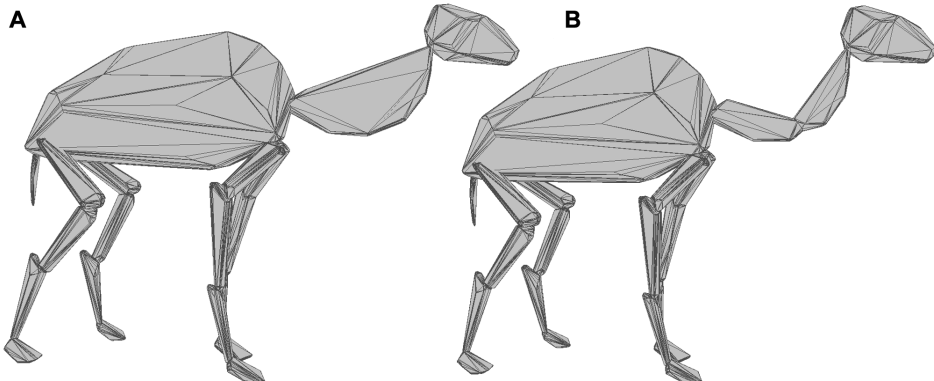


Figure 3. Effect of subdividing neck of *C. dromedaries* on convex hull volume. A, illustrates extent of neck convex hull without subdivision due to curvature of cervical series; B, tighter fit of convex hulls when divided into two parts.
doi:10.1371/journal.pone.0091691.g003

birds scale M_b slower than predicted by geometry similarity ($b = 0.81$, 95%CI = 0.70–0.91, $p = 0.011$). Comparing all three models in a one-way analysis of covariance (ANCOVA) finds a significant difference between slopes ($F_{(2,26)} = 7.18$, $p < 0.003$). A post-hoc Tukey test confirms birds scale M_b to vol_{CH} significantly slower than primates ($p < 0.05$). No other pairwise comparison is significant however. Mean apparent density (vol_{CH}/M_b) was not significantly different between groups ($F = 0.23$, $p = 0.80$). Mean apparent density did not scale with M_b in non-primate mammals. However, mean apparent density was found to increase with M_b in primates ($r^2 = 0.46$, $p = 0.025$), and decrease with M_b in birds ($r^2 = 0.36$, $p < 0.05$) (Figure 5B).

Due to the considerable amount of reconstruction work necessary on the gorilla skeleton prior to convex hulling and the resulting uncertainties in the placement of the scapulae and reconstruction of the ilium, the effect of excluding the gorilla individual from the sample was investigated. Removing the gorilla from the primate dataset did not significantly affect the slope of the regression line of M_b against vol_{CH} ($b = 1.07$ with gorilla, $b = 1.03$ without gorilla, $p = 0.46$). However, primates scale M_b to vol_{CH} with isometry ($p > 0.34$) and apparent density no longer scales with M_b in primates ($r^2 = 0.21$, $p > 0.12$) when the gorilla is removed from the sample.

In this study, data were collected using two imaging techniques (CT and LiDAR). We investigated how the choice of imaging technique might impact upon our results by exploring the relationship between body size of the specimen, point cloud density and vol_{CH} of the trunk. This sensitivity analysis was conducted on the trunk segment rather than the whole body set, as the trunk comprises the vast majority of total vol_{CH} and any sampling effect demonstrable on the trunk will almost certainly be present in the whole body model. In the CT-scanned specimens, no relationship exists between M_b (used as a proxy for total body size) and the number of points comprising the trunk ($p > 0.05$). This is because pixel size is manually adjusted for each individual during scanning in order to achieve the highest resolution possible.

In LiDAR-scanned skeletons, there is a significant correlation between M_b and number of points comprising the trunk ($p < 0.05$ for LiDAR birds, $p < 0.01$ for LiDAR non-primate mammals). As the LiDAR skeletons were isolated from one larger LiDAR point cloud of the surrounding museum gallery, larger individuals consist of a greater number of points than smaller individuals. The point clouds of trunk segments were randomly subsampled down

in Geomagic Studio, such that all individuals comprised an equal number of points. In a paired Student's t-test, no significant difference existed in vol_{CH} of the trunk between original and down-sampled point clouds in the UMZC ratites ($t = 1.97$, $df = 8$, $p > 0.05$) and OUMNH non-primate mammals ($t = 2.04$, $df = 13$, $p > 0.05$). Furthermore, the scaling exponents of M_b to trunk vol_{CH} were not significantly different between original and down-sampled point clouds in ratites ($p > 0.99$) and non-primate mammals ($p > 0.96$).

Discussion

Convex Hull Mass Estimation

M_b correlates extremely well with vol_{CH} in modern birds and mammals ($r^2 = 0.97$ – 0.99) and mean percentage prediction errors (%PE) of the models are encouragingly low (Table 2). Our values for mean %PE (11–20%, Table 2) compare favourably with bivariate predictive models recently derived from limb bones of mammals (25–71%PE, [2]) and volant birds (13–128%PE, [3]) comprising much larger datasets. The 95% confidence intervals on our mean %PE are similar to those of Campione & Evans [2], but are considerably wider than those of Field et al. [3]. The application of convex hulling to the problem of body mass estimation in fossil species is therefore justifiable when a large proportion of the skeleton is preserved. The authors have previously applied this mass estimation technique to fossil dinosaurs and birds, and here we present a primate-specific calibration curve of interest to those in the field of physical anthropology.

Primates are found to scale M_b to vol_{CH} similarly to non-primate mammals ($p > 0.05$). That primates are found to scale their skeletal dimensions similarly to other mammals is not without precedent. The scaling exponents of primate forelimb and hindlimb length to body mass overlap those of Carnivora, Rodentia and Scandentia [51,52], with Marsupials the only order in this study to scale hindlimb length significantly differently from primates [51]. Similarly Polk et al. [53] found the confidence intervals of primate-specific regressions of hindlimb bone length and cross-sectional properties against mass to overlap considerably with those of Carnivora and Rodentia.

Therefore combining the non-primate mammal and primate datasets, a general mammal calibration curve is derived ($a = 3.13$, $b = 1.011$, $r^2 = 0.993$, $p < 0.001$, mean square error (MSE) =

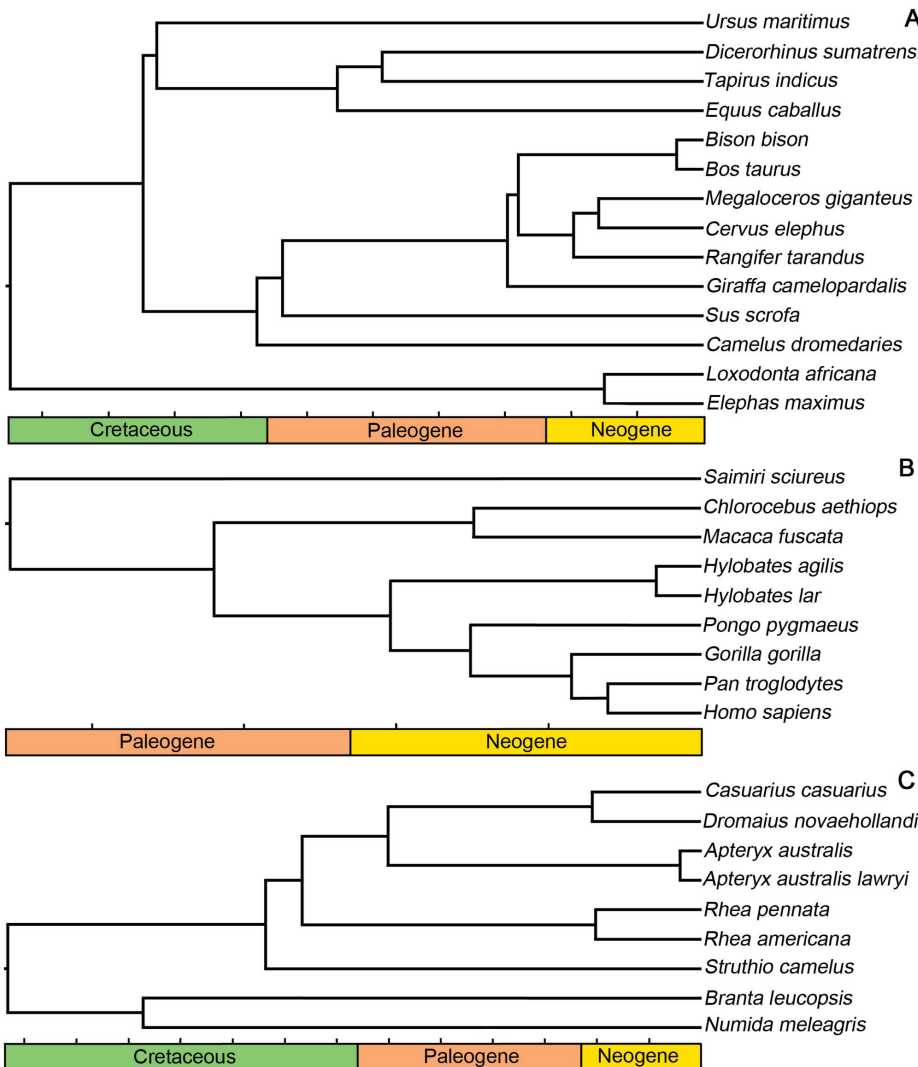


Figure 4. Consensus trees used in phylogenetic analysis. Tick marks represent increments of 10 million years. A, non-primate mammal tree topology and branch lengths derived from [37–44]; B, primate tree derived from [45]; C, bird tree derived from [46–48].
doi:10.1371/journal.pone.0091691.g004

0.0052, mean percentage prediction error (%PE) = 12.0%). Given the log-transformed nature of the data, caution should be exercised if the equations presented here are to be subsequently applied to fossil skeletons in a mass prediction capacity. When back-transforming a linear model of the form:

$$\log_{10}y = \log_{10}a + b\log_{10}x \quad (1)$$

into a power function of the form:

$$y = ax^b \times CF \quad (2)$$

a correction factor (CF) should be applied, which is calculated as:

$$CF = e\left(\frac{MSE}{2}\right) \quad (3)$$

where MSE is the mean square error of the regression [54]. Multiplying by the correction factor converts the geometric mean value of y calculated by taking the antilog of $\log(y)$ into an arithmetic mean value of y . Values of MSE for our regression models are provided in Table 2 for this purpose. However, given the extremely high correlation coefficients and low values for MSE characterizing our models, multiplying by the correction factor will have very little effect on convex hull mass predictions.

Phylogenetic analyses have indicated some degree of biasing of the primate slope due to shared evolutionary history (Table 2). Our limited sample is dominated by hominoids (greater and lesser

Table 2. Ordinary least squares (OLS) and phylogenetically based regression (PGLS, phylogenetic generalised least squares; OU, Ornstein-Uhlenbeck process) of body mass (kg) against convex hull volume (m^3).

Fit	Type	a	a ±95%	b	b ±95%	r ²	AIC	d	MSE	%PE	PE ±95%
Mammals											
Log₁₀	OLS	3.09	3.04–3.14	0.92	0.85–1.00	0.98	-31.2	—	0.005	11.6	6.96–17.1
	PGLS	3.06	2.88–3.21	0.88	0.77–0.97	0.96	-16.9	—	—	—	—
	OU	3.09	3.03–3.13	0.92	0.86–1.00	0.98	-29.2	<0.001	—	—	—
Primates											
Log₁₀	OLS	3.24	3.12–3.35	1.07	1.01–1.12	0.99	-19.7	—	0.004	10.8	3.97–17.6
	PGLS	3.34	3.00–3.74	1.10	0.96–1.24	0.96	-11.8	—	—	—	—
	OU	3.24	3.10–3.35	1.07	1.01–1.12	0.99	-17.7	0.011	—	—	—
Birds											
Log₁₀	OLS	2.70	2.50–2.93	0.81	0.71–0.90	0.97	-9.98	—	0.013	19.7	5.81–33.5
	PGLS	2.43	1.71–3.05	0.71	0.44–0.97	0.77	2.09	—	—	—	—
	OU	2.71	2.47–2.89	0.82	0.71–0.89	0.97	-7.98	<0.001	—	—	—

AIC, Uncorrected Akaike Information Criterion; d, restricted maximum likelihood estimate of the Ornstein-Uhlenbeck transformation parameter; r², 95% confidence intervals of the regression; PE, mean percentage prediction error of the regression; %PE, 95% confidence interval of mean PE. Log₁₀ transformed OLS regressions discussed throughout the text and are highlighted in bold.
doi:10.1371/journal.pone.0091691.t002

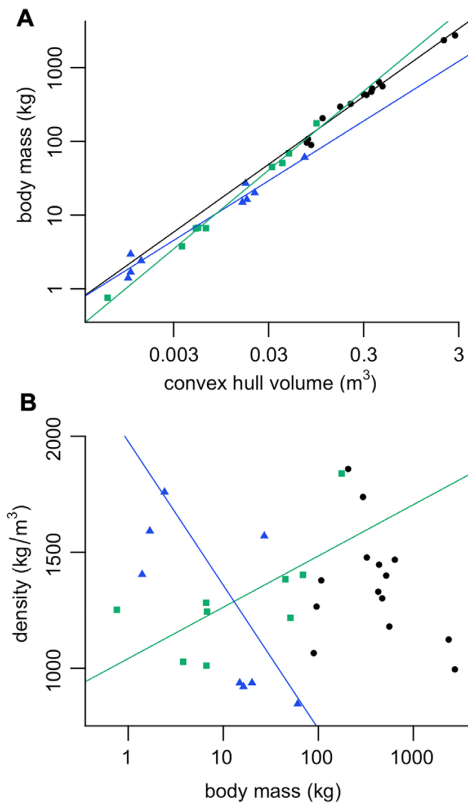


Figure 5. OLS regression results. A, Body mass (kg) against convex hull volume (m^3). For slope equations, see Table 2 (labelled in bold). B, apparent density of convex hull (kg/m^3) against body mass (kg). Density did not scale with body mass in non-primate mammals. Density increases with body mass in primates ($a=1042$, $b=221$, $r^2=0.46$, $p=0.025$) yet decreases with body mass in birds ($a=1977$, $b=-619$, $r^2=0.36$, $p<0.05$). Black circles, non-primate mammals; green squares, primates; blue triangles, birds.
doi:10.1371/journal.pone.0091691.g005

apes constitute two thirds of the primates included). The predictive equation derived here is still applicable to the field of early human evolution, for example, but should be cautiously applied to other primate groups that are not represented in our sample. Furthermore, the performance of PGLS regressions when predicting the body mass of species not included in the original regression remains unclear, and the application of both OLS and PGLS is recommended [55].

The factor limiting the application of this methodology to physical anthropology will be a lack of appropriate specimens. The relative paucity of associated postcranial hominin fossil material at present makes the widespread use of this calibration curve unlikely, and any such attempt would almost certainly require significant reconstruction. This highlights one of the potential concerns regarding the convex hull mass estimation technique. Whilst our methodology removes the need for authors to subjectively recreate soft tissue morphology by working on the skeleton alone, this acts to shift the burden of subjectivity onto those responsible for skeletal mounting of museum specimens. The flaring of the ribcage [16], positioning of the sternum [8], intervertebral spacing [16,56] extent of cartilaginous epiphyses

[57] and placement of the scapulae are known to effect mass estimates and biomechanical functionality of fossil reconstructions.

Recent efforts to remount fossil specimens, such as the Berlin *Brachiosaurus brancai* [58], according to our current understanding of their biology are commendable. However in most instances it is not feasible to physically remount skeletons due to time and financial constraints, alongside the potential for damage to the specimen. In this case, convex hulling provides a solution. The digital nature of our volumetric models allows skeletal components to be easily manipulated and whole skeletons may be digitally remounted. Sensitivity analyses on both the skeletal mount and soft tissue reconstructions are therefore entirely feasible, and should be a prerequisite for functional analyses.

Scaling of Body Mass with vol_{CH}

Non-primate mammals scale body mass isometrically with respect to vol_{CH} , and apparent density is mass invariant (Figure 5B). However in modern primates and birds, vol_{CH} scales allometrically and apparent density therefore changes with body mass (Figure 5B). This may be interpreted in one of two ways:

- The allometric scaling of apparent density reflects a real trend in scaling of carcass density to body mass in birds and primates.
- Carcass density is actually mass-independent, yet convex hulling (and apparent density) is capturing a shift in the distribution of body tissue with size in these groups.

Convex hull volume is certainly an underestimate compared to fleshed-out body volume (vol_{f}) as it neglects any muscle, fat or integument that would have sat outside the contours defined by the maximum extent of the hard tissues. This is confirmed by the extremely high values for mean apparent density calculated here (primates = 1296 kg/m³, non-primate mammals = 1359 kg/m³, birds = 1418 kg/m³) compared to values for whole body density throughout the literature (see later discussion and Table S1).

However, the degree to which vol_{CH} underestimates vol_{f} depends on the distribution of such soft tissues, and this will vary both within and between skeletons. Within the hind limb for example, a greater mass of muscle is held proximally with the distal joints instead being controlled by long tendons [59]. Hence, vol_{CH} will be a smaller proportion of vol_{f} around the thigh compared to the shank and feet. Likewise, interspecific variation in the amount of soft tissue held outside the convex hull envelope will cause variation in $\text{vol}_{\text{CH}}: \text{vol}_{\text{f}}$, and apparent density values between species.

In light of this, it is unsurprising that non-primate mammals scale vol_{CH} isometrically and apparent density does not change with body mass. Our sample consists entirely of terrestrial species without specialist adaptations for climbing, swimming or digging. The bauplan (ground plan of the body segments) is therefore relatively well conserved throughout the sample (with the exception of the giraffe's neck and camel's hump). Apparent densities do vary considerably (Figure 5B) but do not scale to body mass.

When including the gorilla in the dataset, we find primates to scale M_{b} to vol_{CH} with positive allometry ($b = 1.07$, 95% CI = 1.01–1.12) and hence apparent density increases with mass. With the exception of humans, there are extremely sparse data in the literature regarding primate body density (Table S1) and without additional information on non-humans, a conclusion regarding the possible scaling of carcass density cannot be reached. Alternatively, apparent density may be scaling due to a size-related shift in the distribution of soft-tissue around the skeleton. Unpublished data

has found terrestrial primates to be more muscular than arboreal species, regardless of their taxonomic affinity [60]. The largest members of our primate sample (*G. gorilla*, *Homo sapiens*, *Pan troglodytes*) are either entirely or primarily terrestrial. As such, we might expect the increase in apparent density in terrestrial apes to reflect increased muscle mass held outside the convex hull envelope, and therefore an increase in the $\text{vol}_{\text{f}}: \text{vol}_{\text{CH}}$ ratio. However, the scaling exponent for primate M_{b} to vol_{CH} is barely above isometry, and when the gorilla is removed from the dataset due to concerns regarding the reconstruction of the disarticulated skeleton, there is no significant relationship between primate apparent density and body mass ($p > 0.05$). This suggests our results are very sensitive to taxon sampling and more data regarding primate segment density and body composition, to compliment the wealth of existing data regarding segment mass and inertial properties, are sorely needed to resolve this uncertainty. Furthermore, two primates included in this study did not possess associated body mass data (*Hylobates lar*, *Pan troglodytes*). Despite being captive animals, literature values for mass were assigned to these specimens based upon regressions derived from wild-collected specimens (see Table 1). Primate individuals residing in zoos are known to be heavier, possess a higher body mass index (BMI) and percentage body fat composition than wild individuals [61] and our assigned values for body mass are therefore likely to be underestimates.

Despite the reputation of birds as being comparatively 'light-weight' [62], here we find the apparent densities of some avian individuals to be higher than those of modern mammals (Figure 5B). Due to the variety of methodologies employed to calculate carcass density and inconsistencies in the way in which density is reported in the literature, a statistical meta-analysis of previously published values is not possible. With the exception of diving birds however, a trend is visible in the literature whereby carcass density appears to be lower in birds than mammals (Table S1). This divergence between apparent convex hull density and carcass density may therefore be attributed to the convex hulling process itself.

Hypothesised adaptions or exaptations for weight saving in modern birds include possession of more hollow long bones ([63], although see [64–65]) and pneumatisation of the postcranial skeleton [66]. The convex hulling process does not account for the presence of air-filled cavities of a much lower density than soft tissue, resulting in inflated values for apparent density relative to carcass density. This is not a concern when applying the $M_{\text{b}} \propto \text{vol}_{\text{CH}}$ model in a predictive capacity, assuming the degree of pneumaticity also changes in a predictable way with mass. No explicit data exists regarding the scaling of air-sac volume in modern Aves, however a positive relationship has been identified between body mass and a 'pneumaticity index' (scoring the presence/absence of pneumaticity in 12 anatomical units) in 37 species of bird [67]. It is not clear how applicable these results are to the bird calibration curve presented here, given that flightless ratites are not included in their sample. Further work is needed to quantify and incorporate segment-specific variation in body density into avian convex hulls, particularly when the calibration curves are to be subsequently applied to pneumatic saurischian dinosaur and fossil bird skeletons.

Here we find a significant negative relationship between apparent density and body mass within our bird sample (Figure 5B). Re-analysing previously published data [68], in which the feathered and plucked body densities of 26 species of neognath birds were estimated using fluid displacement, a negative relationship is also found (Figure 6). Interestingly plucked carcass density is found to have a much stronger correlation to body mass

than feathered density (plucked $r^2=0.61$, $p<0.001$, feathered $r^2=0.16$, $p=0.04$). Given feather mass appears to scale isometrically with high correlation coefficients in neognaths [69–70], this may be attributed to variability in the volume of air trapped beneath feathers and/or methodological difficulties associated with air escaping prior to submergence.

Superimposing our data points for apparent density onto those calculated by Budgey [68] (Figure 6), our values for large ratites (*Struthio camelus*, *Rhea americana*, *Rhea pennata*, *Dromaius novaehollandiae*) fall very close to those predicted by the plucked carcass model. An exception is the cassowary (*Casuarius casuarius*) which has previously been identified as an outlier in a ratite-specific convex hull calibration curve due to uncertainties in a literature-assigned body mass [8]. In contrast, the smaller ratites (*Apteryx australis*, *Apteryx australis lawryi*) and neognaths possess apparent densities greatly in excess of those predicted for plucked carcasses. This suggests that the volume of ‘missing’ soft tissue located outside the convex hull is greater in smaller birds.

The pectoral muscles constitute the largest organ in flying birds, comprising on average 17% of total body mass [71]. In contrast, pectoral muscle in flightless ratites is considerably reduced relative to volant species [72–73], with pectoralis mass accounting for 0.25% of total mass in kiwi [74]. However variation in pectoralis mass is unlikely to account for the observed trend in apparent densities, as the possession of large pectoralis muscles has an osteological correlate in the occurrence of a keeled sternum. The keel will act to increase vol_{CH} in neognaths by shifting the maximum extent of the convex hull ventrally, and thus account for the presence of an enlarged pectoralis musculature.

As a counterpoint, the reduction in pectoral musculature in ratites is accompanied by an increase in pelvic musculature relative to flighted birds. Values for hindlimb muscle mass as a percentage of total M_b for ostrich (*Struthio camelus*) range from 29% [75] to 34% [76], and values of 25% are reported for the emu (*Dromaius novaehollandiae*) [77]. In contrast, the lower extremities of flighted neognaths (including muscle and skeletal parts) account for 1–17% of body mass in a diverse sample of species [78]. The exclusion of hindlimb musculature by the convex hulling process cannot account for the observed trend in apparent densities however, as proportionally more muscle mass would be excluded from ratite convex hulls than flighted birds. This would result in an increase in apparent density in ratites relative to neognaths, the reverse of the trend observed in this study.

As previously discussed, feather mass is known to scale isometrically with body mass in neognath birds [69–70], averaging 6% of total M_b . A review of literature-reported values for feather mass suggests kiwis also fall within this range (4.7–6.8% of total M_b , [79]). However, large ratites (ostrich, emu and rhea) are found to possess considerably less plumage (1.5–1.9% of total M_b , see Table S2) than neognaths. Thus feather mass may account for a small proportion of the observed ‘missing mass’ in neognaths and kiwi, but cannot adequately explain such a large disparity between our apparent density values and plucked density values of Budgey [68] as observed in small birds. It does however highlight the importance of choosing appropriate modern analogues when reconstructing mass in fossil species. Alexander’s [80] estimates of moa body mass, incorporating a value for feather mass of 5.6% of total M_b (his method (i)), are likely to be overestimates given the plumage values for large ratites presented here.

In addition to muscle and integument, fat deposits are also stored outside the convex hull of the skeleton. Reanalysing the data presented by Daan et al. [81] on 22 neognath species, the average percentage body fat is 7.8% and this does not scale with body mass ($p>0.36$). Caution must be exercised however, as this

study includes long-distance migratory species (known to lay down extensive fat deposits prior to departure) without clarifying the season of data collection. Similar values for average percentage body fat are found for ostrich (5%, [82]) and rhea (7%, [83]), whilst emu body fat composition is exceptionally high due to selection for oil production (28% body fat, [84]).

Regardless of whether total fat mass conforms to isometry, the distribution of adipose tissue across the body is highly uneven both within- and between bird species and this is likely to be reflected in the ‘missing mass’ of the convex hulling process. Wirestam et al. [85] found fat accumulation did not follow a geometrical model in flying birds, with deposition occurring preferentially at the front and back of the body. Neognaths preferentially deposit fat subcutaneously across the abdomen area (from sternum to cloaca) and in the furcula depression [86]. In contrast, large ratites (ostrich, emu, and rhea) are said to possess ‘minimal’ abdominal subcutaneous fat deposits, with a thick layer of adipose tissue stored within the retroperitoneum [87]. Very little body composition data exists for the kiwi, except for an average fat mass of 300 g given for *Apteryx mantelli* [79]. Assuming an average body mass of 1930 g for males and 2360 g for females, this represents a percentage body fat of 13–16% which is stored subcutaneously [79]. High apparent density values calculated here for neognaths and kiwi may therefore reflect a shift in the distribution of body fat to anatomical positions located beyond the convex hull extent defined by the skeleton.

Initial convex hull studies employed museum-based LiDAR scanning as a means of generating a modern calibration dataset [8,18]. LiDAR allows a large dataset (a gallery full of skeletons, for example) to be acquired within 2–3 hours. However skeletal mounts on display in public museums may be mounted incorrectly, and frequently have no body mass data associated with them. In this case body masses must be subsequently assigned using literature values. Here, for the first time, we have derived a primate convex hull calibration curve using CT scan data of whole carcasses. This approach avoids problems associated with skeletal mounting (intervertebral spacing, scapula placement etc. are all

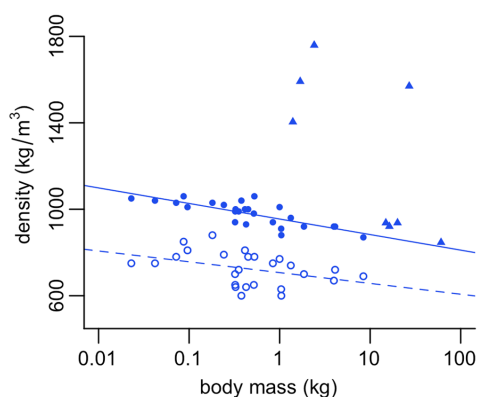


Figure 6. Scaling of density against mass in birds. Feathered carcass density (open circles) scales negatively against body mass ($a=707$, $b=-50.4$, $r^2=0.16$, $p=0.04$). Plucked carcass density (closed circles) scales negatively against body mass ($a=955$, $b=-72.4$, $r^2=0.61$, $p<0.001$). Note the extremely weak correlation between feathered body density and mass, compared to the much stronger correlation between plucked carcass density and mass (see text for further discussion). Feathered and plucked carcass data from Budgey (2000). Convex hull density in birds also given for reference (closed triangles). doi:10.1371/journal.pone.0091691.g006

predefined by the soft tissue still present in the scan), and mass can be recorded directly from the carcass. As CT is becoming cheaper and easier to access, this is a promising area for further research. Furthermore, incorporating magnetic resonance imaging (MRI) data has the potential to illuminate interspecific variation in muscle and fat mass distribution around the skeleton that has been discussed in some detail here.

Conclusions

In summary, we have demonstrated that minimal convex hull volume (vol_{CH}) is an extremely good predictor of body mass in modern groups of non-primate mammals, primates and birds. Our models are characterised by low values for mean percentage prediction error (%PE) equivalent to those recently reported for bivariate regressions of limb bone dimensions [2,3] but with the added advantage of not relying upon single skeletal elements. We have highlighted the potential for the convex hulling method to be applied either solely for the purpose of estimating body mass in fossil species, or as a precursor to a functional biomechanical analysis for which body mass is a required input.

We have found, as expected, that the apparent densities of the convex hull objects calculated here are significant overestimates compared to published values of carcass density. This is due to the exclusion of ‘missing’ soft tissue held outside the contours of the skeleton from our calculations of volume. We have postulated on the possible sources of this missing soft tissue including muscle, integument and body fat, and present data collated from the literature regarding animal body density and composition. We believe this will be of interest to those working in the field of fossil reconstruction, particularly on saurischian dinosaurs and fossil birds.

The convex hulling method presented here sidesteps the requirement for soft-tissue reconstruction prior to mass estimation, and provides a straightforward means to conduct sensitivity analyses of the skeletal mount. However, user subjectivity is not entirely eliminated as decisions must still be made regarding the division of the skeleton into ‘functional’ units prior to convex hulling. The subdivision of the neck, tail and tarsal/phalanges is necessary to ensure a tight-fitting hull, yet requires some degree of user input. In studies focused upon a specific group with a shared body plan (such as ratites, [8]), this process is unlikely to effect the outcome of the calibration curve. However in studies incorporating species of differing bauplans, the way in which the skeleton is

References

- Schmidt-Nielsen K (1984) Scaling: Why is animal size so important? Cambridge: Cambridge University Press.
- Campione NE, Evans DC (2012) A universal scaling relationship between body mass and proximal limb bone dimensions in quadrupedal terrestrial tetrapods. *BMC Biol* 10: 60.
- Field DJ, Lymer C, Brown C, Darroch S (2013) Skeletal Correlates for Body Mass Estimation in Modern and Fossil Flying Birds. *PLoS One* 8: e82000. doi:10.1371/journal.pone.0082000.
- Smith RJ (2002) Estimation of body mass in paleontology. *J Hum Evol* 43: 271–287.
- Smith RJ (1993) Logarithmic transformation bias in allometry. *Am J Phys Anth.* 90: 215–228.
- Smith RJ (2009) Use and misuse of the reduced major axis for line-fitting. *Am J Phys Anth.* 140: 476–486.
- Packard GC, Boardman TJ, Birchard GF (2009) Allometric equations for predicting body mass of dinosaurs. *J Zool* 279: 102–110.
- Brassey CA, Holdaway RN, Packham AG, Anne J, Manning PL, Sellers WI (2013) More Than One Way of Being a Moa: Differences in Leg Bone Robustness Map Divergent Evolutionary Trajectories in Dinornithidae and Emeidae (Dinornithiformes). *PLoS One*. doi: 10.1371/journal.pone.0082668.
- Gregory WK (1905) The weight of the Brontosaurus. *Science* 22: 572.
- Colbert E (1962) The weights of dinosaurs. *Am Museum Novit*.
- Alexander RMN (1985) Mechanics of posture and gait of some large dinosaurs. *Zool J Linn Soc* 83: 1–25.
- Henderson DM (1999) Estimating the masses and centers of mass of extinct animals by 3-D mathematical slicing. *Paleobiol* 25: 88–106.
- Motani R (2001) Estimating body mass from silhouettes: testing the assumption of elliptical body cross-sections. *Paleobiol* 27(4): 735–750.
- Hutchinson JR, Ng-Thow-Hing V, Anderson FC (2007) A 3D interactive method for estimating body segmental parameters in animals: Application to the turning and running performance of *Tyrannosaurus rex*. *J Theor Biol* 246: 660–680.
- Allen V, Paxton H, Hutchinson JR (2009) Variation in center of mass estimates for extant sauropods and its importance for reconstructing inertial properties of extinct archosaurs. *Anat Rec* 292: 1442–1461.
- Bates KT, Manning PL, Hodgetts D, Sellers WI (2009) Estimating mass properties of dinosaurs using laser imaging and 3D computer modelling. *PLoS One* 4(2): e4532. doi:10.1371/journal.pone.0004532.
- Bates KT, Falkingham PL, Breithaupt BH, Hodgetts D, Sellers WI, et al. (2009) How big was “Big Al”? Quantifying the effect of soft tissue and osteological unknowns on mass predictions for *Allosaurus* (Dinosauria: Theropoda). *Palaeont Electron* 12: 14A.
- Sellers WI, Hepworth-Bell J, Falkingham PL, Bates KT, Brassey CA, Egerton VM, Manning PL (2012) Minimum convex hull mass estimations of complete mounted skeletons. *Biol Lett* 8: 842–845.

19. Sellers WI, Margets L, Coria RA, Manning PL (2013) March of the Titans: The Locomotor Capabilities of Sauropod Dinosaurs. *PLoS One* 8: e78733. doi:10.1371/journal.pone.0078733.
20. De Berg M, Cheong O, van Krevel M, Overmars M (2008) Computational Geometry: Algorithms and Applications. Heidelberg: Springerverlag Berlin Heidelberg.
21. Cornwell WK, Schiwill LDW, Ackery DD (2006) A trait-based test for habitat filtering: convex hull volume. *Ecology* 87: 1465–1471.
22. Liu R (2008) Convex Hull Covering of Polygonal Scenes for Accurate Collision Detection in Games. In: Proceedings of Graphics Interface 2008. Windsor, Ontario, Canada: Canadian Information Processing Society.
23. Crair TG (2000) Service network design in freight transportation. *Eur J Oper Res* 122: 272–288. doi:10.1016/S0377-2217(99)00233-7.
24. Falkingham PL (2012) Acquisition of high resolution three-dimensional models using free, open-source, photogrammetric software. *PaleoElectron* 15: 1T.
25. Auerbach BM, Ruff CB (2004) Human body mass estimation: a comparison of “morphometric” and “mechanical” methods. *Am J Phys Anth.* 125: 331–342. doi:10.1002/ajpa.20032.
26. Johanson DC, White TD (1979) A Systematic Assessment of Early African Hominids. *Science* 203: 321–330.
27. Brown F, Harris J, Leakey R, Walker A (1985) Early *Homo erectus* skeleton from west Lake Turkana, Kenya. *Nature* 316: 788–792.
28. Napier J, Davis P (1959) The fore-limb skeleton and associated remains of *Proconsul africanus*. *Foss Mamm Africa* 16: 1–69.
29. Moyà-Solà S, Kohler M, Alba DM, Casanovas-Vilar I, Galindo J (2004) *Pierolapithecus catalanunicus*, a New Middle Miocene Great Ape from Spain. *Science* 306: 1339–1344.
30. Franzen JL, Gingerich PD, Habersetzer J, Hurum JH, von Koenigswald W, Smith HB (2009) Complete primate skeleton from the Middle Eocene of Messel in Germany: morphology and paleobiology. *PLoS One* 4: e5723. doi:10.1371/journal.pone.0005723.
31. Hill W (1953) Primates: comparative anatomy and taxonomy. Vol. 1: Strepsirrhini. Edinburgh: Edinburgh University Press.
32. Scott KM (1990) Postcranial dimensions of ungulates as predictors of body mass. In: Damuth J, MacFadden BJ, editors. *Body size in mammalian paleobiology*. Cambridge: Cambridge University Press. 301–335.
33. Ruff CB (2003) Long bone articular and diaphyseal structure in old world monkeys and apes. II: Estimation of body mass. *Am J Phys Anth.* 120: 16–37.
34. Rosset A, Spadola L, Ratib O (2004) OsiriX: an open-source software for navigating in multidimensional DICOM images. *J Digit Imaging* 17: 205–216.
35. Barber CB, Dobkin DP, Huhdanpaa HT (1996) The Quickhull algorithm for convex hulls. *ACM Trans Math Softw* 22: 469–483.
36. Brassey CA, Kitchever AC, Withers PJ, Manning PL, Sellers WI (2013) The Role of Cross-Sectional Geometry, Curvature, and Limb Posture in Maintaining Equal Safety Factors: A Computed Tomography Study. *Anat Rec* 296: 395–413.
37. Arnason U, Gullberg A, Gretarsdottir S, Ursing B, Janke A (2000) The mitochondrial genome of the sperm whale and a new molecular reference for estimating eutherian divergence dates. *J Mol Evol* 50: 569–578.
38. Guha S, Goyal SP, Kashyap VK (2007) Molecular phylogeny of musk deer: A genomic view with mitochondrial 16S rRNA and cytochrome b gene. *Mol Phylogenet Evol* 42: 585–597.
39. Hasegawa M, Thorne JL, Kishino H (2003) Time scale of eutherian evolution estimated without assuming a constant rate of molecular evolution. *Genes Genet Syst* 78: 267–283.
40. Hassanin A, Douzery EJP (2003) Molecular and Morphological Phylogenies of Ruminantia and the Alternative Position of the Moschidae. *Syst Biol* 52: 206–228.
41. Hughes S, Hayden TJ, Douady CJ, Tougard C, Germonpré M, Stuart A, Lbova L, Carden RF, Hamni C, Sav L (2006) Molecular phylogeny of the extinct giant deer, *Megaloceros giganteus*. *Mol Phylogenet Evol* 40: 285–291.
42. Murphy WJ, Pringle TH, Crider TA, Springer MS, Miller W (2007) Using genomic data to unravel the root of the placental mammal phylogeny. *Genome Res* 17: 413–421.
43. Robinson TJ, Ropiquet A (2011) Examination of Hemiplasy, Homoplasy and Phylogenetic Discordance in Chromosomal Evolution of the Bovidae. *Syst Biol* 60: 439–450.
44. Thomas MG, Hagelberg E, Jones HB, Yang Z, Lister AM (2000) Molecular and morphological evidence on the phylogeny of the Elephantidae. *Proc R Soc B Biol Sci* 267: 2493–2500.
45. Finstermeier K, Zinner D, Bräuer M, Meyer M, Kreuz E, Hofreiter M, Roos C (2013) A mitogenomic phylogeny of living primates. *PLoS One* 8: e69504. doi:10.1371/journal.pone.0069504.
46. Burbidge ML, Colbourne RM, Robertson HA, Baker AJ (2003) Molecular and other biological evidence supports the recognition of at least three species of brown kiwi. *Conserv Genet.* 4: 167–177.
47. Brown J, Rest J, Garcia-Moreno J, Sorenson M, Mindell D (2008) Strong mitochondrial DNA support for a Cretaceous origin of modern avian lineages. *BMC Biol* 6: 6.
48. Phillips MJ, Gibb GC, Crimp EA, Penny D (2010) Tinamous and moa flock together: mitochondrial genome sequence analysis reveals independent losses of flight among ratites. *Syst Biol* 59: 90–107.
49. Lavin SR, Karasov WH, Ives AR, Middleton KM, Garland T Jr (2008) Morphometrics of the Avian Small Intestine Compared with That of Nonflying Mammals: A Phylogenetic Approach. *Physiol Biochem Zool* 81: 526–550.
50. Gartner GEA, Hicks JW, Manzani PR, Andrade D V, Abe AS, Wang T, Secor SM, Garland T Jr (2010) Phylogeny, Ecology, and Heart Position in Snakes. *Physiol Biochem Zool* 83: 43–54.
51. Schmidt M (2005) Hind limb proportions and kinematics: are small primates different from other small mammals? *J Exp Biol* 208: 3367–3383. doi:10.1242/jeb.01781.
52. Schmidt M (2008) Forelimb proportions and kinematics: how are small primates different from other small mammals? *J Exp Biol* 211: 3775–3789. doi:10.1242/jeb.019802.
53. Polk JD, Demes B, Jungers WL, Biknevicius AR, Heinrich RE, Runestad JA (2000) A comparison of primate, carnivore and rodent limb bone cross-sectional properties: are primates really unique? *J Hum Evol* 39: 297–325.
54. Mascaro J, Litton CM, Hughes RF, Uwoko A, Schnitzer SA (2011) Minimizing Bias in Biomass Allometry: Model Selection and Log-transformation of Data. 43: 649–653.
55. De Esteban-Trivigno S, Köhler M (2011) New equations for body mass estimation in bovids: Testing some procedures when constructing regression functions. *Mamm Biol* 76: 755–761. doi:10.1016/j.mambio.2011.07.004.
56. Taylor MP, Wedel MJ (2013) The effect of intervertebral cartilage on neutral posture and range of motion in the necks of sauropod dinosaurs. *PLoS One* 8: e78214. doi:10.1371/journal.pone.0078214.
57. Holliday C, Ridgely R, Sedlmayr J, Witmer L (2010) Cartilaginous Epiphyses in Extant Archosaurs and Their Implications for Reconstructing Limb Function in Dinosaurs. *PLoS One* 5: e13120.
58. Remes K, Unwin DM, Nicole K, Heinrich W-D, Hampe O (2011) Skeletal reconstruction of *Brachiosaurus branickii* in the Museum für Naturkunde, Berlin: Summarizing 70 years of Sauropod research. In: Klein N (Ed.) *Biology of the Sauropod Dinosaurs: Understanding the Life of Giants*. Bloomington: Indiana University Press. 305–316.
59. Currey JD (2003) How well are bones designed to resist fracture? *J Bone Miner Res* 18: 591–598.
60. Grand TI (1990) The functional anatomy of body mass. In: Damuth J, MacFadden BJ (Eds.) *Body size in mammalian paleobiology: Estimation and biological implications*. Cambridge: Cambridge University Press. pp. 39–47.
61. Videan EN, Fritz J, Murphy J (2007) Development of guidelines for assessing obesity in captive Chimpanzees (*Pan troglodytes*). *Zoo Biol* 26: 93–104. doi:10.1002/zoo.
62. Gill FB (2007) Ornithology. New York, NY: W. H. Freeman.
63. Currey JD, Alexander R (1985) The thickness of the walls of tubular bones. *J Zool* 206: 453–468.
64. Prange HD, Anderson JF, Rahn H (1979) Scaling of skeletal mass to body mass in birds and mammals. *Am Nat*: 103–122.
65. Dumont ER (2010) Bone density and the lightweight skeletons of birds. *Proc R Soc B Biol Sci* 277: 2193–2198.
66. Wedel MJ (2006) Origin of postcranial skeletal pneumaticity in dinosaurs. *Integr Zool* 1: 80–85. doi:10.1111/j.1749-4877.2006.00019.x.
67. O'Connor PM (2009) Evolution of archosaurian body plans: skeletal adaptations of an air-sac-based breathing apparatus in birds and other archosaurs. *J Exp Zool Part A Ecol Genet Physiol* 311A: 629–646.
68. Budge R (2000) The development of a substitute artificial bird by the International Birdstrike Research Group for use in aircraft component testing. International Bird Strike Committee, IBSC25/WP-IE3.
69. Turcek FJ (1966) On plumage quality in birds. *Ekol Pol* 14: 617–634.
70. Kendige SC (1970) Energy Requirements for Existence in Relation to Size of Bird. *Condor* 72: 60–65.
71. Greenewalt CH (1962) Dimensional relationships for flying animals. *Smithson Misc Collect* 144: 1–46.
72. Jasinoski SC, Russell AP, Currie PJ (2006) An integrative phylogenetic and extrapolatory approach to the reconstruction of dromaeosaur (Theropoda: Eumaniraptora) shoulder musculature. *Zool J Linn Soc* 146: 301–344. doi:10.1111/j.1096-3642.2006.00200.x.
73. Maxwell EE, Larsson HCE (2007) Osteology and Myology of the Wing of the Emu (*Dromaius novaehollandiae*), and Its Bearing on the Evolution of Vestigial Structures. *J Morphol* 268: 423–441. doi:10.1002/jmor.
74. McNab BK (1994) Energy Conservation and the Evolution of Flightlessness in Birds. *Am Nat* 144: 628–642.
75. Alexander RMN, Maloiy GMO, Njau R, Jayes AS (1979) Mechanics of the running of the ostrich (*Struthio camelus*). *J Zool Lond.* 187: 169–178.
76. Smith NC, Wilson AM, Jespers KJ, Payne RC (2006) Muscle architecture and functional anatomy of the pelvic limb of the ostrich (*Struthio camelus*). *J Anat.* 209: 765–779.
77. Patak A, Baldwin J (1993) Structural and metabolic characterisation of the muscles used for power running in the emu (*Dromaius novaehollandiae*), a giant flightless bird. *J Exp Biol.* 175: 233–249.
78. Hartman FA (1961) Locomotor mechanisms of birds. *Smiths Misc Coll.* 143: 1–91.
79. Reid B, Williams G (1975) The Kiwi. In: Kuschel G (Ed.) *Biogeography and Ecology in New Zealand*. The Hague: Dr W. Junk Publishers. 301–330.
80. Alexander R (1983) Allometry of the leg bones of moas (Dinornithes) and other birds. *J Zool* 200: 215–231.

81. Daan S, Masman D, Groenewold A (1990) Avian basal metabolic rates: their association with body composition and energy expenditure in nature. *Am J Physiol* 259: 333–340.
82. Morris CA, Harris SD, May SG, Jackson TC, Hale DS, Miller RK, Keeton JT, Acuff GR, Lucia LM, Savell JW (1995) Ostrich slaughter and fabrication: I. Slaughter yields of carcasses and effects of electrical stimulation on post-mortem pH. *Poult Sci* 74: 1683–1687.
83. Sales J, Navarro JL, Bellis L, Manero a, Lizurume M, Martella MB (1997) Carcass and component yields of rheas. *Br Poult Sci* 38: 378–380. doi:10.1080/00071669708418006.
84. Sales J, Horbanczuk J, Dingle J, Coleman R, Sensik S (1999) Carcase characteristics of emus (*Dromaius novaehollandiae*). *Br Poult Sci* 40: 145–147.
85. Wiresam R, Fagerlund T, Rosén M, Hedenstrom A (2008) Magnetic Resonance Imaging for Noninvasive Analysis of Fat Storage in Migratory Birds. *Auk* 125: 965–971. doi:10.1525/auk.2008.07145.
86. Kaiser A (1993) A New Multi-Category Classification of Subcutaneous Fat Deposits of Songbirds. *J F Ornithol* 64: 246–255.
87. Fowler ME (1991) Comparative clinical anatomy of ratites. *J Zoo Wildl Med*: 204–227.

5.9 Supporting Information

5.9.1 (S1) Literature values for bird and mammal body density

**5.9.2 (S2) Literature values for percentage contribution of feathers
to total body mass in birds**

Species	Density	Source	Notes
Mammals (ex. primates)			
<i>Equus ferus caballus</i>	893kg/m ³	(Buchner et al., 1997)	Weighted mean of segment densities (n=1)
<i>Bos primigenius</i>	1056kg/m ³	(Garrett, 1967)	Mean density of right half of beef steer carcass (n=48)
<i>Ovis aries</i>	912kg/m ³	(Garrett, 1967)	Mean carcass density (including fat) (7 studies)
<i>Sus scrofa</i>	943kg/m ³	(Garrett, 1967)	Mean carcass density (including fat) (6 studies)
<i>Mesocricetus auratus</i>	1049kg/m ³	(Kodama, 1971)	Mean carcass density of male hamsters (n=34)
<i>Phoca sibirica</i>	1140-1220kg/m ³	(Watanabe et al., 2006)	Estimated from terminal speed of Baikal seals (n=4)
<i>Zalophus californianus</i>	841-1275kg/m ³	(Luque and Auriol-Gamboa, 2002)	California seal pups, mean 17 days old (n=354)
Primates			
<i>Pan troglodytes</i>	1037-1110kg/m ³	(Crompton et al., 1996)	Segment densities excluding trunk (n=1)
<i>Pongo pygmaeus</i>	1030-1116kg/m ³	(Crompton et al., 1996)	Segment densities excluding trunk (n=1)
<i>Homo sapiens</i>	1049kg/m ³	(Shafer et al., 2010)	Male and female average of normal BMI (n=46)
Birds			
<i>Anser anser</i>	937kg/m ³	(Alexander, 1983)	Plucked carcass (n=1)
<i>Duck</i>	900kg/m ³	(Welty and Baptista, 1988)	(n=1)
<i>Flying birds</i>	730kg/m ³	(Hazelhurst and Rayner, 1992)	Unnamed species, plucked with inflated air-sacs (n=12)
<i>Coturnix japonica</i>	1053-1069kg/m ³	(Tservni and Yannakopoulos, 1988)	Plucked and eviscerated Japanese quail (n=80)
<i>Struthio camelus</i>	888kg/m ³	(Hutchinson et al., 2007)	Plucked trunk of ostrich (n=1)
<i>Laridae (gulls)</i>	940kg/m ³	(Wilson et al., 1992)	Whole feathered carcasses with air-sacs (n=5)
<i>Anatidae (dabbling ducks)</i>	980kg/m ³	(Wilson et al., 1992)	Whole feathered carcasses with air-sacs (n=6)
<i>Anatidae (diving ducks)</i>	990kg/m ³	(Wilson et al., 1992)	Whole feathered carcasses with air-sacs (n=3)
<i>Procellariidae (petrels)</i>	990kg/m ³	(Wilson et al., 1992)	Whole feathered carcasses with air-sacs (n=10)
<i>Alcidae (auks)</i>	1000kg/m ³	(Wilson et al., 1992)	Whole feathered carcasses with air-sacs (n=2)

Table 5.2: Supporting Information S1. Literature values for bird and mammal body density. The value for human body density was chosen from a recent study of healthy non-athletes (Shafer et al., 2010). An extensive literature exists on human body density values as a means of assessing body fat composition, but is beyond the scope of the present study. Caution should be exercised when interpreting the body density of domesticated farm animals in particular due to artificial selection for fat deposition. Furthermore, the studies listed below differ in both their methodology for estimating density (fluid displacement, volumetric models, kinematics), and the condition of the carcass (articulated vs. disarticulated, feathered vs. plucked, complete vs. eviscerated). Table continued overleaf.

Species	Density	Source	Notes
<i>Gaviidae (divers)</i>	1060kg/m ³	(Wilson et al., 1992)	Whole feathered carcasses with air-sacs (n=1)
<i>Spheniscidae (penguins)</i>	1020kg/m ³	(Wilson et al., 1992)	Whole feathered carcasses with air-sacs (n=2)
<i>Phalacrocoracidae (cormorants)</i>	1030kg/m ³	(Wilson et al., 1992)	Whole feathered carcasses with air-sacs (n=1)
<i>Gallus gallus</i>	894kg/m ³	(Allen et al., 2009)	Estimated from CT volumetric model (n=1)
<i>Gallus gallus domesticus</i>	953kg/m ³	(Allen et al., 2009)	Estimated from CT volumetric model (n=1)
<i>Gallus gallus domesticus</i>	918kg/m ³	(Hammershock et al., 1993)	Whole feathered carcasses (n=1)
<i>Quiscalus quiscula</i>	809kg/m ³	(Hammershock et al., 1993)	Whole feathered carcasses (n=1)
<i>Sturnus vulgaris</i>	776kg/m ³	(Hammershock et al., 1993)	Whole feathered carcasses (n=1)
<i>Passer domesticus</i>	751kg/m ³	(Hammershock et al., 1993)	Whole feathered carcasses (n=1)
<i>Molothrus ater</i>	750kg/m ³	(Hammershock et al., 1993)	Whole feathered carcasses (n=1)
<i>Anas platyrhynchos</i>	739kg/m ³	(Hammershock et al., 1993)	Whole feathered carcasses (n=1)
<i>Cathartes aura</i>	700kg/m ³	(Hammershock et al., 1993)	Whole feathered carcasses (n=1)
<i>Leucophaeus atricilla</i>	700kg/m ³	(Hammershock et al., 1993)	Whole feathered carcasses (n=1)
<i>Branta leucopsis</i>	669kg/m ³	(Hammershock et al., 1993)	Whole feathered carcasses (n=1)
<i>Columba livia</i>	648kg/m ³	(Hammershock et al., 1993)	Whole feathered carcasses (n=1)
<i>Larus delawarensis</i>	644kg/m ³	(Hammershock et al., 1993)	Whole feathered carcasses (n=1)
<i>Larus smithsonianus</i>	602kg/m ³	(Hammershock et al., 1993)	Whole feathered carcasses (n=1)

Supporting Information Table S1 cont.

Species	Common name	Feather (% M_b)	Source	Notes
Neognaths				
ACCIPITRIFORMES				
<i>Haliaeetus leucocephalus</i>	Bald eagle	12%	(Brodkorb, 1955)	Contour feathers
FALCONIFORMES				
<i>Falco tinnunculus</i>	Common kestrel	10.4%	(Daan et al., 1990)	Dry total feather mass
GRUIFORMES				
<i>Gallinula chloropus sandvicensis</i>	Hawaiian moorhen	3.5%	(DesRochers et al., 2010)	Total feather mass
<i>Fulica atra</i>	Eurasian coot	7.1%	(Daan et al., 1990)	Dry total feather mass
GALLIFORMES				
<i>Meleagris gallopavo</i>	Wild turkey	5.6%	(Schorger, 1966)	Total feather mass
<i>Gallus gallus domesticus</i>	Broiler chicken	5.8% (F) 6.0% (M)	(Leeson and Walsh, 2010)	Total feather mass
<i>Coturnix coturnix</i>	Common quail	4.7%	(Daan et al., 1990)	Dry total feather mass
PSITTACIFORMES				
<i>Melopsittacus undulatus</i>	Budgerigar	9.9%	(Wolf et al., 2003)	Total feather mass
<i>Agapornis sp.</i>	Lovebird	7.4%	(Wolf et al., 2003)	Total feather mass
CHARADRIIFORMES				
<i>Arenaria interpres</i>	Ruddy turnstone	7.4%	(Daan et al., 1990)	Dry total feather mass
<i>Pluvialis apricaria</i>	Golden plover	4.7%	(Daan et al., 1990)	Dry total feather mass
<i>Limosa lapponica</i>	Bar-tailed godwit	4.5%	(Daan et al., 1990)	Dry total feather mass
<i>Larus ridibundus</i>	Black-headed gull	10.1%	(Daan et al., 1990)	Dry total feather mass
<i>Haematopus ostralegus</i>	Eurasian oystercatcher	8.8%	(Daan et al., 1990)	Dry total feather mass
<i>Larus argentatus</i>	European herring gull	10.7%	(Daan et al., 1990)	Dry total feather mass
<i>Calidris maritima</i>	Purple sandpiper	15.6%	(Summers et al., 1992)	Contour feather mass
COLUMBIFORMES				
<i>Sturnopelia decaocto</i>	Eurasian collared dove	9.6%	(Daan et al., 1990)	Dry total feather mass
<i>Zenaidura macroura</i>	Mourning dove	7.7%	(Wetmore, 1936)	Contour feather mass
ANSERIFORMES				
<i>Aythya fuligula</i>	Tufted duck	4.8%	(Daan et al., 1990)	Dry total feather mass

Table 5.3: Supporting Information Table S2. Literature values for percentage contribution of feathers to total body mass in birds. Refer to the original source for sample sizes and further details of the methodology. Protocols differ in terms of weighing total feather mass (contour feathers plus down feathers) vs. contour feathers only; whether feathers are artificially dried prior to weighing; whether male and female plumage is considered separately or grouped. Table continued overleaf

Species	Common name	Feather (% M_b)	Source	Notes
<i>Anas platyrhynchos</i>	Mallard duck	6.4%	(Daan et al., 1990)	Dry total feather mass
<i>Anas platyrhynchos</i>	Mallard duck	6.0%	(Hopps, 2002)	Total feather mass
<i>Brannta bernicla</i>	Brant goose	8.0%	(Daan et al., 1990)	Dry total feather mass
<i>Aix sponsa</i>	Wood duck	5.3%	(Hopps, 2002)	Total feather mass
<i>Anas strepera</i>	Gadwall	6.5%	(Hopps, 2002)	Total feather mass
<i>Anas americana</i>	American wigeon	5.7%	(Hopps, 2002)	Total feather mass
<i>Anas discors</i>	Blue-winged teal	5.8%	(Hopps, 2002)	Total feather mass
<i>Anas carolinensis</i>	Green-winged teal	6.0%	(Hopps, 2002)	Total feather mass
<i>Aythya americana</i>	Redhead	5.3%	(Hopps, 2002)	Total feather mass
<i>Aythya collaris</i>	Ring-necked duck	5.1%	(Hopps, 2002)	Total feather mass
<i>Aythya affinis</i>	Lesser scaup	4.4%	(Hopps, 2002)	Total feather mass
<i>Lophodytes cucullatus</i>	Hooded merganser	5.1%	(Hopps, 2002)	Total feather mass
CAPRIMULGIFORMES				
<i>Chordeiles minor</i>	Eastern nighthawk	8.2%	(Wetmore, 1936)	Contour feather mass
APODIFORMES				
<i>Archilochus colubris</i>	Ruby-throated hummingbird	7.1%	(Wetmore, 1936)	Contour feather mass
PASSERIFORMES				
Tytonidae				
<i>Tyrannus tyrannus</i>	Eastern kingbird	7.5%	(Wetmore, 1936)	Contour feather mass
<i>Myiarchus crinitus</i>	Northern crested flycatcher	7.4%	(Wetmore, 1936)	Contour feather mass
<i>Empidonax virescens</i>	Acadian flycatcher	8.8%	(Wetmore, 1936)	Contour feather mass
<i>Contopus virens</i>	Eastern wood pewee	7.5%	(Wetmore, 1936)	Contour feather mass
Hirundinidae				
<i>Stelgidopteryx sp.</i>	Rough-winged swallow	5.8%	(Wetmore, 1936)	Contour feather mass
<i>Hirundo rustica</i>	Barn swallow	8.0%	(Wetmore, 1936)	Contour feather mass
Coridae				
<i>Cyanocitta cristata</i>	Northern blue jay	7.0%	(Wetmore, 1936)	Contour feather mass
<i>Pica pica</i>	Eurasian magpie	8.5%	(Daan et al., 1990)	Dry total feather mass
<i>Corvus monedula</i>	Western jackdaw	9.1%	(Daan et al., 1990)	Dry total feather mass
<i>Corvus corone</i>	Carriion crow	7.6%	(Daan et al., 1990)	Dry total feather mass
Paridae				
<i>Poecile carolinensis</i>	Carolina chickadee	6.9%	(Wetmore, 1936)	Contour feather mass

Supporting Information Table S2 cont.

Species	Common name	Feather (%M _b)	Source	Notes
<i>Parus major</i>	Great tit	9.7%	(Daan et al., 1990)	Dry total feather mass
<i>Poecile gambeli</i>	Mountain chickadee	4.1%	(Cooper, 2002)	Contour feather mass
<i>Baeolophus ridgwayi</i>	Juniper titmouse	5.3%	(Cooper, 2002)	Contour feather mass
Certhiidae				Contour feather mass
<i>Certhia americana</i>	Brown creeper	7.1%	(Wetmore, 1936)	
Troglodytidae				
<i>Troglodytes aedon</i>	Eastern house wren	5.3%	(Wetmore, 1936)	Contour feather mass
<i>Thryothorus ludovicianus</i>	Carolina wren	3.3%	(Wetmore, 1936)	Contour feather mass
<i>Cistothorus palustris</i>	Long-billed marsh wren	4.4%	(Wetmore, 1936)	Contour feather mass
Mimidae				
<i>Mimus polyglottos</i>	Mockingbird	7.0%	(Wetmore, 1936)	Contour feather mass
<i>Dumetella carolinensis</i>	Catbird	6.5%	(Wetmore, 1936)	Contour feather mass
<i>Torostoma rufum</i>	Brown thrasher	4.6%	(Wetmore, 1936)	Contour feather mass
Turdidae				
<i>Hylocichla mustelina</i>	Wood thrush	5.3%	(Wetmore, 1936)	Contour feather mass
<i>Catharus guttatus</i>	Eastern hermit thrush	7.4%	(Wetmore, 1936)	Contour feather mass
<i>Turdus merula</i>	Common blackbird	9.3%	(Daan et al., 1990)	Dry total feather mass
Regulidae				
<i>Regulus satrapa</i>	Eastern golden-crowned kinglet	11.1%	(Wetmore, 1936)	Contour feather mass
<i>Regulus calendula</i>	Eastern ruby-crowned kinglet	8.9%	(Wetmore, 1936)	Contour feather mass
Laniidae				
<i>Lanius ludovicianus</i>	Migrant shrike	6.1%	(Wetmore, 1936)	Contour feather mass
Vireonidae				
<i>Vireo griseus</i>	White-eyed vireo	5.2%	(Wetmore, 1936)	Contour feather mass
<i>Vireo flavifrons</i>	Yellow-throated vireo	6.0%	(Wetmore, 1936)	Contour feather mass
<i>Vireo olivaceus</i>	Red-eyed vireo	5.0%	(Wetmore, 1936)	Contour feather mass
Parulidae				
<i>Mniotilla varia</i>	Black and white warbler	4.4%	(Wetmore, 1936)	Contour feather mass
<i>Oreothlypis peregrina</i>	Tennessee warbler	6.5%	(Wetmore, 1936)	Contour feather mass
<i>Setophaga petiayumi</i>	Southern parula warbler	5.2%	(Wetmore, 1936)	Contour feather mass
<i>Setophaga magnolia</i>	Magnolia warbler	4.6%	(Wetmore, 1936)	Contour feather mass

Supporting Information Table S2 cont.

Species	Common name	Feather (% M_b)	Source	Notes
<i>Setophaga magnolia</i>	Magnolia warbler	4.6%	(Wetmore, 1936)	Contour feather mass
<i>Setophaga caerulescens</i>	Black-throated blue warbler	6.2%	(Wetmore, 1936)	Contour feather mass
<i>Setophaga virens</i>	Black-throated green warbler	6.5%	(Wetmore, 1936)	Contour feather mass
<i>Setophaga fusca</i>	Blackburnian warbler	4.5%	(Wetmore, 1936)	Contour feather mass
<i>Setophaga pensylvanica</i>	Chestnut-sided warbler	5.8%	(Wetmore, 1936)	Contour feather mass
<i>Setophaga castanea</i>	Bay-breasted warbler	5.0%	(Wetmore, 1936)	Contour feather mass
<i>Setophaga pinus</i>	Northern pine warbler	7.9%	(Wetmore, 1936)	Contour feather mass
<i>Seiurus aurocapilla</i>	Oven-bird	6.9%	(Wetmore, 1936)	Contour feather mass
<i>Pankezia motacilla</i>	Louisiana water-thrush	5.1%	(Wetmore, 1936)	Contour feather mass
<i>Geothlypis formosa</i>	Kentucky warbler	4.9%	(Wetmore, 1936)	Contour feather mass
<i>Opornis agilis</i>	Connecticut warbler	7.6%	(Wetmore, 1936)	Contour feather mass
<i>Geothlypis trichas brachidactyla</i>	Northern yellowthroat	6.0%	(Wetmore, 1936)	Contour feather mass
<i>Geothlypis trichas trichas</i>	Maryland yellowthroat	7.4%	(Wetmore, 1936)	Contour feather mass
<i>Icteria virens</i>	Yellow-breasted chat	6.0%	(Wetmore, 1936)	Contour feather mass
<i>Cardellina canadensis</i>	Canada warbler	8.5%	(Wetmore, 1936)	Contour feather mass
Passeridae				
<i>Passer domesticus</i>	House sparrow	5.3%	(Wetmore, 1936)	Contour feather mass
<i>Passer domesticus</i>	House sparrow	8.6%	(Daan et al., 1990)	Dry total feather mass
Icteridae				
<i>Aegithalos phoeniceus</i>	Eastern red-wing	5.2%	(Wetmore, 1936)	Contour feather mass
<i>Icterus spurius</i>	Orchard oriole	6.3%	(Wetmore, 1936)	Contour feather mass
<i>Quiscalus quiscula</i>	Purple grackle	7.1%	(Wetmore, 1936)	Contour feather mass
<i>Molothrus ater</i>	Eastern cowbird	4.6%	(Wetmore, 1936)	Contour feather mass
Cardinalidae				
<i>Piranga olivacea</i>	Scarlet tanager	6.2%	(Wetmore, 1936)	Contour feather mass
<i>Pheucticus ludovicianus</i>	Rose-breasted grosbeak	3.5%	(Wetmore, 1936)	Contour feather mass
<i>Passerina cyanea</i>	Indigo bunting	5.6%	(Wetmore, 1936)	Contour feather mass
Fringillidae				
<i>Carduelis tristis</i>	Eastern goldfinch	6.0%	(Wetmore, 1936)	Contour feather mass
<i>Serinus canaria domestica</i>	Canary	13.9%	(Wolf et al., 2003)	Total feather mass
Emberizidae				
<i>Pipilo erythrorththalmus</i>	Red-eyed towhee	7.4%	(Wetmore, 1936)	Contour feather mass

Supporting Information Table S2 cont.

Species	Common name	Feather (% M_b)	Source	Notes
<i>Passerulus sandwichensis</i>	Savannah sparrow	7.3%	(Wetmore, 1936)	Contour feather mass
<i>Ammodramus savannarum</i>	Grasshopper sparrow	5.5%	(Wetmore, 1936)	Contour feather mass
<i>Ammodramus henslowii</i>	Henslow's sparrow	6.2%	(Wetmore, 1936)	Contour feather mass
<i>Ammodramus sp.</i>	Sharp-tailed sparrow	5.4%	(Wetmore, 1936)	Contour feather mass
<i>Ammodramus maritimus</i>	Northern seaside sparrow	6.2%	(Wetmore, 1936)	Contour feather mass
<i>Poecetes gramineus</i>	Vesper sparrow	5.3%	(Wetmore, 1936)	Contour feather mass
<i>Spizella passerina</i>	Chipping sparrow	5.6%	(Wetmore, 1936)	Contour feather mass
<i>Spizella pusilla</i>	Field sparrow	7.2%	(Wetmore, 1936)	Contour feather mass
<i>Zonotrichia albicollis</i>	White-throated sparrow	6.8%	(Wetmore, 1936)	Contour feather mass
<i>Melospiza melodia</i>	Song sparrow	5.3%	(Wetmore, 1936)	Contour feather mass
<i>Junco hyemalis</i>	Dark-eyed junco	3.4-4.1%	(Swanson, 1991)	Dry total feather mass
Estrildidae				
<i>Poephila guttata</i>	Zebra finch	5.6%	(Daan et al., 1990)	Dry total feather mass
<i>Lonchura striata</i>	White-rumped munia	3.8%	(Daan et al., 1990)	Dry total feather mass
Muscicapidae				
<i>Erythacus rubecula</i>	European robin	9.0%	(Daan et al., 1990)	Dry total feather mass
<i>Saxicola torquata rubicula</i>	European stonechat	6.4%	(Klaassen, 1995)	Feather mass
<i>Saxicola torquata axillaris</i>	East African stonechat	7.2%	(Klaassen, 1995)	Feather mass
Maluridae				
<i>Malurus cyaneus</i>	Superb fairy-wren	3.6%	(Lill et al., 2006)	Dry contour mass
Palaeognaths				
<i>Apertyx sp.</i>	Kiwi	4.7-6.8%	(Reid and Williams, 1975)	Total feather mass
<i>Struthio camelus</i>	Ostrich	1.5% (F) 1.7% (M)	(Brand et al., 2010)	Total body feathers
<i>Struthio camelus</i>	Ostrich	1.9%	(Morris et al., 1995)	Feather mass
<i>Rhea americana</i>	Greater rhea	1.5%	(Sales et al., 1997)	Feather mass
<i>Rhea pennata</i>	Lesser rhea	1.8%	(Sales et al., 1997)	Feather mass
<i>Dromaius novaehollandiae</i>	Emu	1.7%	(Sales et al., 1999)	Feather mass

Supporting Information Table S2 cont.

5.10 Supporting Information References

- Alexander, R. (1983). Allometry of the leg bones of moas (Dinornithes) and other birds. *Journal of Zoology*, 200:215–231.
- Allen, V., Paxton, H., and Hutchinson, J. (2009). Variation in center of mass estimates for extant sauropsids and its importance for reconstructing inertial properties of extinct archosaurs. *Anatomical Record*, 292:1442–1461.
- Brand, T., Jordaan, J., Bhiya, C., and Aucamp, B. (2010). Effect of slaughter age and sex on the production output of south african black ostriches. *British Poultry Science*, 51:510–514.
- Brodkorb, P. (1955). Number of feathers and weights of various systems in a bald eagle. *Wilson Bulletin*, 67:142.
- Buchner, H., Savelberg, H., Schamhardt, H., and Barneveld, A. (1997). Inertial properties of dutch warmblood horses. *Journal of Biomechanics*, 30:653–658.
- Cooper, S. (2002). Seasonal metabolic acclimatization in mountain chickadees and juniper titmice. *Physiological and Biochemical Zoology*, 75:386–395.
- Crompton, R., Li, Y., Alexander, R., Wang, W., and Gunther, M. (1996). Segment inertial properties of primates: new techniques for laboratory and field studies of locomotion. *American Journal of Physical Anthropology*, 99:547–570.
- Daan, S., Masman, D., and Groenewold, A. (1990). Avian basal metabolic rates: their association with body composition and energy expenditure in nature. *American Journal of Physiology*, 259:333–340.
- DesRochers, D., Silbernagle, M., Nadig, A., and Reed, J. (2010). Body size, growth, and feather mass of the endangered hawaiian moorhen (*Gallinula chloropus sandvicensis*). *Pacific Science*, 64:327–333.
- Garrett, W. (1967). Experiences in the use of body density as an estimator of body composition in animals. In *Proceedings of the conference "Body Composition in Animals and Man"*, pages 170–185, Columbia. University of Missouri.

- Hamershock, D., Seamans, T., and Bernhard, G. (1993). Determination of body density for twelve bird species. Flight Dynamics Directorate, Wright Laboratory.
- Hazlehurst, G. and Rayner, J. (1992). Flight characteristics of triassic and jurassic pterosauria: an appraisal based on wing shape. *Paleobiology*, 18:447–463.
- Hopps, E. (2002). Information on waterfowl feather characteristics. *Transactions of the Illinois State Academy of Science*, 95:229–237.
- Hutchinson, J., Ng-Thow-Hing, V., and Anderson, F. (2007). A 3D interactive method for estimating body segmental parameters in animals: Application to the turning and running performance of *Tyrannosaurus rex*. *Journal of Theoretical Biology*, 246:660–680.
- Klaassen, M. (1995). Moult and basal metabolic costs in males of two subspecies of stonechats: the European *Saxicola torquata rubicula* and the East African *S. t. axillaris*. *Oecologia*, 104:424–432.
- Kodama, A. (1971). In vivo and in vitro and body water determinations of body fat in the hamster. *Journal of Applied Physiology*, 31:218–222.
- Leeson, S. and Walsh, T. (2010). Feathering in commercial poultry i. feather growth and composition. *World's Poultry Science Journal*, 60:42–51.
- Lill, A., Box, J., and Baldwin, J. (2006). Do metabolism and contour plumage insulation vary in response to seasonal energy bottlenecks in superb fairy-wrens? *Australian Journal of Zoology*, 54:23–30.
- Luque, S. and Aurioles-Gamboa, D. (2002). Estimation of body volume and body density in California sea lion pups. *Journal of the Marine Biological Association of the United Kingdom*, 82:1019–1022.
- Morris, C., Harris, S., May, S., Jackson, T., Hale, D., Miller, R., Keeton, J., Acuff, G., Lucia, L., and Savell, J. (1995). Ostrich slaughter and fabrication: 1. slaughter yields of carcasses and effects of electrical stimulation on post-mortem ph. *Poultry Science*, 74:1683–1687.

- Reid, B. and Williams, G. (1975). The kiwi. In Kuschel, G., editor, *Biogeography and Ecology in New Zealand*, pages 301–330. Dr W. Junk B.V., Publishers, The Hague.
- Sales, J., Horbaczuk, J., Dingle, J., Coleman, R., and Sensik, S. (1999). Carcase characteristics of emus (*Dromaius novaehollandiae*). *British Journal of Poultry Science*, 40:145–147.
- Sales, J., Navarro, J., Bellis, L., Manero, A., Lizurume, M., and Martella, M. (1997). Carcase and component yields of rheas. *British Journal of Poultry Science*, 38:378–380.
- Schorger, A. (1966). *The wild turkey. Its history and domestication*. University of Oklahoma Press, Norman.
- Shafer, K., Siders, W., Johnson, L., and Lukaski, H. (2010). Body density estimates from upper-body skinfold thicknesses compared to air-displacement plethysmography. *Clinical Nutrition*, 29:249–254.
- Summers, R., Underhill, L., Nicoll, M., Rae, R., and Piersma, T. (1992). Seasonal, size- and age-related patterns in body-mass and composition of purple sandpipers *Calidris maritima* in britain. *Ibis*, 134:346–354.
- Swanson, D. (1991). Seasonal adjustments in metabolism and insulation in the dark-eyed junco. *Condor*, 93:538–548.
- Tservni, A. and Yannakopoulos, A. (1988). Specific gravity, carcass fat and prediction of fatness in quail carcasses. *Journal of Agricultural Science*, 111:95–98.
- Watanabe, Y., Baranov, E., Sato, K., Naito, Y., and Miyazaki, N. (2006). Body density affects stroke patterns in baikal seals. *Journal of Experimental Biology*, 209:3269–3280.
- Welty, J. and Baptista, M. (1988). *The Life of Birds*. Centage Learning, Stanford.
- Wetmore, A. (1936). The number of contour feathers in passeriform and related birds. *Auk*, 53:159–169.

- Wilson, R., Hustler, K., Ryan, P., Burger, A., Christian, E., and Url, S. (1992). Diving birds in cold water: Do Archimedes and Boyle Determine energetic costs? *American Naturalist*, 140:179–200.
- Wolf, P., Rabehl, N., and Kamphues, J. (2003). Investigations on feathering, feather growth and potential influences of nutrient supply on feathers' regrowth in small pet birds (canaries, budgerigars and lovebirds). *Journal of Animal Physiology and Animal Nutrition*, 87:134–141.

Chapter 6

Discussion

The central issue addressed in my research has been the stress behaviour of hind limb long bones in both extant and extinct vertebrates. Phyletic, developmental, physiological and biomechanical processes control bone morphology, which in turn determines limb function. Various methodologies and analyses (i.e. scaling, phylogenetic comparative methods, finite element analysis and volumetric body mass reconstructions) were used to address limb bone biomechanics and make inferences regarding function. The results obtained from these studies can be summarised as follows:

1. Across a phylogenetically diverse sample, scaling of limb bone geometry alone is insufficient to achieve constant safety factors in the mammal femur and tibia and avian tibiotarsus under static loading. Some degree of postural modification is also required.
2. In the avian femur, static safety factors can be maintained by allometric scaling of bone geometry and postural modification is not required. It is unlikely that the maximum body size of modern birds is constrained by skeletal stresses induced by the subhorizontal orientation of the femur, and other factors must also be at work.
3. Classical beam theory equations and FEA diverge in their estimates of skeletal stress as a function of the underlying morphology of the bone in question. In long bones, the extent of this divergence is found to be significantly correlated with shaft curvature and cross-sectional asymmetry.

4. By applying a whole-body volumetric mass estimation technique, the body masses of two species of extinct flightless bird (the moa) are revised down compared to previously published values.
5. Under equivalent loading conditions simulated using FEA, the hind limb bones of the giant moa (*Dinornis robustus*) are found to be similarly/less robust than those of modern ratites. In contrast, stress levels in the hind limb of the Southern stout moa (*Pachyornis australis*) are found to be considerably lower than those of modern ratites.
6. New volumetric mass prediction equations for birds, primates and non-primate mammals are characterised by high correlation coefficients and low percentage prediction errors. Application of the convex hulling technique to the fossil record is considered to be justified when a large proportion of the skeleton is preserved.
7. Apparent body densities of primates and birds are found to scale allometrically with respect to body mass. This is interpreted in terms of variation in the ‘missing mass’ of soft tissue excluded from the convex hulling process, including muscle, fat and integumentary structures.

Whilst the body of work presented here comprises a series of stand-alone peer reviewed articles, several themes run throughout this thesis. These include the use of simplistic biomechanical models to simulate complex real-world biological systems, body mass as a necessary precursor to biomechanical models, the use of linear regressions techniques and the application of CT to imaging the vertebrate skeleton. The following discussion explores these themes, before concluding with suggestions for future areas of research.

6.1 Assumptions and interpretations of biological models

The relationship between skeletal form and function has been explored through a variety of modelling techniques. These have included mathematical models (classical beam theory, Chapter 2), computer-simulation based models (FEA, Chapters 3 and 4) and digital volumetric models (convex hulling, Chapters 4 and 5). However a unifying factor across all methodologies has been the creation of a simplified model to describe the properties and behaviour of a complex system (in this case, the vertebrate skeleton). When applying such models it is crucial to understand; (a) the assumption inherent within the model, and (b) the extent to which the results are representative of the ‘real-world’ system they seek to model.

In Chapter 2 for example, simple beam theory equations are applied in a novel way to estimate the maximum force a long bone is capable of withstanding before yield. Unlike previous applications of beam theory to long bones, shaft curvature is incorporated into our calculations. However other assumptions implicit in beam formulae, such as constant wall thickness, are upheld. As subsequently recognised in Chapter 3, long bones do not meet these assumptions. As a consequence, failure to account for this deviation in geometry away from ‘idealised’ slender beams can result in a change in rank order within a diverse interspecific sample. In Chapter 2, care is taken to *explicitly* state the assumptions and potential sources of error present in the model. Nonetheless, it is likely that the results presented in Chapter 2 do not accurately describe the situation present *in vivo* across all modern mammals and birds, due to the application of a simplified model to a small subset of species.

When undertaking modelling, it is crucial to select the technique most appropriate for the question under investigation. In Chapter 3, stress estimates produced by beam theory and FEA are compared in a methodological study. It is concluded that FEA should be the preferred modelling technique when stress values are to be estimated across a morphologically diverse sample of long bones. This is because FEA benefits from the incorporation of irregular bone

geometry into its results, and produces a strain map representing the distribution of strain across the whole skeletal element. However, following on from this conclusion, no suggestions are made regarding how best to interpret such results once such large dataset of FEA models has been generated.

In Chapter 4 for example, the robustness of ratite limb bones is quantified by sampling values of maximum stress located at the midshaft of FEA models. This is because a tool for rigorously comparing whole strain fields within- and between populations does not currently exist (Weber et al., 2011). We must therefore assume that stress values extracted at midshaft are informative of the behaviour of the whole FE model and can subsequently be used in comparative analyses. In doing so, potentially interesting patterns in strain distribution across the object are ignored.

In recent years geometric morphometric (GMM) methods have significantly improved our capacity to quantify and compare the output of FEA in terms of model deformation (O'Higgins et al., 2011). By describing the change in landmark configuration before and after loading, large scale patterns in deformation can be assessed. It is thus possible to statistically relate bone deformation to covariates of interest such as ecology, whilst accounting for phylogenetic history. This combination of GMM and FEA offers a promising tool for comparing the results of FEA from homologous locations on geometrically different models, and provides a means to answer previously difficult questions regarding *how* and *why* FE models differ.

In Chapters 2 and 4, beam models and FEA are used to quantify stress levels in hind limb bones. We assume a single force equivalent to a multiple of body mass is applied at the proximal condyles and only acts in one direction at a time. In reality, force is also applied via the action of numerous antigravity muscles attached at various locations along the element and pulling in multiple directions. The model chosen is therefore highly simplified. Yet, regardless of the approach used, a model will always be a simplification because the musculoskeletal system itself is so complex. A careful trade-off must therefore be made between model reductionism and realism, with the model assumptions keeping pace with (but not exceeding) our current state of understanding

(Hutchinson, 2011)

In Chapter 2 for example, scaling of long bone geometry and posture is explored as a potential means of maintaining bone stresses in larger species. However, a complementary mechanism for minimising the skeletal effects of increased body mass could be the modification of muscle and tendon attachment sites. Within Xenarthra, a distal shift in the location of the third trochanter (and the attached gluteus maximus muscle) between small armadillos and giant glyptodonts has been suggested as a means of reducing medial bending in larger animals (Milne and O'Higgins, 2012). Building upon Chapter 2, the same CT dataset could be used in a worthwhile investigation of the role of shifting muscle attachment sites in achieving constant safety factors under quasi-static loading across modern birds and mammals. However, assumptions would still need to be made regarding muscle properties and force vectors due to a lack of myological data for such a diverse sample. Recent work has found the results of biomechanical analyses to be highly sensitive to variation in muscle properties and force vectors (Gröning et al., 2013), and such a study is at risk of increasing model complexity at the cost of incorporating much greater uncertainty into the results.

6.2 Body mass in biomechanical modelling

An additional theme running throughout this thesis has been animal body mass. In particular, acquiring the mass of modern museum-curated specimens and estimating the mass of extinct species. Body mass is the most fundamental descriptor of an organism, and is a necessary precursor to almost all biomechanical models. Yet considerable difficulties were encountered throughout this project in obtaining mass values for use in subsequent beam theory and FE analyses of modern and fossil species

In terms of modern species, the majority of specimens included in this thesis originated from the osteological collections of natural history museums (National Museums Scotland, Manchester Museum, The World Museum Liverpool, Cambridge Museum of Zoology, Oxford University Museum of Natural History). These museums differ (or have previously differed) in their approach to specimen acquisition, and as such conferred contrasting problems with regards to body mass.

By virtue of their age, wild caught specimens collected opportunistically in the 19th to mid-20th century still comprise the majority of natural history museums' collections (Winker, 2004), with specimens accumulated during early exploration trips and later by trophy hunters. Figure 6.1 illustrates the frequency of specimen acquisition across various U.K. natural history museums, using the genus *Cervus* as an example. Oxford and Cambridge's collections are dominated by specimens acquired prior to 1950, whilst the Natural History Museum, London has collected consistently throughout the 20th century (Figure 6.1).

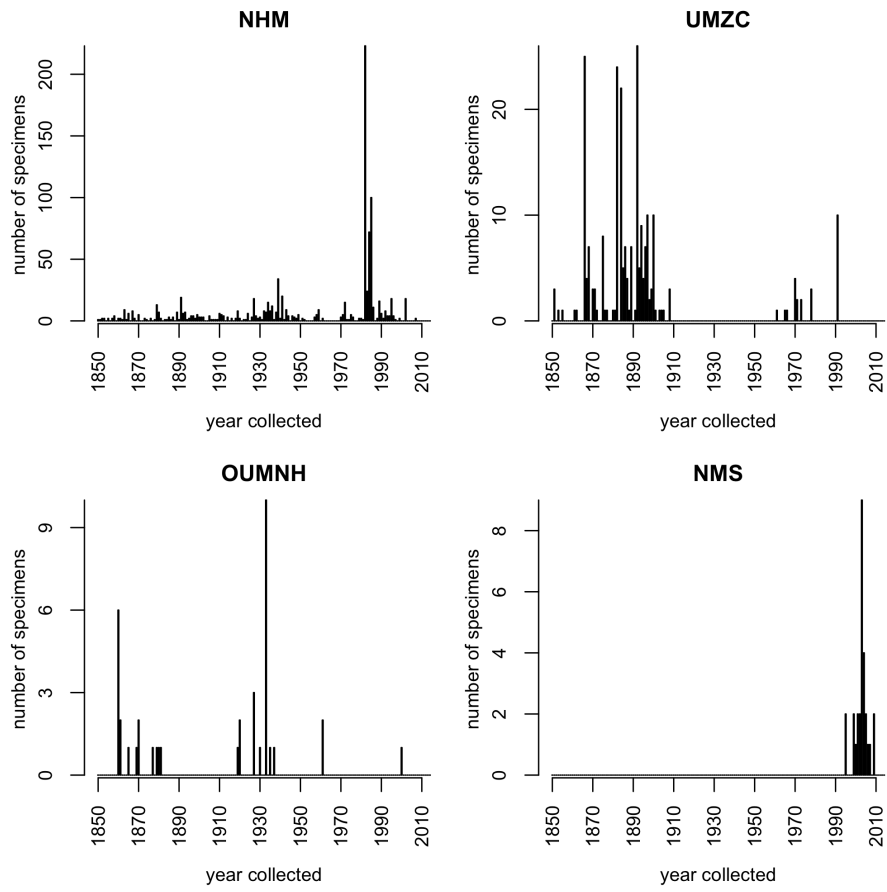


Figure 6.1: Acquisition of specimens belonging to the genus *Cervus* across several U.K. natural history museums. Data presented refers to the total number of specimens of genus *Cervus* acquired in a given year. Data sourced from online collection catalogues for the Natural History Museum (Natural History Museum, 2014, NHM), University Museum of Zoology, Cambridge (University Musuem of Zoology Cambridge, 2014, UMZC) and Oxford University Museum of Natural History (Oxford Museum of Natural History, 2014, OUMNH). Data for National Museum of Scotland (NMS) provided by Andrew Kitchener (*pers. comm*) Note the frequent spikes in specimen acquisition, correlated to specific research projects and intensive efforts to catalogue previously accessioned specimens.

Older zoological specimens rarely possess an associated body mass, either due to difficulties associated with weighing in the field, a lack of interest in body mass by those involved in the collection process or the data may simply have been misplaced. Furthermore, variation in stomach content, intestinal content and hydration can considerably affect body mass (wild elephant mass is subject to daily fluctuations of 15%, Roth, 1990) and is difficult to quantify in wild

specimens. However wild caught specimens have the advantage of being more likely to possess a percentage body fat composition within the ‘healthy’ range compared to captive individuals (Videan et al., 2007).

A minority of U.K. museums are now actively collecting captive specimens from zoos and aquaria. Under the impetus of Dr Andrew Kitchener, National Museum Scotland in Edinburgh is particularly efficacious in terms of collecting carcasses from zoos across the U.K (see Figure 6.1). Fortunately, as part of their veterinary treatment, zoo animals are more likely to have had their weight measured and recorded and this information is frequently available in museum records (see Figure 6.2). However, captive individuals are also more likely to be overweight compared to wild caught animals (Videan et al., 2007), and the last-recorded value for body mass can capture sudden illness-related wastage prior to death.

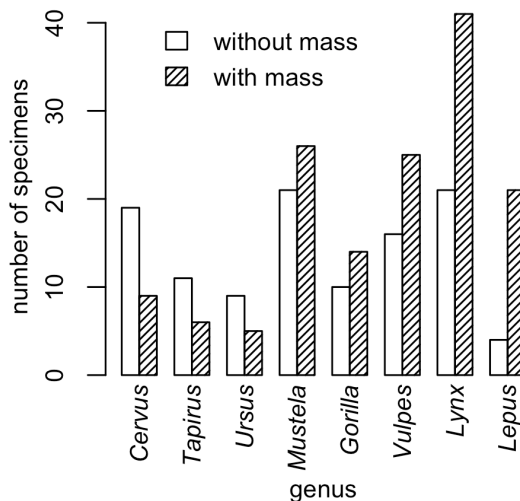


Figure 6.2: Eight genera of mammals chosen to illustrate the proportion of specimens possessing an associated body mass in the NMS collection. In comparison to NMS, no specimens of the above genera were found with associated body mass in the online collections of NHM, UMZC or OUMNH. Data collection as in Figure 6.1

The problem of missing body mass values was addressed in several ways within this thesis. In Chapter 2, specimens without an associated mass were assigned average values from the literature. If gender and geographic origin were known, efforts were made to obtain more specific average values. This approach,

although far from ideal, remains the only viable option when dealing with such large datasets for which mass is not available. In Chapter 4, our modern ratite dataset was considerably smaller and it was therefore feasible to generate species-specific regressions to estimate body mass. Yet in some instances (*Casuarius casuarius*, for example), a lack of published anatomical data resulted in calibration curves based upon extremely small samples and mass estimates that were still possibly unreliable. Finally, when zoo specimens did possess complete body mass records, the data was checked to ensure the last recorded mass did not indicate sudden weight loss prior to death.

The collection policy adopted by a natural history museum is heavily influenced by its individual curators. The large number of *Lynx* specimens with associated body mass acquired by the National Museum Scotland (Figure 6.2) for example, reflects the research interests of the principal curator. In order to improve the research potential of collections, it is therefore essential for scientists and museum staff to work together closely. Research scientists have a responsibility to foster collaborations with natural history museums to ensure collections remain research active and to highlight the importance of collecting metadata alongside specimens. In some instances, this data already exists in one form but has not been entered into a museum database, making it impossible to search for specimens on the basis of associated body mass. When resources for curation are limited, it may therefore be prudent to consider incorporating collections databasing into funding proposals (Lister, 2011). Both sides have obligations however, and curators also have the responsibility to prioritise collections with research potential and to keep abreast of methodological advances applicable to their collections.

The aforementioned difficulty in obtaining body mass in *modern* species also raises concerns regarding the endeavour to predict the mass of *fossil* species. In order to derive a useful mass estimation tool, a modern dataset is first required for which mass values are already known. In Chapters 4 and 5 a novel volumetric technique for estimating fossil body mass is presented which benefits from incorporating the maximum amount of information from the skeleton, and which is less susceptible to biasing by robust or gracile skeletal elements than those based on isolated bones. Yet in both chapters, it was still necessary to

first estimate the mass of some modern individuals before the calibration equation could be derived.

In Chapter 4 a ratite-specific mass prediction equation is generated using mounted skeletons from UMZC. As often the case throughout this project, no values for body mass were available for mounted display specimens. Mass was instead estimated using species-specific regressions derived from the literature. In contrast, the primate-specific mass prediction equation presented in Chapter 5 was based upon CT data. By virtue of being CT scanned, all specimens date from within the last two decades and were captive animals subject to medical treatment and body mass is therefore available for most individuals. As CT scanning is becoming cheaper and easier to access, the methodology applied to primates in Chapter 5 has the potential to become widely adopted as a new volumetric mass prediction technique (see Section 6.5.1 for future applications to the reconstruction of the dodo). Furthermore, the importance of carrying out sensitivity analyses as part of biomechanical studies is emphasised throughout Chapters 4 and 5. A mass estimation technique based on CT will provide a means of quantifying variation in trunk morphology (such as scapula placement, sternal position and rib cage flaring) across modern species, and may therefore place bounds upon these variables in fossil skeleton reconstructions.

6.3 Linear regressions in comparative anatomy

A uniting factor across all data chapters presented within this thesis has been the use of regressions analysis. A regression simply seeks to understand how the value of one variable (the ‘dependent’ variable) changes when another variable (the‘independent’ variable) is changed. In the context of this thesis, regression analysis has been applied to three distinct problems:

1. In Chapter 3 we test the hypothesis that the extent to which two models (beam theory vs. FEA) differ in their stress estimates is correlated to bone morphology. In this instance, regression analysis is used to test for a ‘significant’ relationship between two variables.
2. In Chapters 4 and 5, the relationship between body volume and mass is explored as a potential body mass estimation technique. Here the interest lies not only in a correlation *existing*, but in the strength of the correlation as an indication of the usefulness of a mass prediction equation.
3. In Chapter 2, the *scaling exponent* of regression analyses is explored as means of quantifying changes in bone geometry associated with increased body mass.

Most regression analyses carried out in this thesis therefore include body mass as a variable. Whether body mass is considered the dependent or independent variable is a function of the question being asked. The issue of which variables to assign to the X and Y axes ultimately boils down to: (a) assumptions concerning the distribution of error between said axes and (b) the asymmetry of the commonly-used ordinary least squares (OLS) method causing the slope of the line to differ depending on which variables are assigned to X and Y .

OLS is a least squares method, in that a ‘line of best fit’ is one that minimises the sum of squares of residuals. Specifically, OLS minimises the sum of the vertical deviations of the data points from the line. In OLS, all variation not explained by the line is represented as errors in the observed values of Y . Therefore all error is attributed to Y -axis measurements, and values for the X -axis are assumed to be known without error. This was not a concern in Chapter 3, as an obvious cause-effect relationship made it clear which variables

should be assigned to X and Y , and the X variables could be measured with minimal error.

OLS is also considered the most appropriate regression technique to use for generating predictive equations and was used in this capacity in Chapters 4 and 5. However, the asymmetrical nature of OLS does result in a philosophical dilemma when applied in a predictive sense (Smith, 2009). For example, consider the two variables; body mass and femur diameter. If we accept that the direction of causation is such that animals with a larger body size tend to possess larger skeletal structures, the ‘classical’ calibration (Konigsberg et al., 1998) would have femur diameter as the dependent variable, and mass as the independent variable. However if we were to use femur diameter to predict body mass, convention dictates that equations are calculated in the form in which they are to be used (Smith, 2009) with mass as the dependent variable (i.e. an ‘inverse calibration’). Therefore given one dataset and one ‘true’ relationship between variables, two different estimates of body mass can be generated depending upon whether a classic or inverse OLS equation is used.

Reduced major axis (RMA; also known as standardised major axis, SMA) is a type-II least squares method commonly employed as an alternative to OLS. RMA utilises a different definition of residuals from OLS in which the product of the X and Y deviations from the line is minimised, and hence errors may be attributed to both X and Y variables. For this reason it was deemed appropriate to apply RMA in Chapter 2, as measurement error was introduced in both the X (literature assigned body masses) and Y (CT derived measures of bone geometry) variables (Warton et al., 2006). RMA is also a symmetrical least squares method, in that two RMA slopes are exact reciprocals of each other when the axes are inverted. RMA is therefore appropriate to use when the decision of which variables to assign to X and Y is arbitrary i.e. there is no obvious cause-effect relationship.

A specialised case of linear regression involves interspecific biological datasets for which data points can no longer be treated as independent due to phylogenetic relationships. In such instances, the most commonly used approach is to calculate phylogenetically independent contrasts (Felsenstein,

1985; Harvey and Pagel, 1991). Independent contrasts (ICs) are calculated as the difference in trait values between two adjacent nodes or terminal taxa in the phylogenetic tree divided by the square root of the sum of their branch lengths, and are statistically independent from one another. Contrasts calculated for X and Y variables may then be subsequently regressed against one another using either type I or type II models without violating assumptions of statistical independence.

When IC is applied to estimate the relationship between two variables, the line must be forced through the origin as the intercept of the relationship between two contrasts should theoretically equal zero (Felsenstein, 1985) . Phylogenetic generalised least squares (PGLS) is an alternative phylogenetic correction technique which utilises the same phylogenetic information as IC and produces the same results (Garland Jr and Ives, 2000). Unlike IC however, the PGLS regression model is identical to the standard uncorrected OLS model except for the structure of the error term. In PGLS, a phylogenetic distance matrix calculated from the input phylogeny is incorporated into the variance and covariance of the error term. The benefit of PGLS is therefore that it transforms a phylogenetically-biased regression into a standard OLS model, producing a value for the intercept and allowing diagnostic tests such as those for normality and differences in slope or intercept to be carried out. In contrast, diagnostics for regressions through the origin are less well developed (Garland Jr and Ives, 2000).

Given the prevalent use of IC and PGLS in the biological literature, some authors have raised concerns regarding the ‘hegemony’ of phylogenetic corrections (PC):

"[T]he belief seems to have become very widespread that PC should be automatic and obligatory" (Westoby et al., 1995, pg. 531).

whilst others have compared phylogenetically-corrected and -uncorrected results and found no difference, suggesting:

"If a data set is reasonably diverse phylogenetically (i.e. has a high ratio of number of clades to number of species) and exhibits

reasonably strong correlation, phylogenetic analysis is unlikely to alter conclusions" (Weathers and Siegel, 1995, pg. 539).

PGLS was applied in Chapters 2 and 5 of this thesis as a means of correcting for shared ancestry. In both cases, PGLS equations were published alongside uncorrected OLS equations to facilitate comparisons with previously published models. In all instances, application of PGLS resulted in slope values similar to those of OLS and did not alter the interpretation of the dataset. Furthermore, tests of the relative quality of the PGLS vs. OLS models (such as the Akaike Information Criterion, AIC) consistently favoured the uncorrected model.

In summary, the application of uncorrected OLS remains widespread in the field of biometrics. Yet authors and reviewers are becoming increasingly aware of alternative methodologies and diagnostics that may be more appropriate for the particular problem at hand. This was borne out in the feedback we received during peer review, in which considerable attention was paid to our choice of regression models and statistics. Whilst such enthusiasm for statistics shown by biologists should be encouraged, there is a danger that new statistical techniques become the paradigm when traditional methods may in fact be preferable. Blind application of Type II regressions or phylogenetic corrections without understanding the underlying principles and limitations is equally, if not more, problematic than simply using OLS.

6.4 The application of X-ray imaging to vertebrate morphology

Finally, the technique of computed tomography was applied throughout this project as a means of visualizing the 3D geometry of the vertebrate skeleton. Originally developed as a clinical diagnostic tool, the application of CT to non-human comparative anatomy has increased dramatically in the last decade. CT has many advantages over traditional planar x-ray, the foremost being the ability to visualize internal structures in 3D. This was exploited in Chapter 2, in which CT was used to generate a large dataset from which cross-sectional geometric properties of long bones could be discerned. The resulting CT dataset can also be used to generate 3D models which form the basis of further morphometric and biomechanical analyses. In Chapter 5, whole body primate CT scans were used to generate simple convex hulls models. In Chapters 3 and 4, more complex 3D FEA models were derived from CT scans of long bones.

However, as discussed in Sections 6.1 and 6.3, it is essential that the technique being applied is appropriate for the question under investigation. In the case of CT, the resolution of the scan must be sufficient to resolve the features of interest. As a rule of thumb, only features $2-5 \times$ the voxel size will be reliably distinguished (Abel et al., 2012). CT is a multiscale imaging technique, and therefore the CT facilities used throughout this thesis varied according to the size of the object in question. For the cortex of smaller long bones, μ -CT scanning operating at a resolution of $10-100\mu\text{m}$ was employed, whilst larger individuals were scanned at a courser resolution of $200-800\mu\text{m}$ in a helical veterinary scanner. If details of bone microstructure or trabecular architecture were required, the resolution would need to drop further and/or the sample be reduced in size (see Section 6.5.3).

In some situations, CT may still be the preferred technique when details of internal structure are not required. In Chapter 5 the complete disarticulated skeletons of *D. robustus* and *P. australis* were CT scanned, despite FEA being carried out only on hind limb material. In this instance, the surface geometry of the skeleton required for convex hulling was easier to obtain from medical CT

than by the time-consuming surface laser scanning techniques currently available. Multiple skeletal elements may be CT scanned simultaneously, and both dorsal and ventral surfaces are captured in a single scan (as opposed to stage-based surface laser scanning). Yet in situations when specimens are oversized and/or articulated, laser scanning and photogrammetry remain the only viable technique.

In common with other ‘big data’ techniques (such as genome sequencing, or high energy particle physics), CT suffers from difficulties associated with the sharing of data. Files are generally too large to share peer-to-peer and must instead be made available for download online, either on personal websites (www.animalsimulation.org in the case of Chapters 4 and 5), or via formal data repositories (Data Dryad in Chapter 3). A selection of repositories specific to comparative anatomy do exist (Aves3D for bird skeletal models, NESPOS for Pleistocene fossils, DigiMorph and Morphobank for a wide variety of modern and fossil skeletons). However data are often presented in interactive 3D viewers and are not available for download, and hence cannot be truly ‘open-access’. Furthermore no agreement exists on the format in which data should be shared, nor is there any formal requirement to share CT data at all.

This lack of data availability ties into concerns regarding the replicability of CT-based studies. The data sharing policies of high-profile open-access journals such as PLoS ONE require that the ‘minimal dataset’ used to reach the manuscript’s conclusions are made openly available. Yet this explicitly *does not* include the raw image files of any CT study. The thresholding and masking of CT datasets are the most time-consuming and subjective aspects of segmentation (Abel et al., 2012) and any resulting model is a product of the user’s prior knowledge of anatomy. By only making available the processed 3D meshes, the quality of the original CT dataset remains hidden and the extent of smoothing and mesh repair is unknown. Given the widespread availability of data repositories and supplementary material, a *minimum* requirement should be for authors to provide an extended methodology with details of the segmentation process. Far preferable would be for raw CT datasets be published alongside articles, giving others the opportunity to replicate the author’s segmentation procedure.

6.5 Future work

6.5.1 How fat was the Dodo?

In Chapter 4, the convex hulling technique is applied to estimate the body mass of the extinct flightless bird, the moa. Previous mass prediction equations based upon single skeletal metrics such as long bone diameter or circumference are deemed unsuitable for this purpose, given the disproportionately robust nature of some moa limb bones. Elsewhere, ‘over-development’ of the pelvic apparatus has been found to be significantly correlated with the flightless condition across a diverse sample of palaeognaths and neognaths (Cubo and Arthur, 2000). The applicability of mass prediction equations based solely on hind limb material to flightless avian taxa more generally may therefore be questioned.

For example the skeletal anatomy of the extinct flightless Columbiformes, the dodo (*Raphus cucullatus*) and solitaire (*Pezophaps solitaria*) is comparatively well known, and their pelvic anatomy has indeed been thoroughly investigated. Hind limb bones of *R. cucullatus* and *P. solitaria* have been found to be both considerably shorter and thicker than those of their flighted relatives (Livezey, 1993). Yet, similar to the situation described in Chapter 4 pertaining to moa, previous attempts to estimate the body mass of the dodo have relied upon predictive equations derived solely from hind limb metrics of extant species.

CT scanning of 20 species of modern Columbiformes has been undertaken, including the largest extant pigeon (Victoria crown pigeon, *Goura victoria*) and the close relative of the dodo and solitaire (Nicobar pigeon, *Caloenas nicobarica*) from which a convex hull calibration curve for modern pigeons will be derived. In collaboration with Dr Andrew Kitchener (National Museums Scotland, Edinburgh), LiDAR scans of both dodo and solitaire mounted skeletons have been obtained from which volumetric mass estimates will be derived (Figure 6.3). In doing so, we hope to provide meaningful body mass values with considerably narrower confidence intervals for use in subsequent biomechanical, physiological and life history studies.

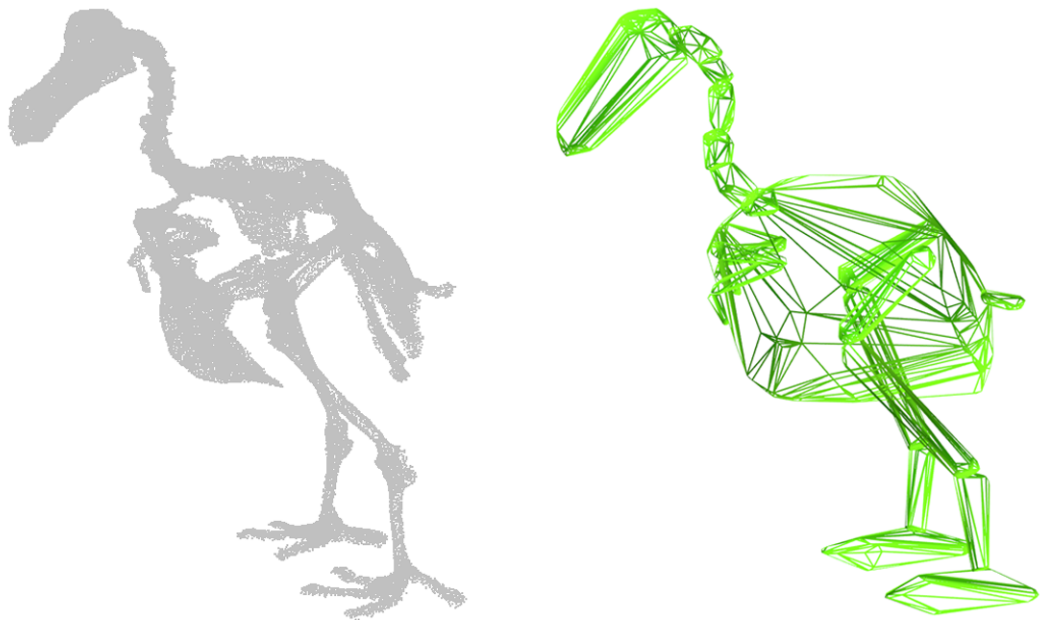


Figure 6.3: LiDAR data of the Edinburgh dodo (*R. cucullatus*). Left, point cloud; right, convex hulls fitted to point cloud data.

6.5.2 Analysis of moa hind limb muscle moment arms

The moment arm of a muscle affects its force-generating capacity, and as such is an important determinant of its function in the vertebrate skeleton. Muscle moment arms are therefore useful when attempting to reconstruct the way in which animals stood and moved (Hutchinson et al., 2005) and have been widely applied to fossil taxa to quantitatively compare locomotor anatomy, with dinosaurs being particularly well studied (Hutchinson et al., 2005; Bates and Schachner, 2011; Bates et al., 2012; Maidment et al., 2013).

Building upon the work of Chapter 5, an analysis of hind limb muscle moment arms in fossil moa is proposed. Articulated 3D models of the skeletons of *Dinornis robustus* and *Pachyornis australis* have already been created (Figure 4.3). A detailed myology of the *Dinornis robustus* hind limb has recently been published by Zinoviev (2013) (Figure 6.4) with whom we are collaborating to generate an additional myology for *Pachyornis australis*. Moment arm analysis will be carried out in GaitSym and the results compared to pre-existing moment arm values for modern ratites (Hutchinson, 2004; Smith et al., 2007) in order to shed new light upon stance and gait in this group of extinct giant birds. The role of prominent features, such as the enlarged cnemial crest on the cranial side of the proximal tibiotarsus (insertion for knee extensor musculature) particularly evident in *Pachyornis australis*, will be discussed in light of the mechanical advantage conferred.

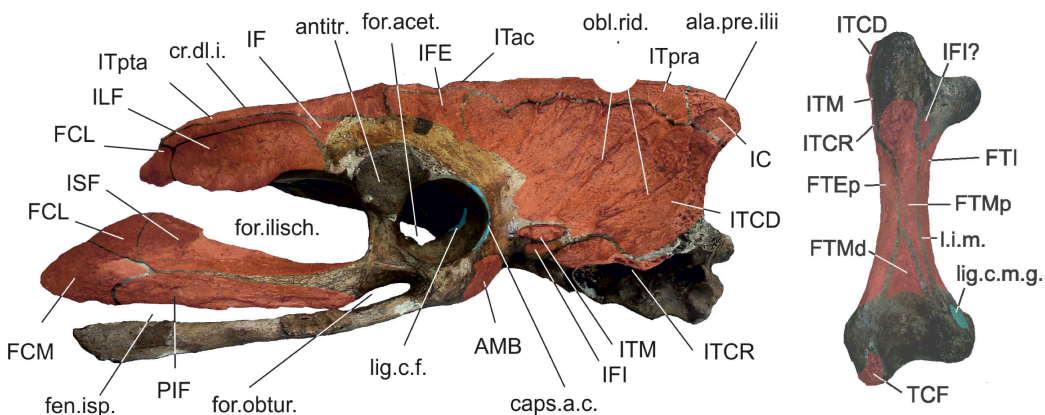


Figure 6.4: Myology of pelvis and femur of *D. robustus*. Origin and insertion of muscles shown in red, ligaments in blue. For abbreviations see Zinoviev (2013)

6.5.3 Whole bone strain mapping of murine tibiae: Rapid-scan computed tomography and digital volume correlation

The finite element method is an extremely useful technique for estimating strain in complex biological structures. However FEA must be validated against experimental data in order to quantify the sources and magnitudes of error incorporated into our models. Digital speckle pattern interferometry (DSPI) is an optical technique used for non-contact, whole-field measurements of displacement from which principal strains may be calculated and compared to FEA predictions. DSPI has been applied to skeletal material as a means of *ex vivo* validation of FE models (Yang et al., 2007; Panagiotopoulou et al., 2010, 2012) and has the advantage of estimating the strain field across whole skeletal elements. DSPI does not, however, make it possible to visualise strains within internal structures such as trabecular bone and the endosteal surface.

Recently, this technique has been applied alongside high-resolution CT to estimate full volume displacement during step-wise loading in 'Digital Volume Correlation' (DVC). This method has the advantage of imaging internal structures that would otherwise be masked by the periosteal surface, and has been successfully applied to estimate strain in trabecular bone (Gillard et al., 2014) and whole vertebrae (Hussein et al., 2012). Whilst DIC has been applied to map the *surface* strain levels across intact mice tibia (Sztefek et al., 2010), DVC has yet to be applied to whole long bones to map strain *within* the cortex.

We have carried out trials using the loading rig illustrated in Figure 6.5 on excised mouse tibiae. Long bones fail at midshaft as predicted under 4-point bending (Figure 6.6). However CT scan resolution has thus far proved too low to conduct DVC. Future work will focus upon improving the rig and scanning protocol to increase the scan resolution. A new rig is being developed in which the top and bottom loading platons are suspended and driven independently, removing the need for the supporting polycarbonate cylinder. In addition, the current 5kN load cell will be replaced with a smaller load cell appropriate for biological samples. The new rig will be designed such that it may also be used with synchrotron radiation-based micro CT (SR- μ CT), ensuring the set-up can be moved between the Henry Moseley facility and the Diamond Light Source.



Figure 6.5: In-situ loading rig for 4D CT scanning. Left, extent of the rig including load cell (top of figure). Right, detail of the 4-point bending set-up. Note the polycarbonate cylinder surrounding the apparatus.

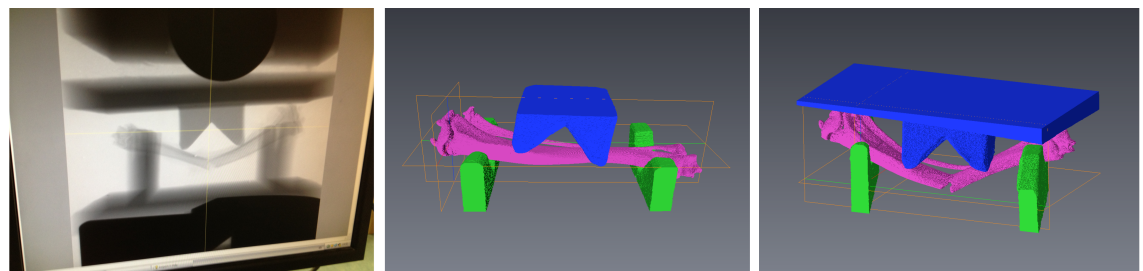


Figure 6.6: 4-point bending of mouse tibia. Far left, radiograph during scanning; centre, intact bone prior to loading; far right, bone fractured at midshaft.

6.6 References

- Abel, R., Laurini, C., and Richter, M. (2012). A palaeobiologist's guide to 'virtual' micro-ct preparation. *Palaeontologica Electronica*, 15:15.2.6T.
- Akça, K., Çehreli, M., and İplikçioğlu, H. (2002). A comparison of three-dimensional finite element stress analysis with *in vitro* strain gauge measurements on dental implants. *The International Journal of Prosthodontics*, 15(2):115–121.
- Bates, K. T., Benson, R. B. J., and Falkingham, P. L. (2012). A computational analysis of locomotor anatomy and body mass evolution in Allosauroidea (Dinosauria: Theropoda)". *Paleobiology*, 38(3):486–507.
- Bates, K. T. and Schachner, E. R. (2011). Disparity and convergence in bipedal archosaur locomotion. *Journal of The Royal Society Interface*, 9(71):1339–1353.
- Cubo, J. and Arthur, W. (2000). Patterns of correlated character evolution in flightless birds: a phylogenetic approach. *Evolutionary Ecology*, 14(8):693–702.
- Felsenstein, J. (1985). Phylogenies and the comparative method. *American Naturalist*, 125:1–15.
- Garland Jr, T. and Ives, A. (2000). Using the past to predict the present: confidence intervals for regression equations in phylogenetic comparative methods. *American Naturalist*, 155:346–364.
- Gillard, F., Boardman, R., Mavrogordato, M., Hollis, D., Sinclair, I., Pierron, F., and Browne, M. (2014). The application of digital volume correlation (DVC) to study the microstructural behaviour of trabecular bone during loading. *Journal of the Mechanical Behaviour of Biomedical Materials*, 29:480–499.
- Gröning, F., Jones, M. E. H., Curtis, N., Herrel, A., O'Higgins, P., Evans, S. E., and Fagan, M. J. (2013). The importance of accurate muscle modelling for biomechanical analyses: a case study with a lizard skull. *Royal Society Interface*, 10:20130216.

- Harvey, P. H. and Pagel, M. S. (1991). *The comparative method in evolutionary biology*. Oxford University Press, Oxford.
- Hussein, A. I., Barbone, P. E., and Morgan, E. F. (2012). Digital volume correlation for study of the mechanics of whole bones. *Procedia IUTAM*, 4:116–125.
- Hutchinson, J. R. (2004). Biomechanical modeling and sensitivity analysis of bipedal running ability. I. Extant taxa. *Journal of Morphology*, 262(1):421–440.
- Hutchinson, J. R. (2011). On the inference of function from structure using biomechanical modelling and simulation of extinct organisms. *Biology Letters*, doi: 10.1098/rsbl.2011.0399.
- Hutchinson, J. R., Anderson, F. C., Blemker, S. S., and Delp, S. L. (2005). Analysis of hindlimb muscle moment arms in *Tyrannosaurus rex* using a three-dimensional musculoskeletal computer model: implications for stance, gait, and speed. *Paleobiology*, 31(4):676.
- Konigsberg, L. W., Hens, S. M., Jantz, L. M., and Junger, W. L. (1998). Stature estimation and calibration: Bayesian and maximum likelihood perspectives in physical anthropology. *Yearbook of Physical Anthropology*, 41:65–92.
- Lister, A. M. (2011). Natural history collections as sources of long-term datasets. *Trends in Ecology and Evolution*, 26(4):153–154.
- Livezey, B. C. (1993). An ecomorphological review of the dodo (*Raphus cucullatus*) and solitaire (*Pezophaps solitaria*), flightless Columbiformes of the Mascarene Islands. *Journal of Zoology*, 230(2):247–292.
- Maidment, S. C. R., Bates, K. T., Falkingham, P. L., VanBuren, C., Arbour, V., and Barrett, P. M. (2013). Locomotion in ornithischian dinosaurs: an assessment using three-dimensional computational modelling. *Biological Reviews*.
- Milne, N. and O'Higgins, P. (2012). Scaling of form and function in the xenarthran femur: a 100-fold increase in body mass is mitigated by repositioning of the third trochanter. *Proceedings of the Royal Society B*, 279:3449–3456.

- Natural History Museum (2014). Zoology collection database.
<http://www.nhm.ac.uk/research-curation/scientific-resources/collections/zoological-collections/zoology-specimen-database/>, note = "[Online; accessed 12-February-2014]".
- O'Higgins, P., Cobb, S. N., Fitton, L. C., Gröning, F., Phillips, R., Liu, J., and Fagan, M. J. (2011). Combining geometric morphometrics and functional simulation: an emerging toolkit for virtual functional analyses. *Journal of Anatomy*, 218:3–15.
- Oxford Museum of Natural History (2014). Life collections: Mammal database.
<http://www.oum.ox.ac.uk/database/zoology/mammals.htm>, note = "[Online; accessed 12-February-2014]".
- Panagiotopoulou, O., Curtis, N., O'Higgins, P. O., and Cobb, S. N. (2010). Modelling subcortical bone in finite element analyses: A validation and sensitivity study in the macaque mandible. *Journal of Biomechanics*, 43:1603–1611.
- Panagiotopoulou, O., Wilshin, S. D., Rayfield, E. J., Shefelbine, S. J., and Hutchinson, J. R. (2012). What makes an accurate and reliable subject-specific finite element model? A case study of an elephant femur. *Journal of The Royal Society Interface*, 9(67):351–361.
- Pandy, M. G. (1999). Moment arm of a muscle force. *Exercise and Sports Science Reviews*, 27:79–118.
- Porro, L. B., Metzger, K. A., Iriarte-Diaz, J., and Ross, C. F. (2013). *In vivo* bone strain and finite element modelling of the mandible of *Alligator mississippiensis*. *Journal of Anatomy*, 223(3):195–227.
- Roth, V. L. (1990). Insular dwarf elephants: a case study in body mass estimation and ecological inference. In Damuth, J. and MacFadden, B., editors, *Body size in mammalian paleobiology: Estimates and biological implications*, pages 151–180. Cambridge University Press, Cambridge.
- Rubin, C. T., Seeherman, H., Qin, Y., and Gross, T. (2013). The mechanical consequences of load bearing in the equine third metacarpal across speed and gait: the nonuniform distributions of normal strain, shear strain, and strain

- energy density. *The Journal of the Federation of American Societies for Experimental Biology*, 27(5):1887–1894.
- Sellers, W. I. and Manning, P. L. (2007). Estimating dinosaur maximum running speeds using evolutionary robotics. *Proceedings of the Royal Society B: Biological Sciences*, 274(1626):2711–2716.
- Smith, N. C., Payne, R. C., Jespers, K. J., and Wilson, A. M. (2007). Muscle moment arms of pelvic limb muscles of the ostrich (*Struthio camelus*). *Journal of Anatomy*, 211(3):313–324.
- Smith, R. (2009). The use and mis-use of the reduced major axis for line-fitting. *American Journal of Physical Anthropology*, 140(3):476–486.
- Stolk, J., Verdonschot, N., Cristofolini, L., Firmati, L., Toni, A., and Huiskes, R. (2000). Strains in composite hip joint reconstructions obtained through fea and experiments correspond closely. In *46th Annual Meeting, Orthopaedic Research Society*, Orlando, Florida.
- Sztefek, P., Vanleene, M., Olsson, R., Collinson, R., Pitsillides, A., and Shefelbine, S. (2010). Using digital image correlation to determine bone surface strains during loading and after adaption of the mouse tibia. *Journal of Biomechanics*, 43(4):599–605.
- Trabelsi, N., Yosibash, Z., Wutte, C., Augat, P., and Eberle, S. (2011). Patient-specific finite element analysis of the human femur: A double-blinded biomechanical validation. *Journal of Biomechanics*, 44(9):1666–1672.
- University Musuem of Zoology Cambridge (2014). Online resources.
<http://www.museum.zoo.cam.ac.uk/collections.archives/catalogues/>, note = "[Online; accessed 12-February-2014]".
- Videan, E. N., Fritz, J., and Murphy, J. (2007). Development of guidelines for assessing obesity in captive Chimpanzees (*Pan troglodytes*). *Zoo Biology*, 26:93–104.
- Warton, D. I., Wright, I. J., Falster, D. S., and Westoby, M. (2006). Bivariate line-fitting methods for allometry. *Biological Reviews*, 81:259–291.

- Weathers, W. W. and Siegel, R. B. (1995). Body size establishes the scaling of avian postnatal metabolic rate: an interspecific analysis using phylogenetically independent contrasts. *Ibis*, 137:532–542.
- Weber, G. W., Bookstein, F. L., and Strait, D. S. (2011). Virtual anthropology meets biomechanics. *Journal of Biomechanics*, 44:1429–1432.
- Westoby, M., Leishman, M. R., and Lord, J. M. (1995). On misinterpreting the ‘phylogenetic correction’. *Journal of Ecology*, pages 531–534.
- Winker, K. (2004). Natural history museums in a postbiodiversity era. *Bioscience*, 54(5):455–459.
- Yang, L., Zhang, P., Liu, S., Samala, P. R., Su, M., and Yokota, H. (2007). Measurement of strain distributions in mouse femora with 3D digital speckle pattern interferometry. *Optics and Lasers in Engineering*, 45:843–851.
- Zinoviev, A. V. (2013). Notes of Pelvic and Hindlimb Myology and Syndesmology of *Emeus crassus* and *Dinornis robustus* (Aves:Dinornithiformes). *Proceedings of the 8th International Meeting of the Society of Avian Paleontology and Evolution*, pages 253–278.